CHARACTERIZING THE NATURE OF THE SUB-CONTINENTAL LITHOSPHERIC MANTLE BENEATH PRINDLE VOLCANO, YUKON-TANANA UPLAND, ALASKA

by

IAN ALLEN USSERY

THESIS

Submitted in partial fulfillment of the requirements for the degree
of Master of Science in Geoscience at The University of Texas at
Arlington May 10th, 2019

Arlington, Texas

Supervising Committee:

Matthew Loocke, Supervising Professor
Merlynd Nestell
Erin Todd

TABLE OF CONTENTS

ACKNOWLEDGEMENTS

I thank Dr. Loocke my Supervising Professor for his unfathomable wealth of knowledge and patience as he guided me through such an academic achievement. The advice given by Dr. Nestell has been a great help in my many years here at the University of Texas at Arlington. I want to thank Dr. Todd from the USGS for allowing me to use samples from such a remote location. I am particularly grateful for the assistance given to me by my colleagues Danelle Carr and Crystal Luna for many fruitful discussions and general commiserating regarding this and ongoing work in the field of petrological geochemistry. My special thanks are extended to the Shimadzu Institute located at the University of Texas at Arlington for without their incredible instruments none of my endeavors would have been fruitful. Thank you to the University of Arkansas for allowing use on their newly acquired laser ablation mass spectrometry. Lastly, I would like to thank Samantha Caputi because without her mentoring and guidance throughout my academic and professional career I probably never have realized my passion for geology and would have most likely have not been put on this path to accomplish this academic milestone.

DEDICATION

I dedicate this thesis to my Supervising Professor, Dr. Loocke, my incredible wife, Tesch Ussery, my father, David Ussery, and my family and friends both professionally and socially. Dr. Loocke, honestly, I don’t know where to even begin. There is so much that I value about you as an educator, a supervisor, a friend, and as a person. I will always cherish our spontaneous conversations about geochemistry, movies, rocks, fences, Shimadzu, dogs, instrumentation, Marvel/DC canon, geology, and life in general. While it is bittersweet to think that I will be concluding this part of my life to which you were an integral part of throughout. I feel confident that our friendship will be one that we can enjoy for many years to come. To my darling and beautiful wife, there are not enough words to ever express the impact you have had on my life. You have supported me the entire way as I trudged through remedial courses at community college, as I embarked on an undergrad that I never dreamed would be in my future, and now to the culmination of me completing a master’s program. All of which would have been impossible for me before I had the honor of you coming into my life. You are my rock, the ultimate teammate, and soulmate for which to go through life. I love you Tesch and will always love you. To my father, David Ussery, for your guidance and support to help me become the man and person I am so blessed to have become over the years. I did not always make it easy for you, but you stuck with me, and I hope every day that I make you proud to call me your son. To Brandi and Baily Ussery, thank you for accepting me for who I am and for helping to keep our family a warm and happy place we can call home. A very heartfelt thank you goes to my Tarrant County College family. With the support of Samantha Caputi, Dr. Tommy Awtry, Danny Aguirre, Susan Davis, and Dr. Melissa Evans, I was able to pursue my educational endeavors while continuing to grow within the TCC community. To my dear friends, Ben and Katie Watkins and Sarah and Tyler Aldridge thank you for helping me keep sane throughout this journey, and I hope to be able to share all my future success with you every step of the way.

ABSTRACT

Characterizing the nature of the sub-continental lithospheric mantle beneath the Prindle Volcano, Yukon-Tanana Upland, Alaska

Ian Allen Ussery, MS.

The University of Texas at Arlington. 2019

Supervising Professor(s): Matthew Loocke, Merlynd Nestell, and Erin Todd

Prindle Volcano, an isolated alkali-basaltic cone in eastern Alaska is the northernmost volcanic center within the northern Cordilleran volcanic province (NCVP), a volcanic region along the northwestern region of North America. Prindle contains an ultramafic xenolith suite unlike any volcanic center within the region and perhaps the North American Cordillera. The suite provides an opportunity to examine the sub-continental lithospheric mantle beneath the region. Prindle volcano's xenolith suite includes various lithologies: lherzolite, harzburgite, olivine-websterite, dunite, and clinopyroxenite. Utilizing petrographical and geochemical analysis, comparisons of mantle xenolith suites within the Cordillera, and suites from similar tectonic settings around the world we can constrain the processes for the Prindle xenolith suite. Textural characteristics within Prindle xenoliths suggest events including shear deformation followed by melt-rock reaction during porous reactive flow. Additionally, the textures and chemistry of the most depleted dunite and harzburgites suggest a supra-subduction zone setting for origination. The lherzolites, websterites, and clinopyroxenites share direct textural and geochemical relationships that suggest an origin through focused, porous reactive flow. Previous studies conducted on other xenoliths within the Cordillera farther south identified a ~100-200°C temperature anomaly in the upper mantle beneath the NCVP due to a subducted slab window. Numerous studies indicate that the anomaly affects volcanic centers in the region. Prindle, however, resides on the margin of the mantle anomaly. With the evidence presented here, we suggest that the Prindle xenolith suite is derived from a localized lithospheric shear zone created by regional uplift above the anomaly located to the southeast. After the shear zone developed, a melt-rock reaction event by focused porous reactive flow with an alkaline fluid/melt occurred. It is surmised that the variability located at Prindle is due to the limited melt volumes during melt-rock interaction compared to those xenolith localities which are located above the regional mantle anomaly.

CHAPTER ONE:

INTRODUCTION

Our understanding of the nature of the mantle beneath the cratonic cores of the continents is the result of studies of peridotite xenoliths entrained in kimberlitic magmas (Walker et al., 1989; Carlson and Irving, 1994; Pearson et al., 1995a,b; Olive et al., 1997; Chesley et al., 1999), however, systematic constraints on the metasomatic processes, mechanisms of formation, and age of the subcontinental lithospheric mantle (SCLM) are limited to that which underlies the Phanerozoic orogenic belts which surround the cratons (e.g., Menzies, 1983; McBride et al., 1996; Handler et al., 1997; Peslier et al., 2000b). Peridotite xenoliths observed in alkali basalt volcanic centers within these Phanerozoic orogenic belts are interpreted to represent fragments of the mantle lithosphere beneath these regions.

One of the most extensively investigated Phanerozoic orogenic belts, the Canadian Cordillera, which borders the western margin of the Canadian craton, serves as a natural laboratory for the investigation of the mechanisms and processes responsible for the formation of the SCLM. The Cordillera formed through the successive accretion of lithologically variable (mainly arc-related) tectonic terranes to the stable margin of ancestral North America during the late Jurassic and Cretaceous (e.g., Monger et al., 1982; Gabrielse and Yorath, 1991; Peslier et al., 2002). The tectonic origin and nature of the lithospheric mantle beneath these terranes is relatively poorly constrained. The reason for the ambiguity is in part due to the potential modification of the SCLM beneath these terranes in the southern regions by subduction-related melts or fluids from the active Cascadia subduction zone which borders the Cordillera to the south (Gabrielse et al., 1991). Spinel peridotite xenoliths are observed to occur in many alkali basalt volcanic centers throughout the Canadian Cordillera. The accretionary nature of these terranes suggests that such mantle xenoliths may thus represent samples of the lithospheric mantle at the transition between oceanic lithosphere and cratonic continental lithosphere (Peslier et al., 2002); hence, these xenoliths can provide vital information regarding the mechanisms and processes responsible for the conversion of oceanic lithospheric mantle (OLM) into SCLM.

Although there have been a number of investigations of the various mantle xenolith suites within the Canadian Cordillera volcanic province (CCVP), those suites located in the northern portion of the province, the northern Canadian volcanic province (NCVP), have been the best documented in regards to their petrochemical and isotopic characteristics (Foster et al., 1966; Nicholls et al., 1982; Francis, 1987; Carignan et al., 1996; Shi et al., 1998; Edwards and Russell, 2000; Peslier et al., 2000a, 2000b) while investigations of the southern Cordillera suites have focused on geothermobarometry (Fiesinger and Nicholls, 1977; Fujii and Scarfe, 1982; Ross, 1983; Brearley and Scarfe, 1984; Brearley et al., 1984; Canil et al., 1987; Canil and Scarfe, 1989), determination of oxidation states (Canil et al., 1990), isotopic systematics (Sun et al., 1991; Xue et al., 1990; Peslier et al., 2000a, 2000b), and major and trace element abundances of whole rock and minerals (Sun and Kerrich, 1995; Peslier et al., 2002). Prindle volcano, an isolated, quaternary volcano (176 ± 16 ka) in eastern Alaska, lies at the northwestern most extent of the CCVP and is among the youngest of the volcanic centers within the province (Blondes et al., 2007). Due to its remote location, the xenolith suite at Prindle has suffered from a general lack of investigation. The extreme distance (~1800 km) between Prindle volcano and the Cascadia Subduction zone at the southern border of the CCVP would suggest that the mantle sampled by the Prindle xenolith suite should be among the least-affected by Cenozoic subduction-related melts and fluids in the province. Here, we report on the first thorough petrological characterization of the Prindle xenolith suite and provide a direct comparison with existing observations for other xenolith suites within the broader CCVP. In characterizing these samples, we seek to understand and constrain (i) the origin and petrogenetic history of the lithospheric mantle beneath Prindle volcano, (ii) the broader geochemical and tectonic context of Prindle volcano regarding the CCVP, and (iii) the mechanisms and processes of the formation of the SCLM.

CHAPTER TWO:

GEOLOGICAL BACKGROUND

THE CANADIAN CORDILLERA

Canadian Cordillera, a convergent orogen from the Phanerozoic which lies on the western border of the Canadian craton (Edwards and Russell, 1999 & 2000), is composed of several tectonostratigraphic terranes that were accreted to the margin of North America between the Jurassic to the Tertiary, of which the majority have oceanic-island arc affinities (Peslier et al., 2000; Colpron and Nelson, 2011; Figure 1). Spanning more than ~6400 km north and south down the western edge of the North American craton, the Canadian Cordillera includes over a dozen Late Tertiary to recent volcanic centers which have produced fresh mantle xenoliths. Modern magmatism in the Cordillera of North America is related closely to the tectonic setting between the Pacific, Juan de Fuca and North American plates which are characterized by convergent boundaries producing calc-alkaline stratovolcanoes and extensional or transtensional boundaries producing mafic alkaline magmatism which give rise to the NCVP (Edwards and Russell, 2000).

The NCVP is one of the most expansive Miocene to Holocene volcanic provinces in western North America and is made up of mostly mafic, alkaline volcanic rocks or basanite, and many of the volcanos contain abundant peridotite xenocrysts and xenoliths (Shi et al., 1998). The NCVP stretches from north to northwest starting in northwest British Colombia and the Alaskan panhandle up through the Yukon and eastern Alaska (Colpron et al., 2007; Figure 2). NCVP magmatism stretches across four major allochthonous tectonostratigraphic terranes:

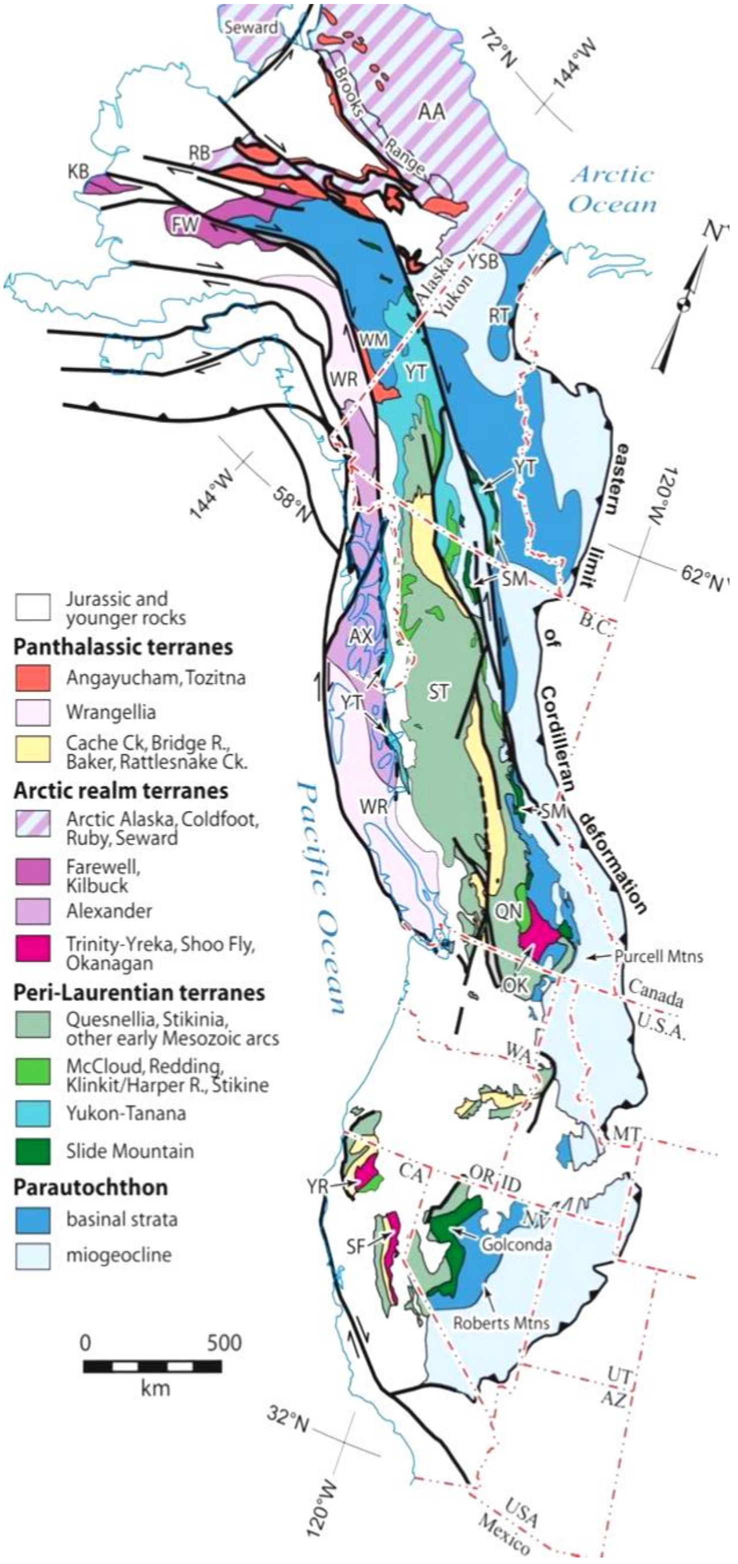

Figure 1: An overview map of the Paleozoic and Mesozoic terranes of the North American Cordillera (after Colpron and Nelson, 2011). Terranes are grouped according to faunal affinity and/or source region in early Palaeozoic time. Terrane and geological abbreviations: KB, Kilbuck; QN, Quesnellia; RT, Richardson trough; SM, Slide Mountain; ST, Stikinia; YSB, Yukon Stable Block; YT, Yukon–Tanana terrane in the Coast Mountains; WR, Wrangellia.

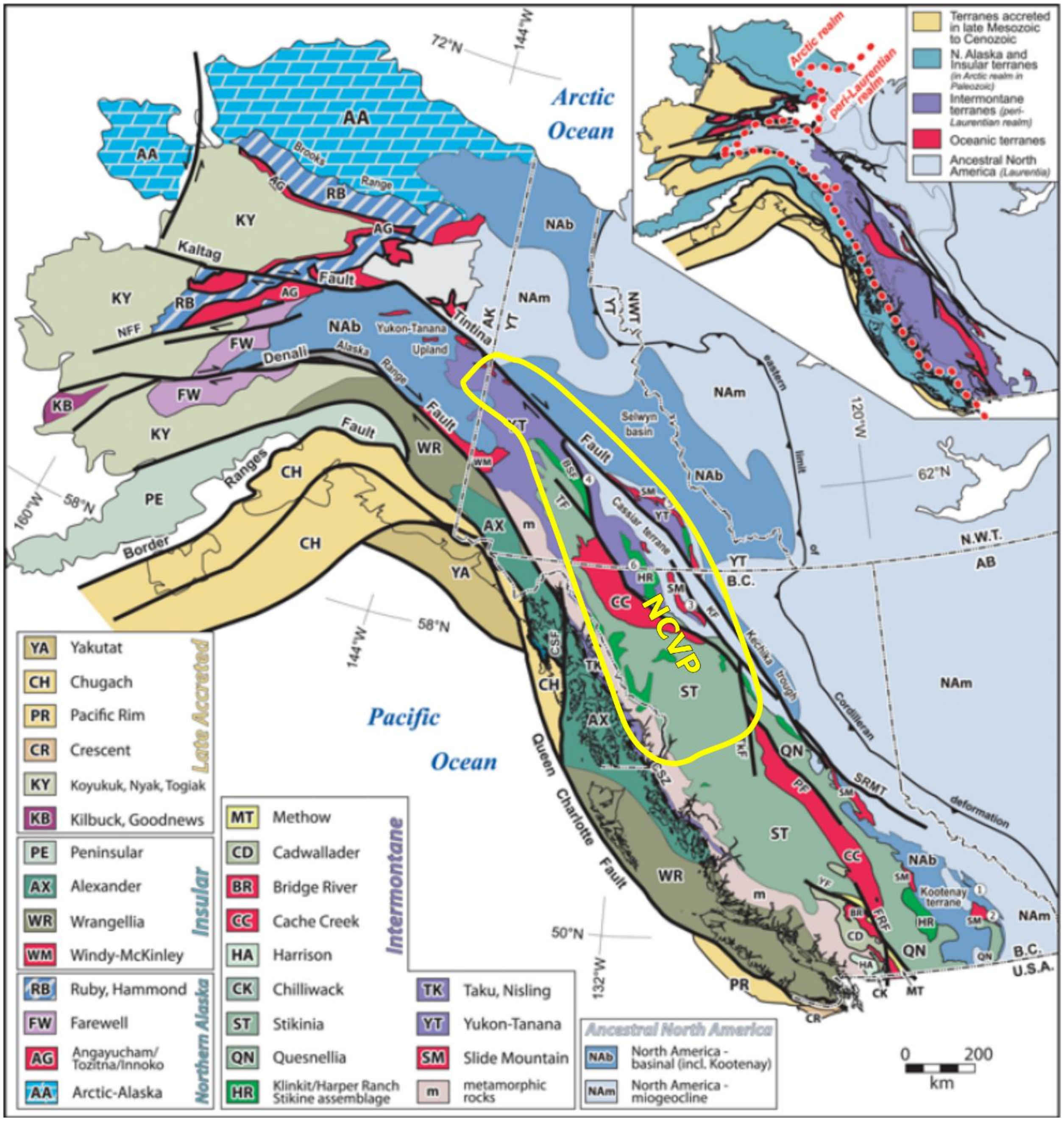

Figure 2: Regional context of the NCVP with regards to the terranes of the Canadian-Alask Cordillera (modified after Colpron et al., 2007). Abbreviations for major post-accretionary faults: BSF—Big Salmon fault; CSF—Chatham Strait fault; CSZ—Coast shear zone; FRF —Fraser River fault; KF—Kechika fault; NFF —Nixon Fork–Iditarod fault; PF—Pinchi fault; SRMT —southern Rocky Mountain trench; TkF—Takla-Finlay-Ingenika fault system; YK—Yalakom fault. Other abbreviations: AB—Alberta; AK—Alaska; B.C.—British Columbia; N.W.T.—Northwest Territories; YT —Yukon.

Cache Creek, Stikinia, Cassiar, and Yukon-Tanana terranes (Edwards and Russell, 2000; Figure 3). Cache Creek is thought to have originated from an oceanic basin since it consists of an oceanic mélange and abyssal peridotites of the late Paleozoic to Mesozoic eras that have been emplaced upon younger granitic plutons (Gabrielse and Yorth, 1991). The Stikinia terrane is a suite of late Paleozoic and Mesozoic plutonic, volcanic, and sedimentary rocks believed to have come from an island-arc setting (Gabrielse and Yorth, 1991). The Cassiar and Yukon-Tanana terranes are pericratonic assemblages comprised of an assortment of autochthonous sedimentary and metamorphic rocks derived from North America and allochthonous pieces of island-arc material which would have been emplaced onto the plate during the Mesozoic collision (Tempelman-Kluit, 1979; Gabrielse and Yorath, 1991; Mortensen, 1992).

The different mechanisms for triggering magmatism within the NCVP are highly debated and include, but are not limited to slab windows, mantle plumes, deglaciation, and crustal extension (Edwards and Russell, 1999). Currently, a crustal extension or back arc expansion mechanism is favored: five factors contribute to this conclusion: (I) the province is dominated by magmatism that is dominantly alkaline, silica undersaturated basalt; (II) the spatiotemporal pattern of magmatism originating from the center, then migrating north and south; (III) the high heat flow in the region indicative of a thinning lithosphere; (IV) the all but absent seismic activity in the NCVP; (V) the most substantial amounts of magmatism correlate to a period of greatest extension approximately 10 Ma in the Neogene (Edwards & Russell, 2000; Figure 4). However, there is strong evidence suggesting that the NCVP mantle source is depleted MORB mantle (DMM) that was later enriched, supporting a slab-window or a ridge subduction event hypothesis (Andronikov and Mukasa, 2010). In this model, mantle enrichment is related to flat-slab subduction of the North

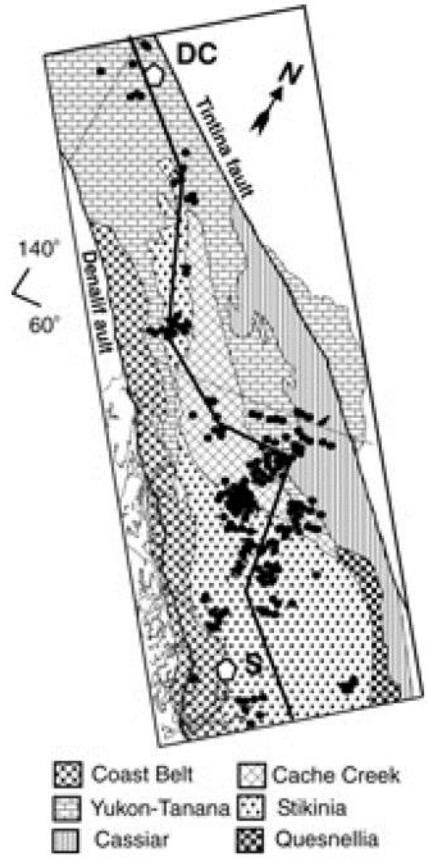

Figure 3: Map showing the distribution of volcanic centers in the NCVP with respect to major terrane boundaries and the Denali and Tintina fault systems (after Edwards and Russell, 2000).

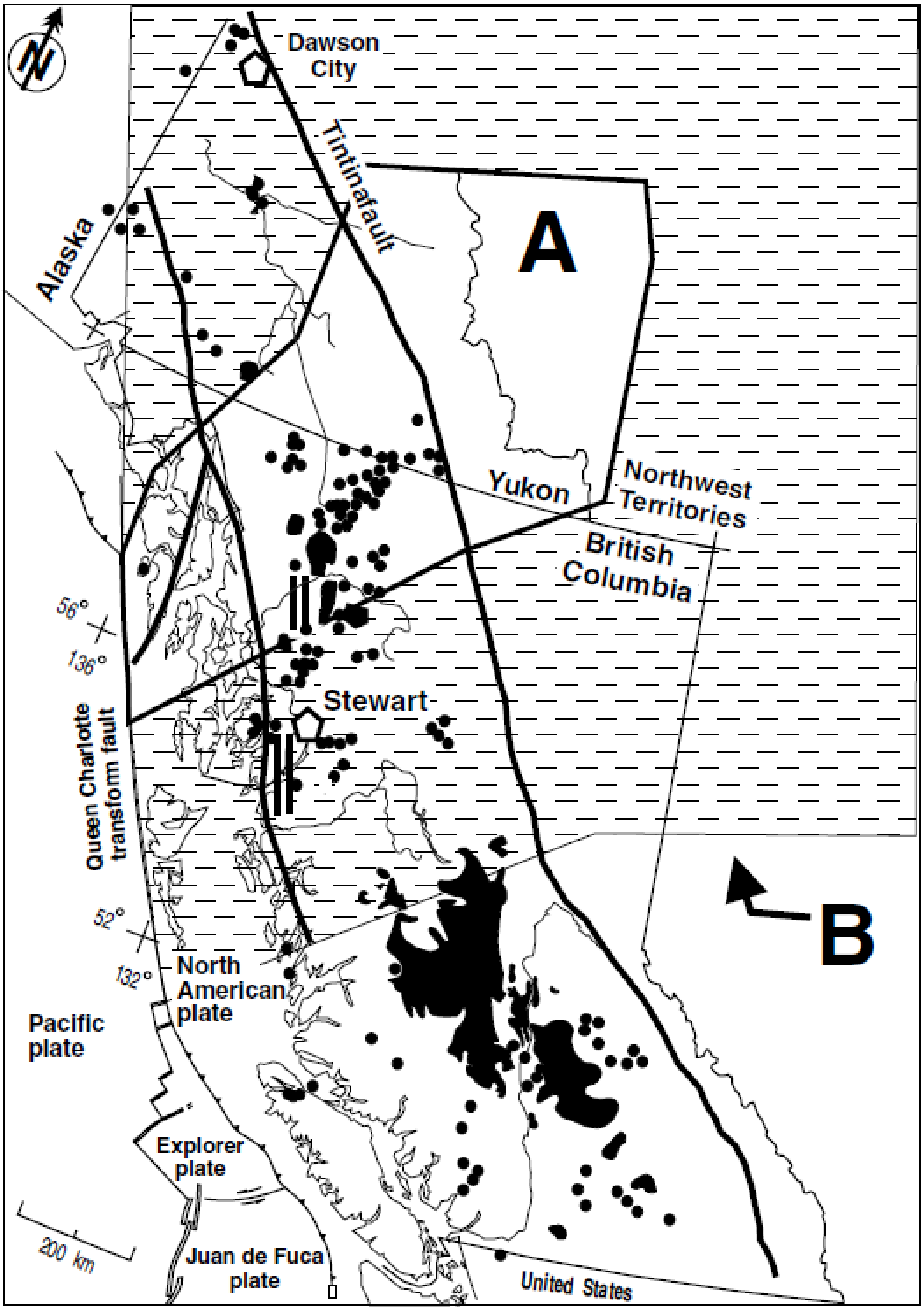

Figure 4: Map showing the distribution of Neogene volcanism in the Canadian Cordillera compared to the projected area of slab window at 20 Ma (A) and the projected area of current slab window (B) (e.g., Edwards and Russell, 1999). After Edwards and Russell, 2000.

Pacific lithospheric slab leading to the eventual subduction of the Pacific-Farallon spreading ridge thus creating a slab window under the NCVP at around 10 Ma that introduces an influx of Pacific material from the asthenosphere to the mantle (Thorkelson and Taylor, 1989; Hyndman and Hamilton, 1993; Hart and Villeneuve, 1999). Several lines of evidence strongly support this model. Gill (1981) developed a model comparing La (ppm) versus Nb (ppm) which illustrates an elemental shift from volcanic arc to mid-ocean ridge to ocean island and/or intraplate affinity for igneous rocks with increasing Nb concentrations. In the western portion of Canada, there was an arc-like signature in Eocene time with La/Nb ratios very similar to mantle metasomatism and subduction. However, a shift is seen from volcanic arc to intraplate tectonic affinity beginning ~47 Ma after the cessation of the Eocene arc and a distinct lack of magmatism in the Oligocene (Morris and Creaser, 2003; Breitsprecher et al., 2003; Ickert et al., 2009; Figure 5). In the late Oligocene to early Miocene (~24 Ma), intraplate volcanism began and by 10 Ma (mid-Miocene) was widespread and lasted until a few hundred years ago (Carignan et al., 1994; Shi et al. 1998; Edwards and Russell, 2000; Madsen et al., 2006). The geochemical shift occurred at the same time as the opening of the Northern Cordilleran slab window and the vanishing of the oceanic lithosphere that was subducted which was under much of the western portion of Canada in the Paleogene. The predicted window continued to expand throughout the Neogene-Holocene, and is believed to be ~1500 km long and extends from near the Alaskan-Canada border to southern British Columbia (Thorkelson et al., 2011; Figure 6). It is argued that the shift observed by the La/Nb model of arc-type mantle to an intraplate volcanic field in western Canada is a passive response to the motion of the Pacific slab towards the north away from the Juan de Fuca slab migrating eastward, and as the slabs grew apart this invited an uprising of asthenosphere to fill the

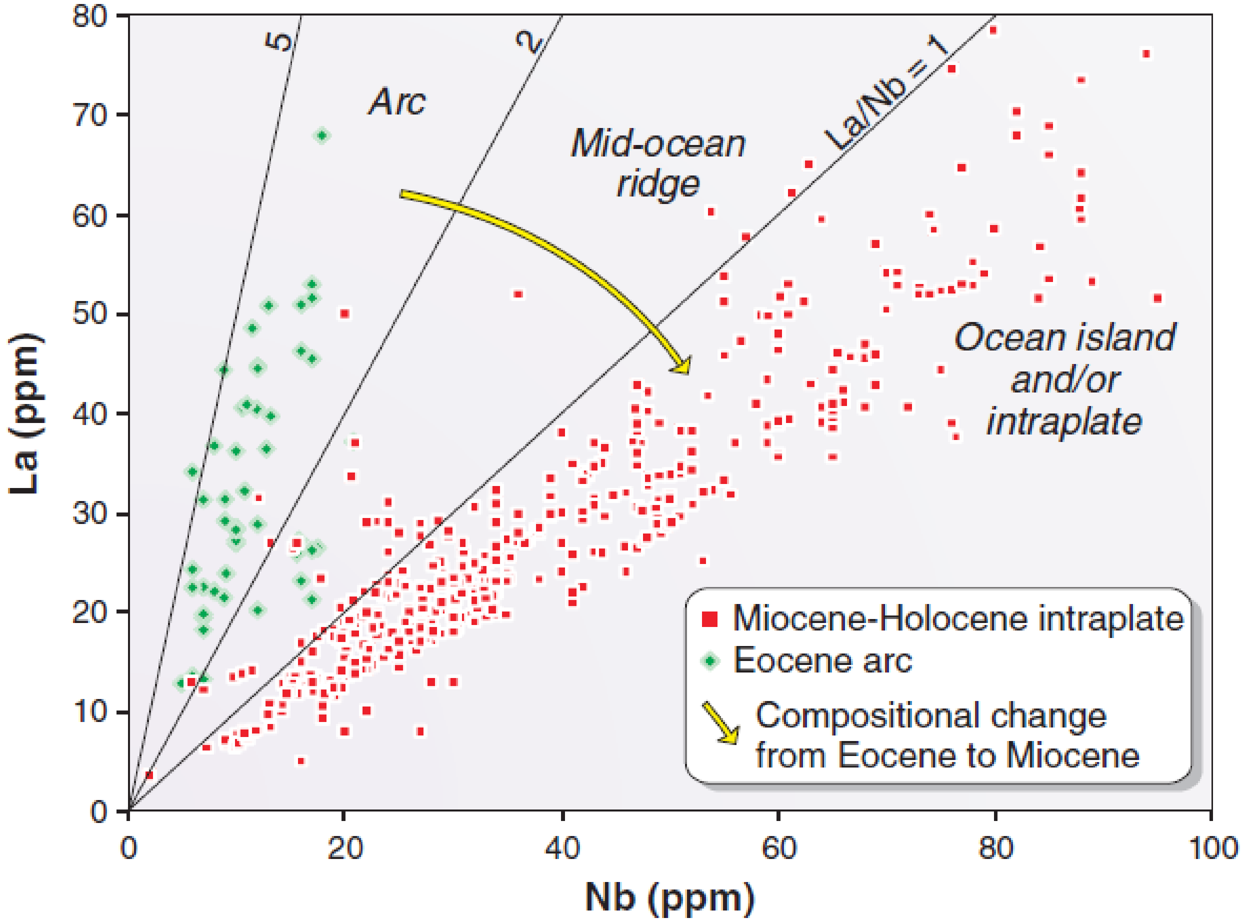

Figure 5: La/Nb tectonic discrimination diagram illustrating the change in the tectonic affinity of igneous rocks in western Canada from Eocene (volcanic arc) to Miocene–Holocene (ocean island and/or intraplate) indicated by the arrow. After Thorkelson et al. (2011).

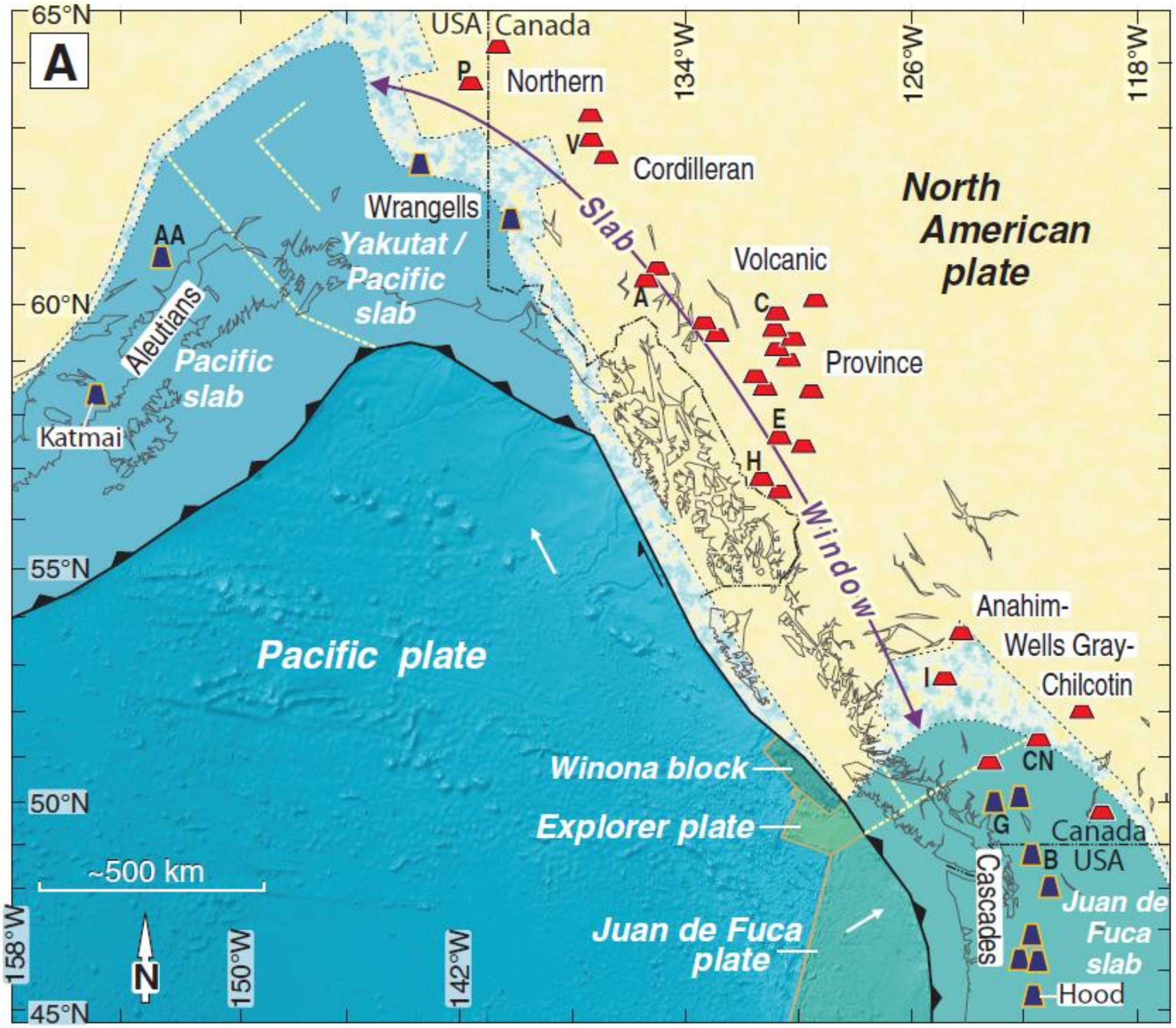

Figure 6: Map showing the regional context of the Northern Cordilleran slab window and late Cenozoic to Holocene volcanic regions (after Thorkelson et al., 2011). Tectonic plates and subducted slabs to a depth of ~250 km beneath North American plate, showing Northern Cordilleran slab window. Mottled pattern along margins of slabs represents subducted crust that is likely to have been physically or thermally degraded, or removed by slab breakoff relative to the model of uneroded slab edges. Volcano symbols represent clusters of volcanoes or individual volcanoes. Columbia River basalts and Neogene forearc volcanic centers were not included in the study. Volcano abbreviations: B—Mount Baker, G—Mount Garibaldi, CN—Chilcotin North, I—Mount Itcha, H—Hoodoo Mountain, E—Mount Edziza, C—Canyon Creek, A—Alligator Lake, V—Volcano Mountain, P—Mount Prindle, AA—Aleutians near Anchorage.

vacancy. (Thorkelson et al. 2011; Figure 6). As the asthenospheric mantle rose, decompression melting occurred which thermally eroded the North American lithospheric mantle, and both the asthenospheric mantle and lithospheric mantle served as sources for the intraplate volcanic field

(Carignan et al., 1994; Shi et al. 1998; Edwards and Russell, 2000). In addition to geochemical signatures supporting the slab window model, teleseismic data from the NCVP supports the claim that a slab window exists for most of the region and intensifies moving southward (Frederiksen et al., 1998). The claim for an existing slab window is illustrated by a distinct P-wave slowness anomaly detected at approximately 61° N 137° W about 220 km inbound from the coast and is approximately 200 km wide and extends to depths of 400-500 km in the mantle beneath the southern Yukon (Frederiksen et al., 1998; Figure 7). The range of the P-wave anomaly would affect xenolith suites within the NCVP such as Alligator Lake, Mt. Llangorse, and Hirschfeld Creek most directly (Shi et al., 1998; Figure 8). Additionally, the P-wave slowness anomaly is also thought to represent a temperature anomaly of 100-200° C compared to the surrounding mantle (Frederiksen et al., 1998). However, there is another anomaly, a relatively shallow region of high-velocity at the extreme west of the teleseismic study which is illustrating the presence of either the subducting Pacific slab or boundary between orogenic and cratonic mantle possibly located in the northwestern portion of the NCVP (Frederiksen et al., 1998; Figure 7).

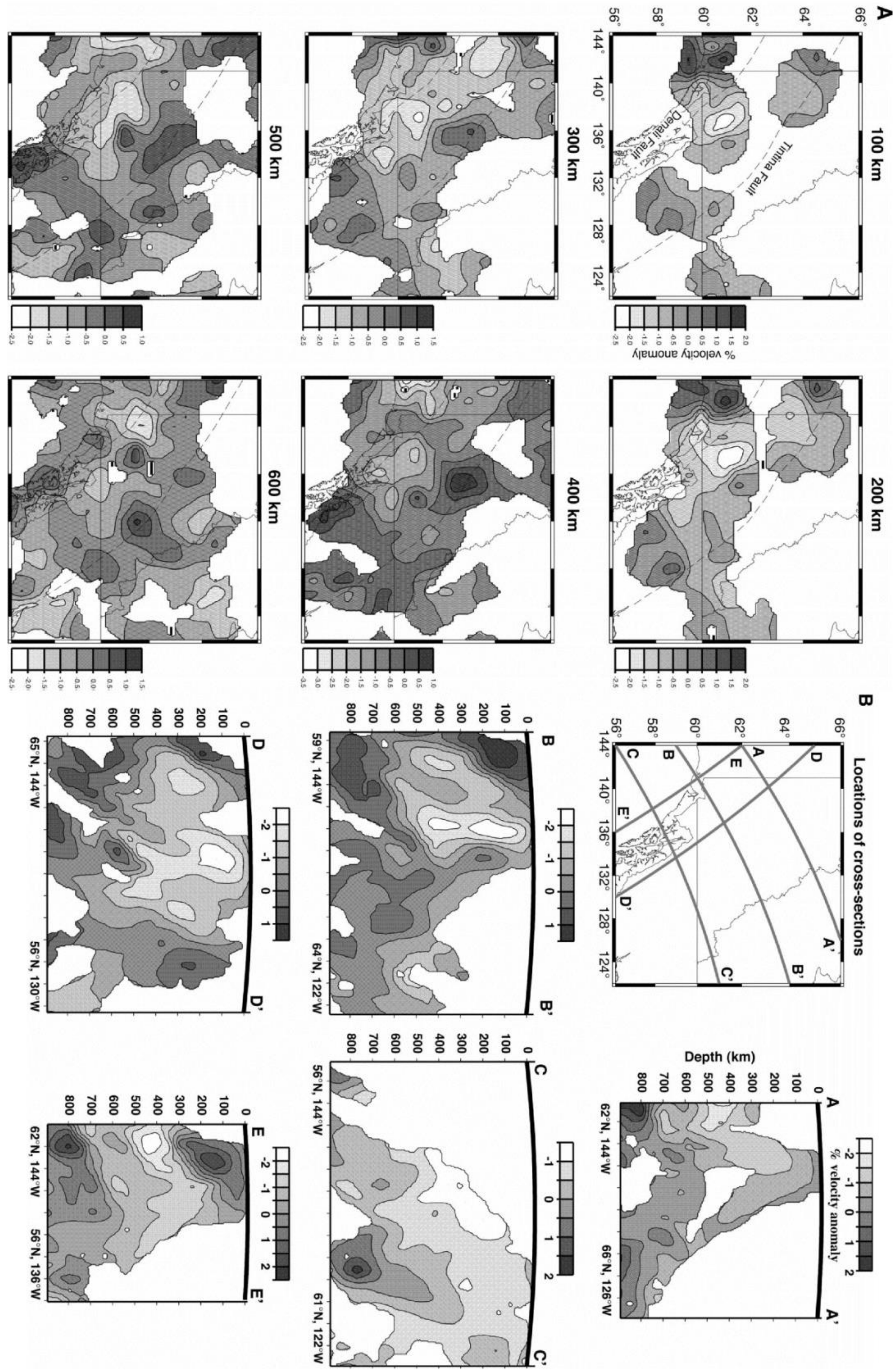

Figure 7: Results of teleseismic data presented as 2D sections through the tomographic model for the NCVP mantle anomaly. (A) Plan views and (B) cross-sections contain whited-out areas where there was inadequate data coverage. After Frederiksen et al. (1998).

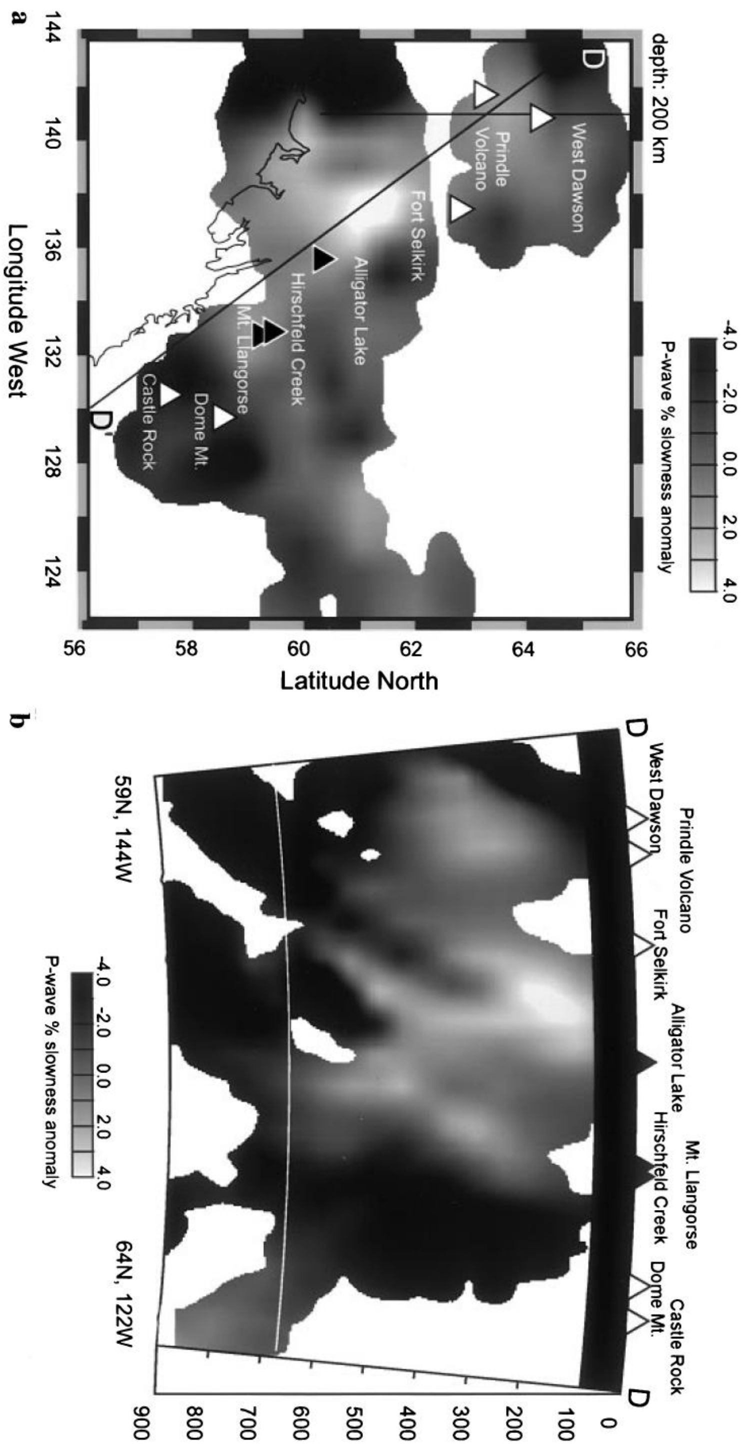

Figure 8: Map and cross-section of teleseismic images for the upper mantle beneath the northern Cordillera with the locations of the various NCVP xenolith suites superimposed in panel A (after Shi et al., 1998).

THE YUKON-TANANA TERRANE

The Yukon-Tanana terrane lies on the north-western portion of the Canadian Cordillera and extends over ~2000 km; it includes both pericratonic rocks from the North American tectonic plate and para-autochthonous pieces of volcano-sedimentary, oceanic, and granitic material which would have been emplaced onto the plate during the Mesozoic collision (Tempelman-Kluit, 1979). The modern Yukon-Tanana terrane is believed to be a series of arc-back arc systems that were formed on a crust of continental or transitional composition (Piercey et al., 2001). On the east-northeastern boundary of this para-autochthonous terrane, there is the Slide mountain terrane. Which is a combination of discontinuous slices and slivers of oceanic terrane that are a product of a marginal rift basin of late Devonian to Permian age that were once between a belt of rifted pericratonic pieces and the continent which was home to a series of arcs from the Devonian through the Jurassic (Ghent et al., 2008; Figure 9). The nucleus of the terrane, the Snowcap assemblage, is believed to have originated along the distal Laurentian continental margin but was rifted away along with portions of the Slide Mountain terrane starting in the mid-Paleozoic formation of the Slide Mountain Ocean because the basement possess isotopic, geochemical, and provenance characteristics that are similar to the northwestern Laurentian margin (Nelson et al., 2006). Both rifted portions of the Yukon-Tanana and Slide Mountain terranes are believed to have evolved in similar settings during the mid to late Paleozoic time, as arc magmatism developed in the Yukon-Tanana, so did rift magmatism in the Slide Mountain terrane (Colpron et al., 2007; Figure 10).

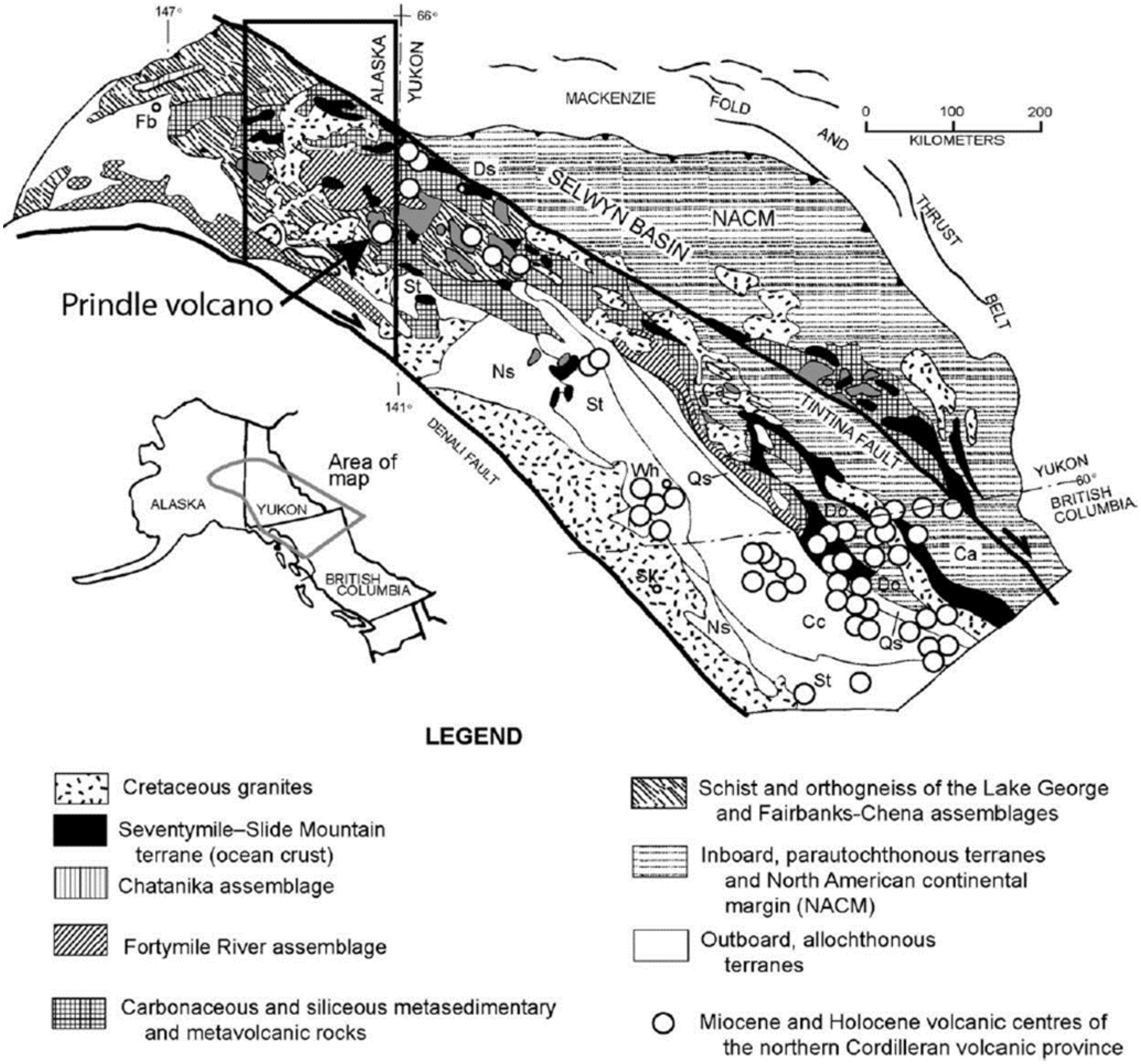

Figure 9: Map representing the regional geology of the Yukon-Tanana terrane within Alaska, Yukon, and British Columbia. Location of Prindle volcano and other volcanic centers (open circles) throughout the terrane. Box illustrates the location of Tanacross C-2 quadrangle (after Ghent et al., 2008).

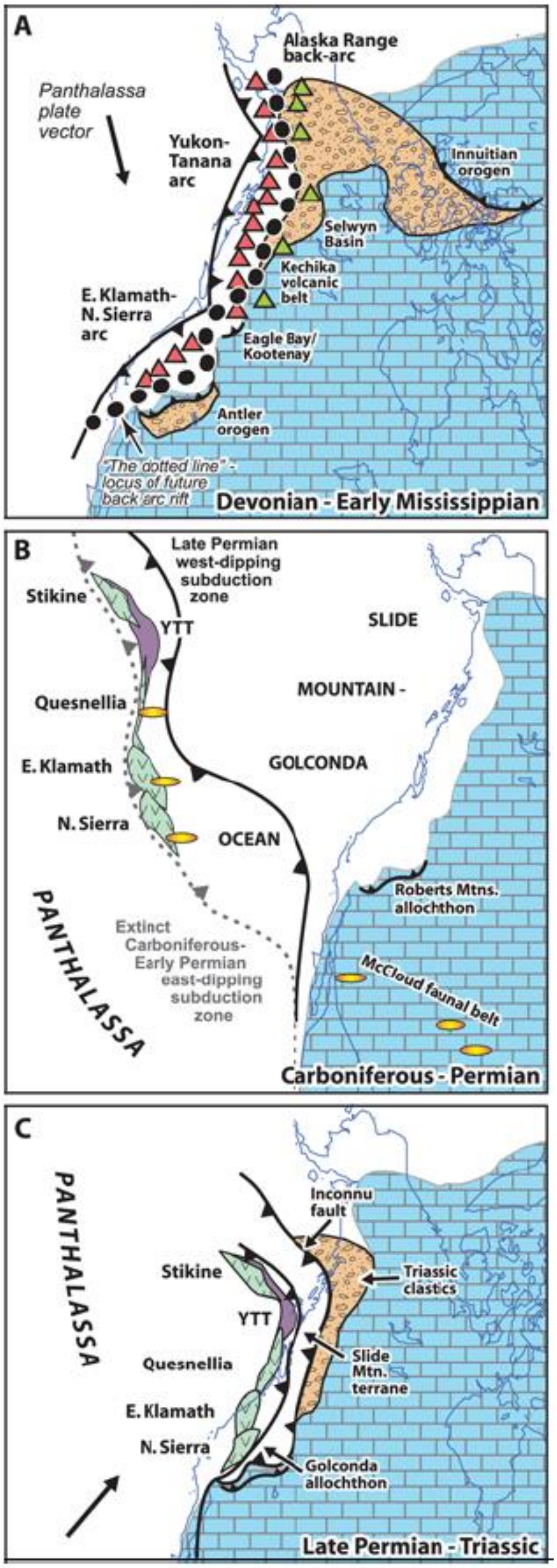

Figure 10: A schematic reconstruction of the paleogeographic evolution of the peri-Laurentian realm from the mid-Paleozoic to the early Mesozoic (after Colpron et al., 2007).

The co-evolution of the two terranes persisted into the late Permian when east-dipping subduction at the eastern edge of the terrane caused the closing of the Slide Mountain Ocean in the mid-Jurassic. The closing brought the remnants of the two terranes and others closer to the Laurentian continental margin which is recorded in Triassic strata on both the terranes and Laurentia (Beranek and Mortensen, 2007).

The other magmatic events in this region occurred in the Mesozoic and lesser Cenozoic and are believed to be a product of extension due to subduction-related events in the zone between the Tintina fault and Denali fault. The extension allowed for the asthenosphere to well-up and produce a small series of decompression melting events in the area during the final stages of amalgamation between the terranes and the continent (Hansen, 1990). Modern magmatism which obscures and overprints the pre-mid-Mesozoic history of the terrane is strongly evidenced to have contributed to decompression melting that is either caused by a nearby termination point of a slab window located to the southeast of the Yukon-Tanana terrane or a product of aggressive expansion in the area (Edwards and Russell, 2000; Thorkelson et al., 2011). However, the true nature of the lithospheric mantle underneath these terranes and its tectonic origin are heavily debated and scrutinized, and it is presumed that the Prindle volcano's xenolith suite is derived from one or both of the sources above.

PRINDLE VOLCANO

Prindle volcano is located in the easternmost part of Alaska, United States, near the Dennison Fork of the Fortymile River and East Fork just west of Dawson City, Yukon Territory within the Yukon-Tanana Upland between the Tintina and Denali fault systems. More specifically, the Prindle Volcano is found in the Tanacross C-2 quadrangle at (63.7196^{o} N 141.6223^{o} W) (Figure 11) around the northwestern-most point of the NCVP within the Canadian Cordillera. Prindle volcano measures 1250 m high in elevation and ~1000 m in diameter with a crater around 90 m (Figure 12), is classified as a cinder-cone volcano, and is solely characterized by alkali-olivine basalt which is more commonly referred to as basanite (Foster et al., 1966, Wood and Kienle, 1990; Blondes et al., 2007; Andronikov and Mukasa, 2010). The basement rock below Prindle Volcano is a combination of Devonian and Mississippian augen gneisses and amphibolite of the Lake George assemblage which formed along the ancient Pacific margin of North America and isotropic granitoids from the Cretaceous which intrude throughout the Yukon-Tanana terrane and have mica cooling ages of approximately 110 Ma (Wilson et al., 1985; Dusel-Bacon et al., 1995).

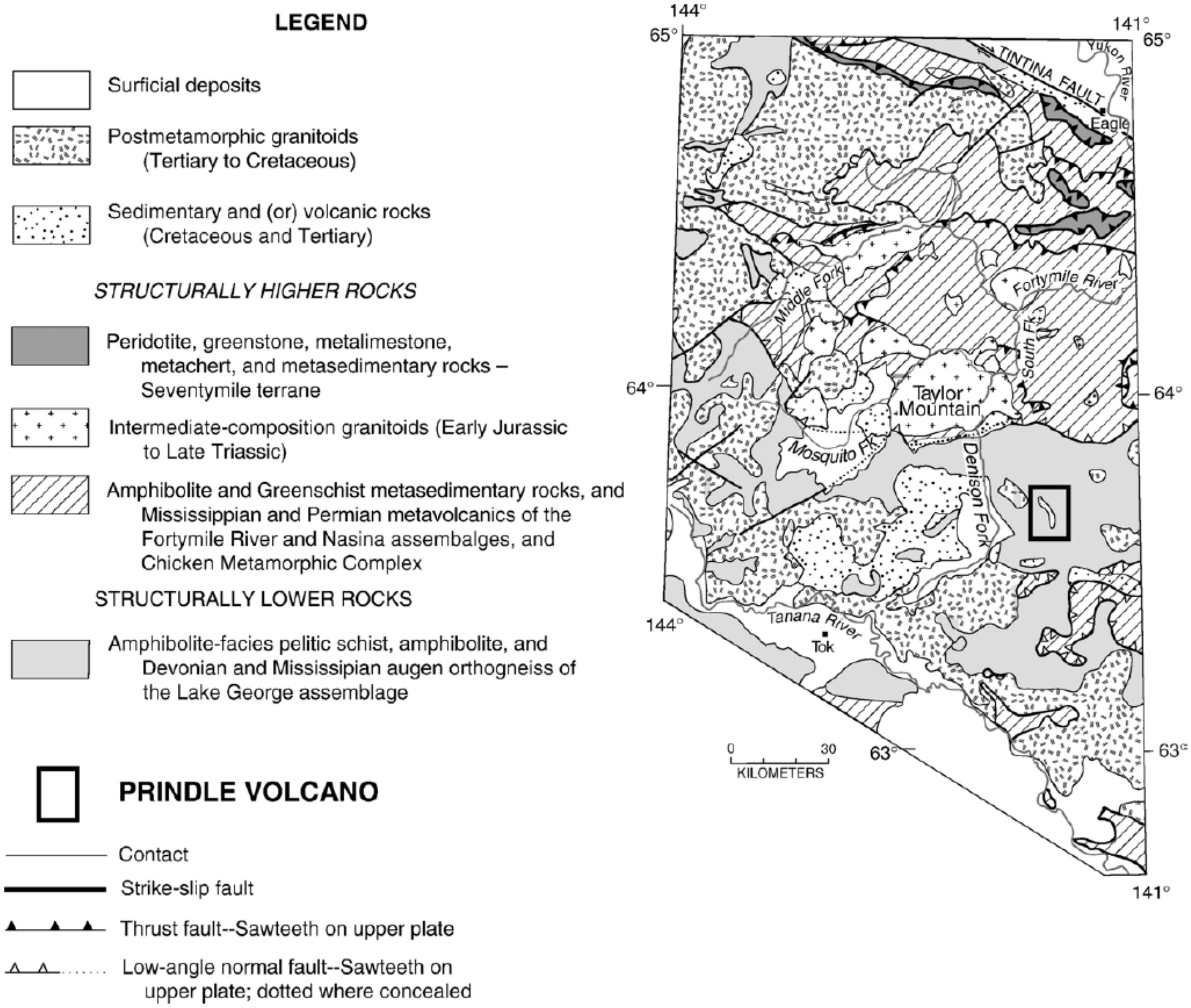

Figure 11: A simplified geologic map of the environment surrounding the Prindle Volcano. After Ghent et al. (2008).

Figure 12: An aerial photograph of the Prindle Volcano caldera. Note the dense vegetation covering the slopes of the volcano.

Although basanite is typically defined as plagioclase bearing basic lava where feldspathoids constitute more than 10% by volume, previous studies of Prindle lavas observe that it is not uncommon to have a complete lack of plagioclase within the flow (Williams et al., 1954; Andronikov and Mukasa, 2010). An assortment of lower crustal and upper mantle xenoliths can be found in abundance within Prindle volcano's basanite flow which varies from quartzofeldspathic to ultramafic and mafic lithologies (Roughley et al., 2000). All samples collected off the basanite flow from Prindle volcano have typically been described as containing either granitic/crustal xenoliths or peridotite/mantle xenoliths or both. According to Shi et al. (1998), when compared to volcanic centers in the southern CCVP, the Prindle volcano mantle xenoliths are a unimodal suite composed of mostly fertile lherzolite which lacks refractory harzburgite xenoliths. Fertility, in the petrological sense, is based on the fraction of low-solidus minerals which affects the ability of the rock to produce magma (Albarede, 2009).

MANTLE XENOLITH AND THE CCVP

Mantle xenoliths such as those from unimodal suites are interpreted to have been brought up from depths of 30-80 km by the alkaline basalt; hence, the xenoliths are samples of lithospheric mantle and can retain evidence of past melting events (Shi et al., 1998). However, bimodal suites which contain both refractory harzburgites and fertile lherzolites are thought to originate from the asthenospheric mantle, potentially reaching depths of 400-500 km (Shi et al., 1998). Olivine, clinopyroxene, and orthopyroxene, the dominant phases in peridotites such as lherzolites and harzburgites, are complex solid solutions that have wide stability fields which depend on bulk composition and pressure. These major phases are accompanied by plagioclase, spinel, or garnet depending on the boundaries between low, moderate, or high pressures, respectively, thus resulting in a depth-dependent, 4-phase or, rarer, 5-phase assemblage. Plagioclase peridotite is stable over a shallow pressure/depth range (0-15 Kbar, 0-1.5 GPa, or 0-45 km), while spinel peridotite is stable at moderate depths (5-27 Kbar, 0.5-2.7 GPa, or 15-90 km) and garnet peridotite is stable at the deepest depths in the upper mantle (15+ Kbar, 1.5+ GPa, or 45+ km) (Simon et al., 2008; Figure 13). All three varieties can generally be found as xenoliths in alkaline basalts around the world, though spinel peridotites are more common than those of the plagioclase or garnet-bearing varieties (Perkins and Anthony, 2011). Rare spinel + plagioclase-bearing xenoliths are generally characterized by areas with a thin lithosphere and are often interpreted to represent the broad transition between the spinel and plagioclase stability fields (Sen and Leeman, 1991; Worner and Zipfel, 1996; Ducea et al., 2002). Additional geochemical studies indicate that the plagioclase found in these types of rocks may have a metasomatic origin (Ducea et al., 2002). The reactions from transitioning from the plagioclase to spinel and then to the garnet stability fields are a reflection of the minerals differences in densities which is in part due to their different aluminum coordination (Perkins and Anthony, 2011).

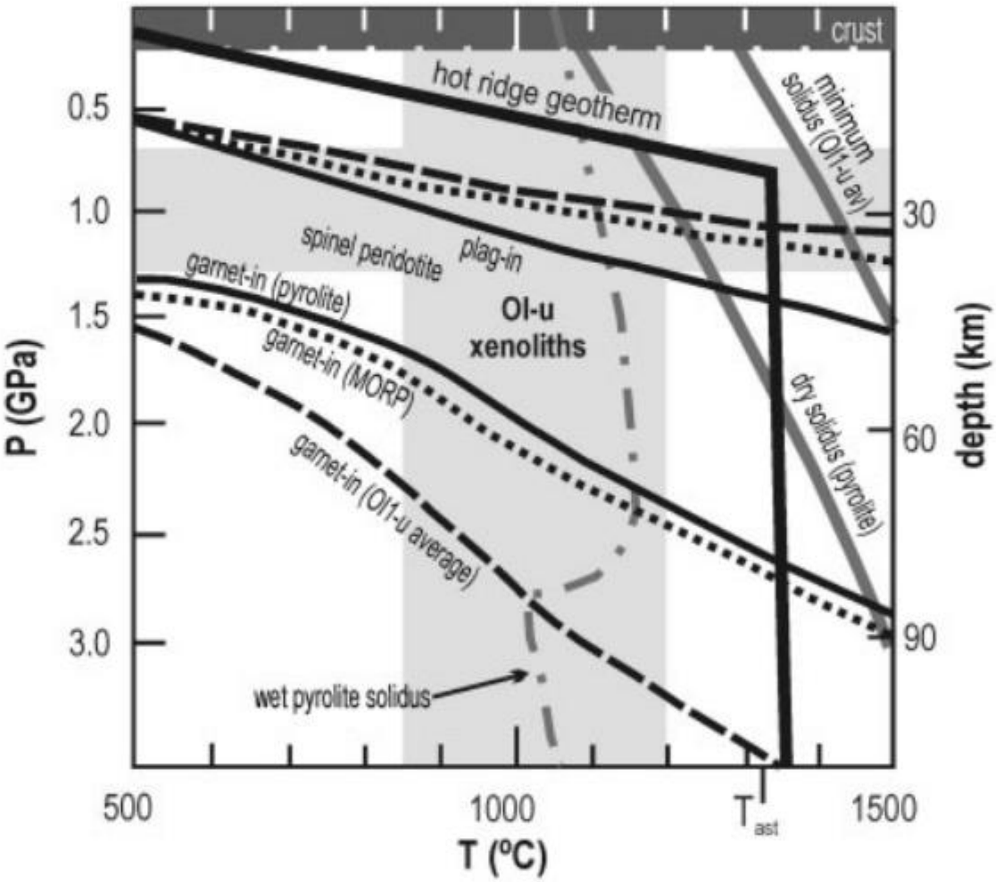

Figure 13: A pressure-temperature-depth diagram illustrating the general relationships between the various phase boundaries that govern the transition between the plagioclase-, spinel-, and garnet-facies assemblages in mantle peridotites. After Simon et al. (2008).

The following oxides are the major components in peridotites, SiO_2, Al_2O_3, FeO, MgO, and CaO. Though Na_2O and Cr_2O_3 are generally present in concentrations at or around 1 wt%, these two oxides may be significant because variations in both of their compositions can alter the depth and pressure of the transition from plagioclase to spinel peridotite (Nickel 1986; Klemme, 2004).

Previous studies have shown that northern Canadian Cordillera harzburgites contain higher SiO_2 and Na_2O but are poorer in FeO when compared to those from the southern Canadian

Cordillera (Francis, 1987). The lack of FeO is thought to be, in part, due to the reaction of ascending melts with the surrounding upper mantle causing the dissolution of clinopyroxene, which produces a modified melt that will be undersaturated in clinopyroxene (Kelemen et al., 1992). The characteristics observed of the lherzolites within the Canadian Cordillera, thus far, are not unique and resemble lithospheric mantle found under newly formed orogenic belts that border cratons (Peslier et al., 2002).

CHAPTER THREE:

SAMPLES AND SAMPLE PREPARATION

Nineteen samples collected and provided by Dr. Erin Todd (U.S. Geological Survey – USGS), were made available for this study. They have been categorized and indexed using provided sample information (Table 1 and Appendix I), including a brief qualitative sample description, a visual count of xenoliths, and broad average measurements of the size of xenoliths. Preliminary whole rock analyses funded by the USGS- in support of a broader study of tectonics and metallogeny of the Yukon-Tanana uplands in Eastern Alaska, were done in 2016 and 2017 by ALS Global (Vancouver, CA) utilizing inductively coupled plasma atomic emission spectroscopy (ICP-AES: major elements) and inductively coupled plasma mass spectroscopy (ICP-MS: trace elements).

SAMPLE DESCRIPTIONS

Once in our lab, all samples were photographed and described in detail with regards to texture, fabric, weathering, alteration, color, size, shape, and mass (see Appendix II for xenolith descriptions). Xenoliths ≥ 0.1 cm in length along any axis were measured at the maximum width. Each xenolith has been hand drawn and described utilizing a 20x hand lens. These descriptions include grain size, grain shape, texture, color, mineralogy, weathering, and alteration. At least one piece from every sample was chosen based on the greatest amount of exposed xenoliths to slab and thin-section for further petrographic and geochemical analysis.

Table 1: Sample locations and notes provided by the USGS and a count of the number of thin sections derived from each sample.

Sample ID	Latitude	Longitude	Dominant Lithology	Thin Sections	Material Notes from the USGS
	Datum: WGS84				
15ATe122C	63.712	-141.633	basalt	4	2 pieces of basalt; one with 2+ large oxidized perid. xenoliths; other with at least 6 small (≤1cm) "fresh" perid. xenoliths
15ATe122D	63.712	-141.633	basalt	1	Multiple perid. xenoliths (>>cm) in lava; fresh, relatively unoxidized
15ATe122E	63.712	-141.632	tonalite	1	Inclusion of tonalite/orthogneiss in lava
15ATe122F1	63.712	-141.632	peridotite	1	Single xeno, 2pcs.; dunite, unoxidized
15ATe122F2	63.712	-141.632	peridotite	3	2 xenos, both more oxidized; one more banded, one more speckled
15ATe122F3	63.712	-141.632	peridotite	2	Single xeno, 3 pcs; mostly oxidized; one piece from core, two cut from margins (with glassy/reaction margin)
15ATe122F4	63.712	-141.632	peridotite	2	Single xeno, 2pcs.; mosly oxidized; blebby oxidized zone in one piece
15ATe122F5	63.712	-141.632	peridotite	2	Single xeno, multiple pieces; mostly oxidized, but heterogeneously /blebby distributed
15ATe122F6	63.712	-141.632	peridotite	1	Single xeno, 2pcs; unoxidized
15ATe122F7	63.712	-141.632	peridotite	3	Single xeno 3 small pieces; mostly oxidized
15ATe122F8	63.712	-141.632	peridotite	0	Single xeno 2 small pieces; mostly oxidized
16ATe101A1	63.650	-141.546	basalt	2	More dense lava, from distal flow lobe; 2 large pieces, each with multiple <cm crustal AND peridotite xenoliths
16ATe101C	63.650	-141.546	basalt	2	More dense lava, from distal flow lobe; 2 pieces, each with multiple <cm crustal AND peridotite xenoliths (one crustal xeno >cm)
16ATe102A	63.716	-141.628	peridotite	2	Moderately oxidized peridotite xeno
16ATe102C	63.715	-141.628	peridotite	1	Mostly oxidized perid. xeno
16ATe102D	63.714	-141.628	peridotite	3	Lava with several small xenos (>cm and <cm), including both unoxidized perid, plus other potentially crustal xeno (circled)
16ATe102E1	63.713	-141.629	peridotite	1	Small xeno fragment in basalt; perid. fragment has mineral seg zone/vein of unoxidized min. (pyx?)
16ATe102E2	63.713	-141.629	peridotite	0	Pyroxenite xeno, 4 <cm pieces, two on margins, two homogeneous fragments.
16ATe102F	63.713	-141.629	basalt	2	3 pieces of vesicular basalt from near crater rim, each within cm's of glassy margin (glassy rim preserved in 2 pieces); at least 4 perid. Xenos preserved in these pieces, 3 unoxidized, on smaller oxidized one.

Hand samples include both massive and vesicular dark-grey basanites with microcrystalline to fine-grained crystalline groundmass each hosting fresh, unoxidized to heavily oxidized ultramafic xenoliths. The ultramafic xenoliths exhibit little to no fabric in hand sample; however, flow lineation defined by elongate vesicles are observed within most of the basanite host rock. Observed xenoliths are a combination of pyroxenite and peridotite that range from websterites to lherzolites, harzburgites, or dunites. Of note is that the observed peridotite is "dry," lacking hydrous minerals (e.g., mica, amphibole) in hand sample.

SAMPLE PREPARATION

Selected samples were trimmed to fit a series of silicon molds measuring ~3 cm wide, 3-4 cm long, and ~2.5 cm thick. The interior of the silicone molds was coated with high vacuum grease, and the samples were placed within the molds and submerged in Buehler Epoxicure 2. The molds were then placed in a bell jar attached to a vacuum pump and left overnight, to ensure sufficient impregnation while the epoxy cured. Hardened samples were placed on a grinding wheel to remove epoxy and bubbles from the area of interest and to provide a flat surface. The samples were then trimmed, if necessary, to orient the xenoliths of interest to fit on a standard 2.67 x 4.62 cm thin section slide. Selected thin section surfaces were polished with 240 grit silicon carbide paper on a lap wheel, followed by a 600 grit paper and then 12.5 grit and 0.05 µm grit alumina polishing powder on a glass plate. Samples were then placed in an ultrasonic bath and rinsed with isopropyl alcohol to ensure that all polishing grit was removed from the polished surface. The samples were then mounted to labeled, frosted thin-section glass using the same epoxy as the impregnation step, using a thin section press to ensure even epoxy distribution and bubble-free adhesion. Epoxy cured for at least twenty-four hours, after which the samples were removed from the press and then trimmed using a thin section saw and grinder designed for establishing a specific thin section thickness. Thin sections were trimmed/ground to ~50 μm to 70 μm thick to ensure sufficient sample material on the thin section for various types of non-destructive and destructive analysis. Finally, sample preparation for electron probe microanalyzer (EPMA) analyses, requiring thin sections polished to a mirror finish, included additional hand-polishing stages using a slurry of alumina grit on frosted glass, stepping down from 240, 600, to 1200 grit alumina powders to remove scratches and ensure an even surface. Lastly, polished surfaces were machine-buffed with a series of alumina slurries on felt pads on the lap wheel; first, a 1 μm grit to buff out any remaining visible scratches, followed by a 0.3 μm slurry and then a final 0.05 μm slurry.

CHAPTER FOUR:

ANALYTICAL METHODS

PETROGRAPHY

A flatbed thin section scanner was used to collect high resolution full thin section images in plane-polarized and cross-polarized light (see Appendix III for the full collection of thin section scans). Further characterization using a petrographic microscope aided in the description and identification of sample lithology, texture, grain size distribution, and mineral modes as well as shape and habits, deformation, alteration types and extents, and general notes and comments. Using the coarse, full thin section imagery and the more detailed petrographic characterizations, we identified approximately six to nine areas of interest per sample for targeted microanalysis. Areas of interest were chosen which were either characteristic of the bulk of the sample or exhibit anomalous textures or phases. Photomicrographs were taken of each area of interest in plane polarized light, cross-polarized light, and reflected light. Using these photographs, we established analytical points-of-interest for the electron probe microanalyzer (EPMA). Following petrographic analysis and sample imaging, a carbon coating must be applied prior to EPMA, to ensure that the flow of electrons is readily conducted across the thin sections to ground.

MAJOR ELEMENT ANALYSIS

Major element analyses of olivine, orthopyroxene, clinopyroxene, and spinel were carried out using the Shimadzu EPMA-1720HT located at the facilities in the Shimadzu Center for Environmental, Forensic, and Material Science at the University of Texas at Arlington. For most thin sections, a core and at least one rim analysis were collected for anywhere from 3 to 9 grains.

For larger grains, intermediate analyses were taken from positions located between the core and rim positions; thus enabling the identification of the presence (or lack) of chemical zoning within individual grains. Olivine, orthopyroxene, and clinopyroxene were all measured using an accelerating potential of 15 kV, a beam current of 20 nA, and a spot size of 5 μm. Spinel analyses were carried out using an accelerating potential of 15 kV, a beam current of 40 nA, and a spot size of 1 μm. Plagioclase analyses were carried out using an accelerating potential of 15 kV, a beam current of 10 nA, and a spot size of 5 μm. Counting times for OPX and CPX were 30 s for Mg, Al, Si, K, Ca, Ti, Cr, Mn, and Fe and 20 s for Na. Counting times for olivine were 40 s for Mg, Si, Ti, Ni, and Mn, 60 s for Al and Ca, and 30 s for Fe. Counting times for spinel were 40 s for Mg, Si, Ti, Mn, Fe, V, and Ni and 30 s for Al, Ca, and Cr. To verify that the analytical results had not been affected by mechanical drift, sample analyses were interspersed with standard analyses. Analyses were rejected if their totals were greater than 101.5 wt. % or less than 98.5 wt. % and if they showed evidence for mixed analysis or phase misidentification (e.g., excessive SiO_2 in spinel). The detailed methods and analytical precision for the EPMA analyses can be found in Appendix IV.

TRACE ELEMENT ANALYSIS

Representative samples for the lithologies (N = 11) were chosen for in situ clinopyroxene trace element analysis using the laser ablation-inductively coupled plasma mass spectrometer (LA-ICPMS) at the University of Arkansas (Thermofisher ICAPQ ICP-MS) using an NWR193 excimer laser ablation system with a 193 nm laser source. Two to three grains previously measured by EPMA in thin sections were measured in situ with the laser at a 5 Hz shot rate ranging from 150 to 170 bursts (i.e., 30 to 40 second measurement times). Three to five spots with a spot size of 60 μm were analyzed per grain. Data reduction was performed using the Iolite software package

(Paton et al., 2011). Calcium concentrations determined by EPMA were used as internal standards to correct the measured trace element ratio concentrations or drift throughout an analytical session. A more detailed analytical procedure for the LA-ICP-MS analysis can be found in Appendix IV.

CHAPTER FIVE:

RESULTS

PETROGRAPHY

The ultramafic xenoliths chosen for analysis are predominantly characterized by harzburgitic (N = 6) to lherzolitic (N = 13) lithologies and are comprised of the four-phase assemblage, olivine + orthopyroxene ± clinopyroxene ± spinel (Table 2). Lithological exceptions include three olivine-websterites (122C-1, 122F5-1, 122F5-2), two clinopyroxenites (122F2(B) & 101A1-2), two plagioclase-bearing clinopyroxenites (102D-2 & 102F-2), and three dunites (122F1, 102F1 & 102D-1). All of the xenoliths appear to be sulfide-free except the plagioclase-bearing clinopyroxenites, where they are associated with the interstitial plagioclase. Alteration in the Prindle xenolith suite is limited to localize, rust-red iddingsite alteration associated with olivine.

Spinel-bearing lherzolite represents the dominant lithology within the Prindle xenolith suite (Figure 14) with average relative modal proportions of 64% olivine, 17% orthopyroxene, 16% clinopyroxene, and 3% spinel. The second most abundant lithology is harzburgite with average modal proportions of approximately 70% olivine, 25% orthopyroxene, 4% clinopyroxene, and 1% spinel. Average modal proportions for the other lithologies are 28% olivine, 36% orthopyroxene, 33% clinopyroxene, and 3% spinel for the olivine-websterites, >90% clinopyroxene, <10% orthopyroxene ± olivine ± plagioclase ± sulfide for the clinopyroxenites, an >90% olivine, <10% orthopyroxene, and <1% spinel for the dunites. For the sake of simplification and for reasons which will be addressed in the discussion, we will

Table 2: Sample localities and thin section lithologies including mineral modes for the dominant xenolith clasts in each thin section.

Sample ID	Longitude	Latitude	Thin Section ID	Lithologic Group	Dominant Xenolith Lithology	Mineral Mode (%)					
						Ol	Opx	Cpx	Sp	Plag	Sul
15ATe122C	*-141.63275*	*63.71186*	122C-1	Websterites	Ol-websterite	17.6	65.7	12.6	4.1	-	-
			122C-2	Lherzolites	Lherzolite	54.4	24.2	19.3	2.1	-	-
			122C3-A	Harzburgites	Harzburgite	81	14.3	3.4	1.3	-	-
			122C3-B	Harzburgites	Harzburgite	85.6	5.9	6.4	2.1	-	-
15ATe122D	*-141.63293*	*63.71191*	122D-1	Lherzolites	Lherzolite	68.2	14	14.4	3.4	-	-
15ATe122E	*-141.63178*	*63.71211*	122E	Granulite	Tonalite	-	-	-	-	-	-
15ATe122F1	*-141.63178*	*63.71211*	122F1	Dunites	Dunite	92	6.4	0.6	1	-	-
15ATe122F2	*-141.63178*	*63.71211*	122F2(A)	Lherzolites	Lherzolite	81.5	9.5	5.8	3.2	-	-
			122F2(B)	Pyroxenites	Ol-bearing Clinopyroxenite	9	8.5	82	0.5	-	-
			122F2	Lherzolites	Lherzolite	67.5	18.3	12.2	2	-	-
15ATe122F3	*-141.63178*	*63.71211*	122F3-A	Lherzolites	Lherzolite	58	21.5	18	2.5	-	-
			122F3-B	Harzburgites	Harzburgite	60.9	33.1	4.9	1.1	-	-
15ATe122F4	*-141.63178*	*63.71211*	122F4-1	Lherzolites	Lherzolite	52.8	21.3	21.9	4	-	-
			122F4-2	Lherzolites	Lherzolite	61.3	16.2	18.9	3.6	-	-
15ATe122F5	*-141.63178*	*63.71211*	122F5-1	Websterites	Ol-websterite	36.1	32.7	27.3	3.9	-	-
			122F5-2	Websterites	Ol-websterite	38.3	31.4	26.1	4.2	-	-
15ATe122F6	*-141.63178*	*63.71211*	122F6	Harzburgites	Harzburgite	71.3	22	5.6	1.2	-	-
15ATe122F7	*-141.63178*	*63.71211*	122F7A	Harzburgites	Harzburgite	71.8	24.1	3.9	0.2	-	-
			122F7-A	Harzburgites	Harzburgite	77.9	17.4	4.2	0.5	-	-
			122F7-B	Lherzolites	Lherzolite	54.9	27.9	13.9	3.3	-	-
16ATe101A1	*-141.54572*	*63.64978*	101A1-1	Lavas	Basanite	-	-	-	-	-	-
			101A1-2	Pyroxenites	Clinopyroxenite	-	-	100	-	-	-
16ATe101C	*-141.54572*	*63.64978*	101C-1	Lavas	Basanite	-	-	-	-	-	-
			101C-2	Lavas	Basanite	-	-	-	-	-	-
16ATe102A	*-141.62827*	*63.71571*	102A(A-1)	Lherzolites	Lherzolite	69.5	13.3	14	3.2	-	-
			102A(A-2)	Lherzolites	Lherzolite	67.6	19	11.4	1.9	-	-
16ATe102C	*-141.62756*	*63.71504*	102C	Lherzolites	Lherzolite	64.6	17.7	13.5	4.2	-	-
16ATe102D	*-141.62755*	*63.71438*	102D-1	Dunites	Dunite	98.2	0.8	0.4	0.6	-	-
			102D-2	Pyroxenites	Pl-bearing Clinopyroxenite	-	3.9	90	0.4	4.7	1
			102D-3	Lherzolites	Lherzolite	50.9	18.3	29.2	1.6	-	-
16ATe102E1	*-141.62898*	*63.71337*	102E1(A)	Lherzolites	Lherzolite	58.1	18.3	21.1	2.5	-	-
16ATe102F	*-141.62898*	*63.71337*	102F-1	Dunites	Dunite	94.7	1.2	3	1.2	-	-
			102F-2	Pyroxenites	Pl-bearing Clinopyroxenite	-	-	90.2	-	8	1.8

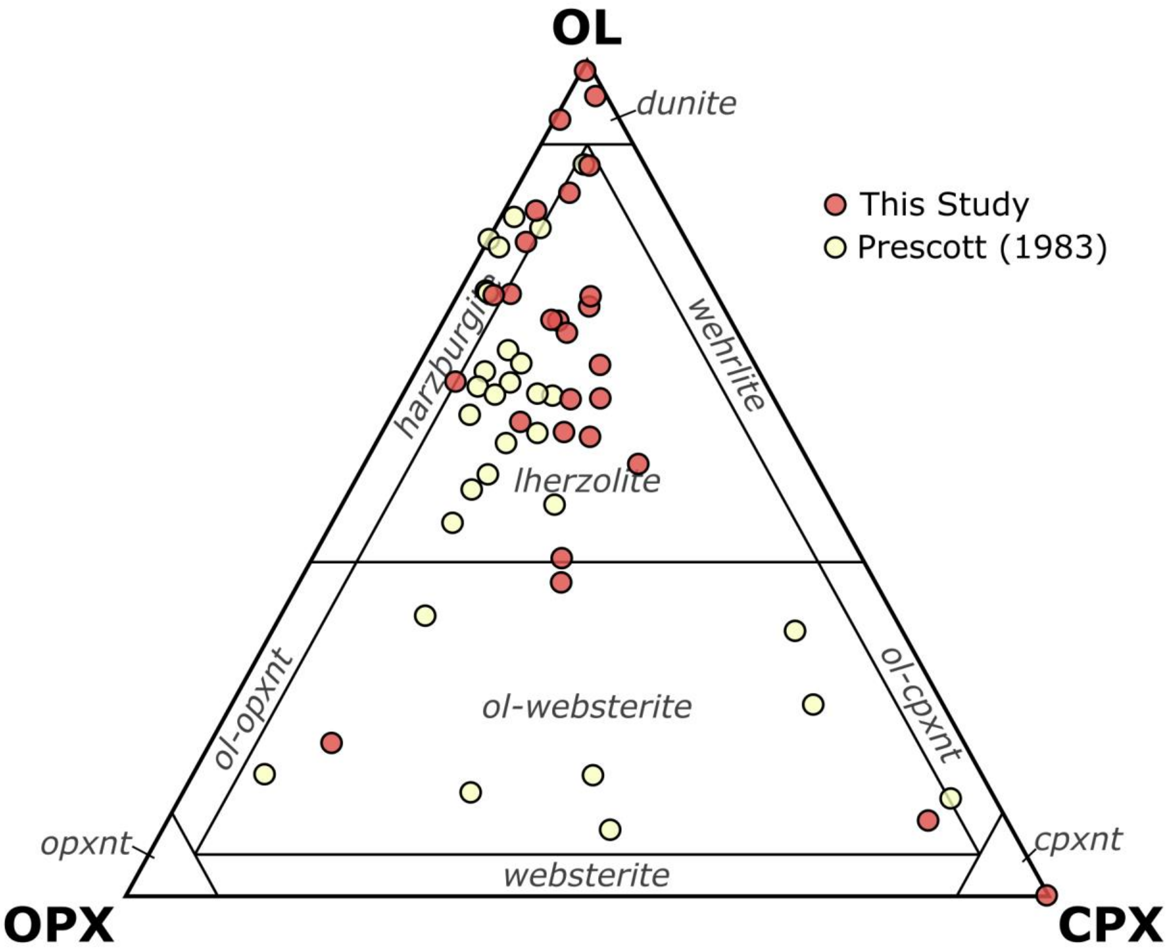

Figure 14: Modal percentages for the samples from this study (red circles) and the unpublished Prescott (1983) McGill University thesis (pale tan circles) plotted on the ultramafic ternary diagram.

refer to the lherzolites, websterites, and clinopyroxenites collectively throughout the rest of this thesis as the CPX-rich lithologies.

The overall texture for the entire xenolith suite can best be characterized as mosaic to granular (grains meet with straight to slightly curvilinear, but not sutured or interlocking, boundaries), although, several samples contain regions characterized by porphyroclastic to protogranular textures. A majority of the samples are characterized by moderate to strong fabrics with roughly equigranular grain size distributions. Additionally, sample 122F1 from the harzburgite sample group displays a unique seriate (having one or more mineral phases in a continuous range of larger to progressively smaller-sized grains) distribution.

Spinel Lherzolites

Spinel lherzolite xenoliths from Prindle volcano (Figure 15) contain olivine grains that are anhedral to subhedral and subequant with an average grain size of ~1.56 mm. Clinopyroxene and orthopyroxene grains are predominantly subhedral to anhedral with a subequant to tabular shape and an average grain size of 1.14 and 1.11 mm, respectively. Spinel grains exhibit a pronounced textural variability throughout the xenoliths with some samples containing strictly euhedral to sub-rounded to interstitial holly-leaf spinels at grain junctions (Figure 15D), some containing strictly wispy, interstitial to symplectitic spinel, while other samples may contain a combination of these two types (Figure 15B) in addition to larger (up to 3 mm) spinels which have interstitial to poikilitic margins. Spinel lherzolites are predominantly equigranular to proto-intergranular with minor occurrences of protogranular samples. They are dominantly characterized by moderate to strong fabrics except for two samples (122F3A & 122F7-B) which exhibit only a weak fabric. We note that several of the samples contain fabric-parallel bands and strings of small, rounded, olivine neoblasts associated with interstitial, clinopyroxene (Figure 15E).

Alteration is most abundant in the spinel lherzolites with all but one sample altered. Iddingsite predominantly occurs in olivine grains and appears as a rust-red, fine-grained, fibrous, opaque phase, typically seen as veins replacing olivine along the grain or sub-grain boundaries. We note that there seems to be a correlation between the intensity of the iddingsite alteration and the presence of the previously described, fabric-parallel stringers of olivine

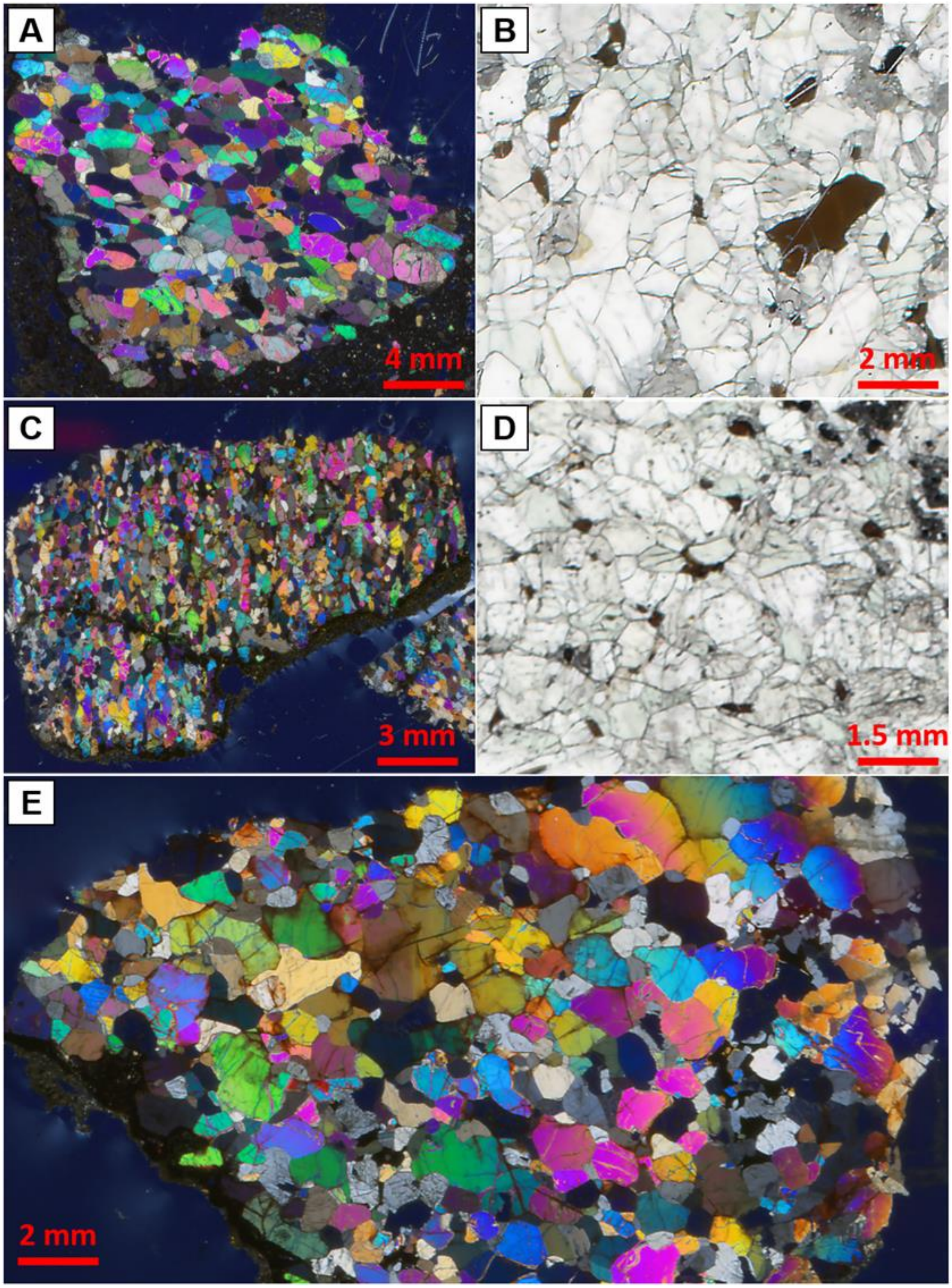

Figure 15: Representative photomicrographs of the spinel lherzolite sample group. (A) Overview of 102D-3, a moderately foliated, type A lherzolite. (B) Example from 102D-3 of the two types of spinels (brown phases) found in the type A samples. (C) Overview of 122F4-2, a strongly-foliated, finer-grained, type B lherzolite. (D) Example from 122F4-2 of the small, wispy, interstitial, spinels which characterize the type B lherzolites. (E) Overview of 122F7-B displaying the typical morphology of the smaller olivine neoblasts as they are distributed throughout the lherzolites.

neoblasts. Additionally, pyroxenes, typically ones in direct contact with the host basalt, display very fine-grained recrystallization around the outer margins.

Harzburgites

Samples within the Harzburgite group are dominantly protogranular and vary in fabric intensity with half displaying isotropic to weakly foliated fabrics and the other displaying moderately to strongly foliated fabrics typically defined by slightly elongate to tabular olivine grains (Figure 16). Olivines in the harzburgites appear to vary widely in shape between and, to some extent, within individual samples. All of the harzburgite samples contain proto-intergranular regions caused by the presence of smaller, equant to subequant olivine neoblasts that form at grain junctions sparsely throughout the sample (e.g., 122F6; Figure 16). Sample 102F-1 characteristically contains disseminated, fabric-parallel, anastomosing veins of finer-grained (~0.1-0.3 mm) olivine neoblasts with minor, interstitial to poikilitic pyroxene (Figure 16A, B, & E). We note that it appears that the spinel in 102F-1 are concentrated, and likely associated with these anastomosing veins. Olivine grains range in size and shape variation in the dominant surrounding protogranular domains between samples with those xenoliths which exhibit little to no fabric possessing a higher percentage of larger (~2 mm), anhedral to subhedral, subequant grains (e.g., 122F7A) and those exhibiting stronger fabrics possessing a greater percentage of smaller (~ 1 mm), euhedral to tabular, equant grains (e.g., 122C3A). Clinopyroxene and orthopyroxene in the harzburgites are typically intergranular to olivine and range from small (~1 mm), euhedral grains at grain junctions to small (~0.2-1 mm), wormy, interstitial grains in half of the samples (e.g., 122F6, 122F3-B, & 122F7A) (Figure 16C) to larger (~1-1.6 mm), interstitial, subhedral to wormy grains in the other half of samples (e.g., 122C3-A, 122F7-A, 122-C3B) (Figure 16A). Spinel grains within harzburgite samples

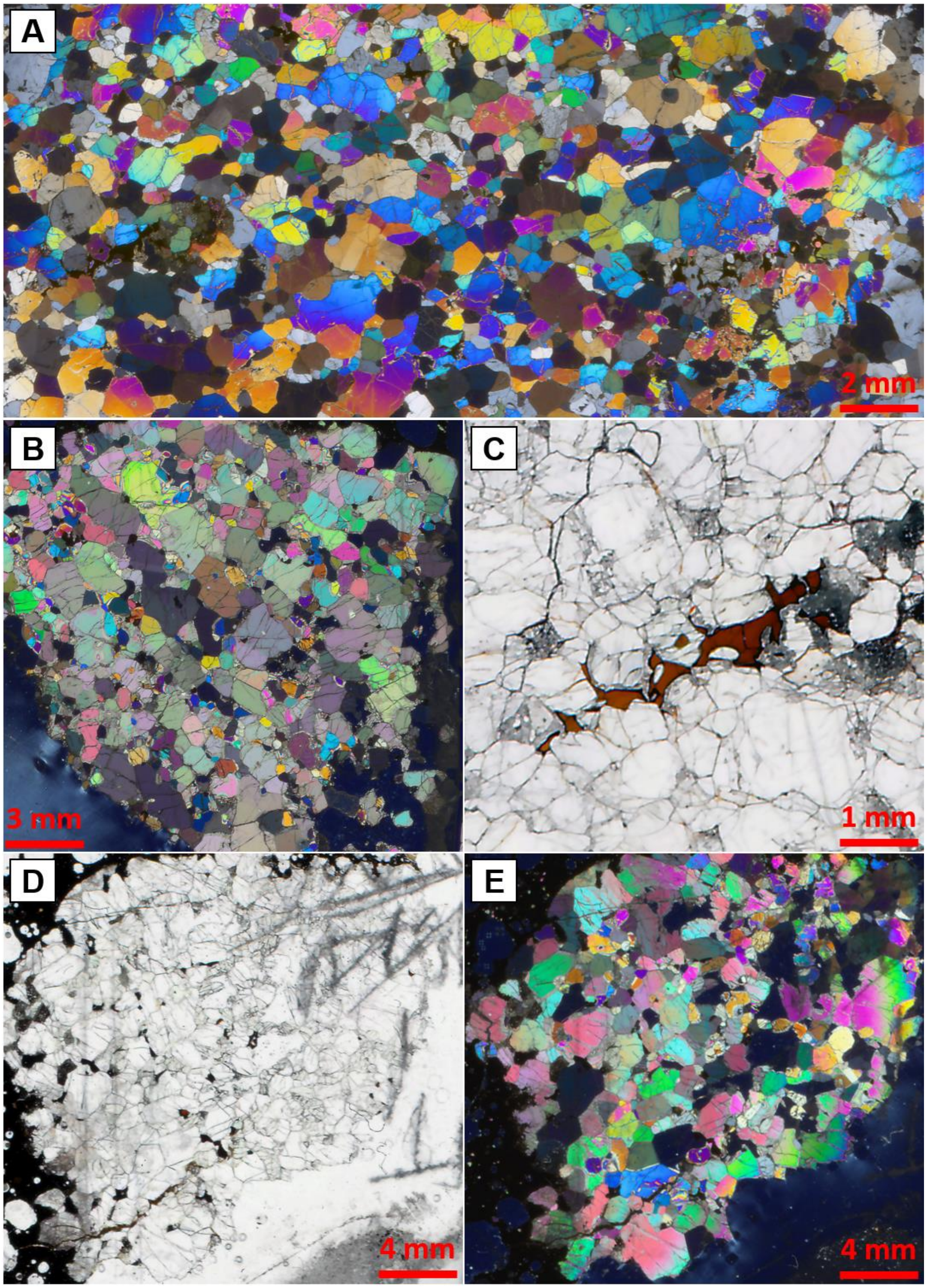

Figure 16: Representative photomicrographs of the harzburgite sample group. (A) Harzburgite 122F6 exhibiting a weak fabric and anastomosing veins of olivine and pyroxene neoblasts; XPL. (B) Overview of 102F-1, another example of the olivine neoblasts within a more moderately-foliated sample; XPL. (C) An example of a typical, wormy, interstitial spinel in sample 122F6; PPL. (D) Overview of 122F3-B, an isotropic harzburgite containing typical wispy spinel; PPL. (E) An XPL version of panel D illustrating the veins of olivine and pyroxene neoblasts which characterize the harzburgites.

exhibiting a strong a fabric predominantly exhibit small (0.4-0.8 mm), holly-leaf to symplectitic shapes while those within samples exhibiting little to no fabric are characterized by smaller (0.2-0.5 mm), euhedral to sub-rounded shapes.

Roughly half of the harzburgite samples exhibit alteration in the form of fine-grained, fibrous, opaque iddingsite that preferentially occurs within olivine grains and along boundaries of some orthopyroxene grains. Those samples which contain iddingsite alteration appear to possess both larger grains of and a greater percentage of pyroxene, on average, compared to those samples which contain little to no iddingsite.

Olivine-websterites

The olivine-bearing websterite sample group (herein referred to simply as websterites) are characterized by moderate to strongly foliated fabrics and exhibit proto- to equigranular textures except for sample 122F5 which exhibits proto-intergranular regions which are, coincidentally, associated with larger degrees of iddingsite alteration (Figure 17 A&B). Olivine grains within the websterites are predominantly subhedral to euhedral and equant to slightly tabular in shape with average grain sizes of ~1.22 mm. Clinopyroxene and orthopyroxene grains within the websterite samples, similar to the olivines, are predominantly subhedral to euhedral and equant to subequant with an average grain size of ~1.52 mm. The spinels in the websterite samples range from small (~0.68 mm), subhedral to euhedral grains to larger (~1 - 2 mm), holly-leaf-shaped grains with vaguely poikilitic margins (Figure 17D).

As previously noted, iddingsite alteration is concentrated in the two thin sections derived from sample 122F5 where there is a preponderance of proto-intergranular textures (Figure 17A). Although there is little to no iddingsite alteration observed in 122C-1, we cannot rule

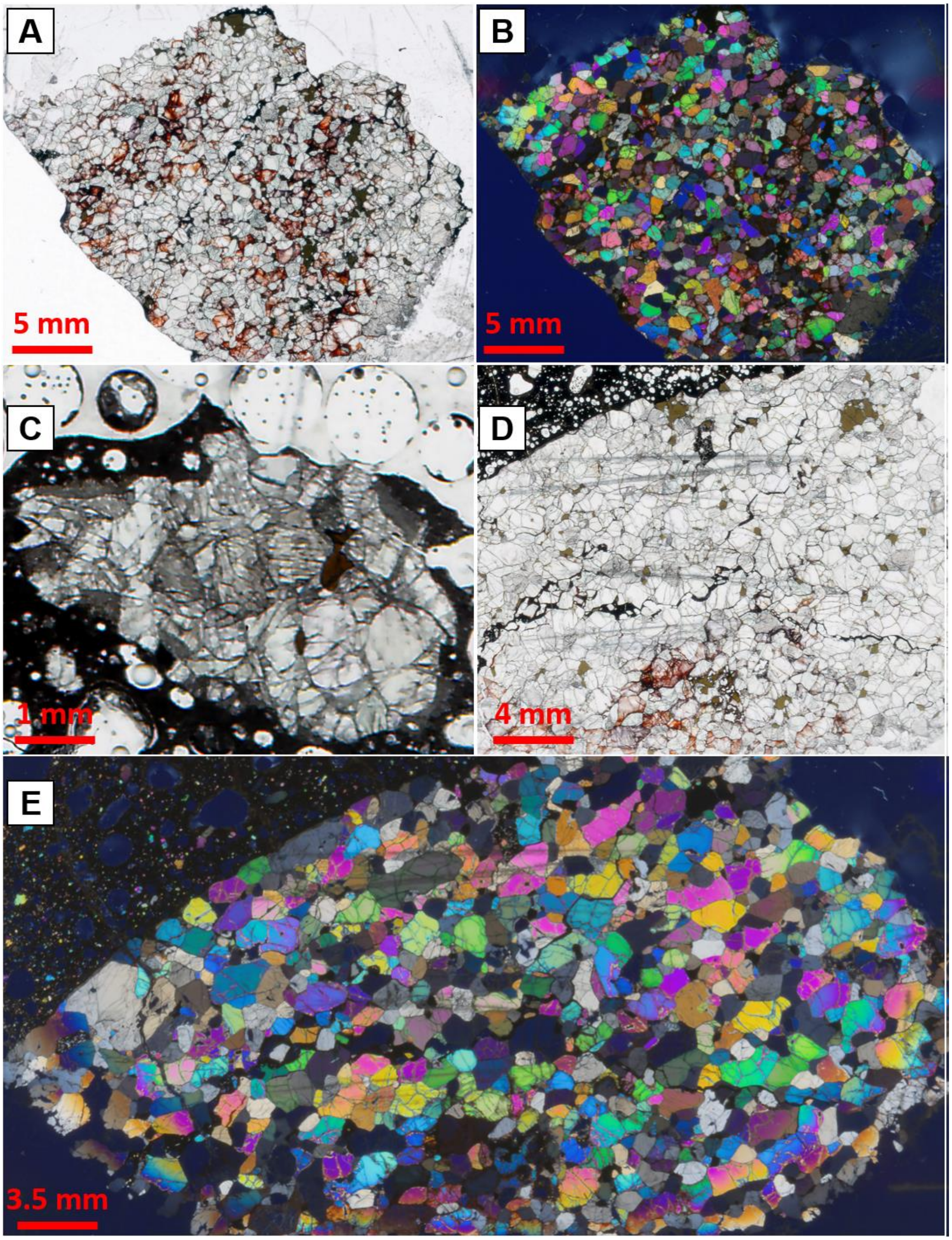

Figure 17: Representative photomicrographs of the websterite sample group. (A) PPL and (B) XPL overviews of 122F5-1, from sample 122F5, which are typical of the websterites exhibiting proto-intergranular patches consisting of olivine and pyroxene neoblasts within a broader protogranular matrix. We note that the red iddingsite alteration seems to typically be associated with the proto-intergranular domains. (C) Overview of the small websterite clast in 122C1 which is dominated by pyroxene; PPL. (D) Overview of the two types of spinels (light brown)found in the websterites from 122F5-2 which are reminiscent of those from type A lherzolites. (E) Overview, in XPL, of 122F5-2 showing the weakly-foliated nature of the sample and the trails/patches of proto-intergranular material.

out that the larger xenolith is unaffected by iddingsite alteration since the thin section only contains a small (~3 x 5 mm) cross-section of the sample.

Dunites

The Prindle Volcano xenolith suite contains three dunite samples, two possessing widely varying textural features and grain-size relationships compared to the other one (Figure 18). Sample 102D-1 (Figure 18A&B) is isotropic and roughly protogranular with predominantly euhedral, equant olivine grains (~1.4 mm), and very small, interstitial pyroxene (~0.2-0.8 mm) and spinel (~0.3 mm) grains residing at grain junctions sparsely throughout the sample. Iddingsite alteration is sparse in 102D-1, where it is concentrated mostly along the margins where the host basanite has intruded along grain boundaries. Sample 102F-2 contains a small dunite clast (~2 x 3 mm across) which is approximately petrographically similar to that of 102D-1. Sample 122F-1 exhibits a well-developed porphyroclastic texture with an extremely strong foliation (Figure 18 C&D). The porphyroclasts within the sample consist of large (~2-3 mm) subequant to tabular, subhedral olivine grains. The surrounding, finer-grained (~0.1-0.5 mm on average), subhedral to tabular grains of olivine and pyroxene with recrystallized rims. There is evidence for abundant, fabric-parallel cataclastic deformation along the grain boundaries within the finer-grained domain which, in some cases has been intruded by the host basanite.

Clinopyroxenites

Overall, the remaining samples can be grouped as clinopyroxenites. However, nearly each of the pyroxenite samples (Figure 19) exhibits its own unique characteristics which must be discussed individually. The only pure pyroxenite sample is a small, singular clinopyroxenite in section 101A1-2 which measures ~4.5 x 3 mm across and consists of anhedral, subequant

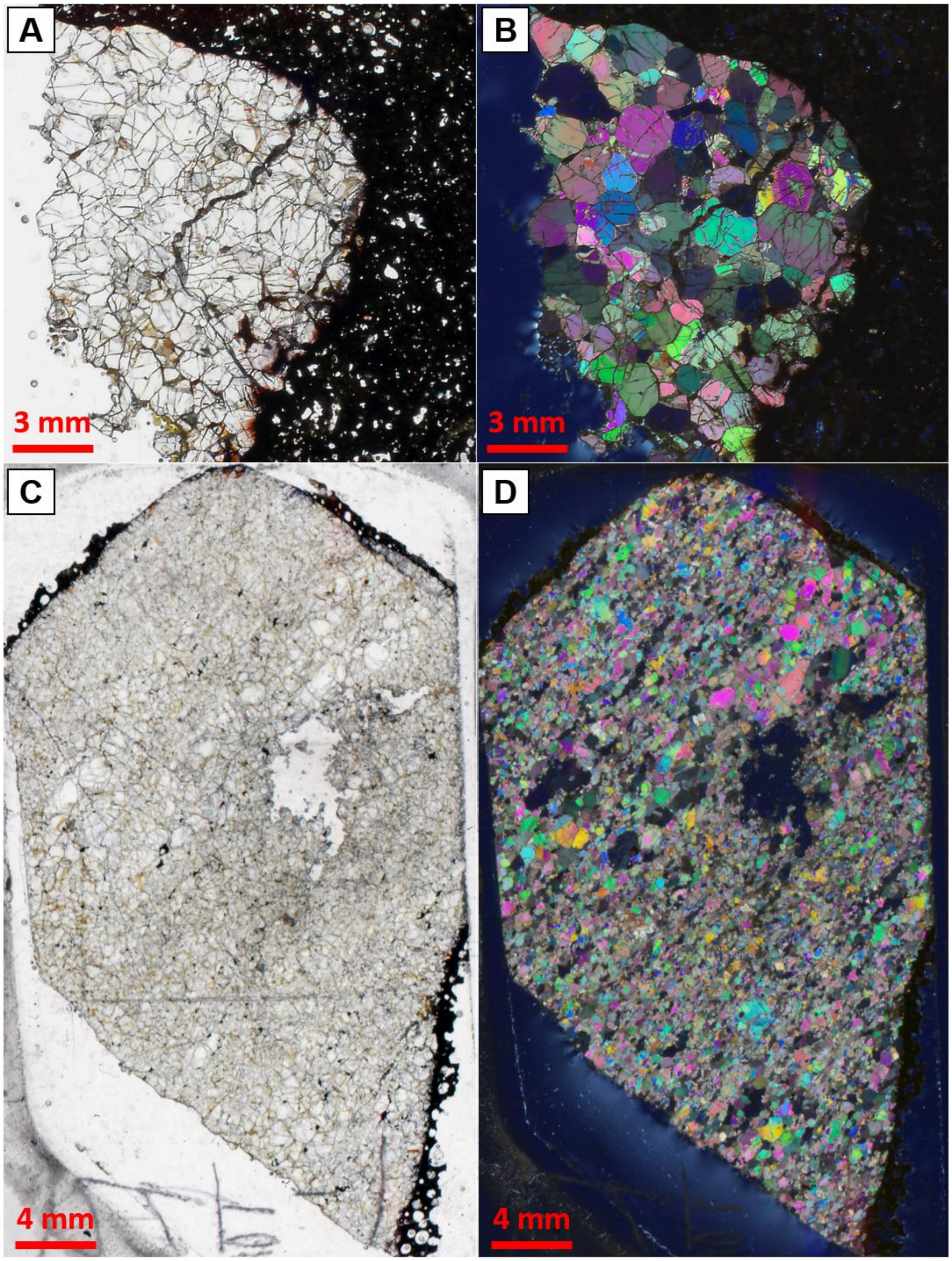

Figure 18: Representative photomicrographs of the dunite sample group. (A) PPL and (B) XPL overviews of dunite 102D-1 which contains little to no phases other than olivine. (C) PPL and (D) XPL overview images of dunite 122F-1 exhibiting a strong, well-developed porphyroclastic texture. The larger phorphyroclasts are generally aggregates of mostly olivine while the finer-grained matrix contains trace amounts of orthopyroxene ± clinopyroxene.

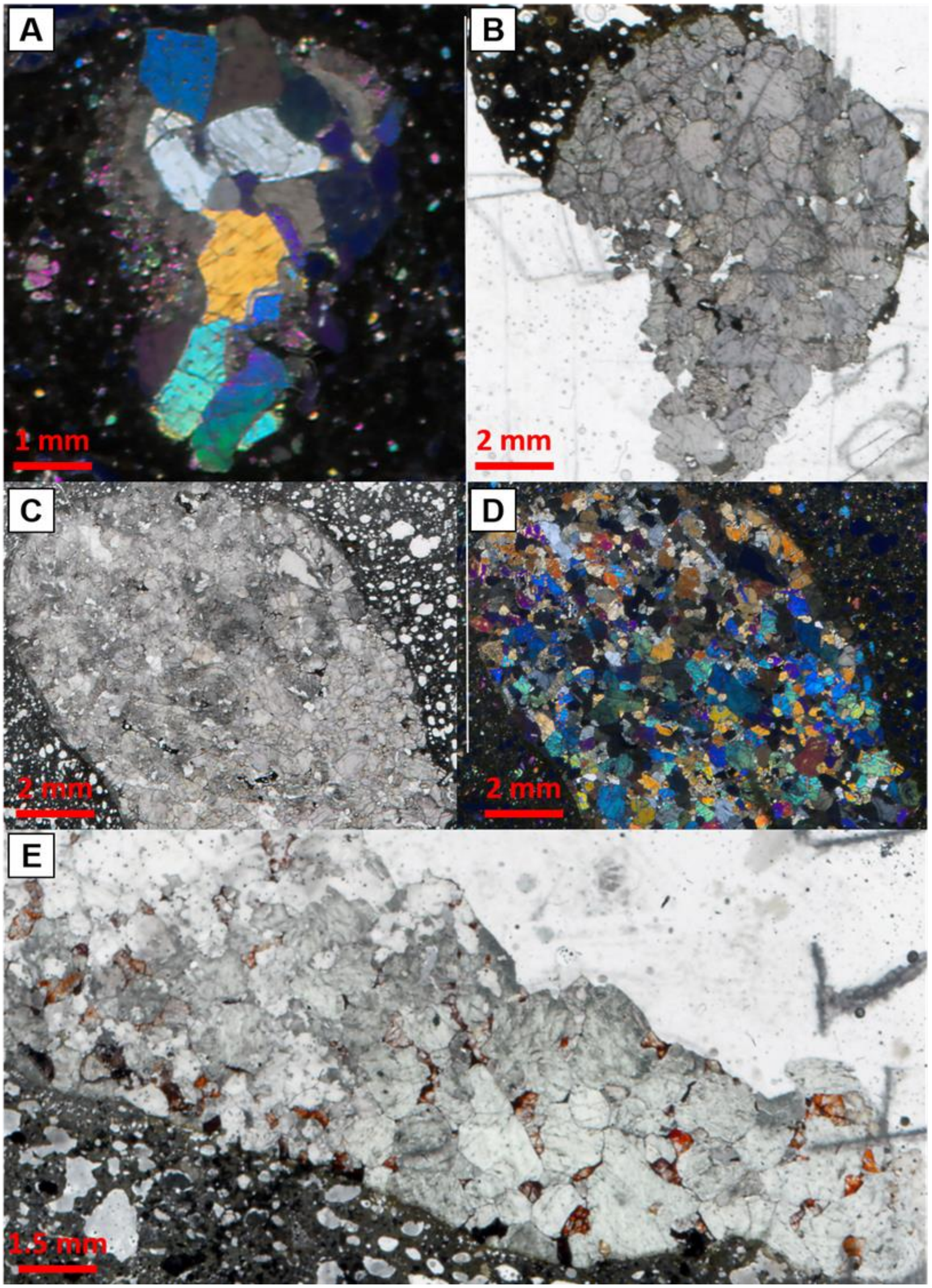

Figure 19: Representative photomicrographs of the pyroxenite sample group. (A) An XPL overview of the small, pure clinopyroxenite clast in 101A1-2. (B) A PPL overview image of plagioclase-clinopyroxenite 102F-2. The dark phases are interstitial sulfides associated with the interstitial plagioclase. (C) PPL and (D) XPL overviews of plagioclase-clinopyroxenite 102D-2. Note the presence of plagioclase-associated sulfide and the vein-like alignment of the plagioclase and small, orthopyroxene neoblasts. (E) PPL overview of 122F2B, an olivine-clinopyroxenite where the accessory phases, highlighted by iddingsite, are present as small, resorbed grains within and between the much larger clinopyroxene.

clinopyroxene with an average grain size of ~1 mm (Figure 19A). The margins of the 101A1-2 clinopyroxenite are generally unreacted with the host basalt with the exception of two grains which have been reacted with to produce a very fine-grained (<10 μm) assemblage of what appears to be olivine and clinopyroxene.

Sample 122F2B (Figure 19E) is an olivine-clinopyroxenite containing ~82% clinopyroxene, 8.5% orthopyroxene, 9% olivine, and 0.5% spinel. The olivine grains in this sample are anhedral to subhedral, exhibit a subequant or lobate habit, and have an average grain size of ~0.80 mm. The orthopyroxene averages ~0.8 mm in size and has similar habits to the olivine. The clinopyroxenes in the sample are anhedral to subhedral with subequant, lobate habits and an average size of ~1.26 mm. Spinel in this sample, though rare, shares the same grain morphologies as the olivine and orthopyroxene and averages ~0.62 mm in size. We note that the orthopyroxene and olivine are generally found to have reactive or lobate grain boundaries with the clinopyroxene and occur primarily as small grains in between large clinopyroxene grains and, occasionally, as small (<0.5 mm) chadacrysts within the clinopyroxene. Olivine is generally the most affected by alteration in this sample with iddingsite both penetrating the grains and growing as interstitial masses around the margins of the olivine and orthopyroxene. We observe that the iddingsite alteration tends to be the most intense where there are abundant fractures in the olivine. A visible breakdown can be observed where the xenolith and host basalt come into contact with one another, but it also occurs at or near the region of the fracture, and so it is hard to decipher whether this is due to fragmentation or an effect of the interaction. This sample has no observable fabric or preferred orientation.

The last two samples consist of two plagioclase-clinopyroxenite samples which lack olivine and contain rare spinel. Sample 102D-2 is an orthopyroxene-bearing plagioclase-clinopyroxenite which is characterized by anhedral, subequant clinopyroxene with an average grain size of ~0.82 mm (Figure 19C&D). The orthopyroxene in this sample is anhedral and subequant, averages ~0.25 mm in size, and is characteristically sparsely intergrown with finer-grained clinopyroxene neoblasts throughout the xenolith. Sample 102D-2 displays a weak fabric and a generally porphyroclastic texture with minor cataclastic deformation. Relatively fresh plagioclase with accessory sulfide is distributed throughout the sample as interstitial, anastomosing veins where the plagioclase displays minor undulose extinction and varies significantly in grain size with a maximum of ~1.5 mm and an average of ~0.5 mm. In contrast, sample 102F-2 (Figure 19B) consists solely of clinopyroxene with ~8% of interstitial plagioclase and ~1.8% sulfide. Clinopyroxene in this sample is subhedral to anhedral, equant to subequant in shape, and averages ~1.54 mm in size. The plagioclase is anhedral and interstitial with an average grain size of ~0.45 mm. Unlike in 102D-2, the plagioclase in 102F-2 is generally altered. Although the plagioclase and sulfide in 102F-2 are interstitial and sometimes form what appear to be short, semi-connected veinlets, it is impossible to tell if they form an interconnected anastomosing vein network like in 102D-2. Further, unlike 102D-2, sample 102F-2 is generally isotropic and protogranular, exhibiting no signs of fabric of preferred orientation. In both samples, the dominant clinopyroxene is relatively fresh, however, there is visible alteration occurring along the margins of the xenolith with the host basalt. In some cases, the alteration rims extend between 0.5 and 1.0 mm into the xenoliths.

MAJOR ELEMENT ANALYSIS

Olivine

Major element analysis of olivines (Table 3) found overall ranges in forsterite content (Fo = 100 x Mg / Mg + Fe + Mn) between $Fo_{87.3}$ and $Fo_{93.9}$ and NiO and MnO from 0.14 to

Table 3: Average core and rim analyses of olivine for each thin section.

Lithology	**Dunite**						**Harzburgite**														
Expedition	15ATe		16ATe				15ATe												16ATe		
Sample	122F		102D		102F		122C				122F								102F		
Thin Section	122F-1		102D-1		102F-2		122C3A		122C3B		122F3B		122F6		122F7A		122F7-A		102F-1		102F-2
Core/Rim	Core	Rim	Core	Rim	Core	Rim	Core	Rim	Core	Rim	Core	Rim	Core	Rim	Core	Rim	Core	Rim	Core	Rim	Core
N	*11*	*10*	*4*	*3*	*2*	*2*	*9*	*8*	*6*	*6*	*6*	*6*	*8*	*8*	*17*	*17*	*9*	*17*	*9*	*9*	*3*
SiO_2	40.04	40.42	39.85	39.74	42.14	42.76	41.38	41.42	40.38	40.26	40.64	40.89	40.85	40.96	40.70	40.90	40.58	40.99	40.86	40.77	41.35
Al_2O_3	0.54	0.02	0.26	0.03	0.02	0.06	0.19	0.13	0.02	0.13	0.03	0.02	0.14	0.12	0.50	0.16	0.78	0.16	0.06	0.17	0.15
TiO_2	0.01	0.02	0.01	0.02	0.02	0.01	0.02	0.02	0.02	0.02	0.02	0.03	0.02	0.01	0.02	0.02	0.02	0.02	0.02	0.02	0.02
FeO	9.72	9.81	12.06	12.33	6.53	4.60	8.71	8.72	8.90	8.90	8.57	8.61	8.61	8.47	8.60	8.84	8.40	6.98	8.70	8.73	7.57
MnO	0.15	0.14	0.20	0.21	0.18	0.19	0.15	0.14	0.14	0.13	0.15	0.13	0.14	0.15	0.14	0.15	0.15	0.15	0.13	0.14	0.12
MgO	49.03	49.14	46.80	47.11	51.04	52.67	48.99	48.94	50.20	50.05	50.25	50.23	50.40	50.55	50.16	50.16	49.92	51.41	50.69	50.52	50.14
CaO	0.02	0.04	0.03	0.03	0.04	0.05	0.06	0.07	0.06	0.07	0.05	0.05	0.06	0.07	0.08	0.06	0.07	0.09	0.05	0.05	0.07
NiO	0.41	0.41	0.16	0.16	0.34	0.35	0.36	0.34	0.38	0.40	0.41	0.40	0.36	0.34	0.35	0.37	0.38	0.36	0.43	0.43	0.34
Total	99.93	99.99	99.38	99.63	100.29	100.67	99.86	99.79	100.09	99.96	100.11	100.35	100.57	100.67	100.54	100.66	100.29	100.17	100.95	100.82	99.76
Cations (O = 4)																					
Si	0.98	0.99	0.99	0.99	1.01	1.02	1.01	1.01	0.99	0.99	0.99	0.99	0.99	0.99	0.99	0.99	0.99	0.99	0.99	0.99	1.01
Al	0.02	0.00	0.01	0.00	0.00	0.00	0.01	0.00	0.00	0.00	0.00	0.00	0.00	0.00	0.01	0.00	0.02	0.00	0.00	0.00	0.00
Ti	0.00	0.00	0.00	0.00	0.00	0.00	0.00	0.00	0.00	0.00	0.00	0.00	0.00	0.00	0.00	0.00	0.00	0.00	0.00	0.00	0.00
Fe	0.20	0.20	0.25	0.26	0.13	0.09	0.18	0.18	0.18	0.18	0.17	0.18	0.17	0.17	0.17	0.18	0.17	0.14	0.18	0.18	0.15
Mn	0.00	0.00	0.00	0.00	0.00	0.00	0.00	0.00	0.00	0.00	0.00	0.00	0.00	0.00	0.00	0.00	0.00	0.00	0.00	0.00	0.00
Mg	1.80	1.80	1.74	1.75	1.83	1.86	1.78	1.78	1.83	1.83	1.83	1.82	1.82	1.83	1.82	1.82	1.81	1.85	1.83	1.83	1.82
Ca	0.00	0.00	0.00	0.00	0.00	0.00	0.00	0.00	0.00	0.00	0.00	0.00	0.00	0.00	0.00	0.00	0.00	0.00	0.00	0.00	0.00
Ni	0.01	0.01	0.00	0.00	0.01	0.01	0.01	0.01	0.01	0.01	0.01	0.01	0.01	0.01	0.01	0.01	0.01	0.01	0.01	0.01	0.01
Fo^A	90.0	89.9	87.4	87.2	93.3	95.3	90.9	90.9	91.0	90.9	91.3	91.2	91.3	91.4	91.2	91.0	91.4	92.9	91.2	91.2	92.2
Fa^B	10.0	10.1	12.6	12.8	6.7	4.7	9.1	9.1	9.0	9.1	8.7	8.8	8.7	8.6	8.8	9.0	8.6	7.1	8.8	8.8	7.8

[A] **Fo = 100 x Mg / Mg + Fe + Mn**

[B] **Fa = 100 x Fe / Mg + Fe + Mn**

Table 3: (Continued)

Lithology	**Lherzolite**																					
Expedition	15ATe																16ATe					
Sample	122C		122D		122F												102A				102C	
Thin Section	122C2		122D-1		122F2		122F2A		122F3A		122F4-1		122F4-2		122F7-B		102A(A-1)		102A(A-2)		102C	
Core/Rim	Core	Rim	Core	Rim	Core	Rim	Core	Rim	Core	Rim	Core	Rim	Core	Rim	Core	Rim	Core	Rim	Core	Rim	Core	Rim
N	*12*	*7*	*11*	*10*	*14*	*15*	*6*	*6*	*9*	*6*	*24*	*20*	*12*	*13*	*23*	*24*	*8*	*11*	*10*	*10*	*7*	*8*
SiO_2	40.93	40.58	40.25	40.29	40.94	40.93	40.52	40.60	40.49	40.51	40.97	41.03	40.59	40.91	39.94	39.86	40.59	40.72	40.37	40.45	39.87	39.91
Al_2O_3	0.03	0.18	0.03	0.02	0.04	0.27	0.22	0.03	0.03	0.61	0.17	0.08	0.34	0.23	1.34	1.07	0.04	0.03	0.03	0.04	0.02	0.04
TiO_2	0.04	0.04	0.02	0.02	0.01	0.02	0.02	0.02	0.02	0.02	0.02	0.02	0.02	0.02	0.02	0.02	0.02	0.02	0.02	0.01	0.01	0.02
FeO	10.14	10.85	10.06	9.88	10.05	9.52	10.17	9.78	9.76	9.12	9.80	9.43	9.97	9.24	8.66	8.73	10.12	9.81	10.19	10.39	10.16	9.97
MnO	0.16	0.18	0.15	0.15	0.16	0.17	0.15	0.16	0.16	0.16	0.16	0.16	0.16	0.16	0.14	0.14	0.15	0.16	0.15	0.16	0.16	0.16
MgO	48.56	47.41	48.99	49.13	49.14	49.31	48.74	49.07	48.48	48.48	48.95	49.47	48.95	49.71	48.95	48.76	48.85	48.97	48.82	48.56	48.68	48.78
CaO	0.04	0.12	0.04	0.05	0.05	0.06	0.04	0.06	0.03	0.08	0.06	0.06	0.04	0.07	0.07	0.08	0.03	0.05	0.04	0.05	0.05	0.05
NiO	0.40	0.36	0.38	0.38	0.40	0.40	0.37	0.45	0.40	0.42	0.44	0.40	0.38	0.39	0.40	0.39	0.35	0.34	0.34	0.34	0.37	0.35
Total	100.29	99.72	99.91	99.92	100.79	100.67	100.24	100.16	99.38	99.38	100.58	100.64	100.46	100.73	99.53	99.05	100.14	100.09	99.96	100.01	99.33	99.28
Cations (O = 4)																						
Si	1.00	1.00	0.99	0.99	1.00	1.00	0.99	1.00	1.00	1.00	1.00	1.00	0.99	0.99	0.98	0.98	1.00	1.00	0.99	1.00	0.99	0.99
Al	0.00	0.01	0.00	0.00	0.00	0.01	0.01	0.00	0.00	0.02	0.00	0.00	0.01	0.01	0.04	0.03	0.00	0.00	0.00	0.00	0.00	0.00
Ti	0.00	0.00	0.00	0.00	0.00	0.00	0.00	0.00	0.00	0.00	0.00	0.00	0.00	0.00	0.00	0.00	0.00	0.00	0.00	0.00	0.00	0.00
Fe	0.21	0.22	0.21	0.20	0.20	0.19	0.21	0.20	0.20	0.19	0.20	0.19	0.20	0.19	0.18	0.18	0.21	0.20	0.21	0.21	0.21	0.21
Mn	0.00	0.00	0.00	0.00	0.00	0.00	0.00	0.00	0.00	0.00	0.00	0.00	0.00	0.00	0.00	0.00	0.00	0.00	0.00	0.00	0.00	0.00
Mg	1.77	1.75	1.80	1.80	1.79	1.79	1.78	1.79	1.78	1.78	1.78	1.79	1.78	1.80	1.79	1.79	1.79	1.79	1.79	1.78	1.80	1.80
Ca	0.00	0.00	0.00	0.00	0.00	0.00	0.00	0.00	0.00	0.00	0.00	0.00	0.00	0.00	0.00	0.00	0.00	0.00	0.00	0.00	0.00	0.00
Ni	0.01	0.01	0.01	0.01	0.01	0.01	0.01	0.01	0.01	0.01	0.01	0.01	0.01	0.01	0.01	0.01	0.01	0.01	0.01	0.01	0.01	0.01
Fo^A	89.5	88.6	89.7	89.9	89.7	90.2	89.5	89.9	89.8	90.4	89.9	90.3	89.7	90.5	91.0	90.9	89.6	89.9	89.5	89.3	89.5	89.7
Fa^B	10.5	11.4	10.3	10.1	10.3	9.8	10.5	10.1	10.2	9.6	10.1	9.7	10.3	9.5	9.0	9.1	10.4	10.1	10.5	10.7	10.5	10.3

[A] **Fo = 100 x Mg / Mg + Fe + Mn**

[B] **Fa = 100 x Fe / Mg + Fe + Mn**

Table 3: (Continued)

Lithology	**Lherzolite**				**Websterites**						**Pyroxenites**	
Expedition	16ATe				15ATe						15ATe	
Sample	102D		102E		122C		122F				122F	
Thin Section	102D-2		102E-1A		122-C1		122F5-1		122F5-2		122F2B	
Core/Rim	Core	Rim	Core	Rim	Core	Rim	Core	Rim	Core	Rim	Core	Rim
N	*1*	*1*	*7*	*7*	*4*	*3*	*10*	*11*	*8*	*7*	*10*	*9*
SiO_2	40.30	40.12	40.39	40.34	41.36	40.89	39.81	39.78	39.80	39.53	40.30	40.10
Al_2O_3	0.02	0.01	0.05	0.04	0.06	0.37	0.43	0.18	0.17	0.39	0.10	0.25
TiO_2	0.01	0.02	0.02	0.02	0.02	0.02	0.02	0.02	0.02	0.02	0.02	0.02
FeO	9.75	9.81	9.97	9.88	10.10	10.10	10.37	10.93	10.70	10.78	9.95	11.67
MnO	0.16	0.17	0.16	0.16	0.17	0.16	0.16	0.16	0.16	0.16	0.18	0.18
MgO	49.14	48.98	48.81	49.21	47.39	46.66	48.19	47.70	48.53	47.98	48.24	46.75
CaO	0.04	0.04	0.05	0.04	0.04	0.09	0.06	0.05	0.05	0.05	0.08	0.06
NiO	0.36	0.34	0.37	0.40	0.34	0.34	0.38	0.37	0.32	0.34	0.39	0.36
Total	99.77	99.47	99.81	100.10	99.48	98.64	99.41	99.19	99.75	99.25	99.26	99.38
Cations (O = 4)												
Si	0.99	0.99	0.99	0.99	1.02	1.02	0.99	0.99	0.98	0.98	1.00	1.00
Al	0.00	0.00	0.00	0.00	0.00	0.01	0.01	0.01	0.01	0.01	0.00	0.01
Ti	0.00	0.00	0.00	0.00	0.00	0.00	0.00	0.00	0.00	0.00	0.00	0.00
Fe	0.20	0.20	0.21	0.20	0.21	0.21	0.21	0.23	0.22	0.22	0.21	0.24
Mn	0.00	0.00	0.00	0.00	0.00	0.00	0.00	0.00	0.00	0.00	0.00	0.00
Mg	1.80	1.80	1.79	1.80	1.74	1.73	1.78	1.77	1.79	1.78	1.78	1.74
Ca	0.00	0.00	0.00	0.00	0.00	0.00	0.00	0.00	0.00	0.00	0.00	0.00
Ni	0.01	0.01	0.01	0.01	0.01	0.01	0.01	0.01	0.01	0.01	0.01	0.01
Fo^A	90.0	89.9	89.7	89.9	89.3	89.2	89.2	88.6	89.0	88.8	89.6	87.7
Fa^B	10.0	10.1	10.3	10.1	10.7	10.8	10.8	11.4	11.0	11.2	10.4	12.3

[A] **Fo = 100 x Mg / Mg + Fe + Mn**

[B] **Fa = 100 x Fe / Mg + Fe + Mn**

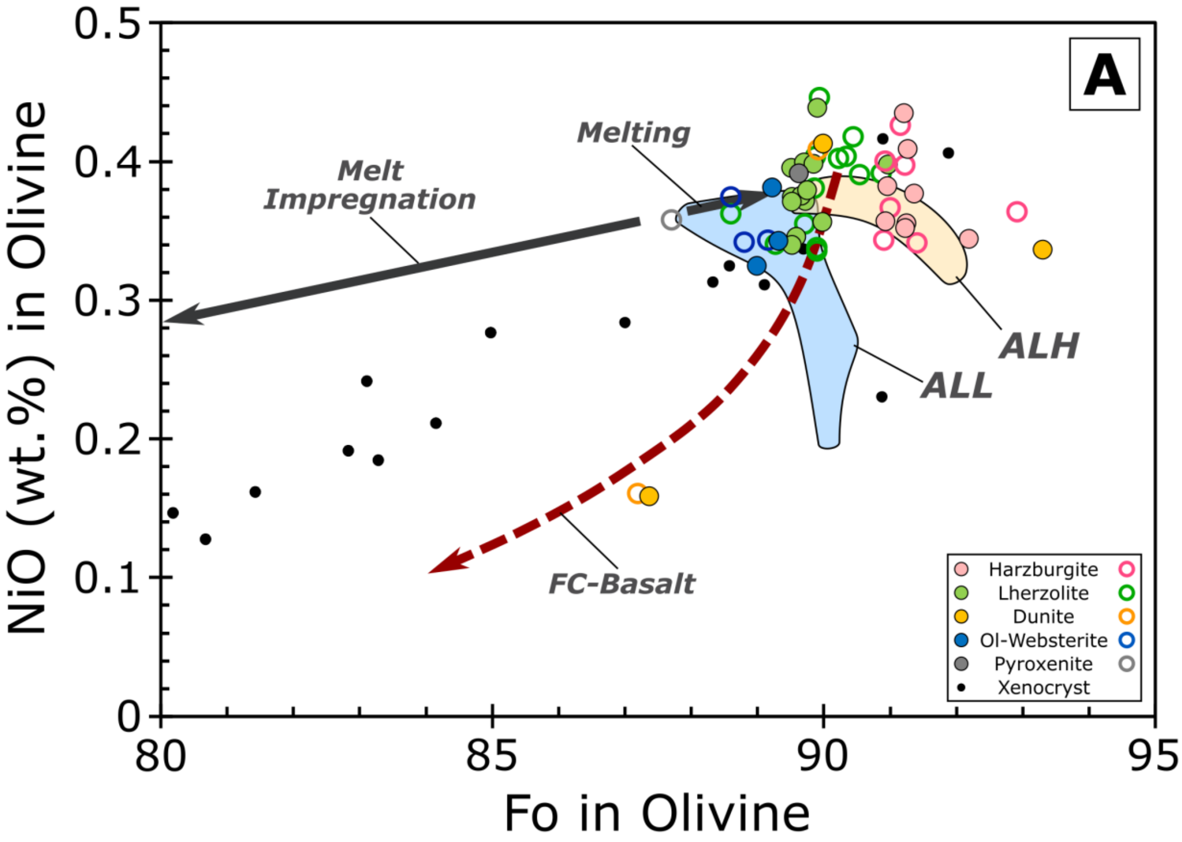

Figure 20: NiO vs. Forsterite in olivine. Fields for Alligator Lake harzburgites (ALH) and Alligator Lake lherzolites (ALL) derived from data in Shi et al. (1998) and Francis (1987). FC-Basalt represents an average fractional crystallization trend for typical tholeiitic basalt. Melting, melt impregnation and crystallization trends after Page et al. (2008).

0.61 and 0.11 to 0.21 wt.%, respectively (Figure 20). Olivines in the harzburgites have compositions of Fo_{90} and $Fo_{92.7}$ and NiO and MnO from 0.29 to 0.48 and 0.11 to 0.19 wt.%, respectively. Olivines in the lherzolites have compositions of $Fo_{88.5}$ to $Fo_{91.2}$ and NiO and MnO from 0.30 to 0.61 and 0.12 to 0.21 wt.%, respectively. Olivines in the websterites have compositions of $Fo_{88.9}$ to $Fo_{89.9}$ and NiO and MnO from 0.28 to 0.44 and 0.13 to 0.21 wt.%, respectively. Olivines in the pyroxenite 122F2B have compositions of $Fo_{88.4}$ and $Fo_{91.4}$ and NiO and MnO from 0.35 to 0.46 and 0.16 to 0.21 wt.%, respectively. Olivines in the dunites have compositions of $Fo_{87.3}$ and $Fo_{93.9}$ and NiO and MnO from 0.14 to 0.45 and 0.13 to 0.21 wt.%, respectively. Note that, though the pyroxenite and websterites overlap the lherzolites, there is generally no overlap with between the pyroxene-rich lithologies and the harzburgites except lherzolite 122F7B. As well, the dunites tend to plot in three different ranges: dunite 102F-2 tends to plot at the most residual range of compositions ($Fo_{93.3}$, NiO = 0.34 wt.%); 122F-1 tend to overlap, in part, the lherzolites (Fo_{90}, NiO = 0.41 wt.%); 102D-1, which is devoid of any phases other than olivine, tends to plot on its own ($Fo_{87.4}$, NiO = 0.16 wt.%) with a composition that falls along the expected fractional crystallization trend of average tholeiitic basalt (Figure 20).

Figure 21 illustrates the relationship between the Fo content and modal percentage of olivine for each of the Prindle xenoliths compared to those of xenoliths from various other xenolith localities as grouped by their Era. The abyssal peridotite trend annotated in Figure 21 effectively follows the expected path of partial melting in upper mantle peridotites, with which the Prindle xenolith suite does not correlate. Instead, the Prindle samples, particularly the more CPX-rich lithologies, tend to vary significantly in modal olivine for a given Fo content.

Spinel

Overall, spinel Cr# (100 x Cr / Cr + Al) and Mg# (100 x Mg / Mg + Fe) in the samples ranges from ~3.3-67.3 and ~42.8-97.3 with Al_2O_3 and TiO_2 ranging from ~2.58 to 63.16 wt.% and ~0 to 0.64 wt.%, respectively (Table 4)(Figure 22). Spinels in the harzburgites span a range of moderate to high Cr# (23.9 to 67.3) with Mg# of ~42.8 to 91.5 and Al_2O_3 and TiO_2 from 2.58 to 46.15 and 0 to 0.64 wt.%, respectively. Spinels in the lherzolites span a range of moderate to high Cr# (8.2 to 39.5) with Mg# of ~67.4 to 96.3 and Al_2O_3 and TiO_2 from 31.78 to 60.51 and 0 to 0.51 wt.%, respectively. Spinels in the websterites span a range of moderate to high Cr# (5.9 to 11.9) with Mg# of ~66.8 to 83 and Al_2O_3 and TiO_2 from 54.04 to 63.16 and 0.06 to 0.13 wt.%, respectively. Spinels in the pyroxenites span a range of moderate to high

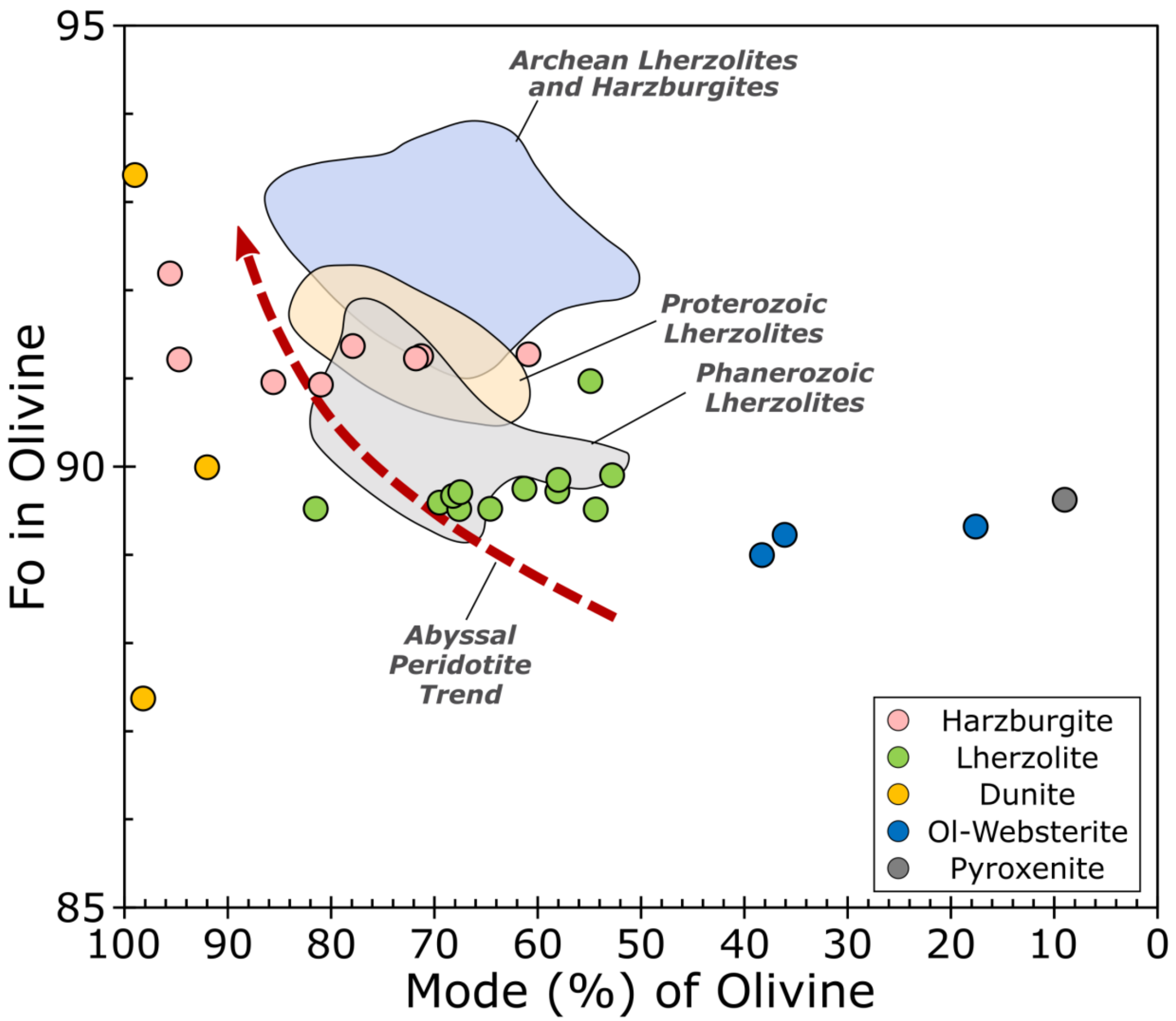

Figure 21: Forsterite in olivine vs. the modal percentage of olivine for the Prindle xenolith suite. Fields for Archean, Proterozoic, and Phanerozoic peridotites are from Griffin et al. (1999) with the data from Alligator Lake (Francis, 1987; Shi et al., 1998) added to the Phanerozoic field. The Abyssal Peridotite Trend is after Boyd (1989).

Table 4: Average core compositions for spinels in each sample.

Lithology	**Dunite**		**Harzburgite**								**Pyroxenite**		**Websterite**		
Expedition	15ATe	16ATe	15ATe						16ATe		15ATe	16ATe	15ATe		
Sample	122F	102D	122C		122F				102F		122F	102D	122C	122F	
Thin Section	122F-1	102D-1	122-C3A	122C3B	122F3B	122F6	122F7A	122F7-A	102F-1	102F-2	122F2B	102D-2	122-C1	122F5-1	122F5-2
N	*11*	*2*	*13*	*6*	*8*	*10*	*11*	*2*	*11*	*2*	*13*	*3*	*2*	*16*	*11*
SiO_2	0.03	0.01	0.04	0.22	0.03	0.08	0.04	0.04	0.03	0.10	0.10	0.01	0.07	0.04	0.07
TiO_2	0.17	0.12	0.02	0.05	0.09	0.05	0.02	0.02	0.11	0.07	0.11	0.12	0.08	0.09	0.09
Al_2O_3	28.17	60.18	37.43	44.50	34.31	43.19	44.75	41.51	34.62	20.94	53.43	60.81	58.24	60.76	60.92
Cr_2O_3	38.62	8.61	32.10	23.39	34.95	23.77	23.67	23.23	33.75	43.02	14.45	3.40	10.98	6.41	6.55
FeO	17.29	11.48	12.10	11.32	12.80	12.01	11.78	13.23	12.46	14.87	11.44	20.51	11.39	11.31	11.13
MnO	0.24	0.14	0.21	0.16	0.21	0.18	0.17	0.17	0.19	0.30	0.16	0.18	0.14	0.11	0.11
MgO	15.15	20.81	17.91	19.92	17.21	20.34	20.06	21.65	17.19	19.52	20.21	15.73	20.90	20.84	20.72
CaO	0.01	0.01	0.02	0.02	0.00	0.03	0.01	0.01	0.01	0.03	0.04	0.01	0.00	0.02	0.02
NiO	0.19	0.16	0.20	0.24	0.17	0.26	0.28	0.28	0.19	0.11	0.36	0.12	0.41	0.38	0.38
V_2O_5	0.24	0.32	0.16	0.12	0.18	0.14	0.14	0.13	0.17	0.16	0.10	0.16	0.09	0.08	0.08
Total	100.11	101.83	100.20	99.95	99.97	100.03	100.91	100.26	98.72	99.10	100.40	101.06	102.31	100.04	100.07
Cations (O = 4)															
Si	0.00	0.00	0.00	0.01	0.00	0.00	0.00	0.00	0.00	0.00	0.00	0.00	0.00	0.00	0.00
Ti	0.00	0.00	0.00	0.00	0.00	0.00	0.00	0.00	0.00	0.00	0.00	0.00	0.00	0.00	0.00
Al	0.98	1.79	1.24	1.42	1.16	1.38	1.42	1.32	1.18	0.73	1.65	1.86	1.74	1.82	1.83
Cr	0.90	0.17	0.72	0.50	0.79	0.51	0.50	0.50	0.77	1.01	0.30	0.07	0.22	0.13	0.13
Fe^{2+}	0.34	0.22	0.25	0.20	0.27	0.18	0.19	0.12	0.26	0.13	0.21	0.39	0.21	0.20	0.21
Fe^{3+}	0.09	0.02	0.04	0.06	0.04	0.10	0.07	0.17	0.04	0.24	0.05	0.05	0.03	0.04	0.03
Mn	0.01	0.00	0.01	0.00	0.01	0.00	0.00	0.00	0.00	0.01	0.00	0.00	0.00	0.00	0.00
Mg	0.67	0.78	0.75	0.80	0.73	0.82	0.80	0.87	0.74	0.87	0.79	0.61	0.79	0.79	0.79
Ca	0.00	0.00	0.00	0.00	0.00	0.00	0.00	0.00	0.00	0.00	0.00	0.00	0.00	0.00	0.00
Ni	0.00	0.00	0.00	0.01	0.00	0.01	0.01	0.01	0.00	0.00	0.01	0.00	0.01	0.01	0.01
V	0.00	0.01	0.00	0.00	0.00	0.00	0.00	0.00	0.00	0.00	0.00	0.00	0.00	0.00	0.00
$Fe^{2+}/\Sigma Fe^{A}$	0.78	0.79	0.87	0.77	0.87	0.68	0.73	0.42	0.87	0.36	0.76	0.94	0.86	0.84	0.87
$Mg\#^{B}$	66.5	77.7	75.1	80.4	73.3	82.4	80.6	87.5	73.8	86.7	79.1	60.9	79.2	79.6	79.2
$Cr\#^{C}$	48.0	8.8	36.6	26.1	40.6	27.0	26.2	27.3	39.5	57.9	15.4	3.6	11.2	6.6	6.7

[A] **Calculated following the method of Droop (1987)**

[B] **Mg# = 100 x Mg / Mg + Fe**

[C] **Cr# = 100 x Cr / Cr + Al**

Table 4: (Continued)

Lithology	Lherzolite														
Expedition	15ATe									16ATe					
Sample	122C		122D	122F						102A		102C	102D		102E
Thin Section	122C2	122-C3A	122D-1	122F2	122F2A	122F3A	122F4-1	122F4-2	122F7-B	102A (A-1)	102A (A-2)	102C	102D-2	102D-3	102E-1A
N	5	3	6	14	6	10	29	16	18	15	19	8	1	6	8
SiO_2	0.05	0.06	0.03	0.02	0.02	0.02	0.02	0.02	0.03	0.02	0.05	0.04	0.08	0.02	0.04
TiO_2	0.08	0.25	0.07	0.08	0.06	0.08	0.06	0.06	0.02	0.09	0.09	0.11	0.07	0.09	0.09
Al_2O_3	58.52	49.58	57.77	55.82	57.39	49.72	58.19	57.80	44.14	59.07	58.79	58.73	59.25	57.76	58.78
Cr_2O_3	9.09	19.16	10.54	11.82	9.71	13.54	9.33	9.29	23.17	8.83	8.93	9.96	10.45	10.13	9.67
FeO	10.84	10.16	10.80	10.59	10.83	11.36	10.88	10.85	11.33	11.00	11.36	11.34	10.79	12.14	11.44
MnO	0.13	0.21	0.12	0.12	0.13	0.14	0.13	0.12	0.18	0.12	0.13	0.11	0.11	0.13	0.12
MgO	20.99	20.40	20.43	21.43	21.53	24.63	20.49	21.85	19.98	20.20	20.43	20.55	21.12	20.67	20.50
CaO	0.01	0.00	0.01	0.00	0.01	0.01	0.01	0.01	0.01	0.01	0.01	0.01	0.00	0.00	0.01
NiO	0.40	0.27	0.36	0.36	0.37	0.36	0.38	0.40	0.26	0.39	0.38	0.39	0.37	0.38	0.40
V_2O_5	0.08	0.13	0.08	0.09	0.08	0.09	0.09	0.08	0.13	0.08	0.07	0.08	0.10	0.09	0.09
Total	100.19	100.22	100.20	100.35	100.12	99.96	99.58	100.49	99.26	99.80	100.24	101.30	102.34	101.41	101.14
Cations (O = 4)															
Si	0.00	0.00	0.00	0.00	0.00	0.00	0.00	0.00	0.00	0.00	0.00	0.00	0.00	0.00	0.00
Ti	0.00	0.01	0.00	0.00	0.00	0.00	0.00	0.00	0.00	0.00	0.00	0.00	0.00	0.00	0.00
Al	1.77	1.54	1.75	1.69	1.73	1.51	1.77	1.74	1.42	1.78	1.76	1.76	1.76	1.74	1.77
Cr	0.18	0.41	0.21	0.24	0.20	0.28	0.19	0.19	0.50	0.18	0.18	0.20	0.21	0.20	0.20
Fe^{2+}	0.19	0.20	0.21	0.17	0.17	0.12	0.20	0.16	0.18	0.24	0.24	0.21	0.20	0.21	0.22
Fe^{3+}	0.04	0.03	0.02	0.06	0.06	0.16	0.03	0.07	0.07	0.02	0.03	0.03	0.02	0.05	0.03
Mn	0.00	0.00	0.00	0.00	0.00	0.00	0.00	0.00	0.00	0.00	0.00	0.00	0.00	0.00	0.00
Mg	0.80	0.81	0.78	0.82	0.82	0.95	0.79	0.83	0.81	0.77	0.77	0.78	0.79	0.79	0.78
Ca	0.00	0.00	0.00	0.00	0.00	0.00	0.00	0.00	0.00	0.00	0.00	0.00	0.00	0.00	0.00
Ni	0.01	0.01	0.01	0.01	0.01	0.01	0.01	0.01	0.01	0.01	0.01	0.01	0.01	0.01	0.01
V	0.00	0.00	0.00	0.00	0.00	0.00	0.00	0.00	0.00	0.00	0.00	0.00	0.00	0.00	0.00
$Fe^{2+}/\Sigma Fe^{A}$	0.83	0.87	0.90	0.76	0.75	0.35	0.87	0.70	0.72	0.93	0.89	0.93	0.92	0.81	0.88
$Mg\#^{B}$	80.6	80.5	78.9	82.7	82.8	89.6	79.4	83.6	81.5	76.6	76.2	78.5	79.5	79.0	78.3
$Cr\#^{C}$	9.4	20.9	10.9	12.4	10.2	15.6	9.7	9.7	26.0	9.1	9.3	10.2	10.6	10.5	9.9

[A] **Calculated following the method of Droop (1987)**

[B] **Mg# = 100 x Mg / Mg + Fe**

[C] **Cr# = 100 x Cr / Cr + Al**

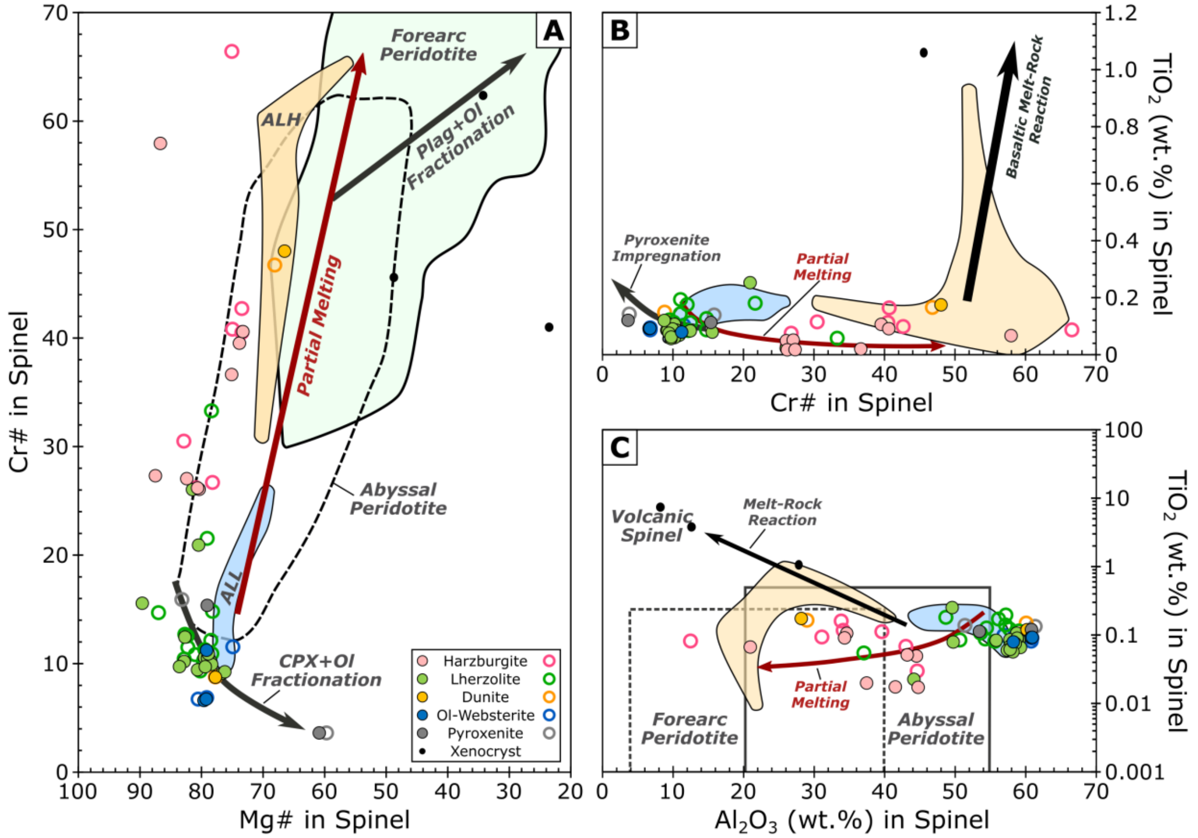

Figure 22: Geochemical plots for spinels from the Prindle xenolith suite. (A) Cr# vs. Mg# in spinel. Fields for Abyssal Peridotite and Forearc Peridotite as well as melting and fractionation trends are from Dick and Bullen (1984) with data from Loocke et al. (in prep) added to the Forearc Peridotite field. (B) TiO_2 vs. Cr# in spinel with trends after Dick and Bullen (1984) and Loocke et al. (in prep). (C) TiO_2 vs. Al_2O_3 in spinel with fields after Kamenetsky et al. (2001). Fields for Alligator Lake same as in Figure 20.

Cr# (3.3 to 21.9) with Mg# of ~57.3 to 97.3 and Al_2O_3 and TiO_2 from 32.78 to 61.91 and 0.05 to 0.33 wt.%, respectively. Spinels in the dunites plot at two different compositional extremes: dunite 122F-1 averages a moderate Cr# of 48 with Mg# of ~66.5 and Al_2O_3 and TiO_2 of 28.17 and 0.17 wt.%, respectively; dunite 102D-1 averages a low Cr# of 8.8 with Mg# of ~77.7 and Al_2O_3 and TiO_2 of 60.18 and 0.12 wt.%, respectively.

Generally speaking, the spinels in the Prindle harzburgites follow established partial melting trends (Figure 22) with the exception of their Cr# vs. Mg#, which mimics the expected partial melting trend at higher Mg#s; suggesting that the Prindle harzburgites are likely derived from a more pristine, previously un-melted upper mantle. We also note that the more CPX-rich lithologies tend to plot along with trends which are typically associated with melt addition and crystallization of primarily CPX and olivine.

Orthopyroxene

Overall, analyzed orthopyroxenes (Table 5) have Mg# and Cr#s that range from 73.8 to 95.8 and 1.7 to 14, respectively (Figure 23), with Al_2O_3, Cr_2O_3, TiO_2, and Na_2O ranging from 1.39 to 6.21, 0.16 to 0.58, 0 to 0.22, and 0.01 to 0.08 wt.%, respectively (Figure 24). Orthopyroxenes in the harzburgites have Mg#s and Cr#s that range from 90.3 to 95.8 and 8.3 to 14, respectively, with Al_2O_3, Cr_2O_3, TiO_2, and Na_2O ranging from 1.98 to 4.15, 0.48 to 0.58, 0 to 0.06, and 0.02 to 0.08 wt.%, respectively. Orthopyroxenes in the lherzolites have Mg#s and Cr#s that range from 85.8 to 92.4 and 3.5 to 9.2, respectively, with Al_2O_3, Cr_2O_3, TiO_2, and Na_2O ranging from 3.4 to 4.82, 0.19 to 0.53, 0.02 to 0.22, and 0.03 to 0.06, respectively. Orthopyroxenes in the websterites have Mg#s and Cr#s that range from 88 to 89.5 and 2.8 to 4.8, respectively, with Al_2O_3, Cr_2O_3, TiO_2, and Na_2O ranging from 3.81 to 4.97, 0.19 to 0.32, 0.08 to 0.12, and 0.03 to 0.05 wt.%, respectively. Orthopyroxenes in the pyroxenites have Mg#s and Cr#s that range from 73.8 to 89.9 and 1.7 to 5.1, respectively, with Al_2O_3, Cr_2O_3, TiO_2, and Na_2O ranging from 3.92 to 6.21, 0.16 to 0.33, 0.06 to 0.15, and 0.03 to 0.05, respectively. Orthopyroxenes in the dunites have Mg#s and Cr#s that range from 86.7 to 89.1 and 3.4 to 11.4, respectively, with Al_2O_3, Cr_2O_3, TiO_2, and Na_2O ranging from 1.39 to 3.88, 0.2 to 0.38, 0.03 to 0.09, and 0.01 to 0.05 wt.%, respectively.

As with olivine and spinel, orthopyroxene in the harzburgites roughly correlates with expected partial melting trends for most elements (Figure 24) and molar ratios (Figure 23) except for Cr_2O_3. Actually, the Cr_2O_3 contents in orthopyroxene for all of the Prindle

Table 5: Average composition of orthopyroxene for each sample.

Lithology	**Dunite**		**Harzburgite**								**Websterite**			**Pyroxenite**	
Expedition	15ATe	16ATe	15ATe						16ATe		15ATe			15ATe	16ATe
Sample	122F	102F	122C		122F				102F		122C	122F		122F	102D
Thin Section	122F-1	102F-2	122C3A	122C3-B	122F3B	122F6	122F7A	122F7-A	102F-1	102F-2	122C1	122F5-1	122F5-2	122F2B	102D-2
N	*6*	*2*	*9*	*4*	*6*	*8*	*8*	*5*	*7*	*3*	*3*	*10*	*6*	*8*	*9*
SiO_2	54.21	56.58	56.55	55.12	56.52	55.35	54.96	55.11	55.10	57.65	56.02	54.76	54.27	55.40	52.09
Al_2O_3	1.97	3.88	4.15	3.71	2.62	3.96	3.71	3.70	2.55	1.98	4.81	4.97	4.58	4.14	6.21
Cr_2O_3	0.38	0.20	0.55	0.52	0.51	0.52	0.55	0.51	0.53	0.48	0.32	0.21	0.21	0.33	0.16
TiO_2	0.03	0.09	0.06	0.01	0.03	0.01	0.02	0.02	0.03	0.01	0.10	0.12	0.12	0.07	0.15
FeO	9.22	7.19	5.99	6.07	5.91	5.84	6.07	5.99	5.91	5.58	6.93	7.22	7.36	7.53	16.00
MgO	33.79	33.06	32.99	33.01	34.46	32.88	33.25	33.31	34.68	34.81	31.59	32.47	31.97	32.29	25.23
MnO	0.12	0.12	0.12	0.14	0.12	0.13	0.13	0.13	0.11	0.10	0.13	0.14	0.16	0.15	0.27
CaO	0.37	0.44	0.72	0.67	0.62	0.67	0.66	0.67	0.59	0.65	0.53	0.53	0.52	0.55	0.45
Na_2O	0.01	0.05	0.08	0.02	0.02	0.02	0.02	0.02	0.02	0.02	0.03	0.05	0.05	0.05	0.03
K_2O		0.01	0.02	0.02	0.00	0.00	0.00			0.00			0.01		
Total	100.45	101.62	101.22	99.29	100.87	99.41	99.37	99.46	99.83	101.28	100.46	100.52	99.28	100.52	100.61
Cations (O = 6)															
Si	1.88	1.93	1.93	1.92	1.93	1.92	1.91	1.91	1.90	1.96	1.94	1.89	1.90	1.91	1.87
Al	0.08	0.16	0.17	0.15	0.11	0.16	0.15	0.15	0.10	0.08	0.20	0.20	0.19	0.17	0.26
Cr	0.01	0.01	0.01	0.01	0.01	0.01	0.01	0.01	0.01	0.01	0.01	0.01	0.01	0.01	0.00
Ti	0.00	0.00	0.00	0.00	0.00	0.00	0.00	0.00	0.00	0.00	0.00	0.00	0.00	0.00	0.00
Fe	0.42	0.20	0.18	0.21	0.19	0.20	0.21	0.19	0.17	0.16	0.20	0.24	0.23	0.23	0.48
Mg	1.75	1.68	1.68	1.71	1.75	1.70	1.72	1.72	1.78	1.76	1.63	1.67	1.66	1.66	1.35
Mn	0.00	0.00	0.00	0.00	0.00	0.00	0.00	0.00	0.00	0.00	0.00	0.00	0.00	0.00	0.01
Ca	0.01	0.02	0.03	0.02	0.02	0.02	0.02	0.02	0.02	0.02	0.02	0.02	0.02	0.02	0.02
Na	0.00	0.00	0.01	0.00	0.00	0.00	0.00	0.00	0.00	0.00	0.00	0.00	0.00	0.00	0.00
K		0.00	0.00	0.00	0.00	0.00	0.00			0.00			0.00		
En	0.86	0.88	0.89	0.89	0.89	0.90	0.90	0.90	0.94	0.91	0.88	0.87	0.88	0.87	0.41
Fs	0.13	0.11	0.09	0.09	0.09	0.09	0.09	0.09	0.05	0.08	0.11	0.11	0.11	0.11	0.58
Wo	0.01	0.01	0.01	0.01	0.01	0.01	0.01	0.01	0.01	0.01	0.01	0.01	0.01	0.01	0.01
Mg#[A]	86.7	89.1	90.7	90.6	90.3	90.9	90.7	90.8	95.2	91.7	89.0	88.0	88.6	88.2	73.8
Cr#[B]	11.4	3.4	8.7	8.6	11.6	8.3	9.0	8.5	12.3	14.0	4.3	2.8	3.0	5.1	1.7

[A] **Mg# = 100 x Mg / Mg + Fe**

[B] **Cr# = 100 x Cr / Cr + Al**

Table 5: (Continued)

Lithology	Lherzolite													
Expedition	15ATe								16ATe					
Sample	122C	122D	122F						102A		102C	102D		102E
Thin Section	122C2	122D-1	122F2	122F2A	122F3A	122F4-1	122F4-2	122F7-B	102A (A-1)	102A (A-2)	102C	102D-1	102D-3	102E-1A
N	*4*	*10*	*11*	*5*	*6*	*17*	*11*	*14*	*9*	*7*	*4*	*1*	*4*	*6*
SiO_2	55.19	53.27	55.34	53.66	55.45	55.48	55.55	55.23	54.58	54.45	55.71	55.66	55.28	54.63
Al_2O_3	4.82	4.01	4.09	4.16	4.09	4.15	4.05	3.96	4.61	4.34	4.12	4.03	4.05	4.11
Cr_2O_3	0.26	0.28	0.31	0.27	0.31	0.25	0.25	0.53	0.28	0.26	0.25	0.22	0.26	0.28
TiO_2	0.11	0.09	0.10	0.08	0.08	0.09	0.09	0.02	0.11	0.12	0.10	0.22	0.09	0.12
FeO	6.64	9.30	6.91	9.48	6.67	6.74	7.04	6.03	7.10	7.10	6.92	8.04	7.18	6.99
MgO	32.28	32.44	33.32	32.10	33.03	32.92	33.40	33.04	31.69	32.19	32.84	32.00	32.92	33.11
MnO	0.12	0.13	0.13	0.13	0.14	0.14	0.13	0.12	0.12	0.14	0.13	0.13	0.15	0.14
CaO	0.53	0.50	0.52	0.49	0.49	0.46	0.45	0.67	0.55	0.50	0.49	0.44	0.49	0.49
Na_2O	0.05	0.04	0.05	0.04	0.05	0.05	0.03	0.03	0.05	0.05	0.05	0.04	0.04	0.05
K_2O						0.04		0.01	0.01	0.01				0.01
Total	100.07	100.39	100.87	100.69	100.35	100.31	101.08	99.63	99.10	99.19	100.61	100.78	100.52	100.10
Cations (O = 6)														
Si	1.91	1.85	1.90	1.86	1.91	1.91	1.90	1.91	1.91	1.90	1.92	1.92	1.90	1.89
Al	0.20	0.16	0.17	0.17	0.17	0.17	0.16	0.16	0.19	0.18	0.17	0.16	0.16	0.17
Cr	0.01	0.01	0.01	0.01	0.01	0.01	0.01	0.01	0.01	0.01	0.01	0.01	0.01	0.01
Ti	0.00	0.00	0.00	0.00	0.00	0.00	0.00	0.00	0.00	0.00	0.00	0.01	0.00	0.00
Fe	0.25	0.40	0.23	0.37	0.22	0.21	0.23	0.21	0.21	0.21	0.20	0.23	0.21	0.20
Mg	1.66	1.68	1.70	1.66	1.70	1.69	1.70	1.71	1.65	1.68	1.68	1.65	1.69	1.71
Mn	0.00	0.00	0.00	0.00	0.00	0.00	0.00	0.00	0.00	0.00	0.00	0.00	0.00	0.00
Ca	0.02	0.02	0.02	0.02	0.02	0.02	0.02	0.02	0.02	0.02	0.02	0.02	0.02	0.02
Na	0.00	0.00	0.00	0.00	0.00	0.00	0.00	0.00	0.00	0.00	0.00	0.00	0.00	0.00
K						0.00		0.00	0.00	0.00				0.00
En	0.87	0.85	0.87	0.85	0.88	0.89	0.87	0.90	0.66	0.68	0.67	0.64	0.89	0.91
Fs	0.10	0.14	0.10	0.14	0.10	0.10	0.10	0.09	0.33	0.32	0.32	0.36	0.10	0.08
Wo	0.01	0.01	0.01	0.01	0.01	0.01	0.01	0.01	0.01	0.01	0.01	0.01	0.01	0.01
Mg#^{A}	88.4	86.1	88.2	85.8	89.2	89.4	88.2	90.7	88.8	89.0	89.4	87.6	90.0	91.6
Cr#^{B}	3.5	4.4	4.8	4.1	4.9	3.9	4.0	8.4	4.0	3.9	3.9	3.6	4.1	4.4

^{A} Mg# = 100 x Mg / Mg + Fe

^{B} Cr# = 100 x Cr / Cr + Al

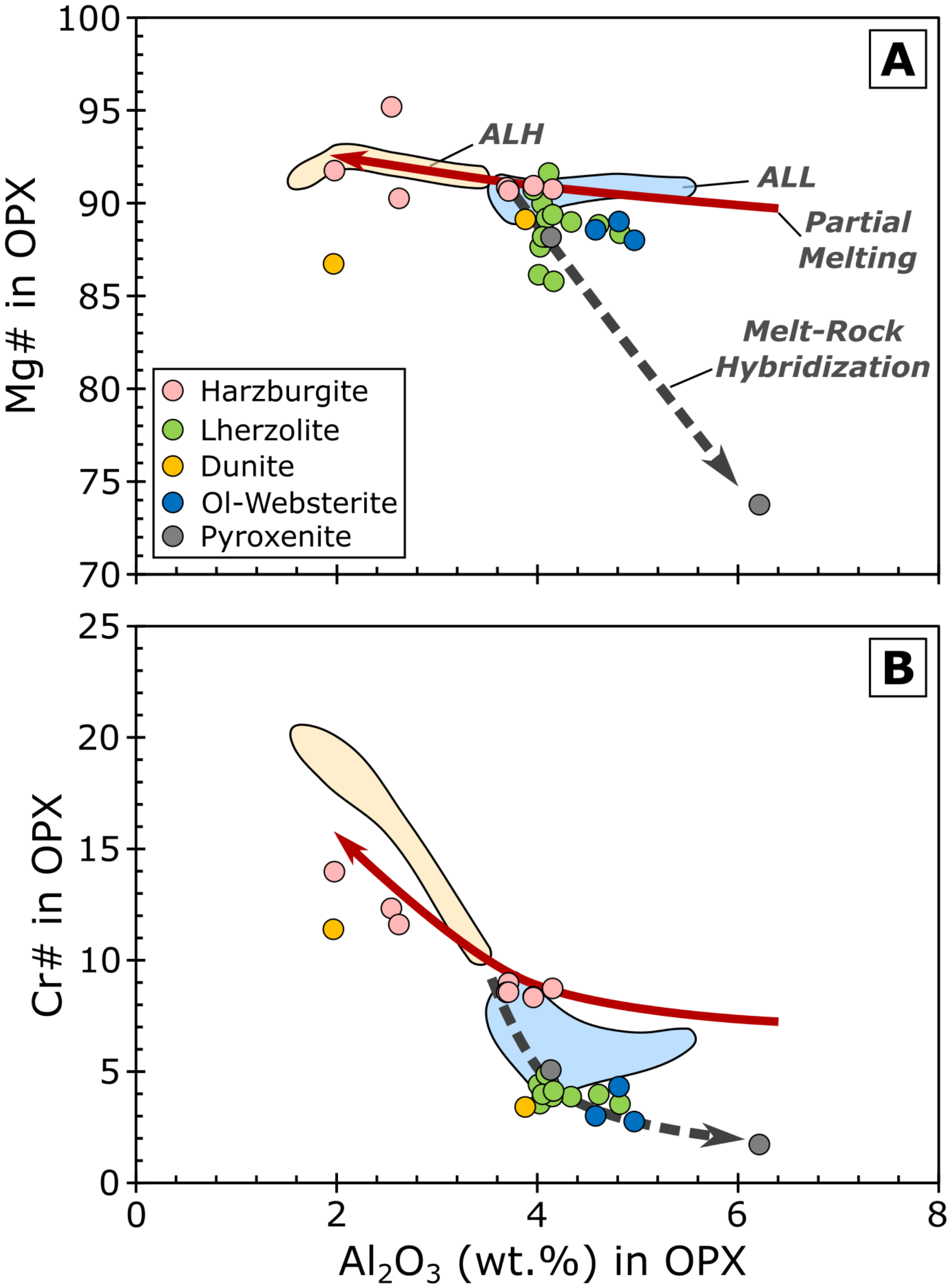

Figure 23: Plots of (A) Mg# and (B) Cr# vs. Al_2O_3 in orthopyroxene. Fields for Alligator Lake as in Figure 20.

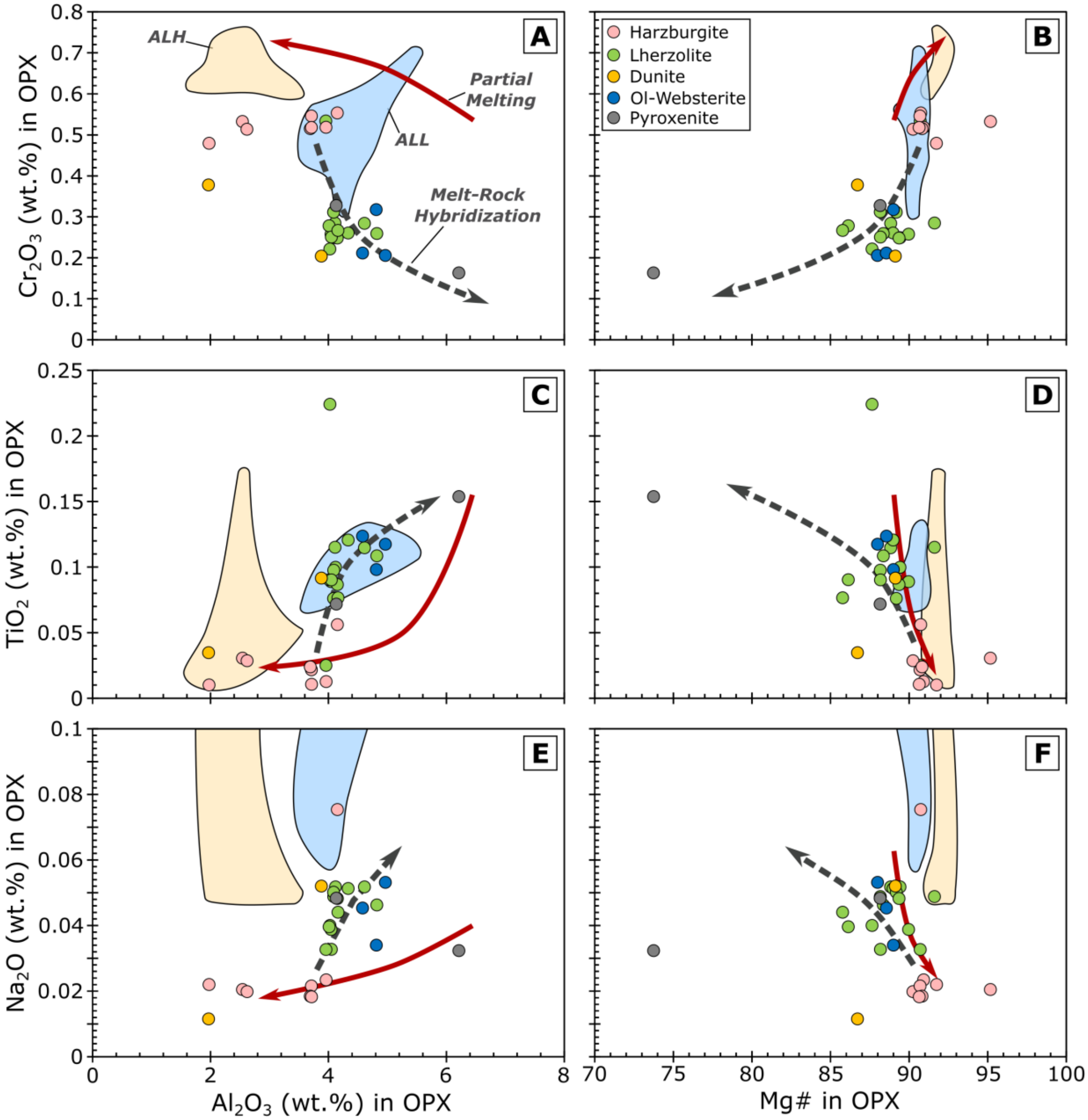

Figure 24: Plots of Cr_2O_3, TiO_2, and Na_2O vs (A,C,E) Al_2O_3 and (B,D,F) Mg# in orthopyroxene. Fields for Alligator Lake as in Figure 20.

lithologies are markedly lower than expected, especially when compared to similar lithologies from other NCVP localities, like Alligator Lake (Shi et al., 1998; Peslier et al., 2002, Kilgore et al., 2018). Further, the Prindle xenolith orthopyroxenes are also found to have significantly lower Na_2O contents when compared with those from Alligator Lake. The only Prindle lithologies which come close to the same Na_2O contents as the Alligator Lake xenoliths are the CPX-rich lithologies which form a trend towards higher Na_2O which is decoupled from the expected partial melting trend. In general, the orthopyroxenes in the CPX-rich lithologies from Prindle are found to trend apart from the harzburgites towards higher Al_2O_3, TiO_2, and Na_2O and lower Cr_2O_3, Cr#, and Mg# (Figures 23 & 24). We note that these trends seemingly are demarked by orthopyroxenes from the pyroxenites, with the orthopyroxene from sample 122F2B forming the lead of the trend.

Clinopyroxene

Overall, analyzed clinopyroxenes (Table 6) have Mg# and Cr#s that range from 71.7 to 93.2 and 0.1 to 18.8, respectively (Figure 25), with Al_2O_3, Cr_2O_3, TiO_2, and Na_2O ranging from 1.63 to 11.46, 0.02 to 1.02, 0.02 to 1.30, and 0.35 to 1.55 wt.%, respectively (Figure 26). Clinopyroxenes in the harzburgites have Mg# and Cr#s that range from 89.2 to 93.2 and 12.7 to 18.8, respectively, with Al_2O_3, Cr_2O_3, TiO_2, and Na_2O ranging from 2.62 to 4.36, 0.77 to 1.02, 0.02 to 0.18, and 0.39 to 0.54 wt.%, respectively. Clinopyroxenes in the lherzolites have Mg# and Cr#s that range from 87.5 to 91.6 and 6.1 to 13.5, respectively, with Al_2O_3, Cr_2O_3, TiO_2, and Na_2O ranging from 3.51 to 6.87, 0.5 to 0.86, 0.03 to 0.61, and 0.46 to 1.50 wt.%, respectively. Clinopyroxenes in the websterites have Mg# and Cr#s that range from 87.4 to 91.1 and 4.1 to 7.5, respectively, with Al_2O_3, Cr_2O_3, TiO_2, and Na_2O ranging from 5.21 to 7.61, 0.42 to 0.68, 0.37 to 0.57, and 1.04 to 1.36 wt.%, respectively. Clinopyroxenes in the pyroxenites have Mg# and Cr#s that range from 71.7 to 89.2 and 0.1 to 9.5, respectively, with Al_2O_3, Cr_2O_3, TiO_2, and Na_2O ranging from 5.7 to 11.46, 0.02 to 0.91, 0.28 to 1.18, and 0.79 to 1.26 wt.%, respectively. Only two small clinopyroxenes were found in the dunites with Mg# and Cr#s that range from 87.5 to 90.1 and 5.3 to 16.3, respectively, with Al_2O_3, Cr_2O_3, TiO_2,

Table 6: Average composition of clinopyroxene for each sample.

Lithology	**Dunite**		**Harzburgite**							**Websterite**		
Expedition	15ATe	16ATe	15ATe						16ATe	15ATe		
Sample	122F	102D	122C		122F				102F	122C	122F	
Thin Section	122F-1	102D-1	122C3A	122C3B	122F3B	122F6	122F7A	122F7-A	102F-1	122C1	122F5-1	122F5-2
N	*1*	*4*	*7*	*6*	*3*	*9*	*9*	*5*	*9*	*4*	*8*	*7*
SiO_2	53.55	51.54	53.30	52.72	53.17	52.86	52.31	52.64	53.32	52.77	51.58	51.26
Al_2O_3	1.63	7.26	3.88	4.36	2.93	3.97	3.89	3.85	2.76	5.65	7.61	6.74
Cr_2O_3	0.48	0.61	0.80	0.92	1.02	0.88	0.91	0.92	0.85	0.68	0.48	0.49
TiO_2	0.11	1.30	0.09	0.04	0.08	0.03	0.03	0.02	0.09	0.37	0.57	0.57
FeO	3.36	2.81	2.41	2.68	2.28	2.40	2.50	2.42	2.33	2.70	3.08	3.09
MgO	17.03	14.29	16.88	16.39	17.46	16.50	16.81	16.55	17.83	15.52	14.85	14.77
MnO	0.05	0.09	0.07	0.07	0.08	0.07	0.08	0.06	0.07	0.07	0.06	0.07
CaO	23.63	20.41	21.82	21.76	22.28	22.44	22.49	22.46	21.95	21.31	20.93	21.22
Na_2O	0.35	1.55	0.48	0.49	0.41	0.44	0.49	0.47	0.39	1.07	1.36	1.28
K_2O	-	-	0.02	0.04	0.00	0.00	0.01	0.00	0.01	0.01	-	0.01
Total	100.31	99.86	99.73	99.49	99.73	99.60	99.51	99.39	99.63	100.15	100.59	99.58
Cations (O = 6)												
Si	1.944	1.871	1.936	1.923	1.931	1.925	1.904	1.921	1.935	1.908	1.856	1.866
Al	0.070	0.311	0.166	0.188	0.126	0.170	0.167	0.165	0.118	0.241	0.322	0.289
Cr	0.014	0.017	0.023	0.027	0.029	0.025	0.026	0.027	0.024	0.019	0.014	0.014
Ti	0.003	0.036	0.002	0.001	0.002	0.001	0.001	0.000	0.002	0.010	0.016	0.016
Fe	0.149	0.085	0.073	0.105	0.077	0.087	0.109	0.084	0.077	0.083	0.119	0.124
Mg	0.922	0.774	0.914	0.891	0.945	0.896	0.912	0.900	0.965	0.837	0.796	0.801
Mn	0.002	0.003	0.002	0.002	0.002	0.002	0.002	0.002	0.002	0.002	0.002	0.002
Ca	0.919	0.794	0.849	0.851	0.867	0.876	0.877	0.878	0.854	0.825	0.807	0.827
Na	0.025	0.109	0.034	0.035	0.029	0.031	0.035	0.033	0.028	0.075	0.095	0.090
K			0.001	0.002	0.000	0.000	0.000	0.000	0.001	0.000		0.000
En	0.474	0.405	0.498	0.488	0.500	0.486	0.489	0.486	0.512	0.480	0.464	0.465
Fs	0.053	0.178	0.040	0.045	0.037	0.040	0.041	0.040	0.035	0.047	0.055	0.055
Wo	0.473	0.416	0.463	0.467	0.461	0.475	0.470	0.474	0.453	0.473	0.476	0.480
Mg#[A]	90.0	90.1	92.6	91.6	92.5	92.5	89.3	92.0	93.2	91.1	87.4	89.5
Cr#[B]	16.3	5.3	12.9	12.7	18.8	13.1	13.5	13.8	17.1	7.5	4.2	4.6

[A] **Mg# = 100 x Mg / Mg + Fe**

[B] **Cr# = 100 x Cr / Cr + Al**

Table 6: (Continued)

Lithology	**Pyroxenite**			**Lherzolite**												
Expedition	15ATe	16ATe		15ATe								16ATe				
Sample	122F	102D	102F	122C	122D	122F						102A		102C	102D	102E
Thin Section	122F2B	102D-2	102F-2	122C2	122D-1	122F2	122F2A	122F3A	122F4-1	122F4-2	122F7-B	102A (A-1)	102A (A-2)	102C	102D-3	102E-1A
	7	*13*	*8*	*8*	*10*	*11*	*6*	*6*	*19*	*13*	*13*	*18*	*11*	*6*	*5*	*7*
SiO_2	52.64	49.36	47.61	52.25	51.04	52.27	51.72	52.89	51.99	52.02	52.28	51.29	51.26	52.29	51.96	51.81
Al_2O_3	5.79	8.99	11.46	6.78	6.07	6.05	6.43	6.28	5.94	6.06	4.66	6.87	6.74	6.51	5.90	6.17
Cr_2O_3	0.91	0.30	0.02	0.66	0.72	0.82	0.69	0.82	0.60	0.64	0.86	0.66	0.66	0.71	0.65	0.64
TiO_2	0.28	1.18	1.12	0.46	0.42	0.43	0.45	0.42	0.47	0.45	0.03	0.56	0.58	0.61	0.43	0.55
FeO	3.12	5.80	6.98	2.59	3.70	2.65	3.78	2.63	2.82	2.94	2.45	3.00	3.00	2.91	3.02	2.98
MgO	15.28	12.45	10.26	14.80	15.16	15.31	14.88	15.07	15.28	15.44	16.40	14.31	14.54	14.86	15.15	15.30
MnO	0.08	0.13	0.11	0.09	0.06	0.07	0.07	0.07	0.08	0.07	0.08	0.07	0.08	0.07	0.07	0.07
CaO	21.15	20.94	22.46	21.01	21.06	20.76	20.99	20.96	21.38	21.21	22.35	20.42	20.50	20.60	21.10	20.93
Na_2O	1.26	0.94	0.85	1.20	1.15	1.35	1.32	1.38	1.09	1.16	0.47	1.49	1.50	1.40	1.25	1.19
K_2O			0.01	0.01		0.00			0.01	0.01	0.01	0.01	0.01		0.01	0.00
Total	100.54	100.10	100.90	99.85	99.49	99.73	100.42	100.55	99.69	100.04	99.58	98.70	98.90	99.97	99.59	99.70
Cations (O = 6)																
Si	1.898	1.813	1.748	1.895	1.863	1.895	1.870	1.904	1.890	1.883	1.903	1.882	1.876	1.894	1.890	1.882
Al	0.246	0.389	0.496	0.290	0.261	0.258	0.274	0.266	0.254	0.259	0.200	0.297	0.291	0.278	0.253	0.264
Cr	0.026	0.009	0.001	0.019	0.021	0.023	0.020	0.023	0.017	0.018	0.025	0.019	0.019	0.020	0.019	0.019
Ti	0.008	0.033	0.031	0.013	0.011	0.012	0.012	0.011	0.013	0.012	0.001	0.016	0.016	0.017	0.012	0.015
Fe	0.109	0.178	0.224	0.079	0.164	0.088	0.149	0.092	0.103	0.105	0.111	0.107	0.095	0.088	0.092	0.093
Mg	0.821	0.682	0.562	0.800	0.825	0.827	0.802	0.808	0.828	0.833	0.890	0.783	0.793	0.802	0.822	0.829
Mn	0.002	0.004	0.003	0.003	0.002	0.002	0.002	0.002	0.002	0.002	0.002	0.002	0.002	0.002	0.002	0.002
Ca	0.817	0.824	0.884	0.817	0.823	0.806	0.813	0.808	0.832	0.822	0.871	0.803	0.804	0.800	0.822	0.815
Na	0.088	0.067	0.061	0.085	0.081	0.095	0.093	0.097	0.077	0.081	0.033	0.106	0.106	0.099	0.088	0.084
K			0.000	0.000		0.000			0.000	0.000	0.000	0.000	0.000		0.000	0.000
En	0.472	0.307	0.338	0.472	0.468	0.482	0.464	0.475	0.472	0.473	0.485	0.407	0.416	0.411	0.477	0.482
Fs	0.054	0.321	0.129	0.460	0.064	0.047	0.066	0.047	0.049	0.051	0.041	0.175	0.162	0.180	0.046	0.044
Wo	0.472	0.372	0.532	0.482	0.468	0.470	0.470	0.477	0.477	0.472	0.475	0.418	0.422	0.409	0.477	0.474
Mg#[A]	88.9	79.3	71.7	91.0	88.0	90.8	87.5	90.4	89.8	88.9	91.3	89.5	89.6	90.1	89.9	90.1
Cr#[B]	9.5	2.2	0.1	6.2	7.3	8.3	6.7	8.1	6.4	6.7	12.0	6.1	6.2	6.8	6.9	6.5

[A] Mg# = 100 x Mg / Mg + Fe

[B] Cr# = 100 x Cr / Cr + Al

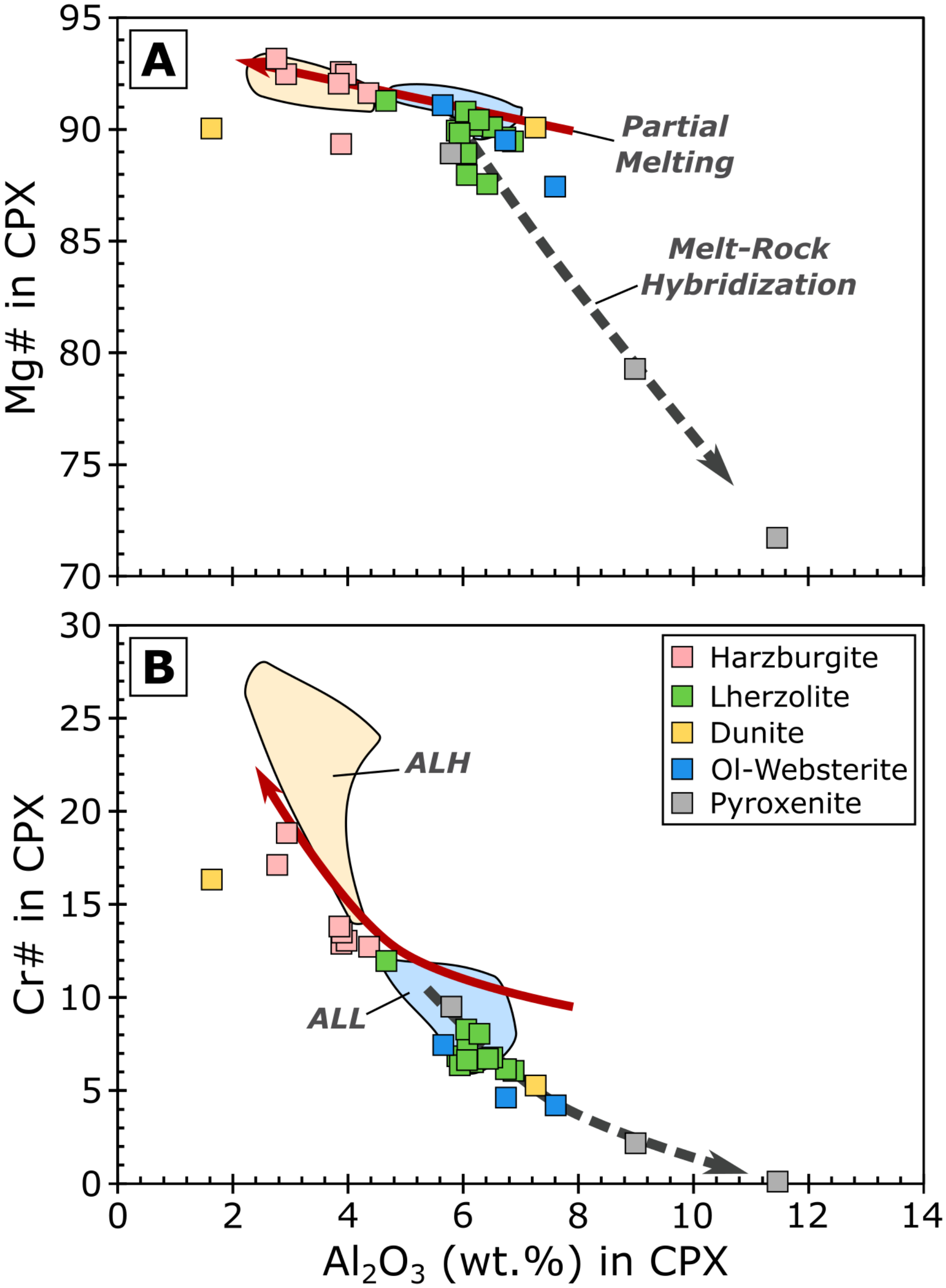

Figure 25: Plots of (A) Mg# and (B) Cr# vs. Al_2O_3 in orthopyroxene. Fields for Alligator Lake as in Figure 20.

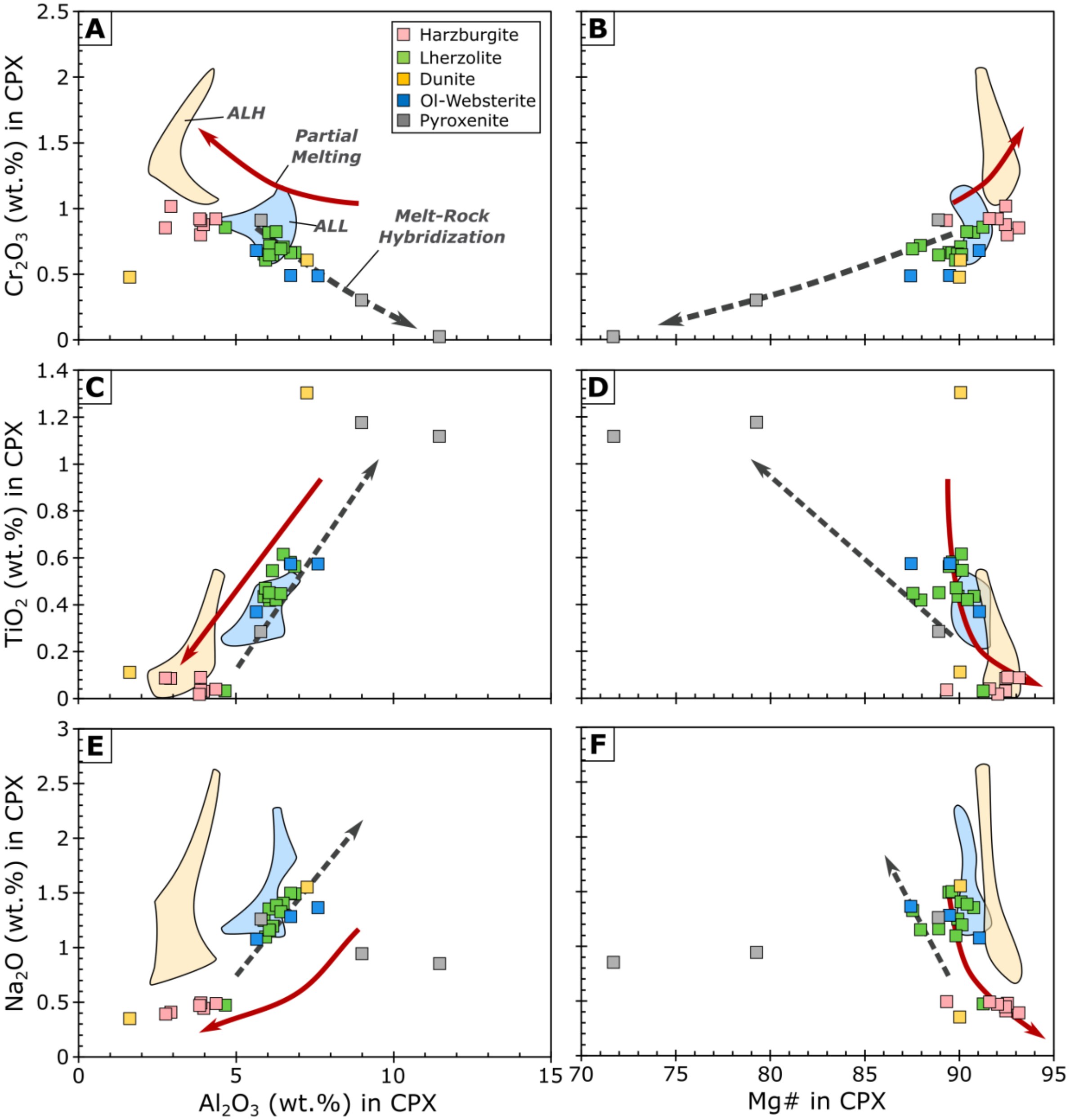

Figure 26: Plots of Cr_2O_3, TiO_2, and Na_2O vs (A,C,E) Al_2O_3 and (B,D,F) Mg# in clinopyroxene. Fields for Alligator Lake as in Figure 20.

and Na_2O ranging from 1.63 to 7.26, 0.48 to 0.71, 0.11 to 1.30, and 0.35 to 1.55 wt.%, respectively.

In general, the major and minor element chemistry of the harzburgite clinopyroxenes correlates with the expected partial melting trends for the primitive upper mantle (Figure 26). The possible exception to this correlation is Cr_2O_3 which, like the Prindle orthopyroxenes, falls to lower values than expected for the PUM. Regarding Cr_2O_3, the clinopyroxene across the Prindle lithologies tends to form a general trend of decreasing Cr_2O_3 with increasing Al_2O_3. In contrast to the harzburgites, the CPX-rich lithologies tend to form arrays apart from the expected partial melting trends which are characterized by increasing Al_2O_3, TiO_2, and Na_2O and decreasing Cr_2O_3, Cr#, and Mg# (Figures 25 & 26). As with the orthopyroxenes, the trends in the CPX-rich lithologies are seemingly demarked by the clinopyroxenes from the pyroxenites which form relatively linear arrays with the clinopyroxene from 122F2B forming the lead.

Geothermometry

Equilibrium temperatures were estimated using the two-pyroxene and Ca-in-OPX thermometer of Brey and Kohler (1990). Two-pyroxene geothermometry is a reliable method for estimating the equilibrium temperatures based on the solubility of diopside and enstatite in coexisting orthopyroxene and clinopyroxene (e.g., Wood and Banno, 1973; Wells, 1977; Brey and Kohler, 1990). One of the most widely used two-pyroxene geothermometers, the Brey and Kohler (1990) geothermometers employ more realistic pyroxene compositions to provide a revised calibration of previous estimations of the two-pyroxene thermometer (Wood and Banno, 1973; Wells, 1977). Previous authors (e.g., Harder and Russell, 2006) have shown that temperatures calculated with the Wells (1977) thermometer from the sample mineral pairs are consistently lower than and higher than the calculated B&K temperatures below 900°C and above 980°C, respectively. Hence, we have chosen to use the B&K thermometer since it has been calibrated over a wider composition and temperature range and is a more recent calibration. We have assumed pressures 15 kbar (or 1.5 GPa) for the spinel peridotite facies. For reference, we examined the effect of the chosen pressure on the resulting temperature for the B&K thermometer and found that an increase or decrease of 5 kbar in pressure resulted in an equivalent increase or decrease in temperature by ~12.6°C. Therefore, our choice in pressure should not significantly affect the resulting temperatures and, subsequently, our interpretations. For the calculations, we first used the average core compositions of grains which were analyzed adjacent to one another. After finding that there was no significant variability between the grains for each thin section, we carried out the calculations with the average core compositions for each thin section.

Overall, temperatures calculated with the two-pyroxene Mg-Fe exchange thermometer of Brey and Kohler (1990) range from ~753 to 1018°C with an average of 945°C (Table 7). Temperatures calculated for the harzburgites range from 925-1018°C with an average of 971°C. Temperatures calculated for the lherzolites range from 907-983°C with an average of 948°C while temperatures for the websterites range from 913-965°C with an average of 946°C. The temperatures calculated for the two pyroxenites range from 891-952°C with the plagioclase-bearing clinopyroxenite (102D-2) falling towards lower temperatures. Finally, the temperature calculated for dunite 122F-1 is 753°C.

Temperatures calculated for the orthopyroxenes using the Ca-in-OPX geothermometers of Brey and Kohler (1990) range from 837 to 971°C with an average of 902°C (Figure 27). Temperatures calculated for the harzburgites range from 932-971°C with

Table 7: Calculated temperatures based on the geothermometers of Brey and Kohler (1990).

Lithology	**Expedition**	**Sample**	**Thin Section**	**Mg-Fe exchange**		**Ca-in-OPX**	
				T (K)	**T (°C)**	**T (K)**	**T (°C)**
Dunites	15ATe	122F	122F-1	1025.6	752.5	1110.3	837.1
Harzburgites	15ATe	122C	122C3A	1282.9	1009.7	1244.0	970.8
			122C3B	1272.2	999.1	1231.4	958.2
		122F	122F3B	1247.9	974.8	1210.6	937.4
			122F6	1213.3	940.2	1232.8	959.6
			122F7A	1198.1	924.9	1230.3	957.1
			122F7-A	1203.8	930.6	1231.5	958.3
	16ATe	102F	102F-1	1291.5	1018.3	1205.1	931.9
Lherzolites	15ATe	122D	122D-1	1180.1	907.0	1171.5	898.4
		122F	122F2	1237.0	963.8	1175.9	902.8
			122F2A	1183.6	910.4	1165.2	892.0
			122F3A	1230.1	957.0	1165.9	892.8
			122F4-1	1213.3	940.2	1154.2	881.1
			122F4-2	1226.7	953.5	1147.7	874.5
			122F7-B	1219.8	946.6	1232.7	959.6
		102A	102A (A-1)	1224.0	950.8	1190.8	917.7
			102A (A-2)	1220.5	947.4	1171.8	898.7
		102C	102C	1256.0	982.8	1164.8	891.7
		102D	102D-3	1214.7	941.5	1162.8	889.7
		102E	102E-1A	1250.6	977.4	1165.4	892.3
Websterites	15ATe	122C	122C1	1238.0	964.8	1181.9	908.8
		122F	122F5-1	1233.4	960.2	1179.5	906.4
			122F5-2	1186.5	913.4	1181.4	908.3
Pyroxenites	15ATe	122F	122F2B	1224.9	951.8	1188.2	915.0
	16ATe	102D	102D-2	1164.4	891.2	1157.0	883.9

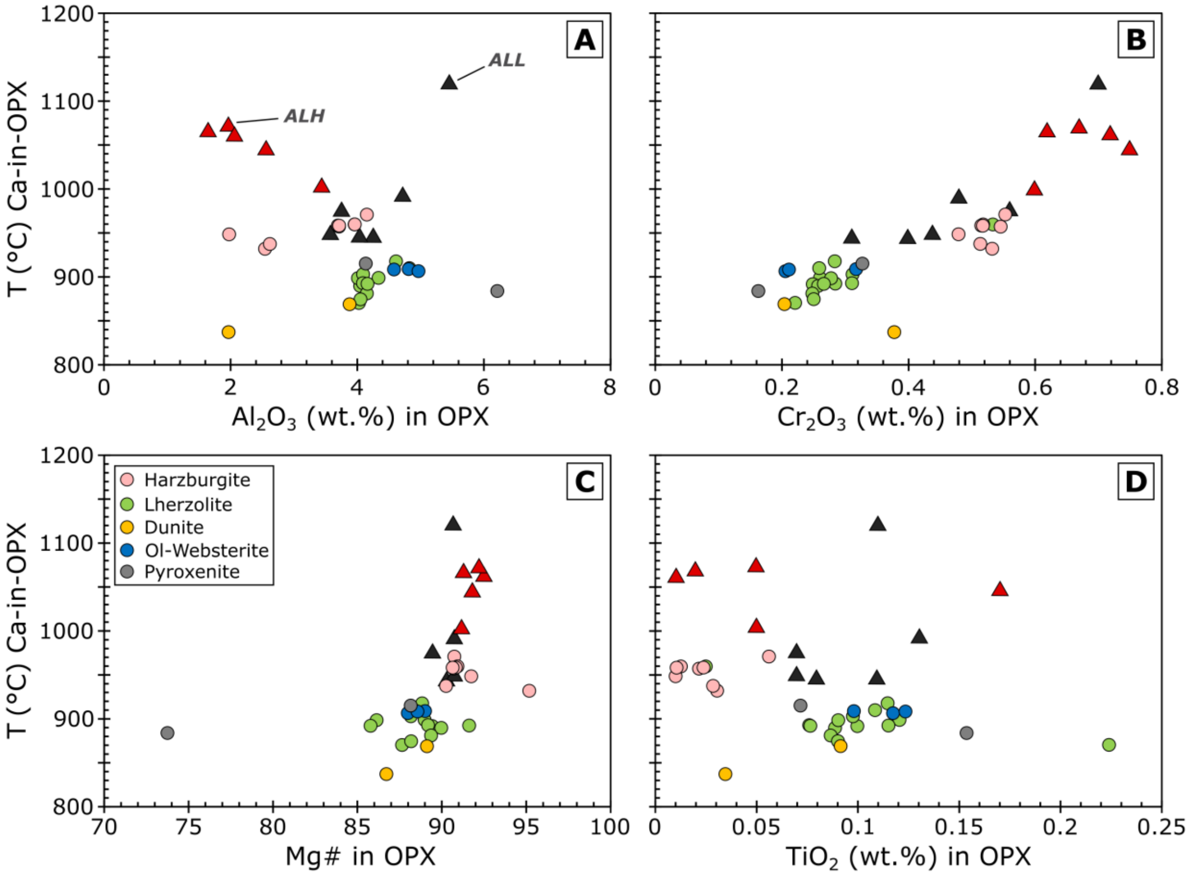

Figure 27: Plots of temperatures (°C) calculated by the Ca-in-OPX geothermometers vs. Al2O3 in orthopyroxene. Temperature calculations for the Alligator Lake samples were calculated for this study using the data from Francis (1987) and Shi et al. (1998).

an average of 953°C. Temperatures calculated for the lherzolites range from 870-960°C with an average of 898°C while temperatures calculated for the websterites and pyroxenites range from 906-909°C with an average of 908°C and 884-915°C with an average of 899°C. Finally, the temperature calculated for the dunite is 837°C. When compared with the temperatures calculated by the same method for the Alligator lake xenoliths (range = 943-1119°C, average = 1014°C), the average calculated the temperature of the Prindle xenolith suite is ~100°C cooler than the Alligator Lake xenoliths. It is worth noting that the Al_2O_3, Cr_2O_3, Mg# and TiO_2 contents of the Prindle orthopyroxene differ systematically with temperature. However, only Mg# and Cr_2O_3 seem to vary similarly for the Alligator Lake xenoliths. On average, the temperatures calculated by each method differ by approximately 45.6°C, with the average temperature difference per lithology coming out to ~85°C for the dunite, ~18°C for the harzburgites, ~49°C for the lherzolites, ~38°C for the websterites and ~22°C for the pyroxenites.

TRACE ELEMENT ANALYSIS

Trace element analyses were collected for clinopyroxenes in a subset of lithologically representative samples from the Prindle suite (Table 8, including two harzburgites (102F1 & 122F3B), four lherzolites (102A (A-2), 102D-3, 122C2, & 122F4-2), one websterite (122F5-2), and three pyroxenites (102D-2, 102F2, & 122F2B). Clinopyroxene trace elements are considered to be representative of the trace elements of the whole xenolith because clinopyroxene is the primary carrier of rare earth elements (REEs) and Sr in dry spinel peridotites (Rampone et al., 1991; McDonough et al., 1992; Roden and Shimizu, 1993). Based on core and rim analyses, we determined that the trace element contents of individual clinopyroxene grains within the Prindle xenoliths are dominantly homogeneous. Overall, the total analyzed trace element concentrations for the measured clinopyroxenes (i.e., the sum of all the measured elements) ranges from ~800 to 1900 ppm with the harzburgites representing the low end and pyroxenite 102D-2 the high end of the range. The trace elements analyzed tend to vary somewhat systematically between the lithologies, with the pyroxenites exhibiting some of the greatest variability. Rather than describe the systematic variations of all the analyzed elements, we have elected to describe a subset of the elements which are of interest to this investigation in the following discussion and interpretation of the petrogenetic history of the Prindle suite.

Table 8: Average clinopyroxene trace elments for Prindle xenoliths.

Lithology	Harzburgites		Lherzolites				Websterites	Pyroxenites		
Thin Section	102F1	122F3B	102A (A-2)	102D-3	122C2	122F4-2	122F5-2	102D-2	102F2	122F2B
N	*4*	*4*	*6*	*4*	*4*	*4*	*4*	*9*	*6*	*2*
Sc (ppm)	63.01	63.07	58.98	55.77	60.37	62.08	61.42	57.67	17.18	50.29
Ti	120.6	123.7	**445.6**	**364.0**	**368.2**	**367.5**	**453.7**	**870.9**	**847.7**	**268.5**
V	164.4	167.4	290.1	264.6	297.0	281.6	297.0	**677.4**	**114.8**	**268.9**
Co	22.19	22.80	19.41	20.71	20.20	19.74	20.27	30.61	14.91	20.95
Ni	**368.6**	**353.2**	285.0	294.1	299.5	280.1	282.2	**88.4**	**16.6**	**289.9**
Cu	0.951	2.72	1.41	0.834	3.10	1.84	0.860	4.33	0.770	1.15
Zn	10.29	10.32	8.33	8.91	8.16	6.95	6.70	26.83	125.22	11.15
Ga	1.60	1.82	4.22	4.09	3.64	3.38	4.46	11.17	15.23	4.51
Ge	1.60	3.95	1.84	1.63	1.62	4.00	2.78	2.29	2.38	2.60
Rb	-	-	0.010	0.034	0.056	0.150	-	0.012	0.015	-
Sr	47.27	51.47	53.84	52.57	10.63	16.34	44.82	**31.75**	**123.90**	**42.64**
Y	5.17	5.16	16.64	13.51	16.02	16.07	18.30	21.76	14.05	8.75
Zr	5.40	5.31	23.74	19.12	7.54	9.27	21.92	**46.81**	**136.75**	**8.05**
Nb	0.669	0.612	0.020	0.041	0.058	0.119	-	0.805	1.022	-
Cs	0.002	-	0.000	-	-	-	-	-	0.081	-
Ba	0.147	0.245	0.024	0.052	0.194	-	-	0.184	0.110	-
La	2.33	2.49	0.618	0.714	0.165	0.398	0.502	2.29	4.81	0.445
Ce	5.63	5.92	2.93	2.99	0.7490797	1.54	2.56	**8.40**	**16.84**	**2.30**
Pr	0.730	0.790	0.628	0.594	0.215	0.344	0.598	1.52	2.78	0.441
Nd	3.21	3.40	4.04	3.56	1.79	2.73	3.68	8.32	12.63	3.08
Sm	0.820	0.902	1.70	1.36	1.09	1.34	1.69	3.01	2.98	1.12
Eu	0.341	0.370	0.680	0.559	0.484	0.580	0.732	1.00	0.779	0.400
Gd	0.933	0.967	2.31	1.89	1.86	1.83	2.20	3.73	2.71	1.51
Tb	0.162	0.171	0.433	0.345	0.383	0.432	0.473	0.658	0.432	0.240
Dy	0.990	1.03	2.99	2.42	2.79	2.88	3.26	4.25	2.65	1.43
Ho	0.203	0.196	0.655	0.525	0.617	0.633	0.660	0.889	0.538	0.337
Er	0.561	0.465	1.87	1.52	1.87	1.91	1.99	2.44	1.53	1.02
Tm	0.070	0.059	0.263	0.219	0.258	0.303	0.254	0.331	0.226	0.197
Yb	0.436	0.475	1.78	1.45	1.78	1.84	1.93	**2.20**	**1.58**	**0.855**
Lu	0.063	0.053	0.248	0.203	0.247	0.226	0.294	0.293	0.249	0.148
Hf	0.048	0.032	0.848	0.640	0.520	0.512	0.935	1.63	3.74	0.297
Ta	0.095	0.083	0.003	0.005	0.003	-	-	0.086	0.332	-
Pb	0.055	0.068	0.072	0.091	0.027	0.059	0.115	0.302	0.301	0.027
Th	0.099	0.104	0.006	0.024	0.014	0.023	0.015	0.076	0.058	0.037
U	0.073	0.029	0.003	0.009	0.065	0.011	0.008	0.033	0.038	0.052

For all of the Prindle lithologies, we find that there is large variation in the levels of both the highly incompatible (e.g., light (L)REE, Sr, Ti) and compatible to moderately incompatible (e.g., heavy (H)REE, V, Zr) trace elements, with the abundances of the latter, generally correlating with the Al_2O_3 contents of the CPX and varying distinctly between the harzburgite and CPX-rich lithologies. For example, an inverse correlation exists between Al and Ce/Yb ratios in the harzburgites and lherzolites (Figure 28). Such inverse correlations between highly incompatible elements and major element fertility indices have been observed globally in xenolith suites (McDonough and Frey, 1989). Similar inverse correlations are not consistent with closed system partial melting processes and might reflect a process in which incompatible trace elements are preferentially enriched in mantle peridotites (Shi et al., 1998).

Clinopyroxenes from the two harzburgite samples are very similar in composition with Ti, V, Ni, Sr, and Zr concentrations averaging ~122, 166, 361, 49, and 5 ppm, respectively. We note that the harzburgite clinopyroxenes contain the highest Ni and lowest Ti, V, and Zr concentrations out of the analyzed lithologies. Harzburgite clinopyroxenes are found to have relatively high LREE concentrations (e.g., Ce ~5.8 ppm) compared to their HREEs (e.g., Yb ~0.5 ppm). Ratios of Ce/Yb for the harzburgites, ~12.5, are among the highest of the analyzed lithologies (Figure 28), plotting almost 1.5 orders of magnitude higher than the CPX-rich lithologies for a given clinopyroxene Al_2O_3 content. The enrichment is reflected in their REE patterns (Figure 29A) which have steep, gradual, negative slopes exhibiting an overall enrichment in LREEs relative to the HREEs. Though most of the clinopyroxenes display Nb, Zr, Hf, and Ti (i.e., high-field strength elements, HFSE) depletions relative to similarly compatible REEs, the harzburgites generally exhibit the largest HFSE depletions except for Nb (Figure 29). Characteristically, only the harzburgites are found to have pronounced Hf depletions relative to Zr.

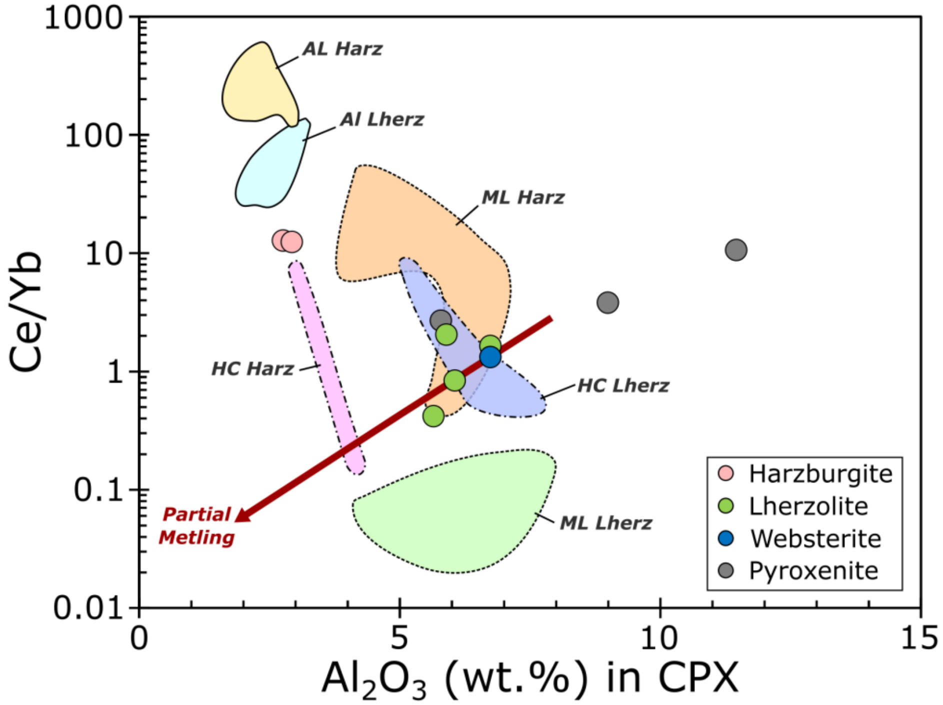

Figure 28: Plot of Ce/Yb vs. Al_2O_3 in clinopyroxene. Fields for Alligator Lake (AL), Mt. Llangorse (ML), and Hirschfeld Creek (HC) lherzolites and harzburgites after Shi et al. (1998).

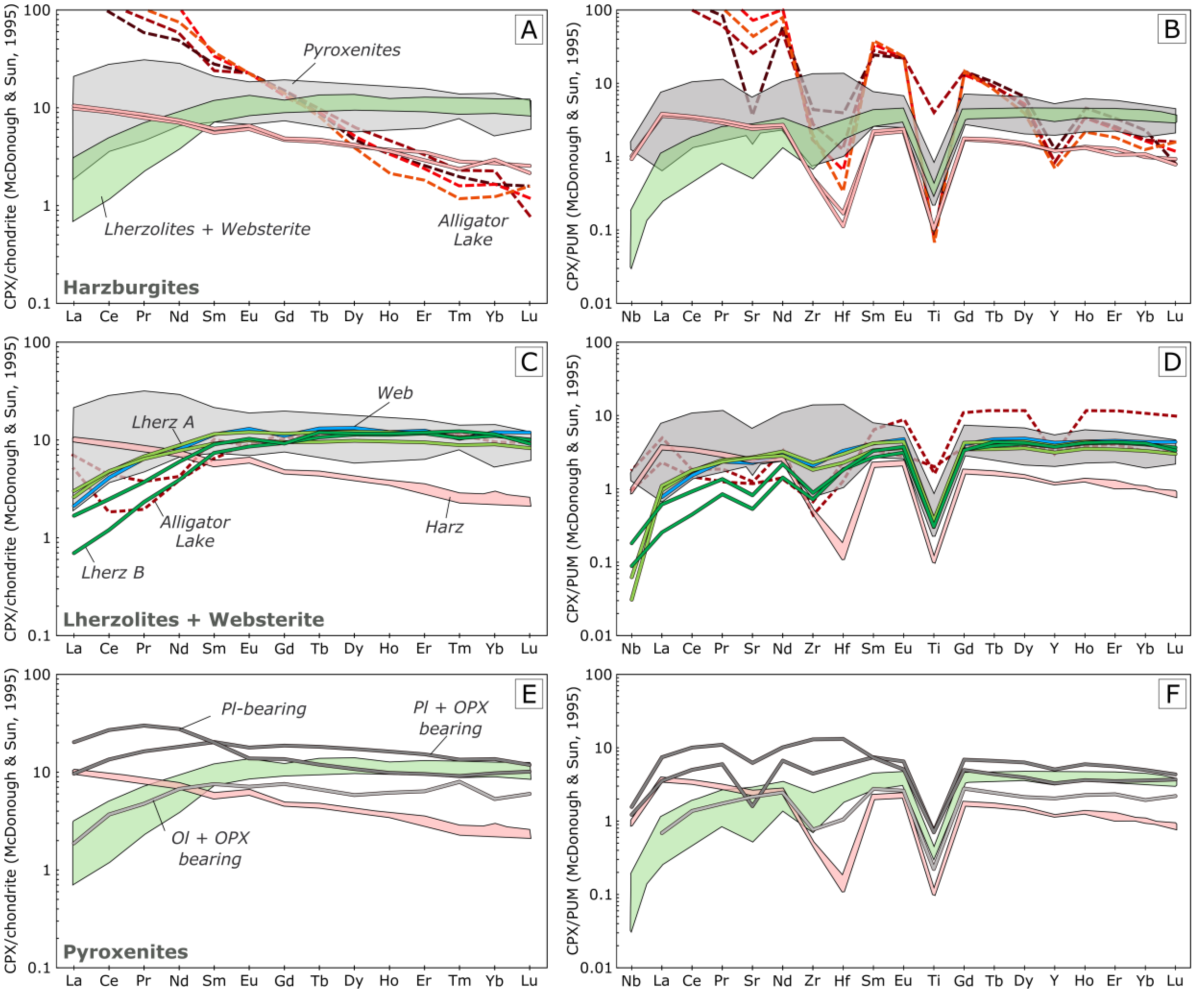

Figure 29: (Left) Plots of REEs normalized to chondrite (McDonough and Sun, 1995) and (Right) Extended-REEs normalized to primitive upper mantle (PUM; McDonough and Sun, 1995) for the Prindle xenolith suite clinopyroxenes with data for the Alligator Lake xenoliths (Shi et al., 1998) plotted as red, dashed lines for comparison. The shaded fields in the various diagrams represent the extent of the data for the other lithologies within the Prindle xenolith suite.

Clinopyroxenes from the lherzolites and the websterite can be split into two groups based on their trace element contents. The first group (lherzolites 102A (A-2) & 102D-3, websterite 122F5-2), referred to as type A herein, have Ti, V, Ni, Sr, and Zr concentrations

averaging ~421, 284, 287, 50.4, and 21.6 ppm, respectively, with ~2.8 ppm of Ce and 1.7 ppm of Yb. The second group (122C2 & 122F4-2), referred to as type B herein, have Ti, V, Ni, Sr, and Zr concentrations averaging ~368, 289, 291, 13.5, and 8.4 ppm, respectively, with ~1.2 ppm of Ce and 1.8 ppm of Yb. Though the lherzolite clinopyroxenes have very similar Al_2O_3 contents (~6 wt.%), their Ce/Yb ratios vary on average between ~1.7 for the type A and ~0.6 for the type B samples (Figure 28). The REE patterns of the lherzolite clinopyroxenes have variability, but typically relatively low LREE with flat MREE to HREEs. The type A lherzolites tend to have the highest LREEs, but the lowest HREEs, while the type B lherzolites have the lowest and most variable LREEs and the highest HREEs. The type B lherzolites are most readily distinguished from the type A lherzolites in Figure 28D by the presence of moderate Sr and Zr depletions and a weak Hf depletion. In contrast to the harzburgites, the lherzolites have greater Zr depletions relative to Hf.

Clinopyroxenes in the pyroxenites are highly variable between the samples. Sample 122F2B, an olivine- and orthopyroxene-bearing clinopyroxenite, has Ti, V, Ni, Sr, and Zr concentrations of 268.5, 268.9, 289.9, 42.6, and 8.05 ppm, respectively, with 2.3 ppm of Ce and 0.86 ppm of Yb. It has a Ce/Yb ratio of 2.7, plotting just above the range of the lherzolites in Figure 28. The REE pattern for 122F2B has similar LREEs to the type A lherzolites (i.e., slightly depleted), but differs in having a slight MREE enrichment with a more depleted HREE signature relative to the type A lherzolites (Figure 29). Sample 102D-2, a plagioclase- and orthopyroxene-bearing clinopyroxenite, has Ti, V, Ni, Sr, and Zr concentrations of 870.9, 677.4, 88.4, 31.8, and 46.8 ppm, respectively, with 8.4 ppm of Ce and 2.2 ppm of Yb. It has a Ce/Yb ratio of 3.8 and Al_2O_3 of ~8.5 wt.%, plotting towards more enriched values compared to the lherzolite and 122F2B clinopyroxenes (Figure 28). The REE pattern for 102D-2 is moderately enriched compared to 122F2B with a broad, pronounced MREE enrichment and HREEs which are comparable to the LREEs. Of note is that 102D-2 has the highest HREE concentrations of the Prindle suite clinopyroxene. Like the type B lherzolites, 102D-2 exhibits a strong, negative Sr anomaly with weak to moderate Zr and Hf anomalies (Figure 29F). Zr is not as depleted relative to Hf in 102D-2 as it is in the type B lherzolites. Sample 102F2, a plagioclase-bearing clinopyroxenite, has Ti, V, Ni, Sr, and Zr concentrations of 847.7, 114.8, 16.6, 123.9, and 136.8 ppm, respectively, with 16.8 ppm of Ce and 1.6 ppm of Yb. Clinopyroxene from 102F2 are among the most enriched in Ti, Sr, Zr, and Ce and most depleted in V and Ni for the Prindle suite. It has a Ce/Yb ratio of 10.7 and Al_2O_3 of ~11 wt.%, plotting as the most enriched of the Prindle samples and forming the enriched endmember of a trend defined by the CPX-rich lithologies in Figure 28. The REE pattern for 102F2 has the most enriched LREEs with a pronounced, spoon-shaped, concave down enrichment in Ce through Sm and a relatively steady, negative slope from the MREEs to the HREEs (Figure 29E). A weak to moderate Sr anomaly characterizes the extended REE pattern for 102F2; however, in contrast to 102D-2, there is no apparent negative anomaly in Zr or Hf (Figure 29F).

CHAPTER SIX:

DISCUSSION

ORIGIN OF THE PRINDLE HARZBURGITE XENOLITHS

SCLM mantle xenoliths are expected to have compositions which are not all that different from the primitive upper mantle (PUM). In contrast, mantle rocks collected from along the mid-ocean ridge (MOR) system (i.e., abyssal peridotites) are expected to have depleted compositions because they have undergone some degree of decompression melting to produce MOR basalt (MORB) during their emplacement beneath the MOR; hence, the term depleted MORB mantle (DMM). Forearc or supra-subduction zone (SSZ) peridotites are expected to be even more depleted than abyssal peridotites due to the introduction of water and fluids into the mantle wedge which acts as a flux and lowers the melting temperature of the mantle to produce pyroxene-poor harzburgites and dunites (Gaetani and Grove, 1998). As illustrated in Figure 22, the spinels in the Prindle xenolith suite fall towards the more primitive extremes (i.e., high-Mg#, low-Cr#) when compared to both abyssal and forearc peridotites. Though there is certainly some evidence to suggest that the Prindle harzburgites have undergone some degree of metasomatism, their chemistry and textures are relatively typical of harzburgite residues produced by partial melting of fertile mantle peridotites (McDonough and Frey, 1989). Partial melting is supported by the negative correlation between modal CPX (i.e., the primary phase consumed during partial melting) and spinel Cr# for the harzburgites in Figure 30A.

Although the Prindle harzburgites exhibit various characteristics which might suggest that they are simply the residues of partial melting, they are observed to have negative

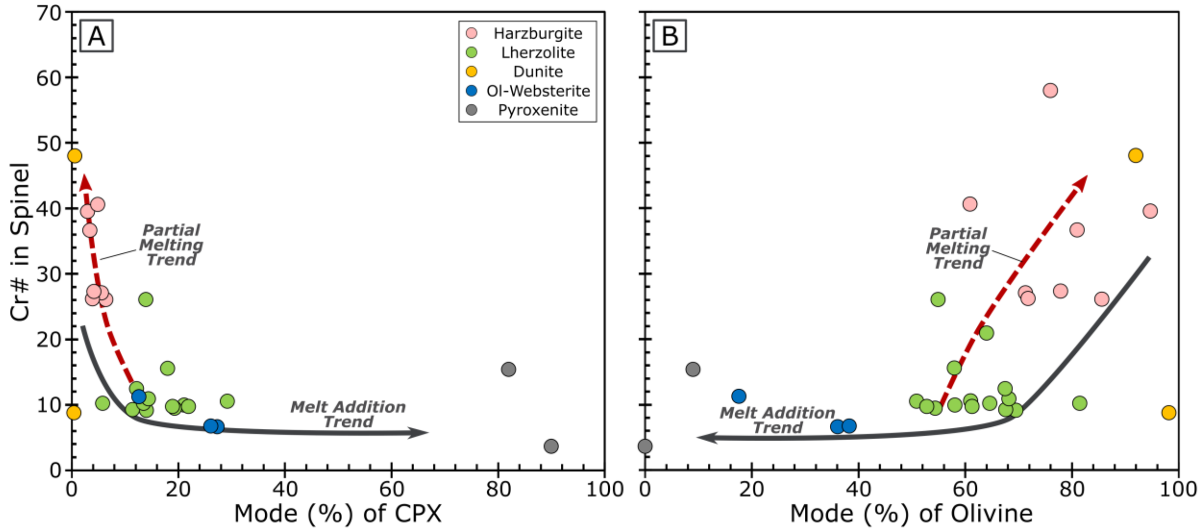

Figure 30: Plots of Cr# in spinel vs. the modal percentage of (A) clinopyroxene and (B) olivine for the Prindle xenolith suite. Partial melting and melt-addition trends are based on established models from Dick and Bullen (1984) and Dick (1989).

anomalies in both Zr_N and Hf_N, and, additionally, they have higher Zr_N than Hf_N (Figure 29). Such strong negative Zr-Hf anomalies are considered to be uncommon in clinopyroxene from other mantle xenolith suites around the world, however, they have been documented in Tok, Siberia (Ionov et al., 2006a, 2006b), the Bearpaw Mountains, Montana (Downes et al., 2004), the Massif Central, France and the Sudetes of SW Poland (Downes et al., 2015), and the subduction-related Avacha Volcano, Kamchatka, Russia (Halama et al., 2009). The extreme depletion of these elements must be due to a process, like partial melting, that would preferentially remove them from the mantle.

In the case of the Massif Central peridotites in France, it has been estimated that extensive (i.e., up to ~30%) partial melting has occurred within the spinel stability field based on modeling of Hf-depletion by Wittig et al. (2006). Such high degrees of partial melting are most commonly associated with supra-subduction zone (SSZ) processes which is consistent with the inferred and observed tectonic histories of the other xenolith localities where this geochemical feature has been observed (Downes et al., 2015). A SSZ is not outside the realm of possibility for the Prindle harzburgites, considering that the rocks that constitute the YTT, and most of the adjacent cordilleran terranes, are dominantly observed as having arc-related chemistries (Peslier et al., 2002). However, the LREE-enriched trace element patterns of the Prindle harzburgite clinopyroxenes are not consistent with an origin by simple partial melting, and, instead, suggest a two-stage process of extensive partial melting followed by metasomatic enrichment. The enrichment in both LREEs and the immobile elements (e.g., Zr) in the Prindle harzburgites, and additionally, the observation that they have $Zr_N > Hf_N$, suggests that the metasomatic agent likely carried some Zr; suggesting that the harzburgites have been subjected to metasomatism by a melt capable of carrying such HFSE, like an alkaline silicate melt.

ORIGIN OF THE CPX-RICH PRINDLE XENOLITHS

Though some lherzolites fall within the compositional and modal ranges expected for a typical fertile, relatively un-melted mantle peridotite, it is unclear if any of the lherzolite samples can be considered primary mantle lherzolite. In Figures 21 and 30, the olivine and clinopyroxene modes are found to vary significantly for a given olivine Fo or spinel Cr# in the CPX-rich (and some harzburgite) lithologies. In the case of simple partial melting, we would expect for the clinopyroxene and olivine modes to vary together with spinel Cr# and olivine Fo and display little or minor variance about this trend. As previously noted, olivines (Figure 20), spinels (Figure 22), orthopyroxenes (Figures 23 & 24), and clinopyroxenes (Figures 25 & 26) in the CPX-rich lithologies, and to some extent dunite sample 122F-1, have a tendency to form compositional arrays which suggest that they are the result of melt-rock interaction or hybridization. Considering this along with the observations provided in the previous sections, we suggest that the majority, if not all, of the Prindle lherzolites and websterites, are the product of varying degrees of melt-rock hybridization and refertilization of previously-depleted mantle peridotite by a melt or series of melts which might be represented by one or more of the pyroxenites

In nearly all of the geochemical figures presented so far, there has been some sort of moderate to strong trend formed by the CPX-rich lithologies with the olivine-orthopyroxene-bearing clinopyroxenite, 122F2B, generally overlapping with the lherzolite and websterites and the plagioclase-bearing clinopyroxenite, 102F-2, plotting as the most enriched or extreme endmember of the trends. The one phase where this trend is significantly less obvious is in olivine. The key observations to defining the relationships between the lherzolites, websterites, and clinopyroxenites are as follows: (1) the petrographic and geochemical observations for pyroxenite sample 122F2B; (2) the textural relationships between the lherzolites and websterites; (3) Sr anomalies in the pyroxenites and lherzolites.

Pyroxenite sample 122F2B could be considered the “Rosetta Stone” for the CPX-rich lithologies of the Prindle xenolith suite. Unlike the other pyroxenite samples, 122F2B lacks plagioclase and contains both olivine and orthopyroxene. The olivine and orthopyroxene in 122F2B, which are highlighted by iddingsite alteration, are unique in that they are found as small (~0.1 to 0.7 mm), anhedral, lobate grains or, rarely, chadacrysts which are highly resorbed by the surrounding coarse (~1.2 mm), sub-euhedral clinopyroxenes that make up the majority of the sample (Figure 19E). The argument for the resorption of the olivine is supported by the chemistry of the associated phases. Considering that the clinopyroxenes in 122F2B generally overlap or plot in the same vicinity as the lherzolitic clinopyroxenes for several of the major elements, then we should expect for them to be consistent with their minor elements similarly. Not surprisingly, the 122F2B clinopyroxenes have higher Cr_2O_3 (0.91 wt.%) and Na_2O (1.26 wt.%) and lower TiO_2 (0.28 wt.%) and MnO (0.08 wt.%) than the other pyroxenites, which generally matches the lherzolitic clinopyroxenes. A pattern extends to trace elements like V, Ni, Zn, Ga, Y, and Zr which have compositions more akin to those of the harzburgites, lherzolites, and websterites than they do the pyroxenites. Of these elements, the high Ni contents of the clinopyroxenes in 122F2B and the Prindle lherzolites suggest that they crystallized from a melt that may have assimilated a phase, like olivine, which was high in Ni. It stands to reason, then, that pyroxenite 122F2B may represent a high melt/rock ratio endmember of melt-hybridization where the melt was solidified before it could completely resorb the olivine and orthopyroxene of the host rock.

One of the primary petrographic observations for the lherzolites and websterites is the near ubiquitous presence of moderate to strong fabrics across the samples. These well-developed, foliated, granular textures seem to partially obliterate the original porphyroclastic textures of the peridotites (Figure 15 & 17) through the crystallization of finer-grained olivine along with undeformed, poikilitic clinopyroxene and, in some cases, spinel. Previous studies of mantle xenoliths with similar fabrics and textural relationships have suggested that such equigranular peridotites may develop as the result of extensive static, melt-assisted annealing and recrystallization due, at least in part, to pervasive melt percolation (Rampone et al., 2009). It is noteworthy that, although the clinopyroxenes in the Prindle peridotites are relatively homogeneous regarding their REE contents, that they exhibit a mixture of both moderately and weakly pronounced Zr and Hf anomalies (Figure 29). Such evidence suggests that those samples with the more weakly pronounced anomalies represent a larger melt-rock ratio over time (i.e., time-integrated) while those with more pronounced anomalies represent a smaller time-integrated melt-rock ratio. Further, this indicates that the clinopyroxene chemistry probably reflects refertilization and/or crystallization by melt-rock interaction. Based on these observations, we interpret the general trend in the modal proportions of the Prindle xenoliths from less lherzolitic to more websteritic and pyroxenitic modes (Figure 14) as reflecting a general trend towards increasing melt-rock ratios.

Prominent Sr anomalies are present in the two type B lherzolites (122C2 & 122F4-2) and two of the pyroxenites (102D-2 & 102F2). According to Hellebrand et al. (2005), the presence of such anomalies in peridotite clinopyroxene can either be an indication of seawater alteration or the co-existence of plagioclase in the rock. In the case of the Prindle samples, the latter is more likely since they lack any obvious signs of serpentinization or seawater-derived alteration. Further, the two pyroxenite samples which exhibit a Sr anomaly are found to contain plagioclase as an interstitial phase (~4.7% plagioclase in 102D-2 and ~8% plagioclase in 102F2). The Sr anomaly would suggest that, although it was not petrographically observed in thin section, there is likely plagioclase present in the type B lherzolite samples. In fact, upon further investigation, we found two small (<0.2 mm) grains of plagioclase associated with anhedral spinels in 122F4-2, however, their size and distribution are such that they do not affect the previously determined modes for the samples. Further, we observe (Figure 15) that the type B lherzolite samples characteristically only contain small, wispy, interstitial spinels, while the type A lherzolites and websterite commonly contain two morphologically distinct spinel populations including those observed in the type B samples alongside large (up to 3 mm), anhedral, interstitial spinels which often exhibit poikilitic textures along their margins.

The variation in the melt-rock reaction assemblages between type A and type B lherzolites suggests that there could be a difference in the compositions of the metasomatic melts/fluids involved. We can estimate the constraints on the composition of the fluids or melts involved during the metasomatic events from the trace element signature of the clinopyroxenes by using equilibrium clinopyroxene-melt partition coefficients ($Kd^{cpx/melt}$, Hart and Dunn, 1993; Green et al., 1992). Figure 31 plots the calculated melts in equilibrium with the Prindle clinopyroxenes regarding their Ce/Zr, Sr/Zr, Ti/Eu, and Zr contents and their chondrite-normalized (i.e., C_N) La/Yb ratios. For reference, melts in equilibrium with the clinopyroxene data from Shi et al (1998) for the Alligator Lake xenolith suite are plotted in Figure 31A and 31B which were interpreted to have resulted from melt-rock interaction with a fluid/melt which had a composition between that of a carbonatite endmember and that of a residual liquid for the host alkaline basalt. Critically, the Prindle xenolith suite does not fall along with the same array as the Alligator Lake xenolith suite. Instead, the CPX-rich lithologies plot along with the array defined by the crystallization trend of the alkaline basalt while the harzburgites plot towards a slightly more enriched composition. This is supported by the plot of Ti/Eu vs. $(La/Yb)_N$ in Figure 31C which shows the CPX-rich lithologies following the expected silicate metasomatism array, indicating reaction with an alkaline basalt, and the harzburgites plotting towards higher $(La/Yb)_N$ values than the CPX-rich lithologies which are not high enough to indicate carbonatite metasomatism.

EVIDENCE OF A LITHOSPHERIC MANTLE SOURCE

Like the other Cordilleran mantle xenolith suites that have previously been investigated (Shi et al., 1998), the Prindle mantle xenoliths belong to the spinel peridotite facies (i.e., depths between 30 and 80 km) and lack any of the textural features typically associated with the garnet-spinel or spinel-plagioclase facies transitions. In particular, the presence of flat HREE patterns and the absence of positive Zr anomalies in the lherzolite clinopyroxenes and pyroxene-spinel symplectites provide strong evidence against the lherzolites originating in the

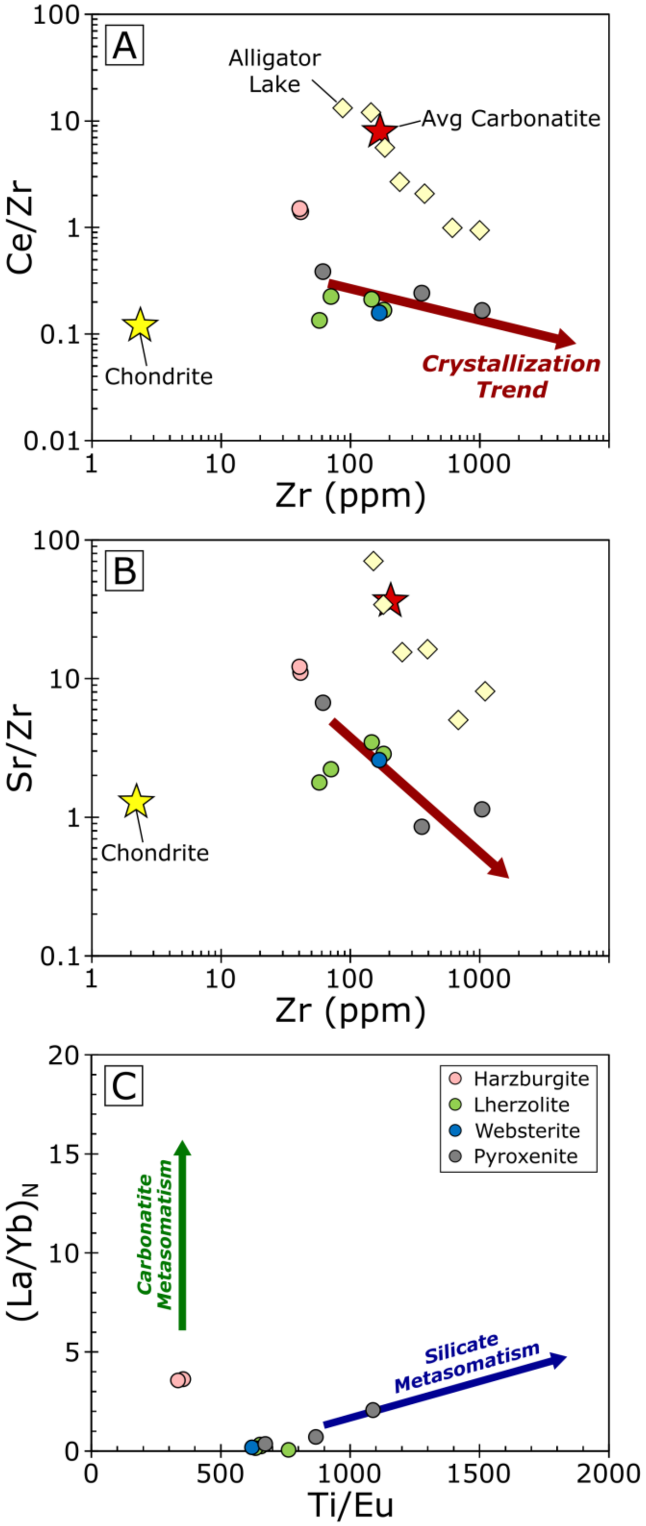

Figure 31: Plots of (A) Ce/Zr and (B) Sr/Zr vs. Zr, in ppm, and (C) chondrite-normalized $(La/Yb)_N$ vs. Ti/Eu for calculated metasomatic fluids/melts in equilibrium with Clinopyroxene from the Prindle xenolith suite. For panels A and B: Average carbonatite from Wooley and Kempe (1989); The arrows indicate the trend expected for 97% fractional crystallization of the average host alkaline basalt for the NCVP xenolith suites. For Panel C: the signatures of the metasomatism by silicate and carbonatite melts/fluids are from Coltorti et al. (1999).

garnet stability field (Shimizu 1975; Hauri and Hart, 1994). These features seem to be ubiquitous amongst the lherzolites of all the Cordilleran xenolith suites and have been interpreted to suggest that they are samples of the regional lithospheric mantle beneath the province (Shi et al., 1998).

As discussed previously, the harzburgites are distinctly different from the CPX-rich lithologies at Prindle; exhibiting distinct major and trace element compositions and textures. Further, geothermometric calculations for the harzburgites tend to result in generally higher equilibration temperatures compared to the CPX-rich lithologies (~60°C on average). Various authors have argued, based on an assumed geotherm calculated for the regional upper mantle by Ranali (1980), that similar temperature differences (i.e., 60-80°C; Shi et al., 1998) likely indicate that the Cordilleran harzburgites were derived from ~8 km below their associated lherzolites. The temperature difference would suggest that the harzburgite xenoliths were sampled from a physically separate portion of the mantle beneath that of the lherzolites. An inference that is not compatible with the observations of this study which suggest that, to some degree, the major element compositions of harzburgite and some of the more depleted lherzolite xenoliths are consistent with the compositional trends of experimental partial melting residues of fertile mantle xenoliths (Mysen and Kushiro, 1977; Jacques and Green, 1980).

Based on the textural and compositional evidence presented here, we suggest that the lithologies present in the Prindle xenolith suite might have been derived from similar lithospheric depths along a shear zone. In this context, the observed trends in the modal mineralogy of the Prindle suite may represent variations between more focused and diffuse melt flow over time along the shear zone. A similar model has been developed for xenoliths with well-developed fabrics from Tallante in the Betic Cordillera, SE Spain (Rampone et al., 2009). In the Tallante xenoliths, it was determined that shearing occurred in the spinel-facies followed by a series of reactive porous flow, melt impregnation, and melt intrusion events which called for elevated temperatures. The evidence for melt-rock reaction in the Tallante xenoliths was attributed to an initial event characterized by the migration of sub-alkaline melts followed by the intrusion of alkaline melts in response to approximately 30 km of crustal and lithospheric thinning in the region. Such a multi-stage history from deformation through recrystallization, melt-rock interaction and melt intrusion in response to lithospheric thinning is consistent with the observations of the Prindle xenolith suite provided here and the established regional tectonic history of the NCVP.

Further, the presence of minor, interstitial plagioclase associated with spinel in the type B lherzolites in addition to the late interstitial plagioclase present in two of the pyroxenites suggests that the melt-rock interaction continued to occur at shallower lithospheric depths, likely within the plagioclase-peridotite facies. However, the fact that the co-existing clinopyroxene with the plagioclase exhibits a negative Sr anomaly but not a corresponding Eu anomaly would suggest that the plagioclase had to crystallize after the clinopyroxene, and likely at relatively lower temperatures. These textural and geochemical features likely record the response of the Prindle lithospheric mantle to interaction with melts from different sources due to progressive thinning of the lithosphere beneath the NCVP.

A REGIONALLY DISTINCT XENOLITH SUITE

Previous authors (e.g., Shi et al., 1998) have classified the Prindle xenolith suite as a unimodal (i.e., containing only lherzolites) suite. According to our observations, Prindle is not only not a unimodal xenolith suite, but also contains such diverse lithologies that it cannot simply be categorized according to the classification scheme of Shi et al. (1998). If one had to place Prindle into this classification scheme, then it could easily be considered a bimodal suite. This contrasts with the conclusions and findings of Shi et al (1998) who correlated the locations of three bimodal suites (i.e., Alligator Lake, Coast Plutonic Belt, and the Mt. Llangorse and Hirschfield Creek suites within the intermontane belt) with the presence of the P-wave slowness anomaly detected teleseismically (Frederiksen et al., 1998) in the mantle beneath the southern Yukon. As we discussed previously, this P-wave anomaly represents a region of the anomalously slow mantle with a ~200 km diameter that extends from the base of the lithosphere down to ~400-500 km. It has been interpreted that the magnitude of the anomaly, if no interstitial melt is present, must represent a ~200°C temperature anomaly relative to the surrounding mantle.

Compared to the locations of the three bimodal suites identified by Shi et al. (1998), Prindle Volcano appears to sit approximately on the northern margin of the P-wave slowness anomaly where there is a relatively sharp transition with the surrounding mantle (Figure 8). Frederiksen et al. (1998) proposed that the mantle anomaly is the result of asthenospheric upwelling from a slab window under the NCVP. In their model, the underlying, hotter asthenosphere partially melted and ascended in response to the retreat of the subducting slab. Based on the association between the bimodal suites and the mantle anomaly in the NCVP, Shi et al. (1998) suggested that the bimodal suites could either represent portions of the upper lithospheric mantle affected by the anomalous mantle or portions of the lithospheric mantle which contain fragments of the anomalous mantle.

Various models for determining the extent of partial melting in mantle peridotites indicate that anywhere from F = 22-25% fractional partial melting has occurred to produce the compositional ranges present in the Alligator Lake and other bimodal xenolith suites (Francis, 1987; Shi et al., 1998). Comparatively, if we apply the equation of Hellebrand et al. (2000) (i.e., $F = 10 \ln(Cr\#) + 24$) to the spinels from the Prindle xenolith suite, we end up with a range from 0 (or negative values) to 18.5% with an average of 6.4%. This, of course, is skewed because many of the CPX-rich lithologies from Prindle have modal pyroxene contents which are too high for fertile, un-melted, upper mantle peridotites, and spinel Cr#s which fall below 10 (the equation of Hellebrand et al., 2000 is optimized for spinels with Cr#s between 10 and 60). If we only use spinels from the harzburgites and the most depleted dunite (122F-1), then we end up with a range of 12.6-18.5% with an average of 12.7%, which would suggest that the most depleted samples in the Prindle xenolith suite have only been affected by a maximum of ~18.5% partial melting, which is comparatively less than the Alligator Lake xenolith suite.

Furthermore, the calculated equilibration temperatures for the Prindle xenolith suite (Figure 27) consistently plot towards lower temperatures (~100°C on average) than the Alligator Lake xenoliths. Considering the calculated ~200°C positive temperature difference between the P-wave slowness anomaly and the surrounding mantle beneath the NCVP (Shi et al., 1998), we suggest that Prindle Volcano's location along the transition between the anomalous and surrounding mantle is responsible. At least in part, for the lower temperatures, lesser extent of partial melting, and the overall greater lithologic variability in the Prindle xenolith suite compared to the Alligator Lake xenolith suite. It stands to reason, then, that the higher temperatures, greater extents of partial melting, and more homogeneous lithologies found in the Alligator Lake xenolith suite are more likely to be a result of their interaction with greater volumes of asthenospheric melts. Rather than the incorporation of fragments of the asthenospheric mantle; thus, supporting the prediction by Shi et al. (1998) that the temperature differences required by the properties of the anomaly and their samples would be significantly reduced by the presence of interstitial melt in the ascending asthenosphere. This model implies that the lithospheric mantle sampled by Prindle would have been subjected to significantly smaller volumes of melt, and potentially different melt compositions, than that of Alligator Lake; thus, xenoliths from Prindle Volcano have the potential to still retain some record of what the lithospheric mantle beneath the NCVP looked like prior to the development of the anomaly.

A GENERAL MODEL FOR THE DEVELOPMENT OF THE PRINDLE XENOLITH SUITE

Based on the observations and models for xenolith suites from other settings (see below) in addition to those for the other NCVP suites, we have established a general model to describe the likely series of events which led to the development of the Prindle xenolith suite (Figure 32). We propose that the Prindle xenolith suite is the result of varying volumes of melt-rock interaction along a lithospheric shear zone which formed or was reactivated in response to the development of the upper mantle anomaly beneath the NCVP.

The chemistry and texture of the most depleted peridotites and dunites suggests that they formed in association with an SSZ environment. For our model, we assume, based on observations of associated dunites and harzburgites from the Moho-transition zone sections of ophiolites (e.g., Kelemen et al., 1995; Kaczmarek and Muntener, 2010) that the dunites were likely present as focused channels within the harzburgites at depth (Figure 32A). Models for other Cordilleran regions which are characterized by anomalously hot mantle (e.g., the Betic Cordillera of southern Spain; Rampone et al., 2009) suggest that extensional thinning of the lithosphere occurred in response to the ascent of hot asthenosphere, leading to subsequent lithosphere-asthenosphere interaction. During such a process, it is thought that the overlying, colder lithospheric mantle would undergo some amount of progressive uplift in response to the rising, hotter material. Progressive uplift of the mantle in the center of the temperature anomaly

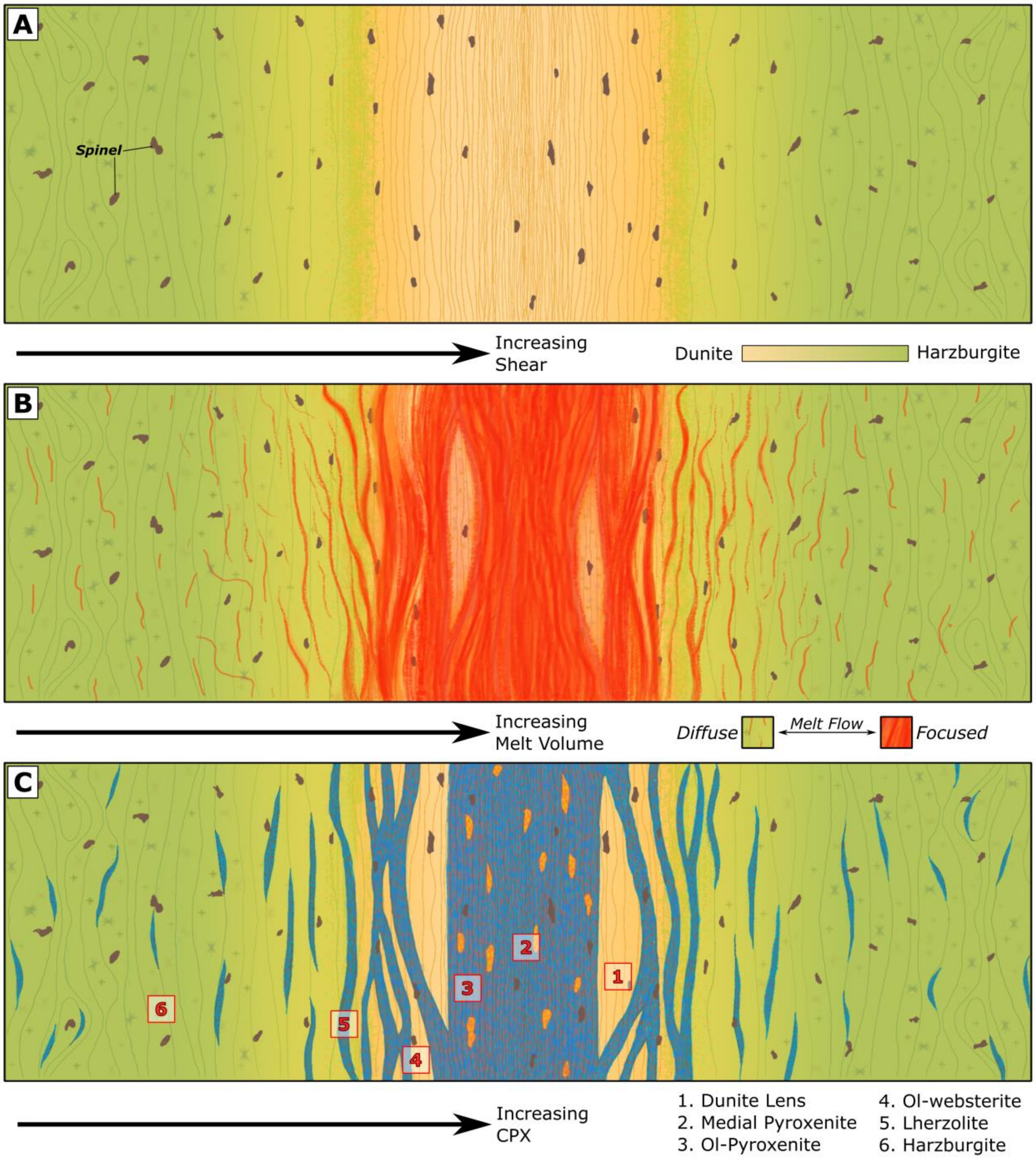

Figure 32: Schematic diagram showing a generalized model for the development of the lithologies and textures observed in the Prindle xenolith suite. (A) The chemistry of the most depleted harzburgites and peridotites suggests that they likely formed in some SSZ environment. This panel assumes a similar relationship between the two lithologies as what is observed in the Moho-transition zone in ophiolites (Kelemen et al., 1995). In this case, a shear zone localized in these pre-existing weaknesses along the margins of the uplifting lithospheric block in response to the upwelling hotter asthenosphere. (B) Sometime after shear zone formation, alkaline fluids/melts associated with the upwelling asthenosphere intruded. As observed in ophiolitic shear zones, melt flow would be localized and focused towards the center of the shear zone with more diffuse melt flow occurring further out. (C) The result of an increase in modal CPX as you approach the center of the shear zone.

would, in turn, lead to the development of ductile shear boundaries at its margins with the surrounding, colder lithospheric mantle. It stands to reason then, that shear zones formed along the margins of the uplifting lithospheric block in response to the upwelling hotter asthenosphere would likely localize in pre-existing weaknesses like those provided by the presence of dunite conduits within the Moho-transition zone. The development of such a shear zone is suggested by the strongly mylonitized fabric of dunite 122F-1, wherein the primary porphyroclastic-granular microstructure, represented by the coarser-grained, elongate aggregates, is preserved.

The next stage in the development of the Prindle xenoliths (Figure 32B), is also represented in dunite 122F-1, where the porphyroclastic aggregates are surrounded and beginning to be overprinted by melt-assisted migration recrystallization (a largely surface energy driven annealing process) leading to a finer-grained, equigranular fabric. The replacement of porphyroclastic minerals by unstrained olivine rims, and the subsequent crystallization of undeformed olivine and poikilitic orthopyroxene, clinopyroxene, and spinel at the expense of both porphyroclasts and newly crystallized olivine suggest that the peridotites were affected by melt migration and melt-rock interaction. Replacement is consistent with fabrics observed in a number of the CPX-rich lithologies where a second generation of olivine and pyroxenes are observed which are finer-grained and exhibit more tabular, equigranular fabrics. Thus, we infer that the recrystallized, finer-grained equigranular microstructure of the Prindle xenoliths represents a melt-assisted migration recrystallization stage which is responsible for obliterating and overprinting the pre-existing porphyroclastic fabric related to the original development of the shear zone within the spinel-facies. We note, however, that the variable nature of the fabric between samples and the presence of harzburgites with weak fabrics and diffuse veins of recrystallized olivines, pyroxenes, and spinels suggests that the melt within the shear zone was not evenly distributed. Considering this, we suggest that the largest volume of melt was focused towards the heavily sheared core of the dunite where it could take advantage of the greater porosity provided by the rock microstructure (Figure 32B). With increasing distance from the zone of focused melt flow, the melt volumes become more diffuse and form meandering channels and increasingly disconnected veinlets within the host peridotite which lack the energy and volume that are required to modify the surrounding peridotite significantly.

Similar textures and fabrics have been described in spinel peridotites from shear zones in ophiolitic and oceanic settings worldwide (e.g., Dijsktra et al., 2003; Piccardo and Vissers, 2007; Piccardo et al., 2007; Seyler et al., 2007; Rampone and Borghini, 2008; Rampone et al., 2008; Rampone et al., 2009) where they have been inferred to be related to open-system reactive porous flow (RPF) of olivine-saturated tholeiitic melts. The mechanisms of melt migration in the lithospheric mantle suggest that adiabatically rising melts are typically saturated in olivine and will, therefore, crystallize olivine and dissolve pyroxenes in the surrounding peridotites until they reach pyroxene saturation and start to crystallize ortho- and/or clinopyroxene (Quick, 1981; Kelemen, 1990; Kelemen et al., 1992, 1995, 1997; Kelemen and Dick, 1995). Though it is established that our samples have interacted with an alkaline basaltic melt, for which the consequences of such a process are unknown, the diffuse crystallization of clinopyroxene at the expense of previous olivine-replacement textures in the Prindle CPX-rich lithologies may thus imply various stages of RPF and interaction with increasingly modified melts. Furthermore, the partial replacement of previous porphyroclastic textures by the developing finer-grained granular textures suggests that the melt-assisted recrystallization of the peridotites was likely not induced by shearing deformation, but may instead be the result of extensive, static recrystallization by way of pervasive melt percolation.

The distribution of lithologies which would result from such reaction and hybridization with the migrating melts is summarized in Figure 32C, where the focused melt flow in the center of the shear zone would result in the crystallization of more homogeneous textures and compositions which are dominated by an abundance of pyroxene-rich lithologies. We interpret the plagioclase-clinopyroxenites to represent a medial pyroxenite formed by such a process where the melt volume was large enough to assimilate any remaining components from the original dunite — moving outwards, the gradual decrease in melt volume and interconnectivity results in clinopyroxenites which did not fully assimilate the host rock (e.g., 122F2-B) followed by olivine-websterites and eventually lherzolites. A consequence of the more diffuse melt flow with distance from the center of the conduit is increasing textural and lithological variety until you reach the most distal, harzburgitic margins where the melt flow is represented by diffuse, anastomosing veins of small olivine and pyroxene neoblasts.

CHAPTER SEVEN:

CONCLUSIONS

The ultramafic xenolith suite from Prindle Volcano, Alaska, is unique in comparison to the other xenolith suites within the NCVP. Whereas the majority of the NCVP xenolith suites are characterized by just lherzolites (i.e., unimodal) or a mixture of lherzolites and harzburgites (i.e., bimodal), the Prindle xenolith suite is characterized by a variety of lithologies including lherzolite, harzburgite, olivine-websterite, dunite, and clinopyroxenite. Furthermore, where past works have postulated that the lithologies of the simple bimodal suites of the NCVP (e.g., Alligator Lake; Shi et al., 1998) originated from different depths and possibly by way of different processes, we argue that the textural and geochemical relationships between the Prindle xenolith lithologies suggest derivation from a similar depth by the same or a related process.

Based on the depleted nature of the dunites and harzburgites and, more specifically, the concentrations of Zr and Hf relative to the REEs in the harzburgites, we suggest that they retain a record of having formed in an SSZ environment. The presence of diffuse, anastomosing veins of finer-grained, proto-intergranular olivine and pyroxene neoblasts is inferred to indicate a period of diffuse, porous reactive melt flow through the harzburgites. The grain size and textures observed within these anastomosing veins is comparable to both the overall morphology of olivines and pyroxenes within the protointergranular to protogranular textures which characterize the well-foliated Ol-websterites and lherzolites. Further, the presence of a clinopyroxenite which retains anhedral, lobate olivine and orthopyroxene grains exhibiting typical resorption textures relative to the host clinopyroxene which, itself, has comparable chemistry to the lherzolites and websterites, suggests there is a direct relationship between the clinopyroxenites and the rest of the lithologies.

The presence of an upper mantle temperature anomaly beneath most of the NCVP has been inferred from teleseismic data (Frederiksen et al., 1998) and employed to explain the origin of several of the NCVP xenolith suites (Shi et al., 1998; Kilgore et al., 2018). Prindle Volcano, however, does not sit directly above this anomaly, it sits on the steeply dipping transition between this anomaly and the surrounding colder mantle. Further, Shi et al. (1998) reasoned that there must be some proportion of interstitial melt present within the anomaly, to have produced the observed anomalous P-wave velocities. Considering Prindle's location together with the observations presented here, we hypothesize that the Prindle xenolith suite is the result of melt-rock reaction and porous reactive flow between alkaline fluids/melts and a depleted mantle (i.e., dunite and harzburgite) shear zone which formed in response to the anomalous upwelling mantle beneath the NCVP.

In our model, pre-existing weaknesses in the lithospheric mantle, like those provided by intercalated dunites and harzburgites in the Moho-transition zones of ophiolites, preferentially localized shear in response to the upwelling asthenosphere. Whereas large volumes of melt would likely characterize the center of the upwelling asthenospheric domain, we expect that the shear zones along the margins would likely only see smaller, more diffuse volumes of the melt. Sometime after the initial formation of the shear zone, the rocks that would become the Prindle xenolith suite were subjected to melt-rock reaction by the porous reactive flow of focused alkaline fluids/melts through the shear zone. The greater porosity which developed due to localized deformation within the dunite would serve to focus the largest volumes of melt, while the less deformed harzburgites at the margins and surrounding the dunites would likely see only small, diffuse volumes of melt. The differences in melt volume would, in turn, result in the development of a relatively homogeneous pyroxenite core in the center of the former dunite channel which would grade outwards into websterites, lherzolites, and then harzburgites.

We suggest that the reason why Prindle has more varied lithologies compared to the other NCVP xenolith localities may be due to it being located above the margin of the mantle anomaly where it is expected to interact with smaller and more diffuse volumes of melt. Critically, it would seem that some of the harzburgites, and at least one of the dunites, likely retain information related to their pre-Cordilleran history. Future studies should seek to examine this possibility further by expanding the trace element dataset to the full sample suite and constraining the isotopic systematics of the assemblage.

APPENDIX I:

SAMPLE

METADATA FROM

THE USGS

This section provides a table (Table A1.1) of the collected metadata provided by Dr. Erin Todd of the USGS for the Prindle Volcano samples sent to UTA.

Table A1.1: Metadata for the Prindle Volcano samples provided by Dr. Erin Todd of the USGS. Reference = Todd, E. DB_Source = USGS.YTT. Series_ID = Yukon-Tanana Upland - New

Sample ID	Serial #	Longitude	Latitude	Elevation (m)	Rock Type	Field Lithology	Alteration	Ig.Form	Material Field Notes	Notes for UTA Cuts
		Datum = WGS84								
15ATe122C	16224	-141.63275	63.71186	1185.182129	Volcanic	basalt	OK	lava flow	Lower/Mid-section sample, comprising down-section series of basalt flows from Prindle volc.	2 pieces of basalt; one with 2+ large oxidized perid. xenoliths; other with at least 6 small (≤1cm) "fresh" perid. xenoliths
15ATe122D	16225	-141.63293	63.71191	1177.731934	Volcanic	basalt	OK	lava flow	Lower-section sample, comprising down-section series of basalt flows from Prindle volc.	multiple perid. xenoliths (>>cm) in lava; fresh, relatively unoxidized
15ATe122E	16226	-141.63178	63.71211	1194	Plutonic	tonalite	OK - Meta	enclave - xeno	leucocratic (tonalite/gneiss?) xenolith within basalt, from near -B (no waypoint)	inclusion of tonalite/orthogneiss in lava
15ATe122F1	16227	-141.63178	63.71211	1194	Plutonic	peridotite	OK - Meta	enclave - xeno	composite of ~10 different ultramafic xenoliths, for TS/GC	single xeno, 2pcs.; dunite, unoxidized
15ATe122F2	16228	-141.63178	63.71211	1194	Plutonic	peridotite	OK - Meta	enclave - xeno	composite of ~10 different ultramafic xenoliths, for TS/GC	2 xenos, both more oxidized; one more banded, one more speckled
15ATe122F3	16229	-141.63178	63.71211	1194	Plutonic	peridotite	OK - Meta	enclave - xeno	composite of ~10 different ultramafic xenoliths, for TS/GC	single xeno, 3 pcs; mostly oxidized; one piece from core, two cut from margins (with glassy/reaction margin)
15ATe122F4	16230	-141.63178	63.71211	1194	Plutonic	peridotite	OK - Meta	enclave - xeno	composite of ~10 different ultramafic xenoliths, for TS/GC	single xeno, 2pcs.; mosly oxidized; blebby oxidized zone in one piece
15ATe122F5	16231	-141.63178	63.71211	1194	Plutonic	peridotite	OK - Meta	enclave - xeno	composite of ~10 different ultramafic xenoliths, for TS/GC	single xeno, multiple pieces; mostly oxidized, but heterogeneously /blebby distributed
15ATe122F6	16232	-141.63178	63.71211	1194	Plutonic	peridotite	OK - Meta	enclave - xeno	composite of ~10 different ultramafic xenoliths, for TS/GC	single xeno, 2pcs; unoxidized
15ATe122F7	16233	-141.63178	63.71211	1194	Plutonic	peridotite	OK - Meta	enclave - xeno	composite of ~10 different ultramafic xenoliths, for TS/GC	single xeno 3 small pieces; mostly oxidized
15ATe122F8	16234	-141.63178	63.71211	1194	Plutonic	peridotite	OK - Meta	enclave - xeno	composite of ~10 different ultramafic xenoliths, for TS/GC	single xeno 2 small pieces; mostly oxidized
16ATe101A1	16261	-141.54572	63.64978		Volcanic	basalt	OK	lava flow	basalt flow, from mt. Prindle; TS bag contains orthogneiss(?) xenolith [cut for polsec]; fairly fresh piece in Chem bag, vessicular olivine phyrric, but rare; assoc with disaggregation of xenoliths?	more dense lava, from distal flow lobe; 2 large pieces, each with multiple <cm crustal AND peridotite xenoliths
16ATe101B	16263	-141.54572	63.64978		Plutonic	peridotite	OK	enclave - xeno	2x pcs w/ 3x xenoliths (2 same?) for p-sec; cut TS piece; cpx peridotite, fairly fresh, kelley green; 1 each xenoliths elongate and rounded, ≥ 1cm	
16ATe101C	16264	-141.54572	63.64978		Volcanic	basalt	OK	lava flow	like A, fresher, abundant feldspathic inclusions, 2-4%, typically >1mm to 2 cm, UM xenoliths more rare	more dense lava, from distal flow lobe; 2 pieces, each with multiple <cm crustal AND peridotite xenoliths (one crustal xeno >cm)
16ATe102A	16265	-141.62827	63.71571		Plutonic	peridotite	OK	enclave - xeno	nice large rounded xenolith within spatter at northern end of Prindle cone, moderately oxidized	moderately oxidized peridotite xeno
16ATe102C	16267	-141.62756	63.71504		Plutonic	peridotite	OK (?)	enclave - xeno	extensive red oxidized peridotite xenolith, subrounded	mostly oxidized perid. xeno
16ATe102D	16268	-141.62755	63.71438		Plutonic	peridotite	OK	enclave - xeno	multiple pcs of sub-angular, fairly fresh peridotite xenolith; cut 3-4 TS	lava with several small xenos (>cm and <cm), including both unoxidized perid, plus other potentially crustal xeno (circled)
16ATe102E1	16270	-141.62898	63.71337		Plutonic	peridotite	OK	enclave - xeno	peridotite w/ xpx vein, unaltered (2pcs)	small xeno fragment in basalt; perid. fragment has mineral seg zone/vein of unoxidized min. (pyx?)
16ATe102E2	16271	-141.62898	63.71337		Plutonic	peridotite	OK	enclave - xeno	pyroxenite	pyroxenite xeno, 4 <cm pieces, two on margins, two homogeneous fragments.

APPENDIX II:

HAND SAMPLE DESCRIPTIONS AND PHOTOGRAPHS

This section provides the hand sample descriptions and photographs as they were collected by the author.

Sample # - 15ATe122C

USGS – Two pieces of basalt; one with 2+ large oxidized peridotite xenoliths; other with at least six small (≤1cm) "fresh" peridotite xenoliths

Analysis: Basalt A

Basalt A – Vesicular basalt matrix; two cut sides and three irregular side. Weight: > 420 gm.

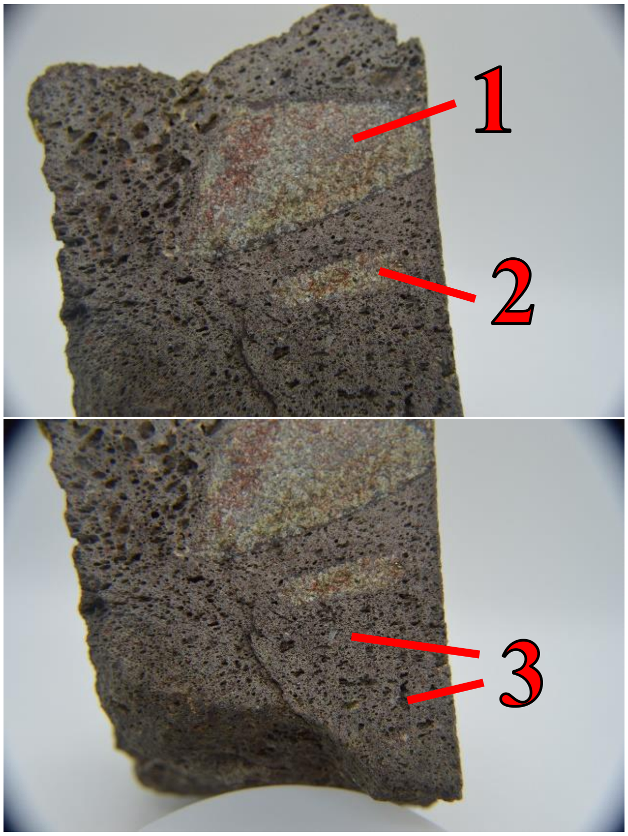

Smaller cut side:

Contains 2 prominent peridotite xenoliths. Both with signs of oxidation. Larger of the two displays prominent rimming along boundary between basalt and xenolith. Vesicular nature shows a discrepancy going from the area with larger xenolith to the smaller xenolith. Texture has larger vesicles near larger xenolith.

1. Large xenolith measures 4 cm across at its widest points; 2.3 cm at widest points perpendicular to widest measurement
2. Smaller xenolith measures 2 cm across at widest points, ~ 0.55 cm at widest points perpendicular to widest measurement
3. Additionally, it appears smaller oxidized peridotites are common throughout the matrix ≤ 0.35 cm xenoliths

<u>Sample # - 15ATe122C (cont.)</u>

Basalt A (cont.) – Vesicular basalt matrix; two cut sides and three irregular side. Weight: > 420 gm.

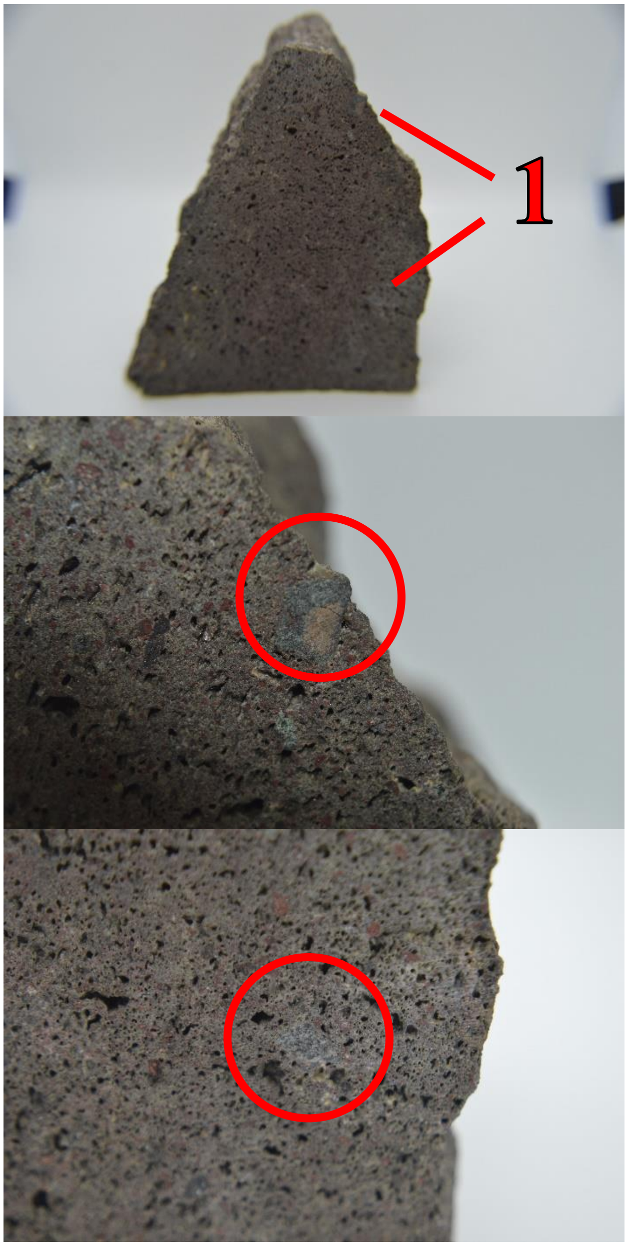

Larger cut side:

Basalt matrix, highly oxidized peridotite xenoliths scattered throughout; vesicular texture is more homogeneous then other cut side.
At least four highly vitreous xenoliths are observed

1. Two square-ish/parallelogram xenoliths with black and white striations

- Spinel, sulfide, augite, hornblende – dark in color

Sample # - 15ATe122C (cont.)

Basalt A (cont.) – Vesicular basalt matrix; two cut sides and three irregular side. Weight: > 420 gm.

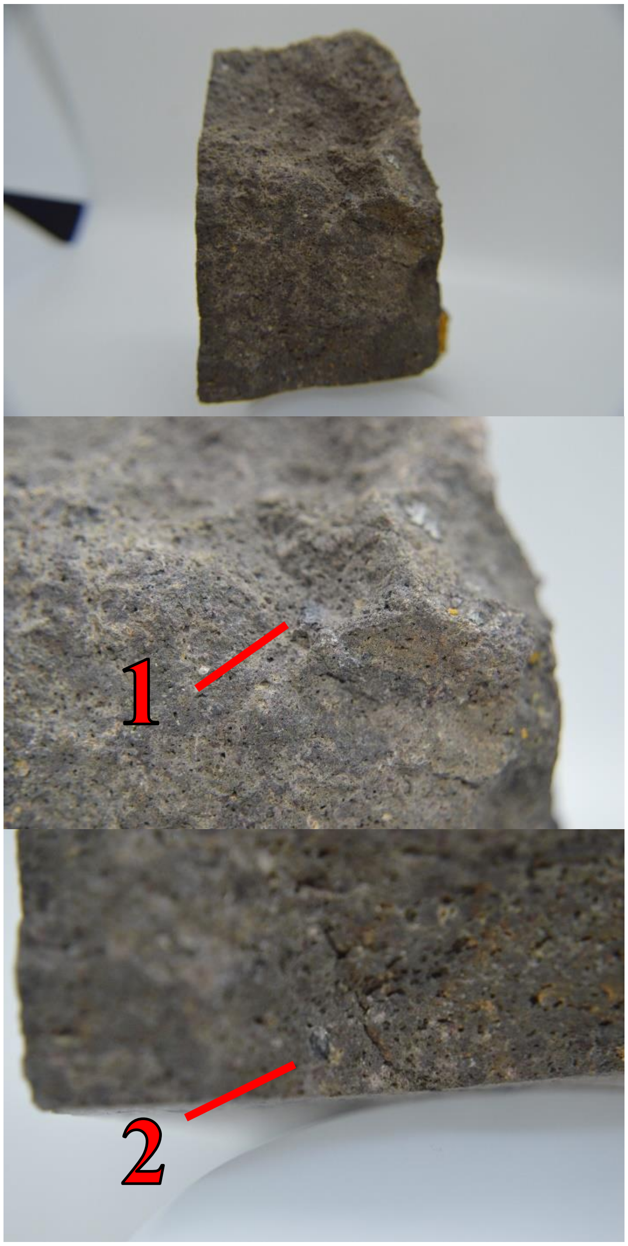

Right side of Larger cut side looking at the sample:

Aphanitic basalt matrix, 2 distinguishable types of xenoliths.

1. Three vitreous, reddish-brown xenocryst grains (largest ~0.4cm) appears to have at least one cleavage plan
2. Approximately three vitreous, black xenocryst grains.

Sample # - 15ATe122C (cont.)

Basalt A (cont.) – Vesicular basalt matrix; two cut sides and three irregular side. Weight: > 420 gm.

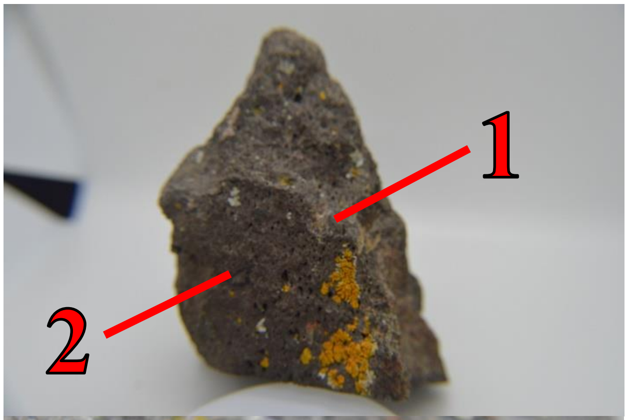

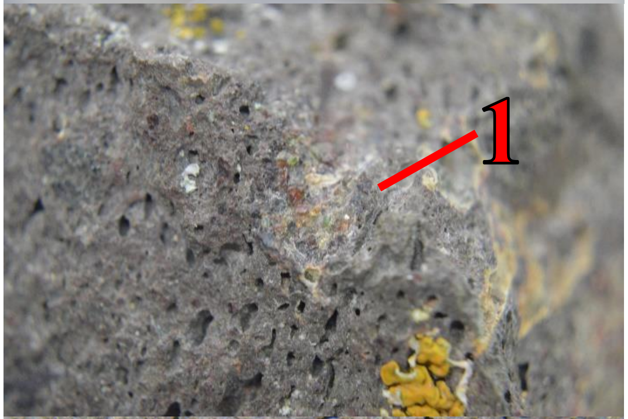

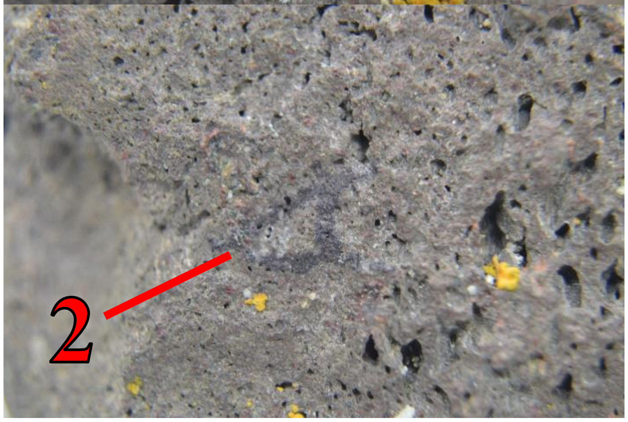

Opposite side of Larger cut side (Back):

Vesicular basalt, heavily lichened, zonation in size of vacuoles
Two distinguishable xenoliths

1. Oxidized peridotite (1 to 1.1 cm long, 0.4 cm wide)
2. Roundish xenolith, black (pyroxene?) (0.3 cm diameter)

Sample # - 15ATe122C (cont.)

Basalt A (cont.) – Vesicular basalt matrix; two cut sides and three irregular side. Weight: > 420 gm.

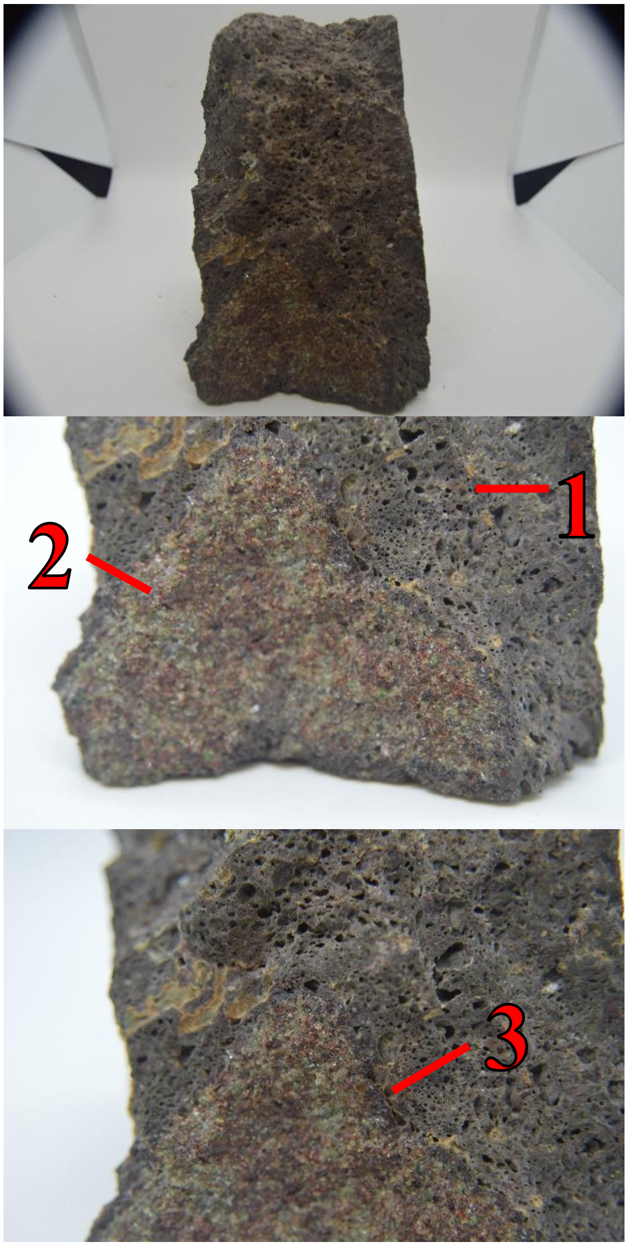

Left side of Larger cut side looking at sample (with small cut side on bottom):

Aphanitic basalt matrix, vesicular texture increases as moving toward smaller cut sample.

1. Oxidized grains (~0.1 to 0.3 cm) throughout
2. Large xenolith of peridotite located in more vesicular region by smaller cut side. Almost spans the entire length of the sample (5 cm in length and ~ 3.7 cm in width)

   Large xenolith is granular in texture, oxidation is present throughout but is quasi zonal.

   - Oxidized grains (55-60%)
     - Reddish brown in color
     - Two cleavage plain?
   - Unaltered grains (40-45%)
     - Green
     - Subhedral
     - Olivine
3. Glassy rim observed around large xenolith peridotite

<u>Sample # - 15ATe122C (cont.)</u>

<u>Analysis:</u> Basalt B

Basalt B – Vesicular basalt, two cut sides, three irregular sides ~ 12.4 cm in length and ~9.2 cm in width. Weight: > 420 gm.

*A distinct gradation of the size of vacuoles from longest irregular side to smallest cut side. The vacuoles increase in size. Appears to be a flow texture in place utilizing the vacuoles.

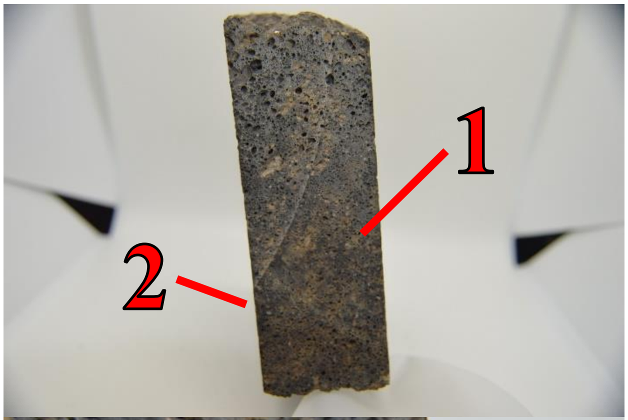

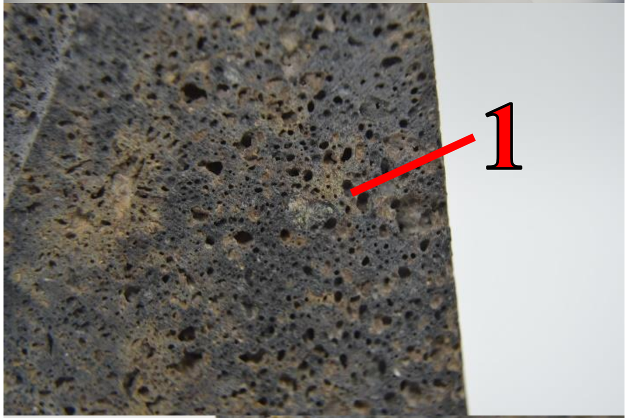

Smallest cut side:

Highly vesicular, aphanitic basalt

1. One xenocryst (~0.3 cm), green-yellow color
2. One granular aggregate, whitish-lit green color (~0.15 cm)

Sample # - 15ATe122C (cont.)

Basalt B – Vesicular basalt, three cut sides, three irregular sides ~ 12.4 cm in length and ~9.2 cm in width. Weight: > 420 gm.

*A distinct gradation of the size of vacuoles from longest irregular side to smallest cut side. The vacuoles increase in size. Appears to be a flow texture in place utilizing the vacuoles.

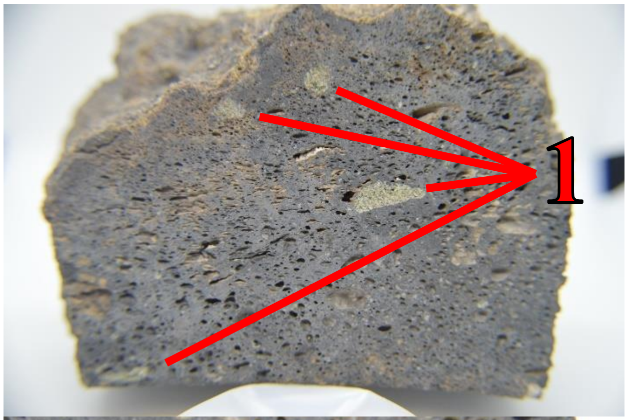

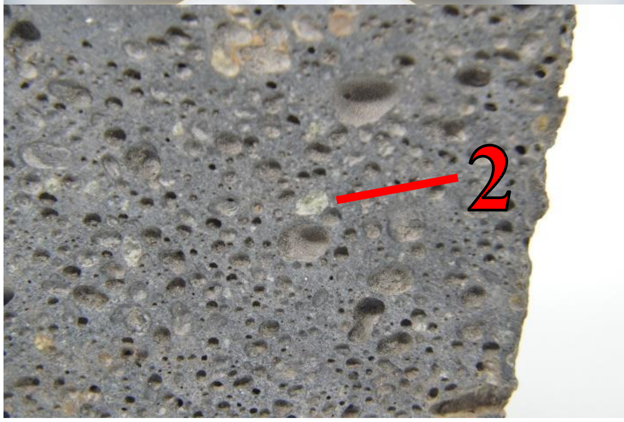

Cut side with smallest surface area (not smallest cut side):

1. Four distinct granular peridotites, oxidation minimal, two irregular shape and two are circular
    - Largest of the four grains is ~1.6 cm in length and ~0.6 cm in width
2. Approximately three indistinct granular peridotites
    - Largest is ~0.2 cm

<u>Sample # - 15ATe122C (cont.)</u>

Basalt B – Vesicular basalt, three cut sides, three irregular sides ~ 12.4 cm in length and ~9.2 cm in width. Weight: > 420 gm.

*A distinct gradation of the size of vacuoles from longest irregular side to smallest cut side. The vacuoles increase in size. Appears to be a flow texture in place utilizing the vacuoles.

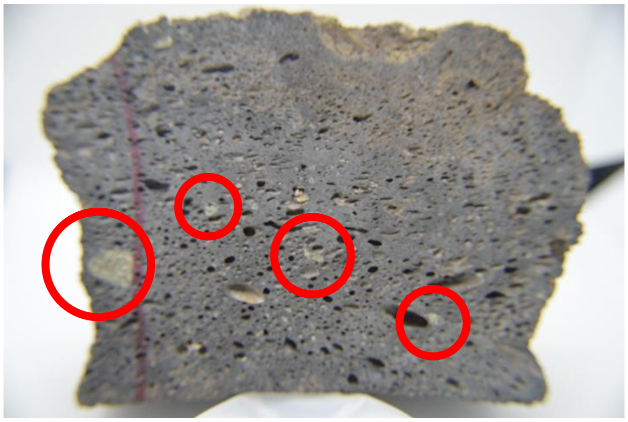

Cut side with largest surface area:

Four peridotite xenoliths, granular, no apparent signs of oxidation.
Graduation of vesicular texture; large and oblong at bottom with size reducing moving upward
Peridotites seem to be restricted to more vesicular section of the basalt

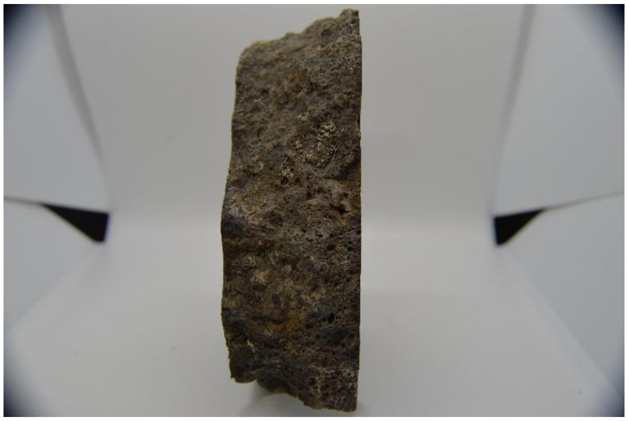

Top of irregular side, opposite smallest cut side:

Characteristic of weathered basaltic rock, slight vesicular texture, aphanitic

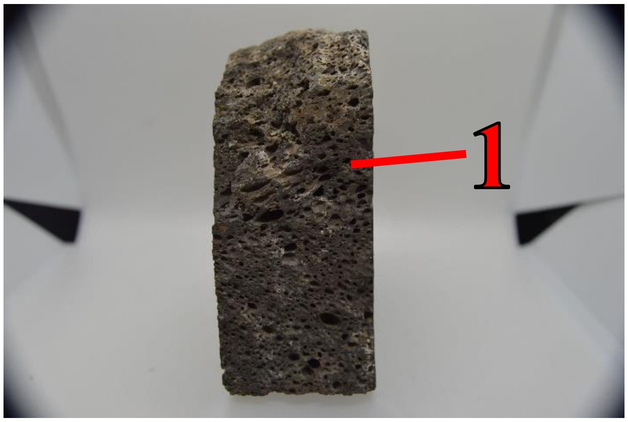

Irregular side that is flusher:

Highly vesicular, weathered basaltic rock, aphanitic

1. One grain, dark in color, brownish-black-green, slight vitreous luster

Sample # - 15ATe122C (cont.)

Basalt B – Vesicular basalt, three cut sides, three irregular sides ~ 12.4 cm in length and ~9.2 cm in width. Weight: > 420 gm.

*A distinct gradation of the size of vacuoles from longest irregular side to smallest cut side. The vacuoles increase in size. Appears to be a flow texture in place utilizing the vacuoles.

Irregular side that is least flush:

Weathered basalt, aphanitic, vesicular flow pattern observed in texture located at bottom (small cut side)

Sample # - 15ATe122D

USGS - multiple peridotite xenoliths (>>cm) in lava; fresh, relatively unoxidized

Analysis: Two pieces of lava (basalt); Lava A - largest of the two is a triangular-pyramid in shape

Lava A – Two cut sides, two irregular and weathered sides (one being the "bottom"). Weight: 205.503 gm.

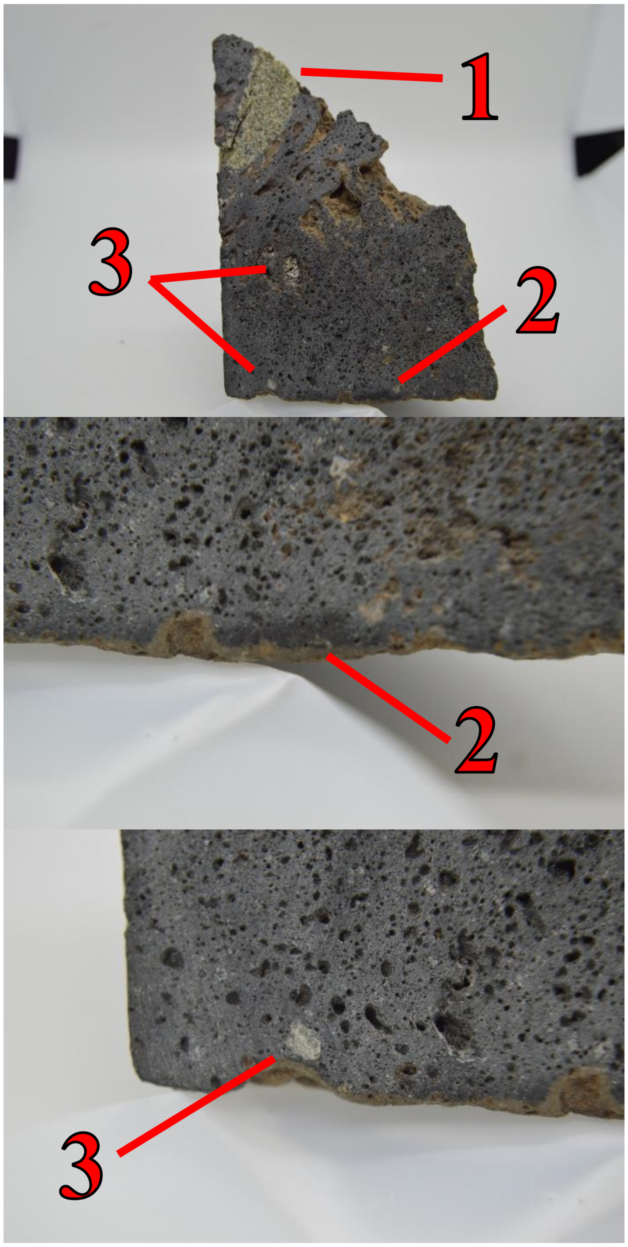

Largest cut side:

Basalt matrix in vesicular and aphanitic; vesicular texture increases in size moving toward peridotite

1. Distinct peridotite xenolith located at "point"
    - Unique in the sense that this fragment "cuts" through the sample and is visible from adjoining sides ~1.2 cm wide and 3 cm long on this side.
2. Small highly reflective "glassy" piece located near "bottom"
    - ~8.4 cm from "bottom" to "point" and 5.6 cm wide
3. Approximately six small inclusions scattered throughout basalt
    - Largest being ~0.2 cm in size

Sample # - 15ATe122D (cont.)

Lava A – Two cut sides, two irregular and weathered sides (one being the “bottom”). Weight: 205.503 gm.

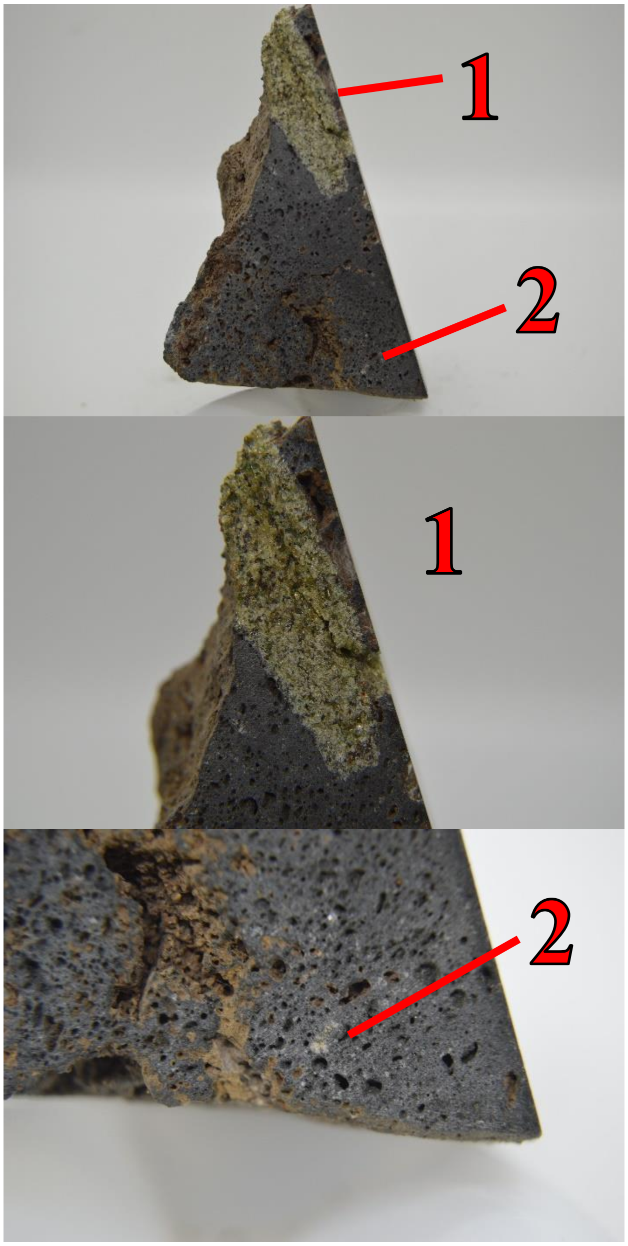

Smaller cut side:

Basalt matrix is vesicular

1. One distinct peridotite located at “point”
    - Unique in the sense that this fragment “cuts” through the sample and is visible from adjoining sides
    - ~1.2 cm in width and 3.9 cm in length
2. Approximately five small inclusions throughout basalt
    - Largest at ~0.25 cm

Sample # - 15ATe122D (cont.)

Lava A – Two cut sides, two irregular and weathered sides (one being the "bottom"). Weight: 205.503 gm.

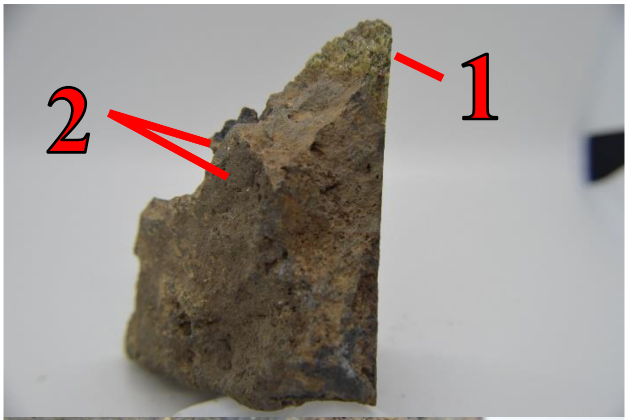

Large weathered side:

Basalt matrix is dirty and highly weathered

1. One distinct peridotite located at "point"
    - Unique in the sense that this fragment "cuts" through the sample and is visible from adjoining sides
    - ~1.2 cm in width and 3.9 cm in length
    - This side contains the fragmented portion of the xenolith
2. Scattered throughout are felsic phenocryst
    - Albite/quartz?

"Bottom" or smallest weathered side:
Basalt that has bees weathered to a smoother texture then what is commonly found in nature. Has a slight gritty feel which could be a type of clay deposit sediment impacted into the specimen
No apparent mineral assemblages

<u>**Sample # - 15ATe122D (cont.)**</u>

<u>Analysis:</u> Two pieces of lava (basalt); Lava B - the smallest piece has a semi-pyramidal shape to it with peridotite xenoliths, dirt caked on top while the bottom is a fresh basalt, vesicular and numerous felsic looking mineral inclusions.

Lava B – Specimen has a dome like structure. Weight: 143.575 gm.

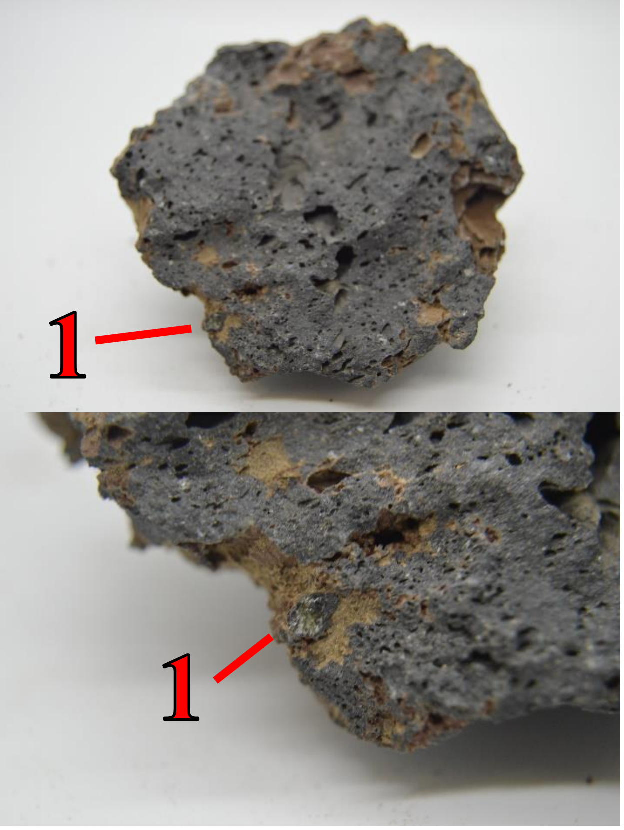

“Bottom” side of specimen:

Highly vesicular, aphanitic basalt

1. One olivine/pyroxene
    - ~0.3 cm

“Top” side of specimen:

Highly weathered basalt
Large peridotite xenolith
~4.2 cm long and 2.8 cm wide
Granular texture

- Olivine, OPX, CPX, Spinel

Sample # - 15ATe122E

USGS - inclusion of tonalite/orthogneiss in lava

Analysis: **Sample is bimodal.** Weight: 74.534 gm.

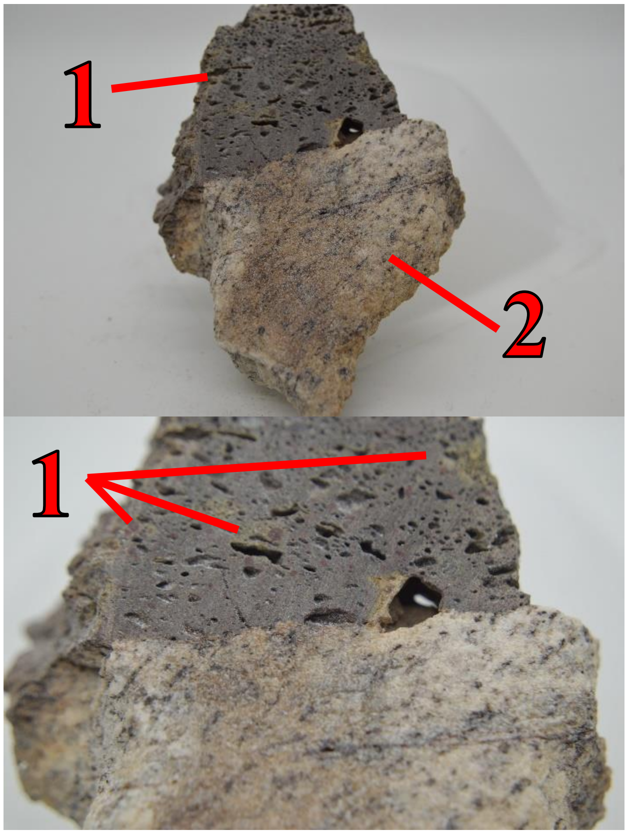

Cut side of specimen:

1. Top half of the specimen is a vesicular basalt that is aphanitic but has various inclusions throughout
    - Largest of the inclusions is ~0.2 cm
    - Vary in their oxidation state
    - Color ranges from all red, black, lite grey, buff, and white
2. Bottom half of the specimen is a distinct felsic rock.
    - Dominant lithology either quartz/feldspar or combination of the two
    - Graphic texture is observed with mafic minerals throughout
    - Observed lineation can be seen when looking at graphic texture

Sample # - 15ATe122F1

USGS - single xenolith, 2pcs.; dunite, unoxidized

Analysis: **Two pieces of a dunite xenolith (A and B) with both encased in a vesicular basalt. Both samples are very similar regarding weathering, oxidation, and texture.**

Piece A: 4.3 cm x 5.6 cm x 2.8 cm; Weight: 54.827 gm.

1. Aphanitic texture of olivine
2. Crusting could be a consequence of OPX and CPX leaching from dunite/peridotite?

Piece B: 3.8 cm x 4.2 cm x 3.2 cm; Weight: 91.766 gm.

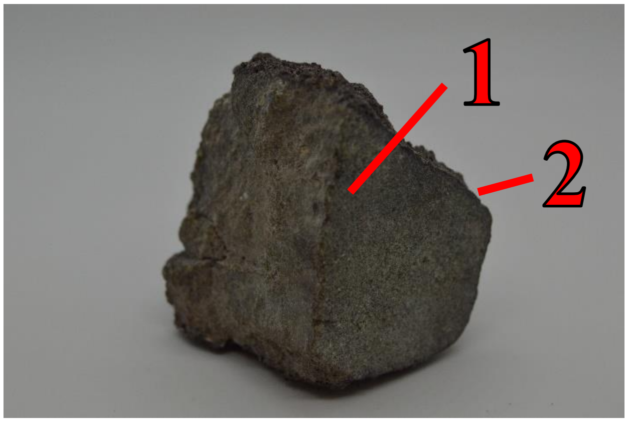

1. Aphanitic texture of olivine
2. Crusting could be a consequence of OPX and CPX leaching from dunite/peridotite?

<u>Sample # - 15ATe122F2</u>

<u>USGS</u> - 2 xenoliths, both more oxidized; one more banded, one more speckled

<u>Analysis:</u> Four samples total, each varying in size. Peridotite xenolith is evident in the three largest samples. Smallest sample appears to be entirely basalt.

Sample A – Almost roundish in shape but flat on two sides (coin shaped). One side highly weathered and the other side produced by cutting of the sample. Weight: 109.442 gm.

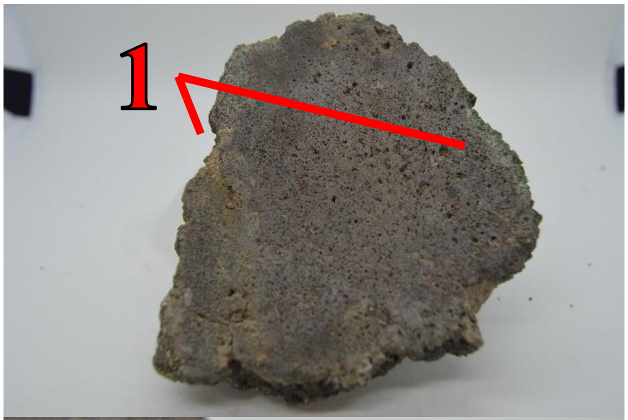

Cut side:
Matrix is a vesicular basalt with numerous pyroxene inclusions that show signs of weathering

1. Two exposed peridotite xenoliths
    - Predominantly olive
    - Granular texture.
    - Both have signs of weathering

Sample # - 15ATe122F2 (cont.)

Sample A – Almost roundish in shape but flat on two sides (coin shaped). One side highly weathered and the other side produced by cutting of the sample. Weight: 109.442 gm.

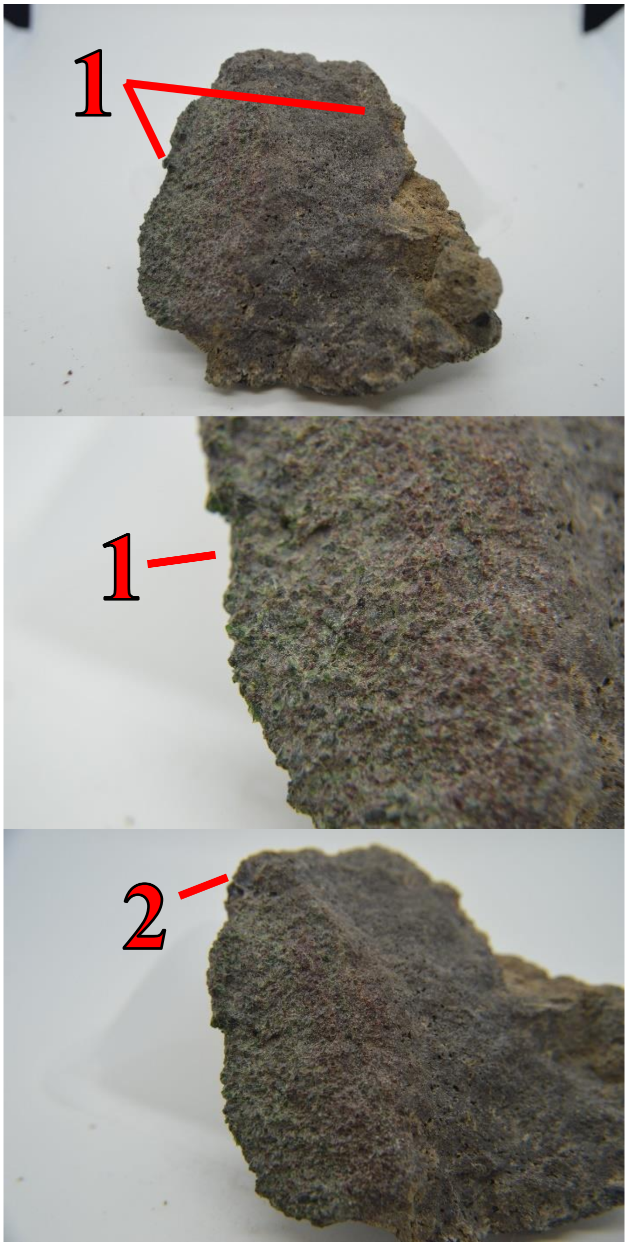

Weathered side:
Matrix is a vesicular basalt with numerous pyroxene inclusions that show signs of weathering

1. Two exposed peridotite xenoliths.
    - Olivine and pyroxene composition.
    - Highly granular
    - Both peridotites have been exposed to weathering
2. Pyroxene? Nodule, fractionated
    - ~0.85 cm x 0.45 cm

<u>Sample # - 15ATe122F2 (cont.)</u>

Sample B - Coin shaped, one side weathered, and one side cut. Weight: 62.493 gm.

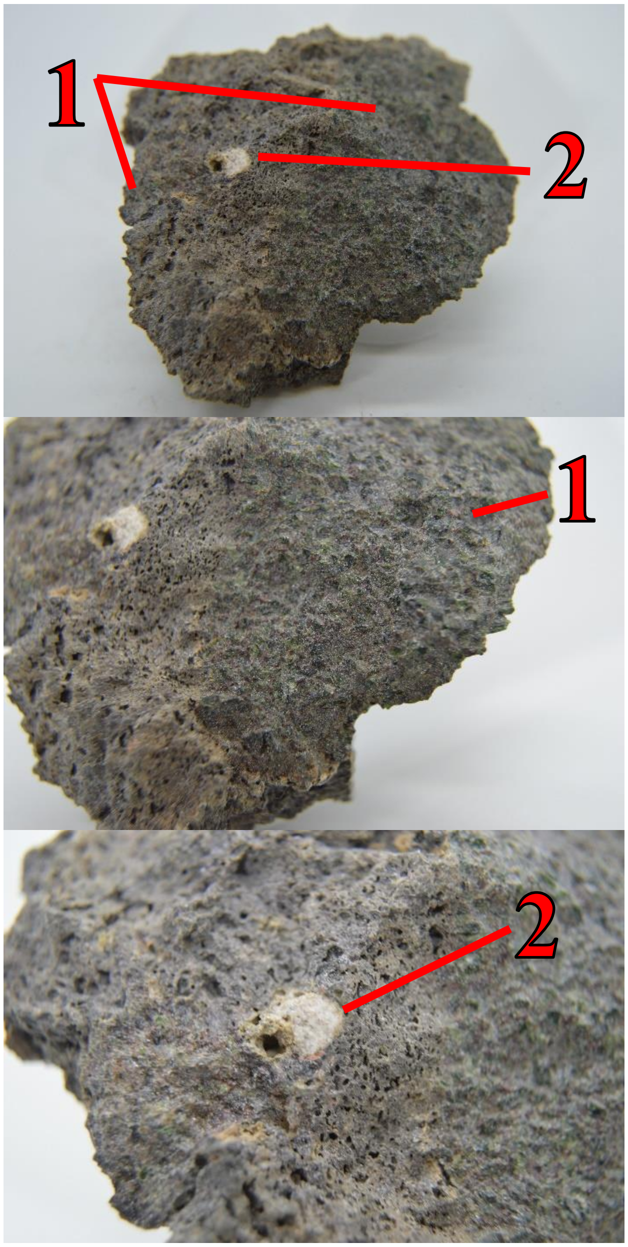

Weathered side:
Over half of the surface is dominated by peridotite.

1. Two separate xenoliths are observable within the basalt.
    - Olivine and pyroxene
    - Granular texture
    - Highly weathered
2. Feldspathic inclusion within basalt
    - ~0.55 cm x 0.55 cm

Sample # - 15ATe122F2 (cont.)

Sample B - Coin shaped, one side weathered, and one side cut. Weight: 62.493 gm.

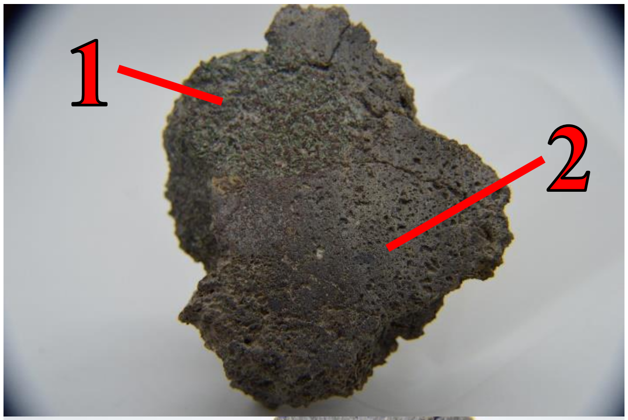

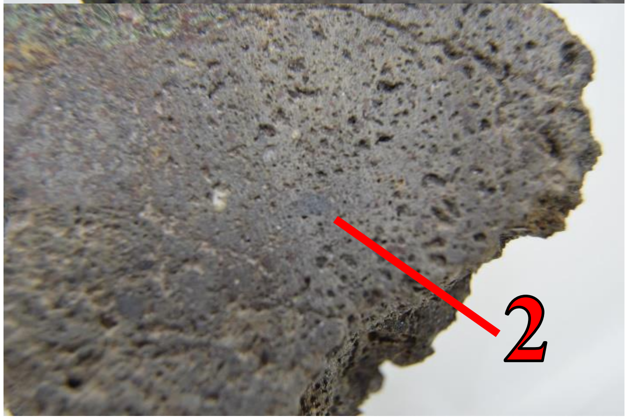

Cut side:

1. One exposed peridotite xenolith, originating from the larger xenoliths from the other side.
    - Composed of olivine and pyroxene.
    - Granular in texture
    - Weathered
2. Pyroxene? Inclusions throughout the basalt

Sample # - 15ATe122F2 (cont.)

Sample C – Coin shaped in nature, one cut side and one weathered semi-domed side. Weight: 21.611 gm.

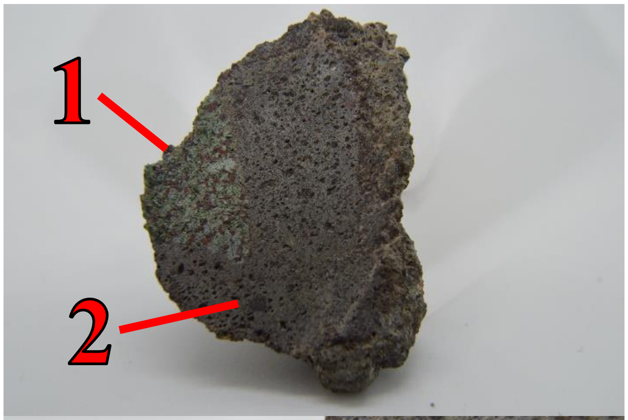

Cut side:

1. Peridotite xenolith
    - Composed of olivine and pyroxene.
    - Granular in texture
    - Slightly weathered
2. Pyroxene inclusions within basalt

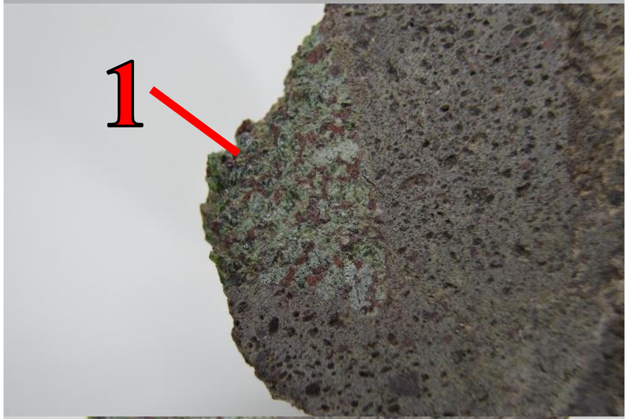

Sample # - 15ATe122F2 (cont.)

Sample C – Coin shaped in nature, one cut side and one weathered semi-domed side. Weight: 21.611 gm.

Semi-domed weathered side:

1. Dominated by peridotite xenolith
    - Olivine and pyroxene
    - Very granular
    - Highly weathered

<u>Sample # - 15ATe122F3</u>

<u>USGS</u> - single xenolith, 3 pcs; mostly oxidized; one piece from core, two cut from margins (with glassy/reaction margin)

<u>Analysis:</u> Three prominent pieces of peridotite with two smaller fragments.

Piece A – Largest of the three, ~4.5 cm in length and 3.4 cm in width. Weight: 35.654 gm.

Seems to be the "core" piece as no basalt is clearly present

- Olive and pyroxene
- Very granular
- Heavily oxidized

Piece B and C – Two fragments that consist of basalt and peridotite

Pieces from the margin so consist of a glassy/reaction margin.

- Olive and pyroxene
    - Grains measure in at almost 0.1 cm.
- Very granular
- Heavily oxidized
- Darker hue margin separates basalt from peridotite

Sample # - 15ATe122F4

USGS - single xenolith, 2pcs.; mostly oxidized; blebby oxidized zone in one piece

Analysis: Six total pieces; two seem to fit together so five will be described

Piece 1 – Broken pieces that fit together. Approximately 2.5 cm x 3.7 cm. Weight: 11.701 gm (8.146 + 3.555 gm.)

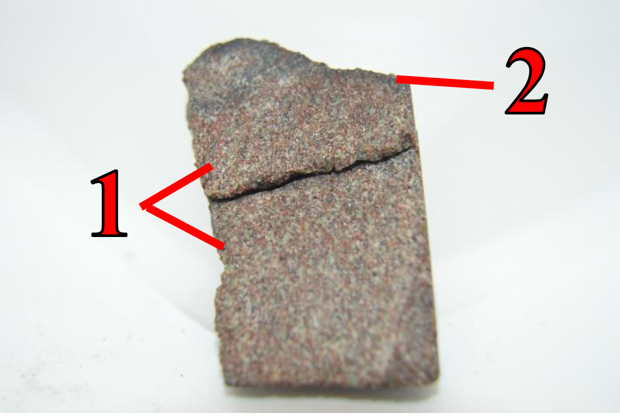

Piece that consists of two of the samples:

1. Large cut side is dominated by xenolith
   - Olivine, pyroxene, and spinel
   - Heavily oxidized
2. Marginal boundary exists between xenolith and lithology crusting the outside

Piece 2 – Dome piece with xenolith residing within the interior. Approximately 3.3 cm x 2.7 cm x 1.9 cm. Weight: 18.232 gm.

Piece that consists of two of the samples:

1. Xenolith
   - Olivine and pyroxene
   - Heavily oxidized
   - Granular texture
2. Exterior a dark basaltic crust-like
   - Possible rimming margin between xenolith and basalt

Sample # - 15ATe122F4 (cont.)

Pieces 3-5 – A collection of fragments that are mostly oxidized peridotite.

Piece 3: 2.1 cm x 1.2 cm x 0.5 cm. Weight: 2.310 gm.

Piece 4: 0.8 cm x 1.0 cm x 0.6 cm. Weight: 0.597 gm.

Piece 5: 2.6 cm x 1.9 cm x 0.9 cm. Weight: 5.903 gm.

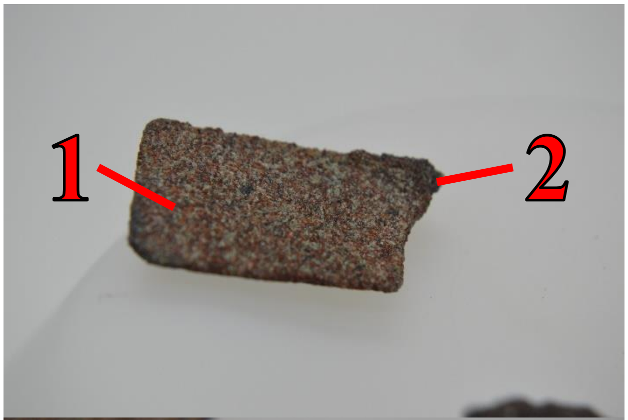

Piece 3:

1. Xenolith
   - Olivine and pyroxene
   - Heavily oxidized
   - Granular texture
2. Hints of marginal boundaries between peridotite and basalt
   - Possible rimming margin between xenolith and basalt

Piece 4:

1. Xenolith
   - Olivine and pyroxene
   - Heavily oxidized
   - Granular texture
2. Marginal boundaries between peridotite and basalt
   - Possible rimming margin between xenolith and basalt

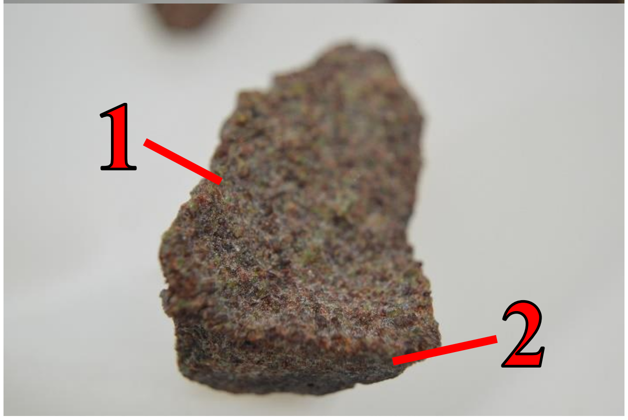

Piece 5:

1. Xenolith
   - Olivine and pyroxene
   - Heavily oxidized
   - Granular texture
2. Marginal boundaries between peridotite and basalt
   - Possible rimming margin between xenolith and basalt

Sample # - 15ATe122F5

USGS - single xenolith, multiple pieces; mostly oxidized, but heterogeneously /blebby distributed

Analysis: Three pieces of one xenolith. The texture is overall aphanitic, could be due to the cutting of the specimen.

Pieces A-B – Two halves of a cut xenolith encased in basalt

Piece A: 4.1 cm x 4.8 cm x 0.3 cm. Weight: 41.688 gm.

Piece B: 3.3 cm x 2.4 cm x 2.8 cm. Weight: 66.675 gm.

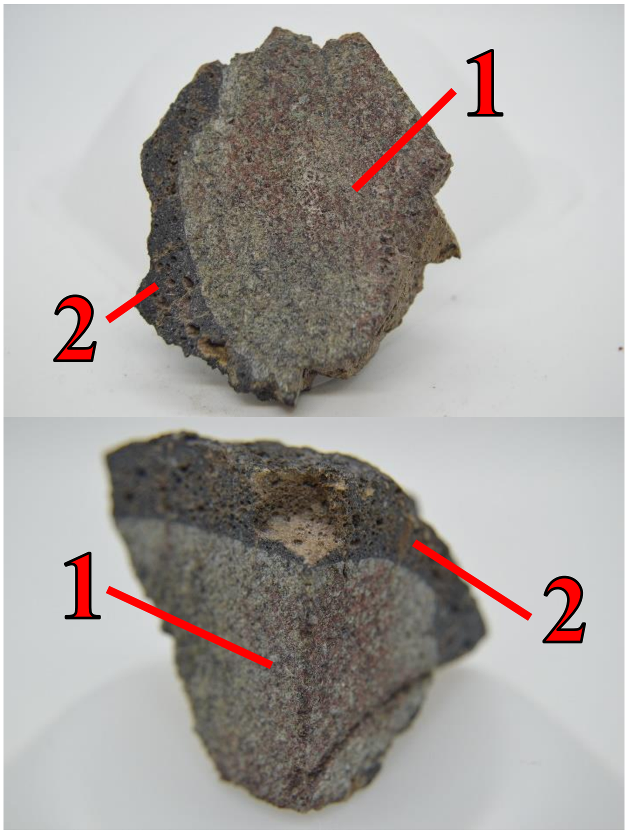

Piece A:

1. Xenolith
    - Olivine and pyroxene
    - Partially oxidized
    - Aphanitic texture
2. Varied textured basalt encasing
    - Aphanitic
    - Glassy
    - Vesicular

Piece B:

1. Xenolith
    - Olivine and pyroxene
    - Partially oxidized
    - Aphanitic texture
2. Varied textured basalt encasing
    - Aphanitic
    - Glassy
    - Vesicular

<u>Sample # - 15ATe122F5 (cont.)</u>

Piece C – Partially cut portion of the xenolith; piece retains more of the natural texture of the peridotite. 2.6 cm x 0.6 cm x 0.5 cm. Weight: 10.906 gm.

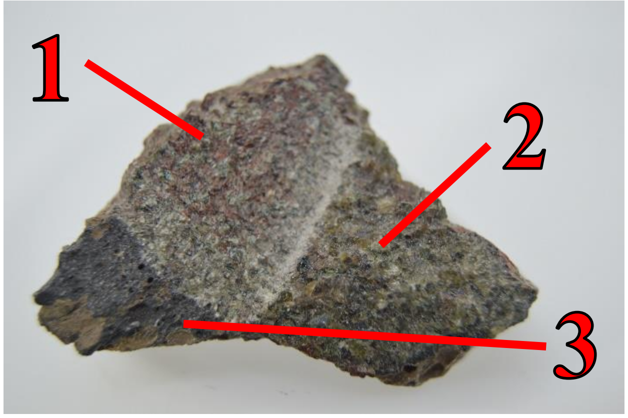

Piece C:

1. Cut xenolith
    - Olivine and pyroxene
    - Partially oxidized
    - Aphanitic texture at cut portion
2. Uncut xenolith
    - Olivine and pyroxene
    - Fresher looking
    - Granular texture
3. Varied textured basalt encasing
    - Aphanitic
    - Glassy
    - Vesicular

Sample # - 15ATe122F6

USGS - single xenolith, 2pcs; unoxidized

Analysis: Two specimens, both have one side that is dominated by xenolith. Mostly vesicular basalt

Specimen 1 – Xenolith consists of the only cut portion of the sample. 3.9 cm x 2.7 cm x 2.5 cm. Weight: 21.009 gm.

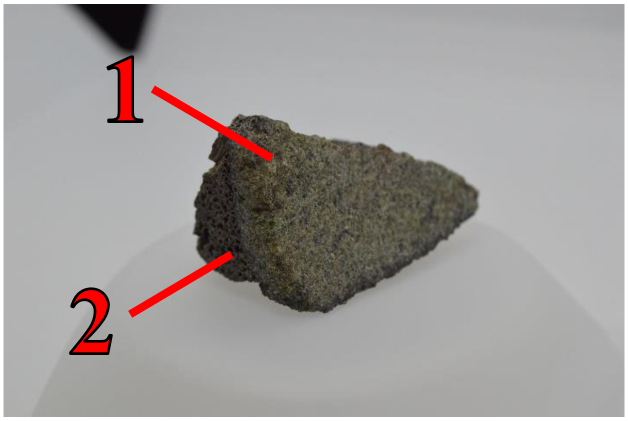

Larger of the two specimens:

1. Cut xenolith
    - Olivine and pyroxene, maybe spinel
    - Granular texture
2. Basalt
    - Boundary observed with a ~0.1 cm thick glassy margin throughout specimen

Specimen 2 – Much like larger piece, xenolith consists of the only cut portion of the sample. 4 cm x 2 cm x 1.3 cm. Weight: 13.510 gm.

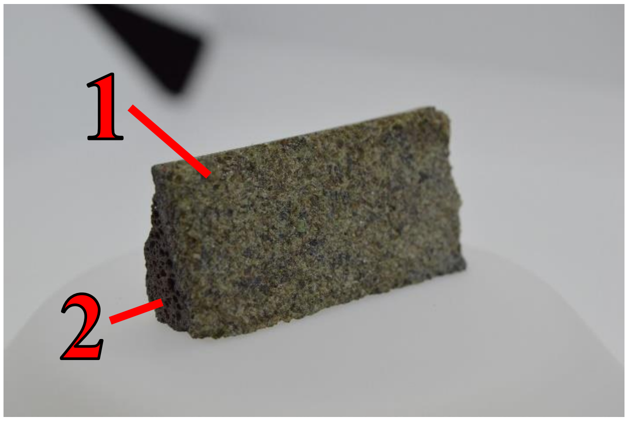

Smaller of the two specimens:

1. Cut xenolith
    - Olivine and pyroxene, maybe spinel, later two in higher concentration than Specimen 1
    - Granular texture
2. Basalt
    - Boundary observed with a ~0.1 cm thick glassy margin throughout specimen

<u>Sample # - 15ATe122F7</u>

<u>USGS</u> - single xenolith 3 small pieces; mostly oxidized

<u>Analysis:</u> Three samples, highly oxidized all with various ratios of basalt to xenolith

Sample 1 – Xenolith consists of larger cut portion. 3.5 cm x 2 cm x 0.7 cm. Weight: 5.767 gm.

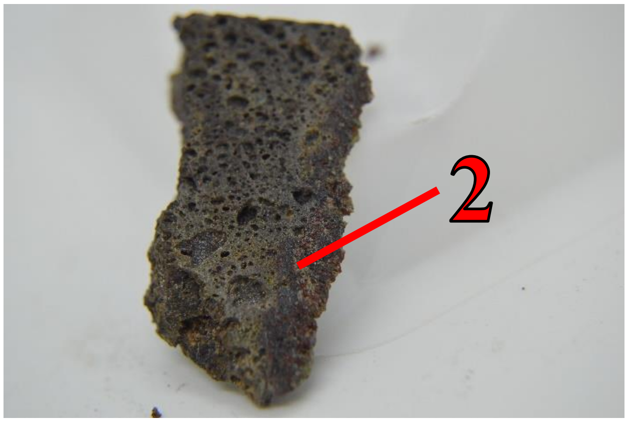

Largest of the three samples:

1. Xenolith
   - Olivine and pyroxene
   - Granular texture
   - Highly oxidized
2. Basalt
   - Highly vesicular
   - Transitional margin observed on the other side between xenolith and basalt; Not quite glassy, almost seems to consist of pure pyroxene.

Sample # - 15ATe122F7 (cont.)

Sample 2 – Irregular sample that is mostly oxidized xenolith. 2.4 cm x 1.2 cm x 2.4 cm. Weight: 5.163 gm.

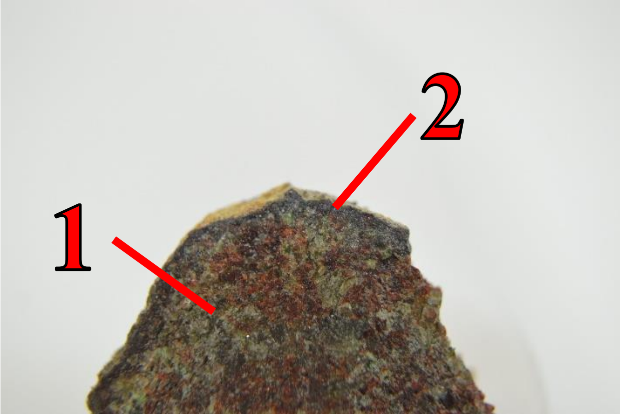

Middle sized sample:

1. Xenolith
   - Olivine, pyroxene and perhaps spinel
   - Very granular texture
   - Highly oxidized
2. Basalt
   - Vesicular
   - Possible marginal boundary but not as distinguishable as Sample 1.
   - Slight crusting along outside of small section
     - Could be pyroxenite lithology

Sample 3 – Predominantly vesicular basalt about 1/3 peridotite xenolith. 1.8 cm x 1.0 cm x 0.6 cm. Weight: 1.407 gm.

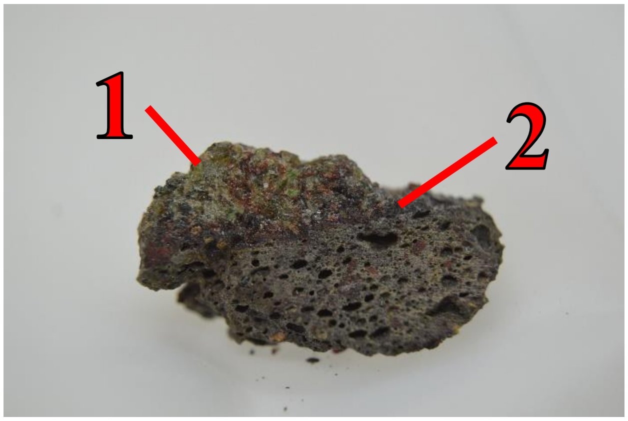

Smallest sample:

1. Xenolith
   - Olivine and pyroxene
   - Very granular texture
   - Oxidized
2. Basalt
   - Vesicular
     - Marginal boundary between xenolith and basalt

Sample # - 15ATe122F8

USGS - single xenolith 2 small pieces; mostly oxidized

Analysis: Sample consisted of two pieces; one piece will be used for this study since it is dominated by the xenolith.

Xenolith piece – Large inclusion of peridotite takes up all of one side. Basalt contains approximately 0.2 cm xenocrysts throughout. 3.45 x 3.6 cm. Weight: 19.101 gm.

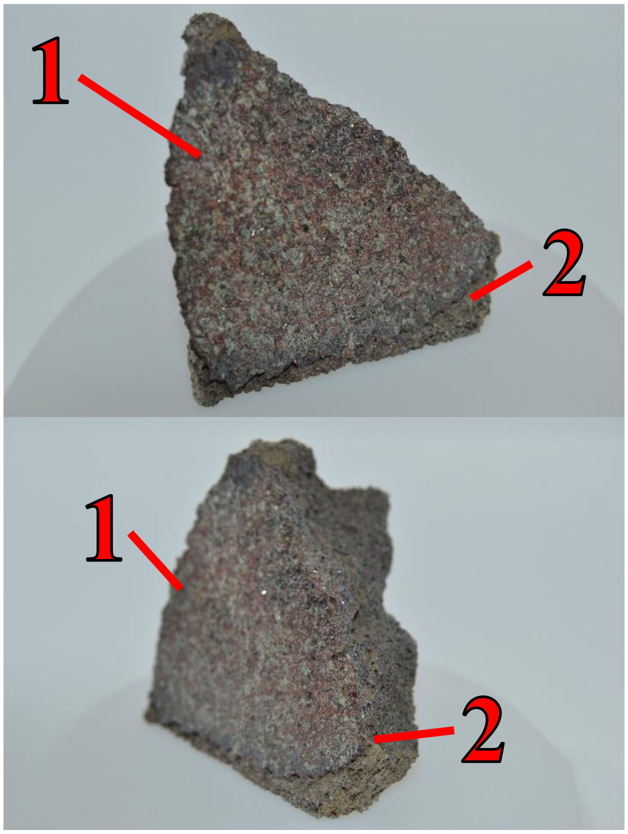

1. Xenolith
    - Peridotite
    - Olivine and pyroxene
    - Highly oxidized
2. Basalt
    - Vesicular
    - Boundary margin separating the basalt from the peridotite inclusion, possibly pyroxene

<u>Sample # - 16ATe101A</u>

<u>USGS</u> - more dense lava, from distal flow lobe; 2 large pieces, each with multiple <cm crustal AND peridotite xenoliths

<u>Analysis:</u> Very dense aphanitic basalt, some major weathering along outside of samples. Two specimens are cut. One is pyramidal in shape and largest of the two. While the other is very flat and triangular.

Sample A – large pyramidal shaped sample with four identifiable peridotites. Weight: 415.135 gm.

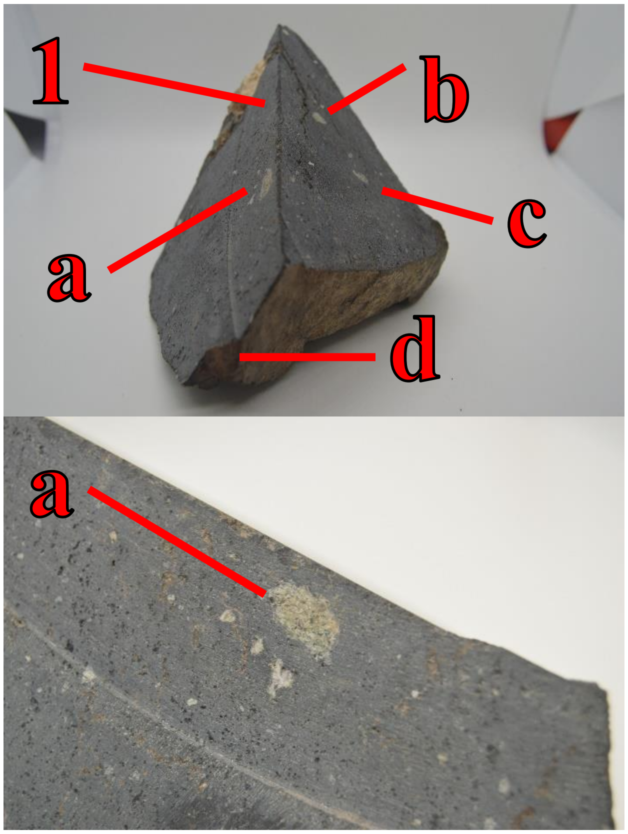

Larger Sample:

1. Consist of four xenoliths, three peridotite and one felsic
    a. Peridotite
        - Olivine
        - Granular
        - Unoxidized
        - 0.53 x 0.97 cm
    b. Peridotite
        - Olivine
        - Granular
        - Unoxidized
        - 0.44 x 0.54 cm
    c. Peridotite
        - Olivine
        - Granular
        - Unoxidized
        - 0.35 x 0.64 cm
    d. Felsic
        - Feldspar
        - Phaneritic
        - 0.63 x 0.93 cm

Sample # - 16ATe101A (cont.)

Sample A – large pyramidal shaped sample with four identifiable peridotites. Weight: 415.135 gm.

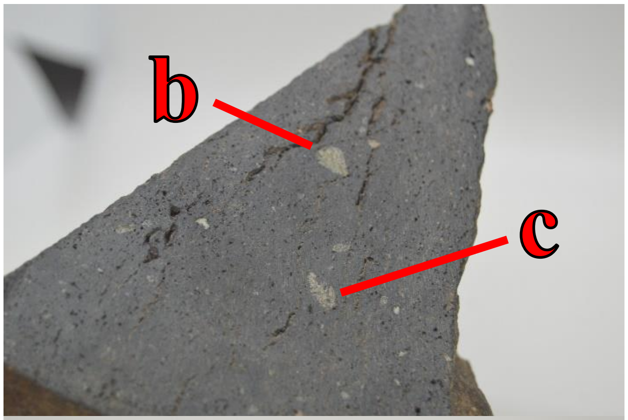

Larger Sample:

1. Consist of four xenoliths, three peridotite and one felsic
    - b. Peridotite
        - Olivine
        - Granular
        - Unoxidized
        - 0.44 x 0.54 cm
    - c. Peridotite
        - Olivine
        - Granular
        - Unoxidized
        - 0.35 x 0.64 cm
    - d. Felsic
        - Feldspar
        - Phaneritic
        - 0.63 x 0.93 cm

Sample # - 16ATe101A (cont.)

Sample B – Flat triangular shaped sample. Weight: 73.680 gm.

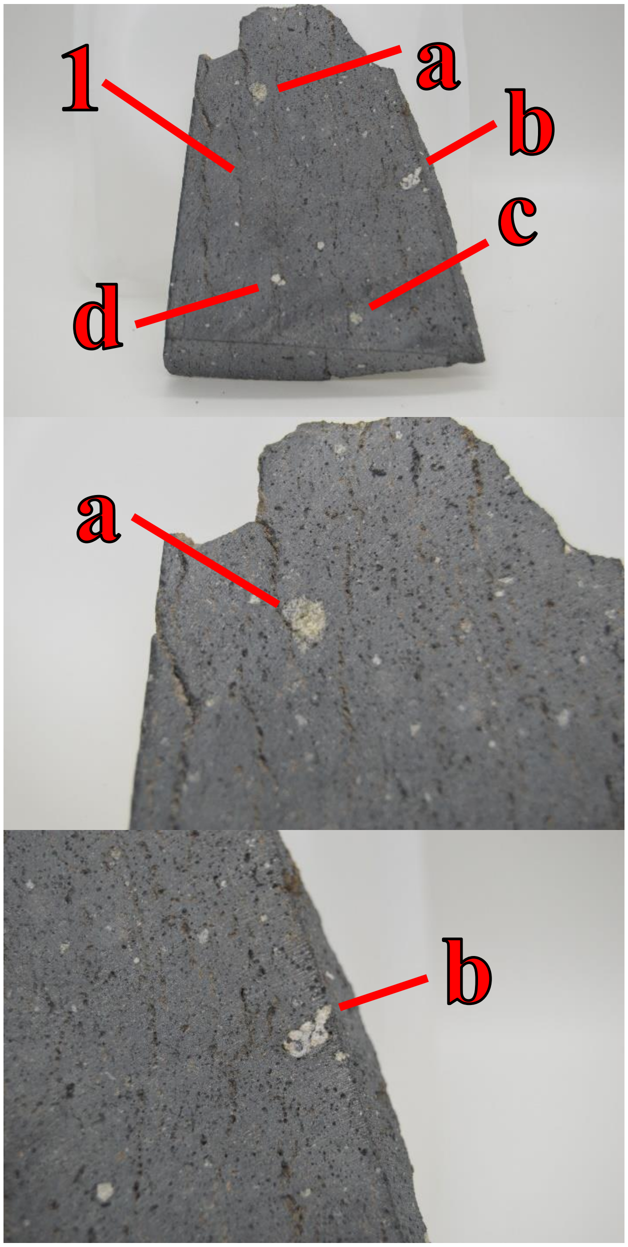

Smaller Sample:

1. Consist of four xenoliths, two peridotite and two felsic
    a. Peridotite
        - Olivine
        - Granular
        - Unoxidized
        - 0.50 x 0.31 cm
    b. Felsic
        - Feldspar and/or quartz
        - Granular
        - Graphic texture
        - 0.24 x 0.67 cm
    c. Peridotite
        - Olivine
        - Granular
        - Unoxidized
        - 0.29 x 0.24 cm
    d. Felsic
        - Feldspar and/or quartz
        - Granular
        - 0.16 x 0.30 cm

Sample # - 16ATe101A (cont.)

Sample B – Flat triangular shaped sample. Weight: 73.680 gm.

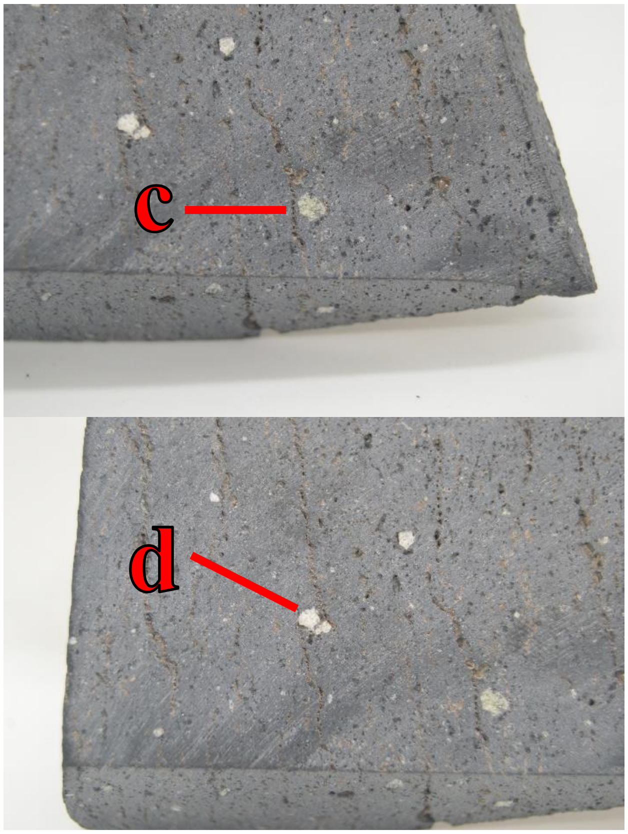

Smaller Sample:

1. Consist of four xenoliths, two peridotite and two felsic
    - c. Peridotite
        - Olivine
        - Granular
        - Unoxidized
        - 0.29 x 0.24 cm
    - d. Felsic
        - Feldspar and/or quartz
        - Granular
        - 0.16 x 0.30 cm

<u>Sample # - 16ATe101C</u>

<u>USGS</u> - more dense lava, from distal flow lobe; 2 pieces, each with multiple <cm crustal AND peridotite xenoliths (one crustal xenolith >cm)

<u>Analysis:</u> Two basalt samples, both very similar. Aphanitic basalt with various xenoliths. Xenoliths consist of both peridotite and crustal fragments.

Basalt A – More rectangular shaped sample. Weight: 253.719 gm.

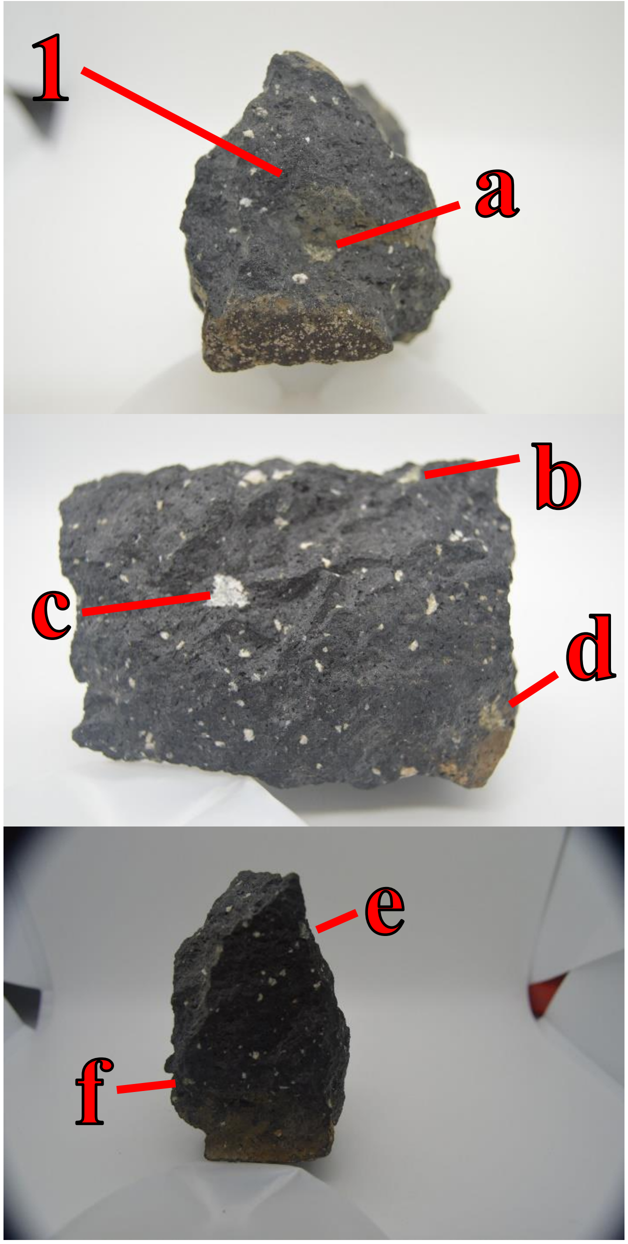

Triangular shaped side:

1. Dense aphanitic basalt with various xenoliths throughout
    a. Peridotite
        - Olivine
        - Granular
        - Unoxidized
        - 0.66 x 0.30 cm
    b. Peridotite
        - Olivine
        - Granular
        - Unoxidized
        - 0.30 x 0.66 cm
    c. Felsic
        - Quartz and feldspar
        - Granular
        - 0.62 x 0.78 cm
    d. Peridotite
        - Olivine
        - Granular
        - Unoxidized
        - 0.65 x 0.52 cm
    e. Peridotite
        - Pyroxene?
        - Unoxidized
        - 0.22 x 0.38 cm
    f. Peridotite
        - Olivine
        - Granular
        - Unoxidized
        - 0.29 x 0.40 cm

<u>Sample # - 16ATe101C (cont.)</u>

Basalt A – More rectangular shaped sample. Weight: 253.719 gm.

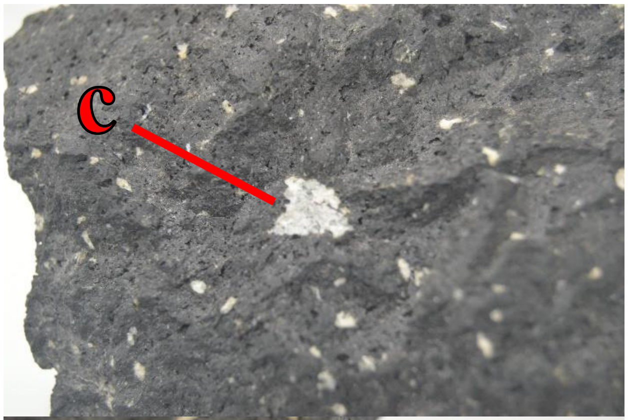

“Bottom” of Triangular shaped side:

1. Dense aphanitic basalt with various xenoliths throughout
    - c. Felsic
        - Quartz and feldspar
        - Granular
        - 0.62 x 0.78 cm
    - d. Peridotite
        - Olivine
        - Granular
        - Unoxidized
        - 0.65 x 0.52 cm
    - e. Peridotite
        - Pyroxene?
        - Unoxidized
        - 0.22 x 0.38 cm

Sample # - 16ATe101C (cont.)

Basalt B – More rounded in nature, dome-like sample. Very similar to Basalt A since it has multiple xenolith inclusions within the basalt. Weight: 241.787 gm.

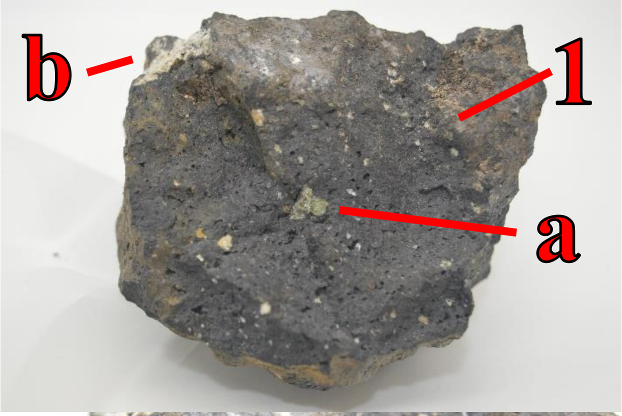

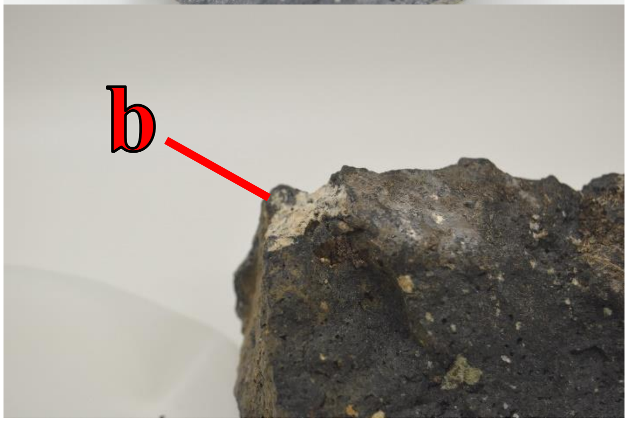

Concave side "Bottom" of dome:

1. Dense aphanitic basalt with one peridotite and one crustal xenolith.
    a. Peridotite
        - Olivine
        - Granular
        - Unoxidized
        - 0.52 x 0.54 cm
    b. Felsic
        - Quartz and feldspar
        - Granular
        - 0.62 x 0.78 cm

Sample # - 16ATe101C (cont.)

Basalt B – More rounded in nature, dome-like sample. Very similar to Basalt A since it has multiple xenolith inclusions within the basalt. Weight: 241.787 gm.

Convex side "Top" of dome:

1. Dense aphanitic basalt with two peridotite xenoliths.
    c. Peridotite
        - Olivine
        - Granular
        - Unoxidized
        - 0.29 x 0.37 cm
    d. Peridotite
        - Olivine
        - Granular
        - Unoxidized
        - 0.27 x 0.23 cm

Sample # - 16ATe102A

USGS - moderately oxidized peridotite xenolith

Analysis: Three pieces of peridotite varying in size. All three have roughly the same mineralogical make-up and be all are in the same degree of weathering and oxidation.

Piece A – Pyramidal piece. Approximately 3.13 cm x 4.28 cm x 3.0 cm. Weight: 73.073 gm.

Largest of the three pieces:

- Peridotite
- Olivine and pyroxene
- Granular
- Oxidized

Second largest piece:

- Peridotite
- Olivine and pyroxene
- Granular
- Oxidized

Sample # - 16ATe102A (cont.)

Piece B – Rectangular piece. Approximately 5.75 cm x 3.59 cm x 1.55 cm. Weight: 56.719 gm.

Second largest piece:

- Peridotite
- Olivine and pyroxene
- Granular
- Oxidized

1. Highly oxidized nodule that is along the outer margin

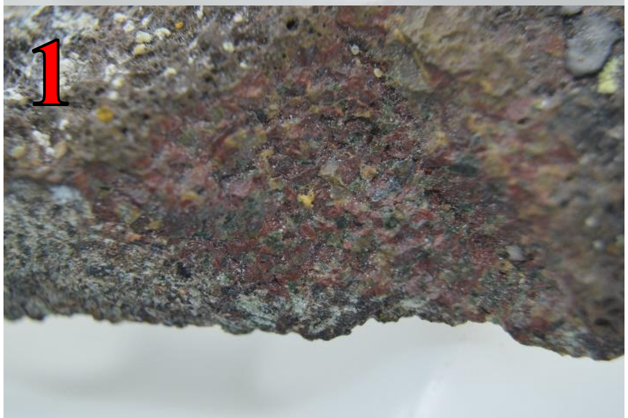

Sample # - 16ATe102A (cont.)

Piece C – Triangular piece. Approximately 1.82cm x 1.57 cm x 1.39 cm. Weight: 3.491 gm.

Smallest piece:

- Peridotite
- Olivine and pyroxene
- Granular
- Oxidized

<u>Sample # - 16ATe102C</u>

<u>USGS</u> - mostly oxidized peridotite xenolith

<u>Analysis:</u> Very dense specimen. Mostly peridotite with basalt crusting.

Sample – Approximately 4.94 cm x 2.75 cm. Weight: 68.174 gm.

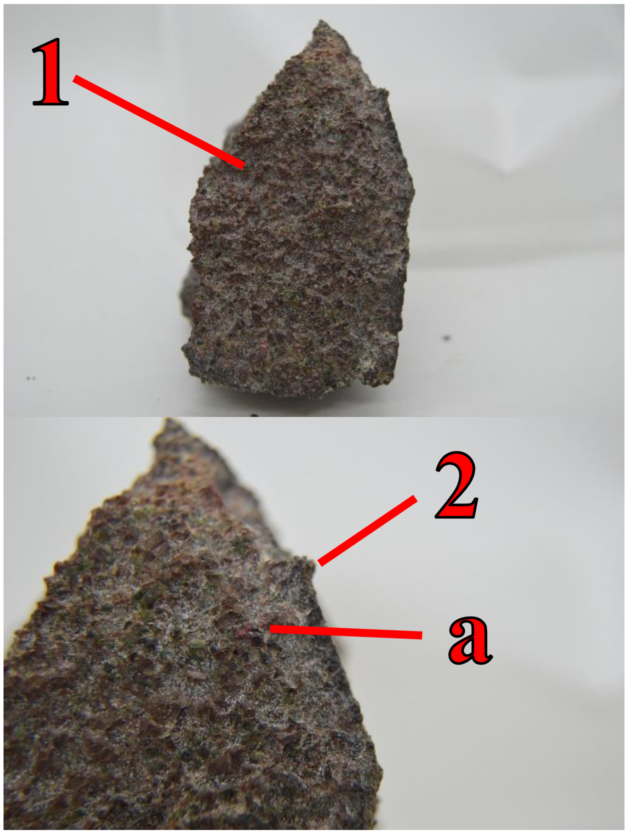

Sample:

1. Peridotite
    - Olivine and pyroxene
    - Granular texture
    - Oxidation very apparent
        a. Bright red grains, unknown
2. Aphanitic basalt along outer edge but lacking vesicular texture found in other samples

<u>Sample # - 16ATe102D</u>

<u>USGS</u> - lava with several small xenoliths (>cm and <cm), including both unoxidized peridotite, plus other potentially crustal xenolith (circled)

<u>Analysis:</u> One sample, triangular slab shaped with three cut sides and two irregular sides. Basalt lithology containing peridotite, felsic, and possibly pyroxenite inclusions.

Sample – Weight: 171.233 gm.

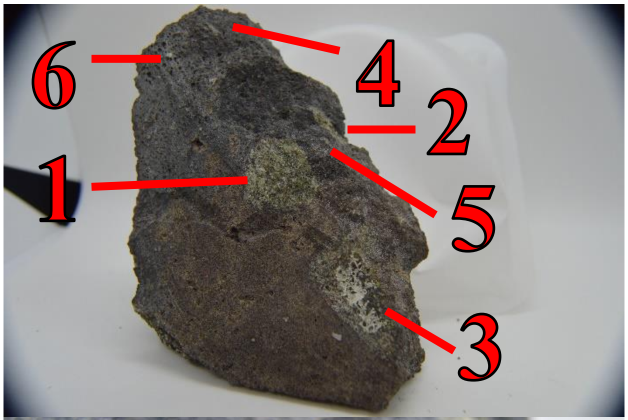

Front:

1. Peridotite
    - Olivine and pyroxene
    - Granular texture
    - “Fresh”
    - 2.0 cm x 1.64 cm
2. Peridotite
    - Olivine and pyroxene
    - Granular texture
    - “Fresh”
    - 0.54 cm x 1.27 cm
3. Peridotite
    - Olivine and pyroxene
    - Granular texture, obscured by lichen
    - 2.04 cm x 2.77 cm
4. Peridotite
    - Olivine and pyroxene
    - Granular texture
    - “Fresh”
    - 0.36 cm x 0.2 cm
5. Peridotite
    - Olivine and pyroxene
    - Granular texture
    - Slight oxidation on a couple of grains
    - 0.15 cm x 0.3 cm
6. Felsic
    - Quartz
    - Granular texture
    - 0.16 cm x 0.16 cm

Sample # - 16ATe102D (cont.)

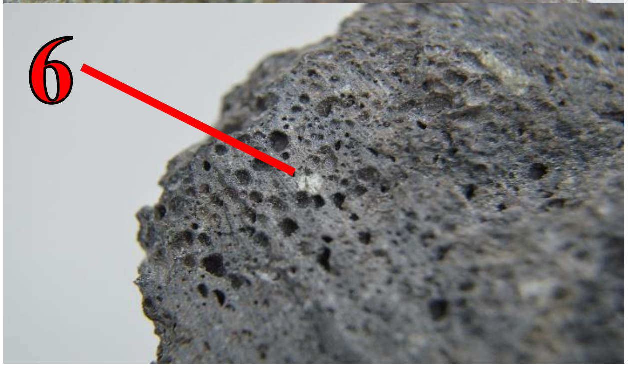

Front:

3. Peridotite
    - Olivine and pyroxene
    - Granular texture, obscured by lichen
    - 2.04 cm x 2.77 cm
4. Peridotite
    - Olivine and pyroxene
    - Granular texture
    - “Fresh”
    - 0.36 cm x 0.2 cm
5. Peridotite
    - Olivine and pyroxene
    - Granular texture
    - Slight oxidation on a couple of grains
    - 0.15 cm x 0.3 cm
6. Felsic
    - Quartz
    - Granular texture
    - 0.16 cm x 0.16 cm

Sample # - 16ATe102D (cont).

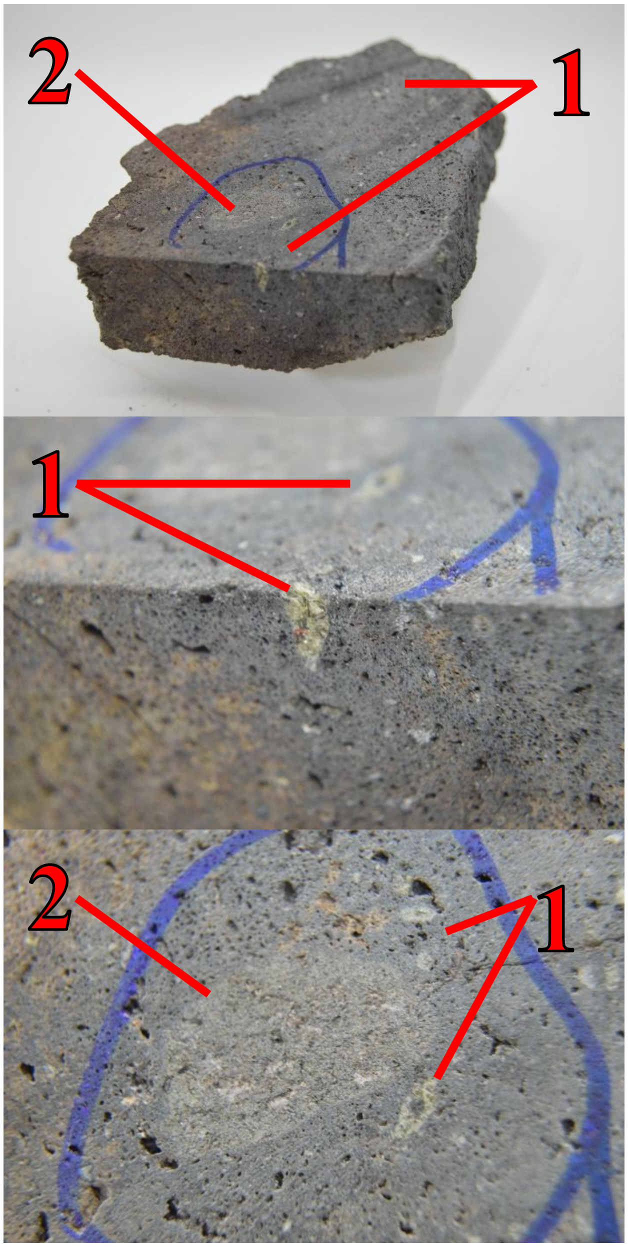

Back:

1. Five peridotite xenoliths can be observed:
    - ~0.3 cm x 0.52 cm and smaller
2. “Crustal” xenolith is identified by a circle
    - Aphanitic
    - Felsic in nature
    - 1.08 cm x 1.79 cm

Sample # - 16ATe102E1

USGA - small xenolith fragment in basalt; peridotite. The fragment has mineral segmented zone/vein of unoxidized mineral (pyx?)

Analysis: Two fragments of basalt both containing peridotite inclusions.

Fragment A – Larger of the two fragments. 4.7 cm x 2.6 cm. Weight: 24.142 gm.

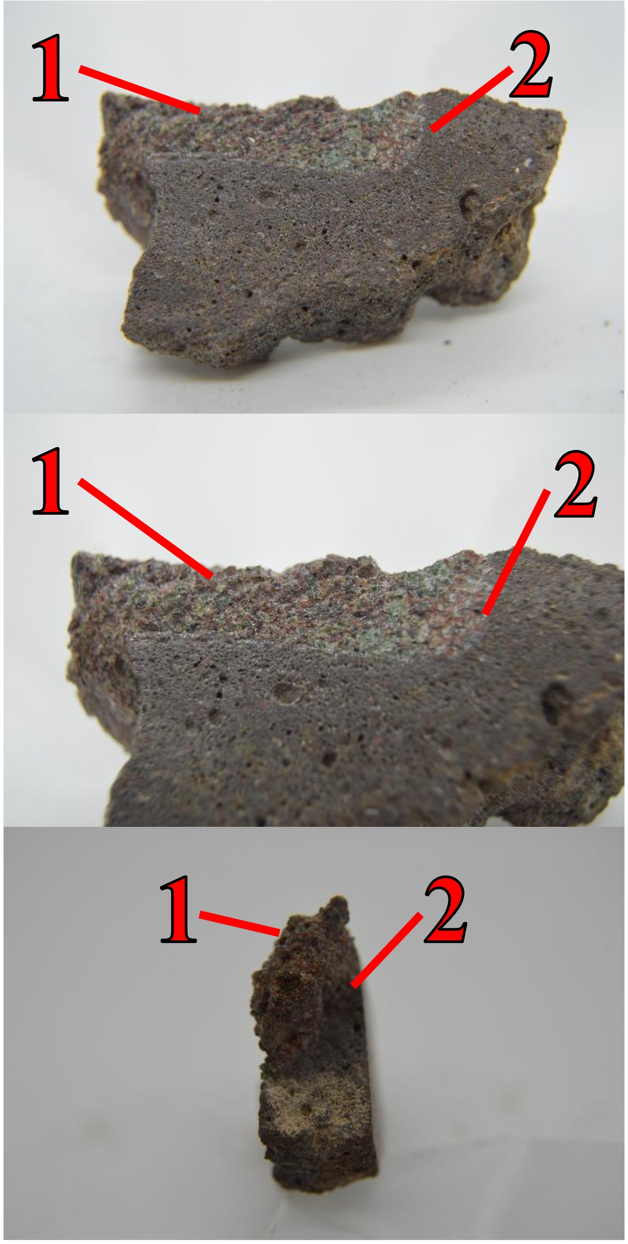

1. Peridotite
    - Olivine and pyroxene
    - Iddingsite
    - Highly granular
    - Heavy oxidation throughout
2. Boundary observed on both sides of the fragment between basalt and peridotite, shorter boundary observed on smallest side of fragment

Sample # - 16ATe102E1 (cont.)

Fragment B – Smaller of the two fragments. Weight: 6.310 gm.

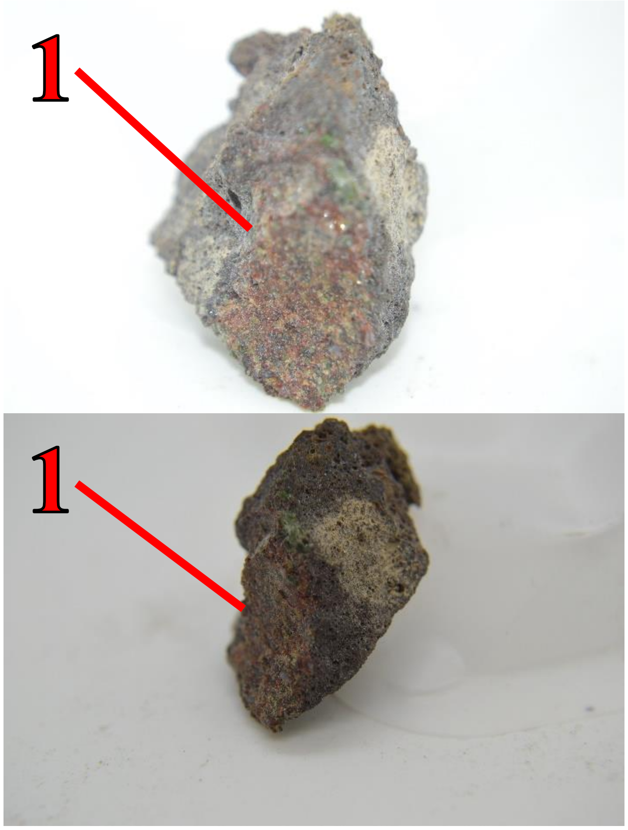

1. Peridotite
    - Olivine and pyroxene
    - Iddingsite
    - Granular
    - Highly oxidized

Sample # - 16ATe102E2

USGS - pyroxenite xenolith, 4 < cm pieces, two on margins, two homogeneous fragments.

Analysis: Four fragments in total. One appears to consist of mostly pyroxenes. Two others appear to have same pyroxene dominant xenoliths with a basaltic matrix. Remaining fragment is the largest of the set. This fragment is mostly basalt but has xenoliths of pyroxenes.

Sample – Largest piece. Weight: 29.026 gm.

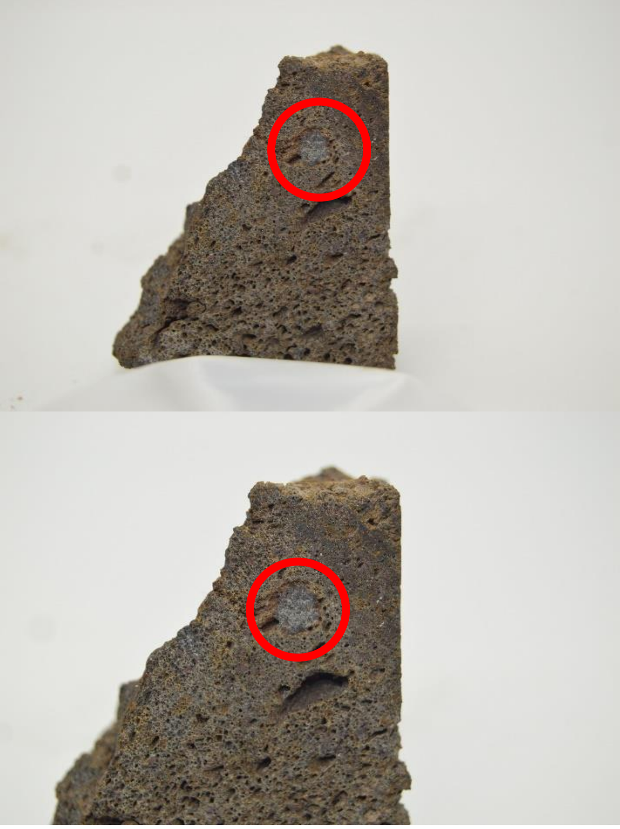

Three cut sides and three weathered
Cut side displays prominent pyroxene

- ~0.45 cm x 0.5 cm

Sample # - 16ATe102E2 (cont.)

Sample – Three remaining fragment, all smaller. Pyroxenite. Weight: 4.241 gm. (2.527 + 0.893 + 0.820)

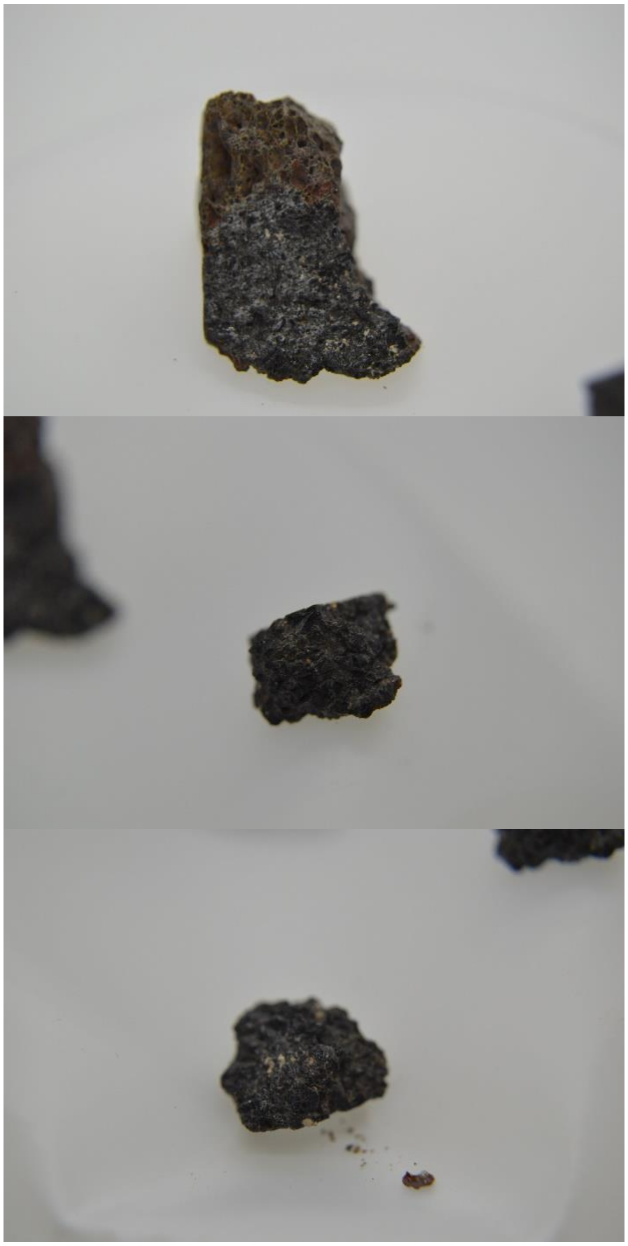

Pyroxenite fragments

- Composed of black pyroxene
- Highly granular
- Little signs of weathering

Sample # - 16ATe102F

USGS - 3 pieces of vesicular basalt from near crater rim, each within cm's of glassy margin (glassy rim preserved in 2 pieces); at least 4 peridotite xenoliths preserved in these pieces, 3 unoxidized, one smaller oxidized one.

Analysis: Three pieces of highly vesicular basalt with distinguishable xenolith. Largest being triangular, another wedge-shaped and the third a combination of wedge and triangle.

Sample 1 – Highly vesicular aphanitic basalt with felsic grains throughout and large xenolith.

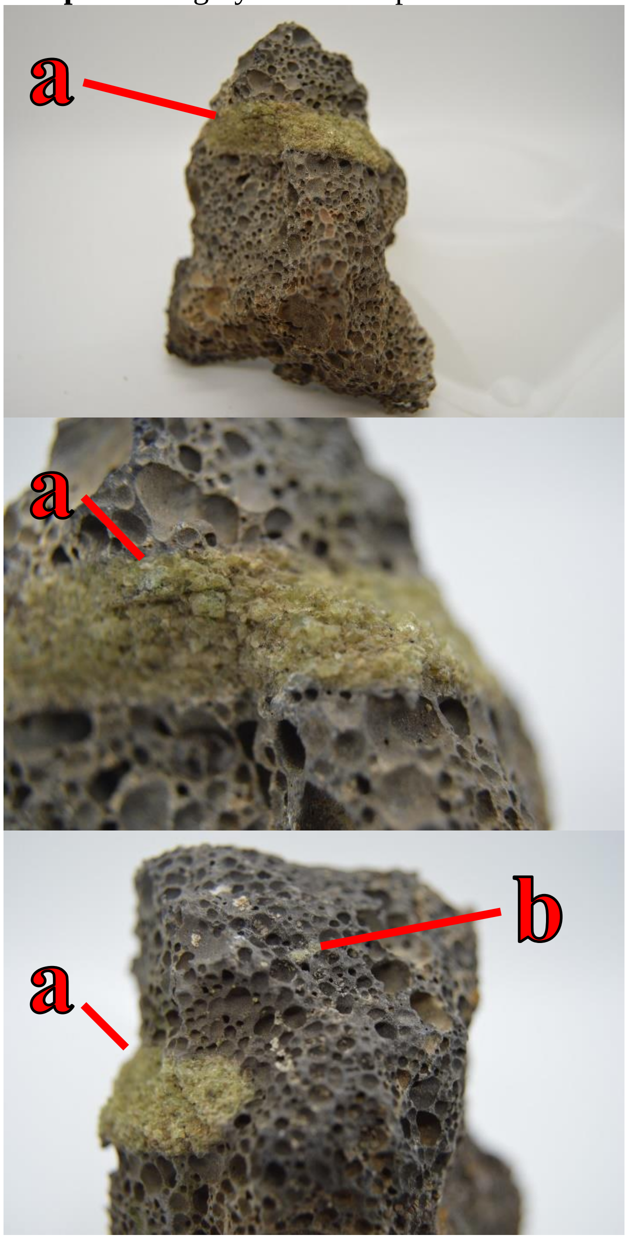

Triangular piece:
Peridotite fragments

- Composed of olivine and pyroxene
- Highly granular
- Little signs of weathering
    a. 1.35 cm x 3.94 cm
    b. 0.2 cm x 0.34 cm

Sample # - 16ATe102F (cont.)

Sample 2 – Highly vesicular basalt. Numerous felsic grains throughout. Glassy crust on the convex side of the wedge. Weight: 60.231 gm.

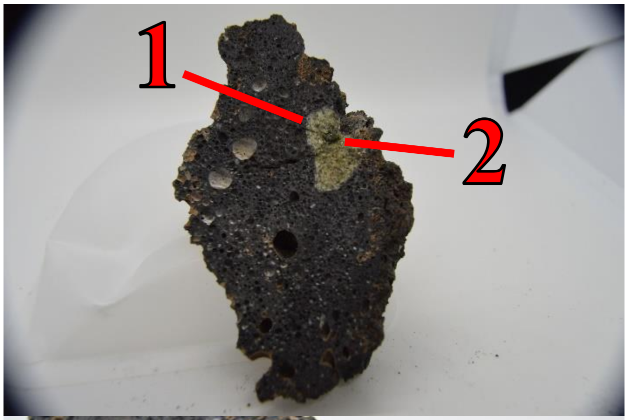

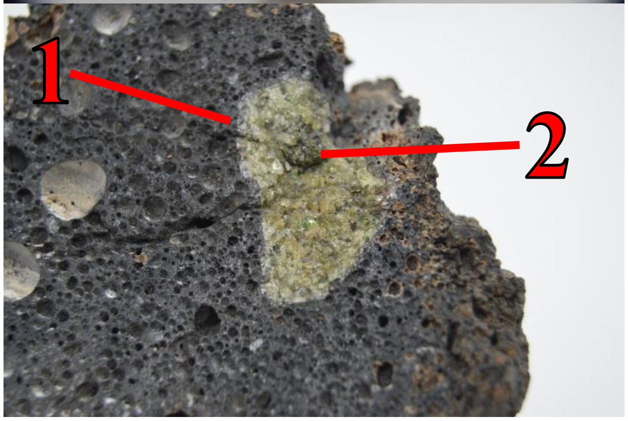

Wedge shaped piece "Top":

1. Peridotite xenolith
    - Olivine and some pyroxene
    - Granular texture
    - "Fresh"
    - 1.85 cm x 1.32 cm
2. Pyroxenite
    - Black minerals
    - Granular
    - Embedded in peridotite
    - 0.46 cm x 0.4 cm

Sample # - 16ATe102F (cont.)

Sample 2 – Highly vesicular basalt. Numerous felsic grains throughout. Glassy crust on convex side of wedge.

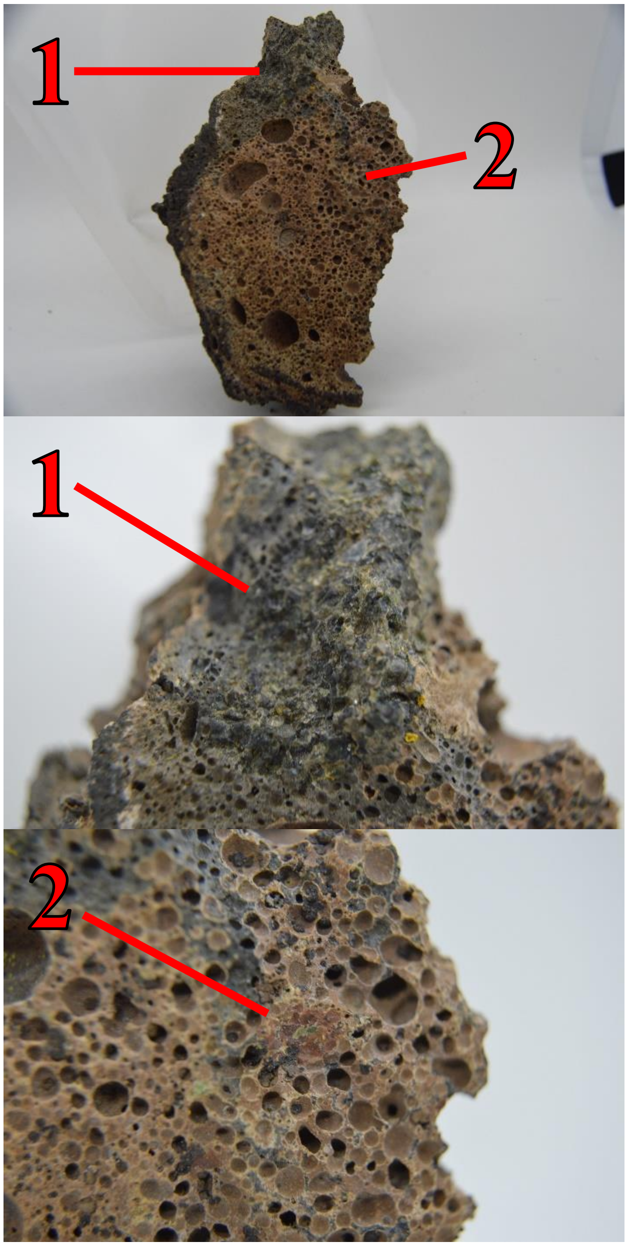

Wedge shaped piece "Bottom":

1. Peridotite
    - Olivine and pyroxene in equal shares
    - Highly granular
    - Minimal oxidation
    - 2.7 cm x 1.55 cm
2. Peridotite
    - Olivine
    - Granular
    - Highly oxidized

Sample # - 16ATe102F (cont.)

Sample 3 – Highly vesicular basalt piece with glassy/aphanitic texture on the concave portion of wedge. Felsic grains throughout. Weight: 60.938 gm.

Wedge/triangular piece:

1. Peridotite
    - Dominantly olivine and pyroxene
    - Granular
    - Highly oxidized
    - 1.48 cm x 0.93 cm

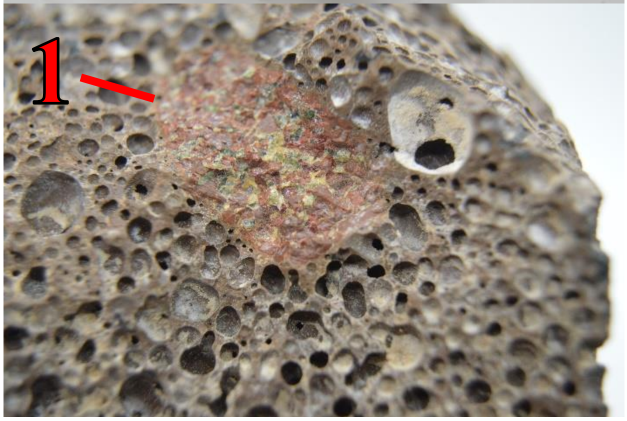

APPENDIX III:

PETROGRAPHIC THIN SECTION SCANS

This section provides the full thin section scans for each thin section in both plane- and cross-polarized light.

101A1-1

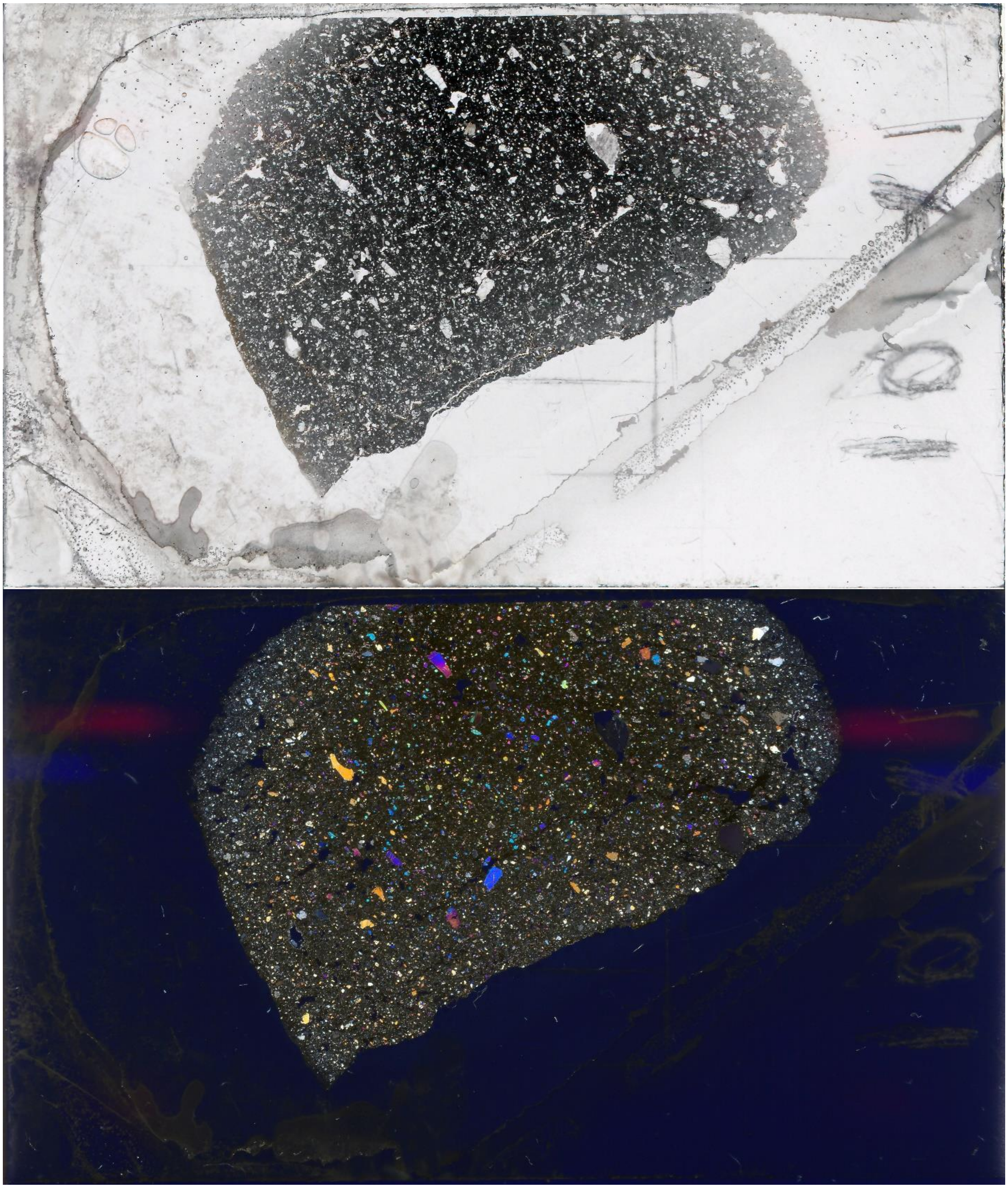

101A1-2

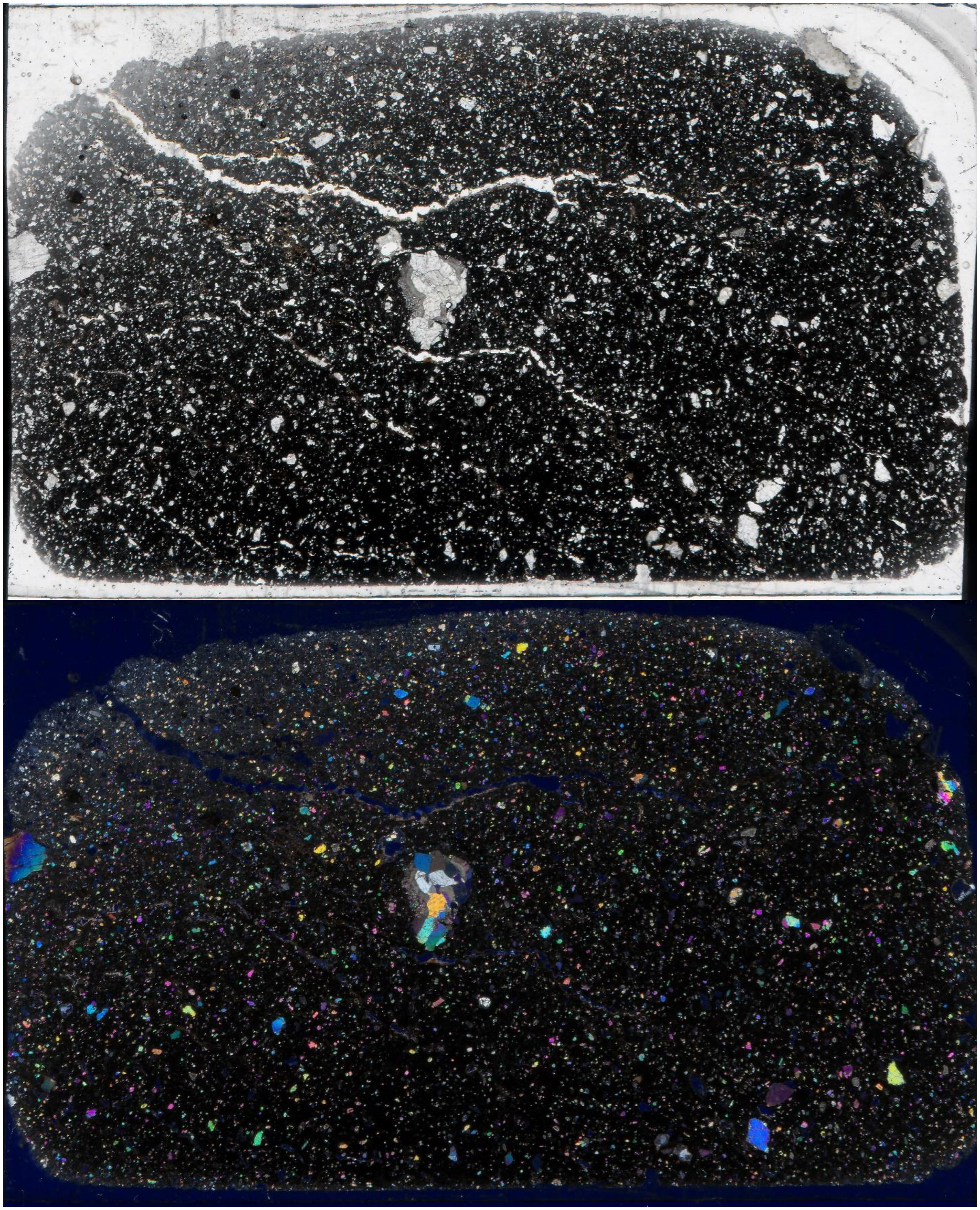

101C-1

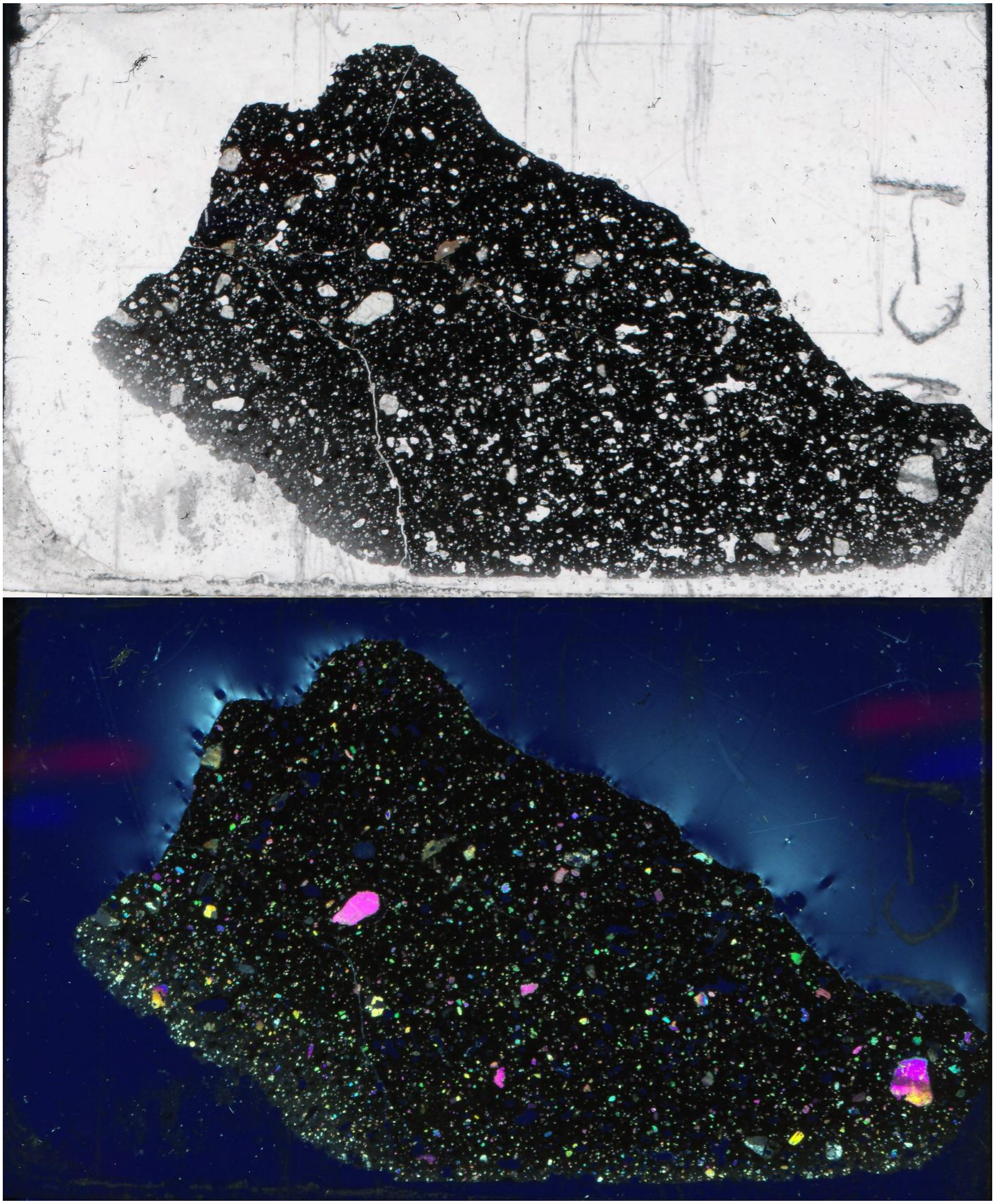

101C-2

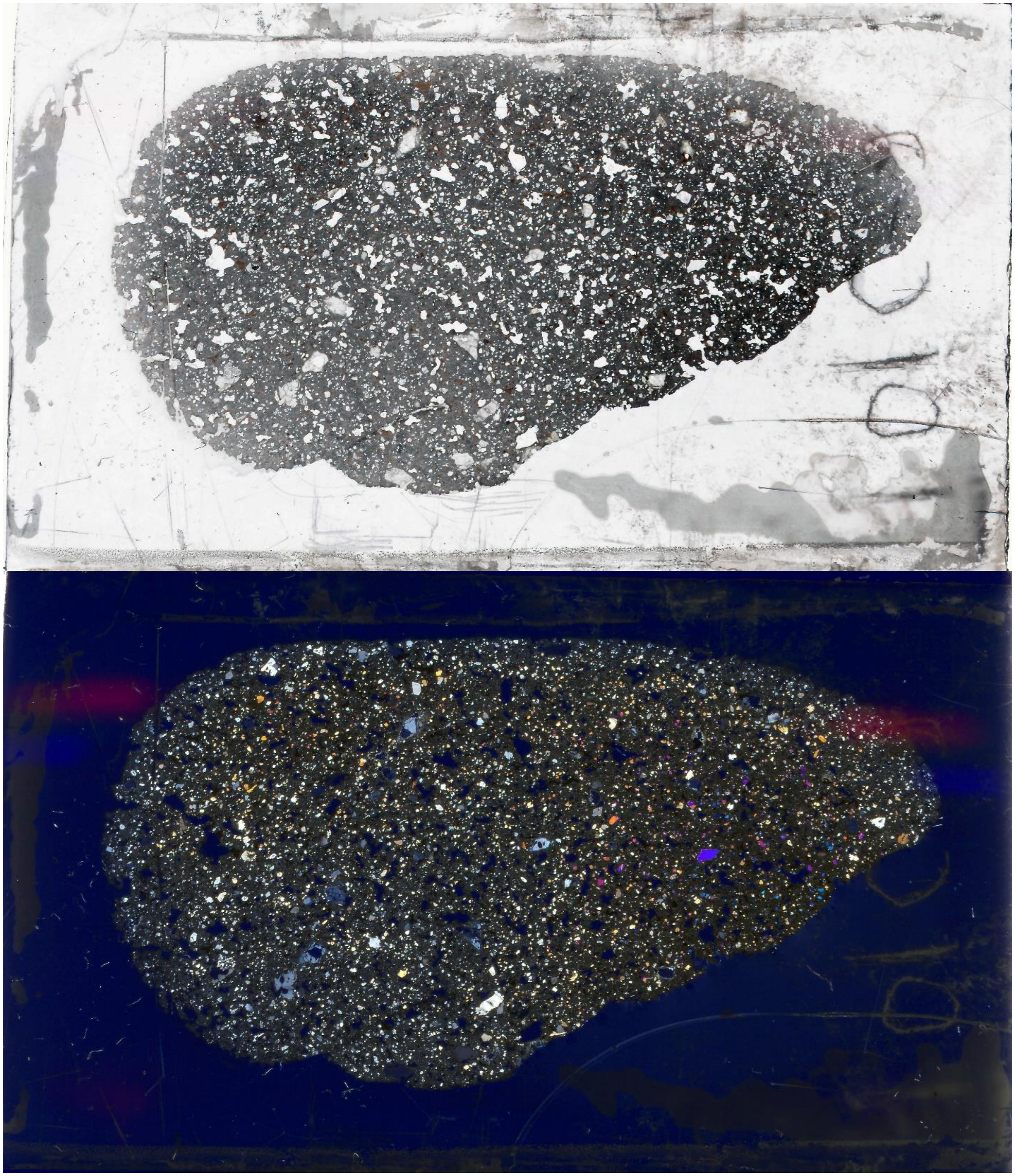

102A(A-1)

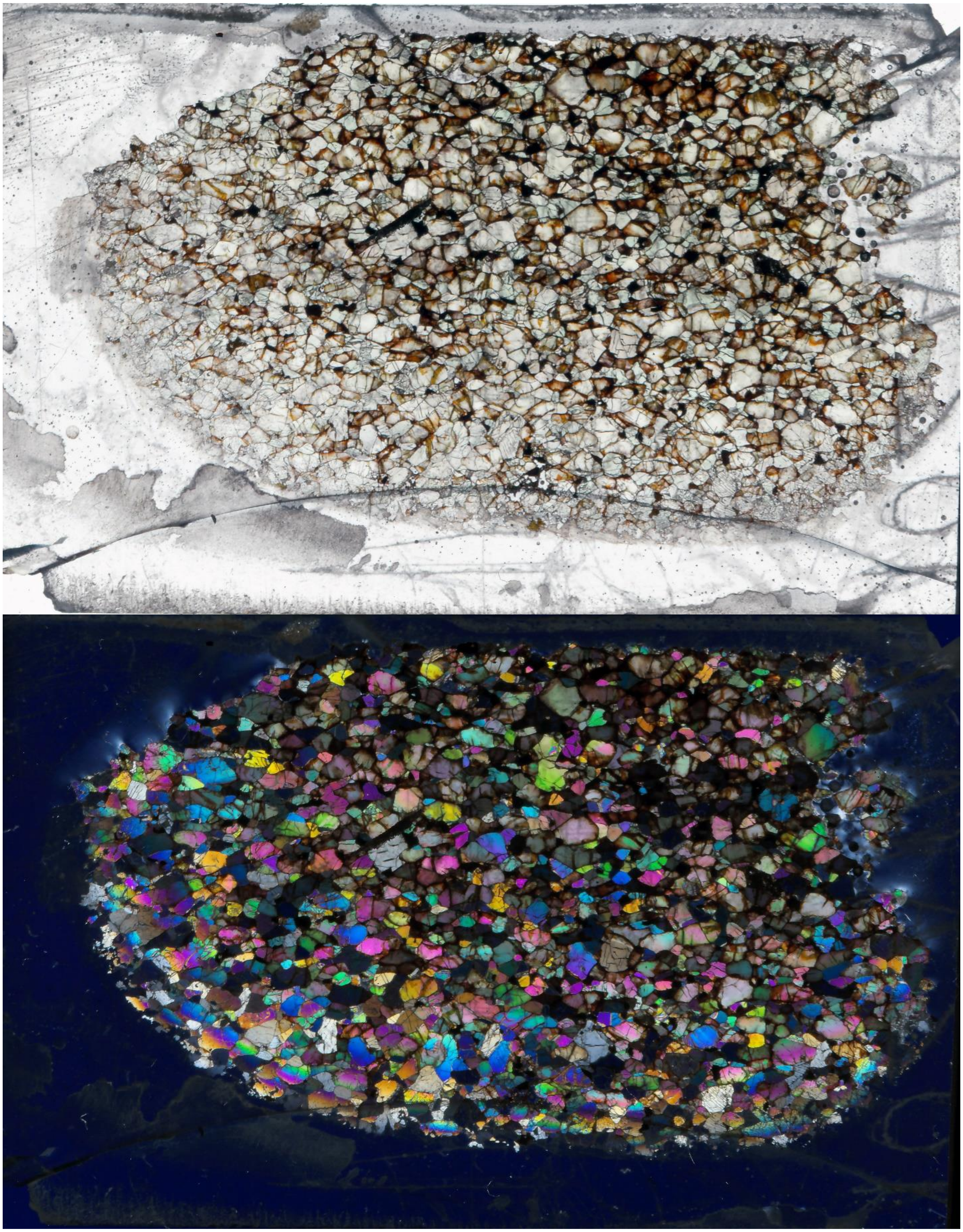

102A(A-2)

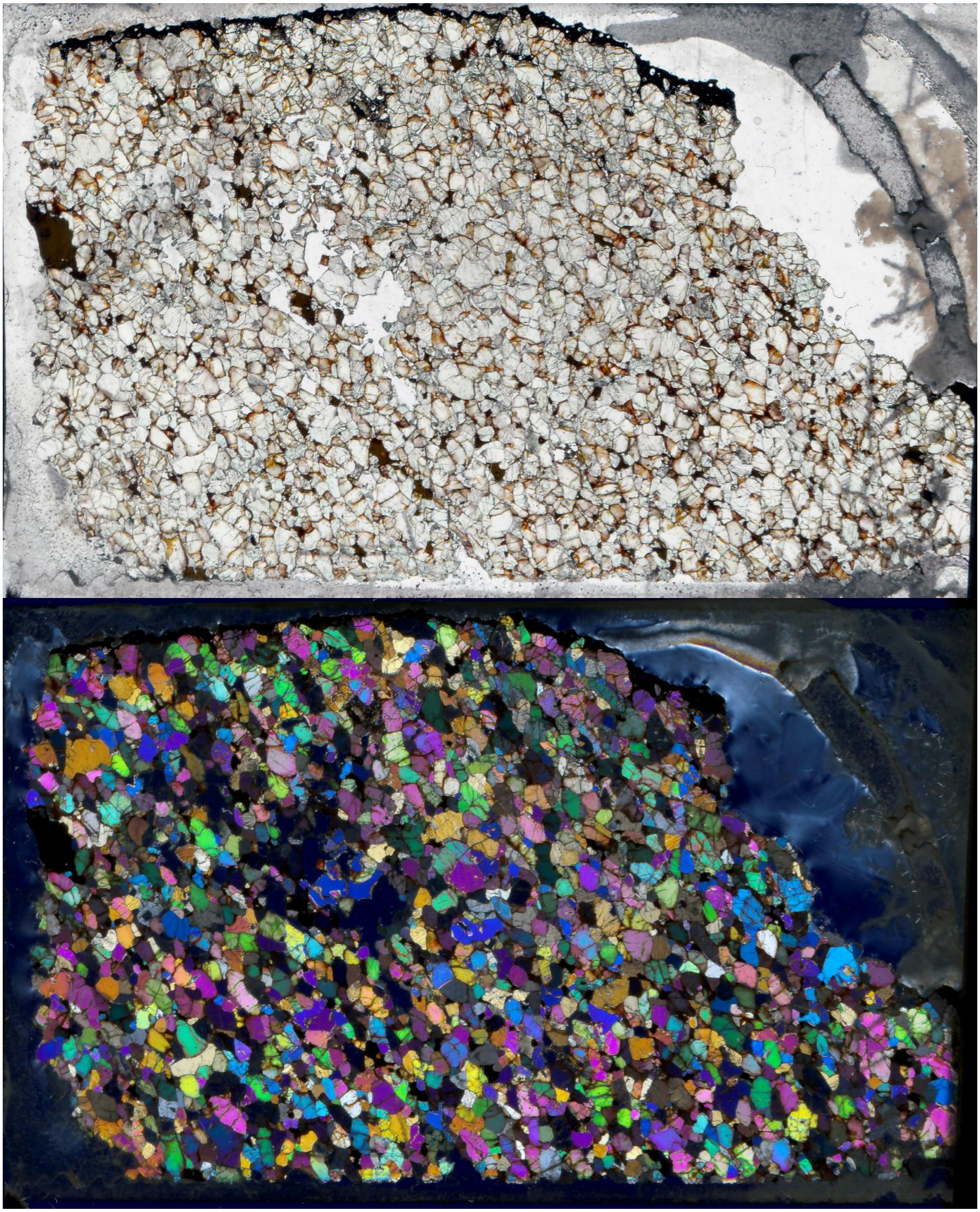

102C

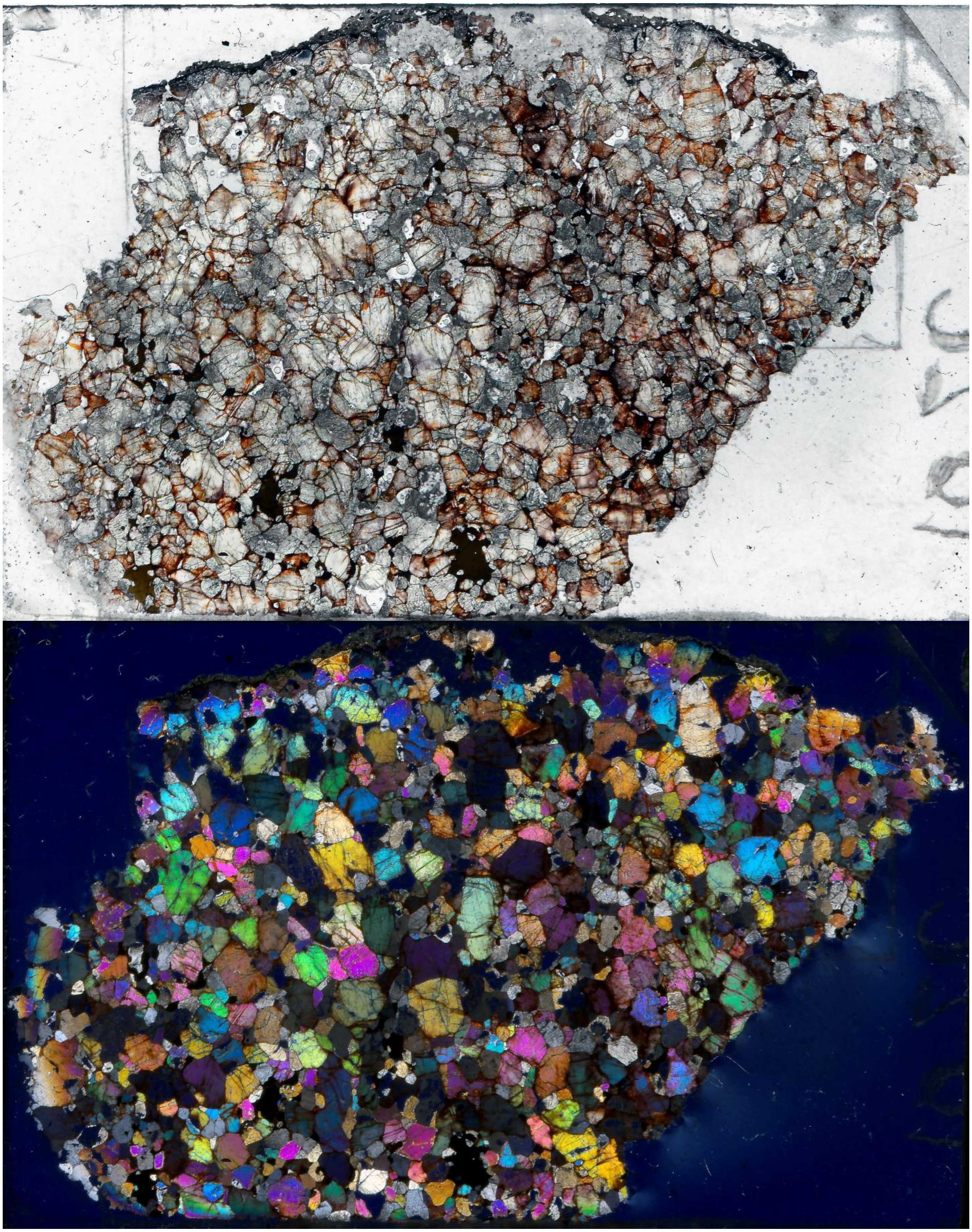

102D-1

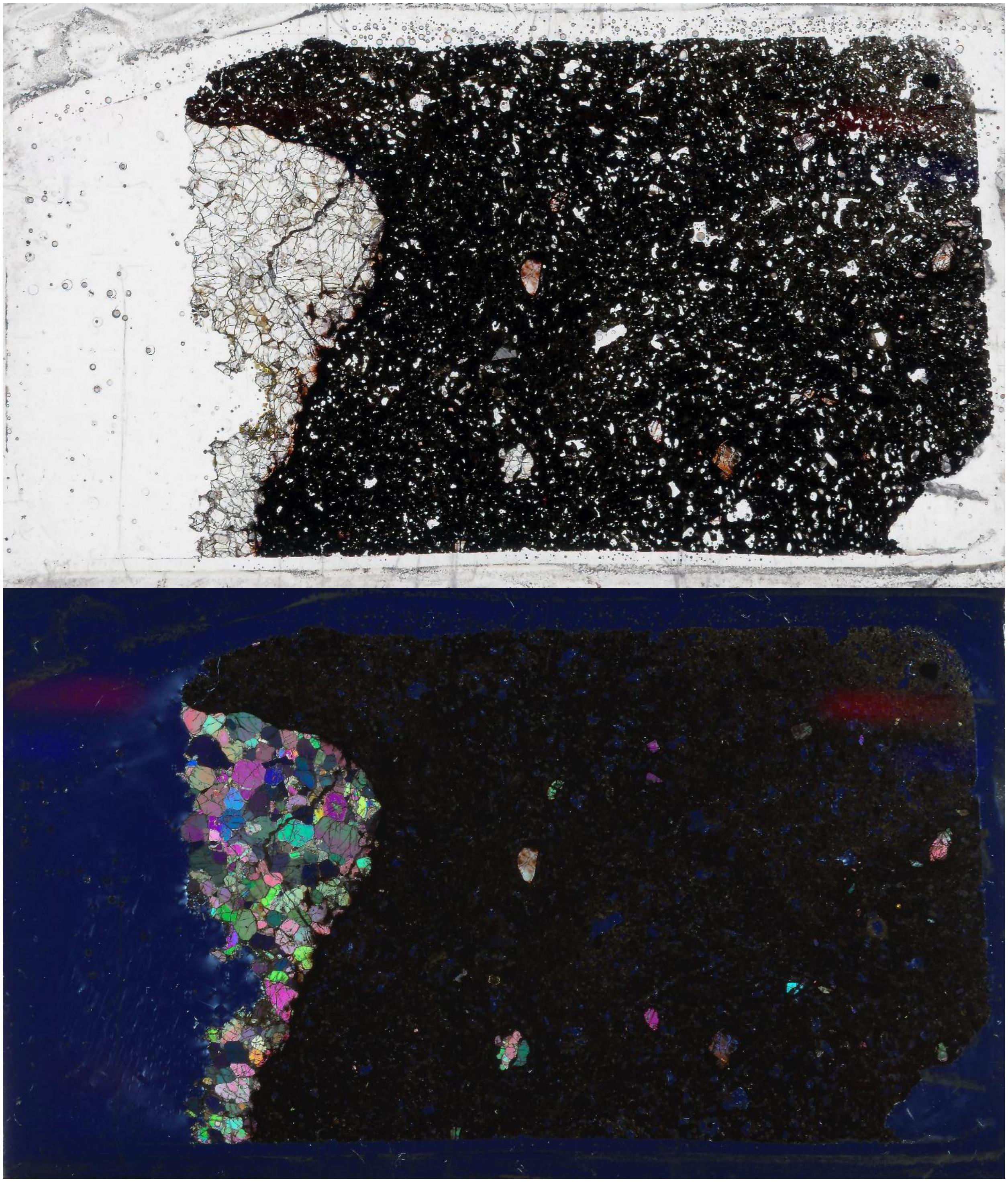

102D-2

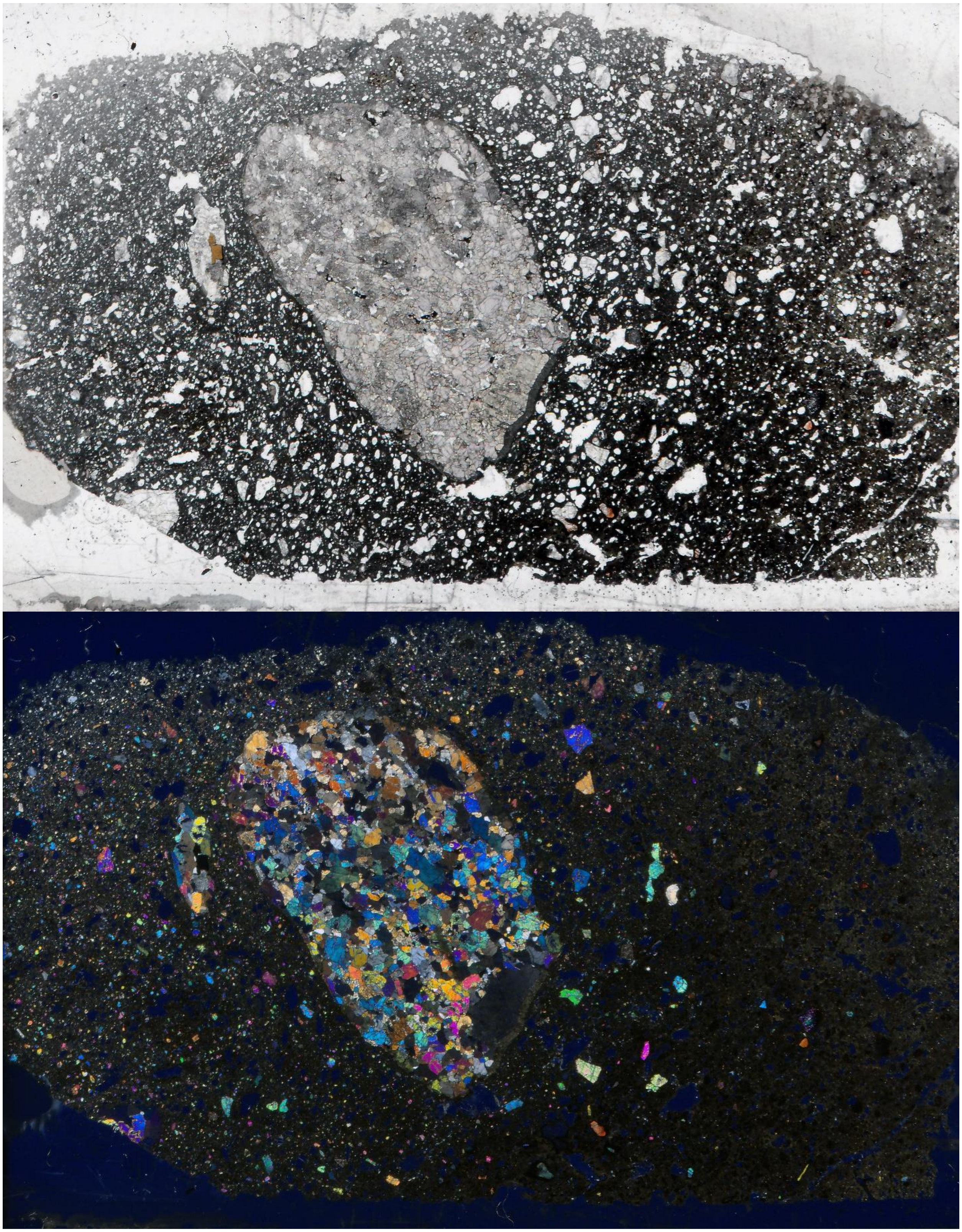

102D-3

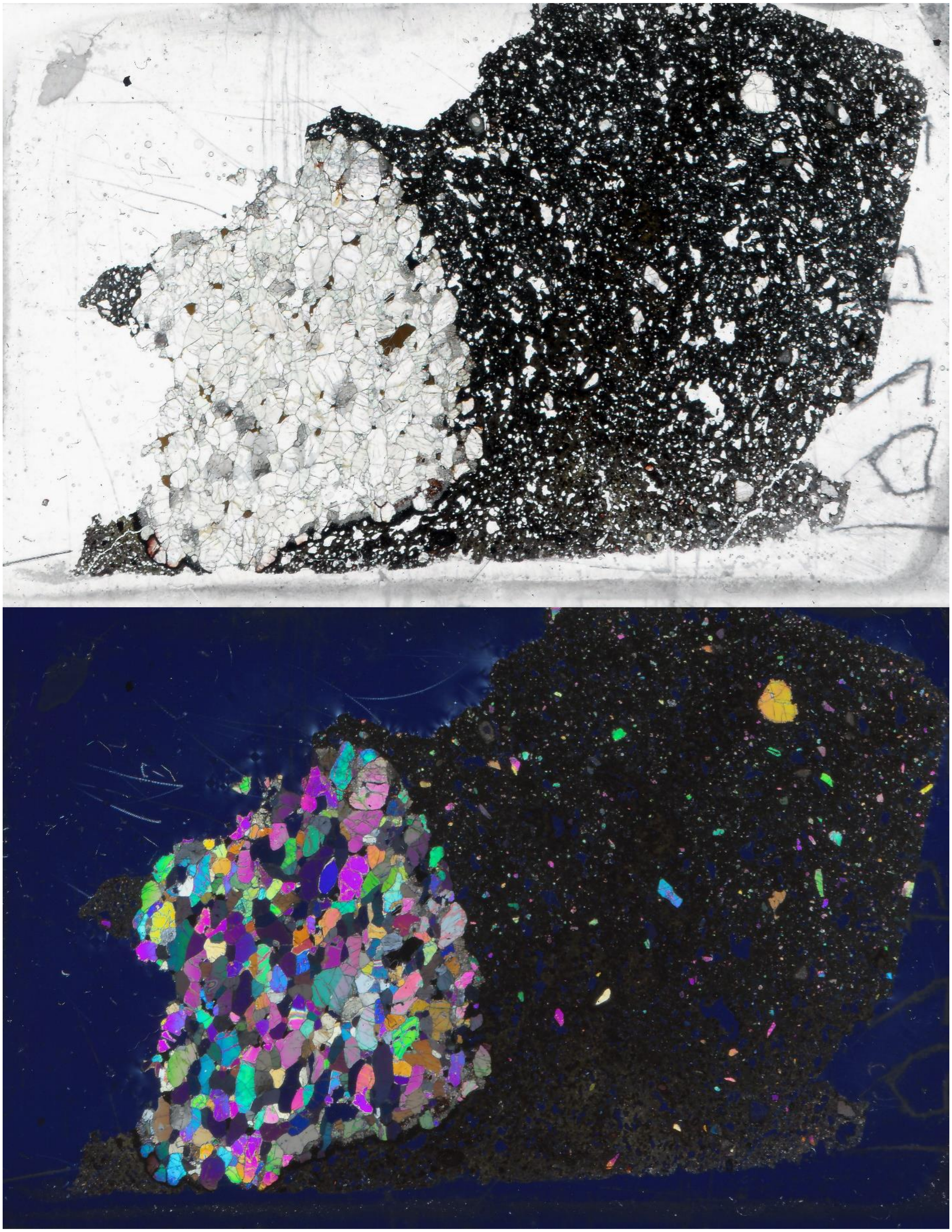

102E1(A)

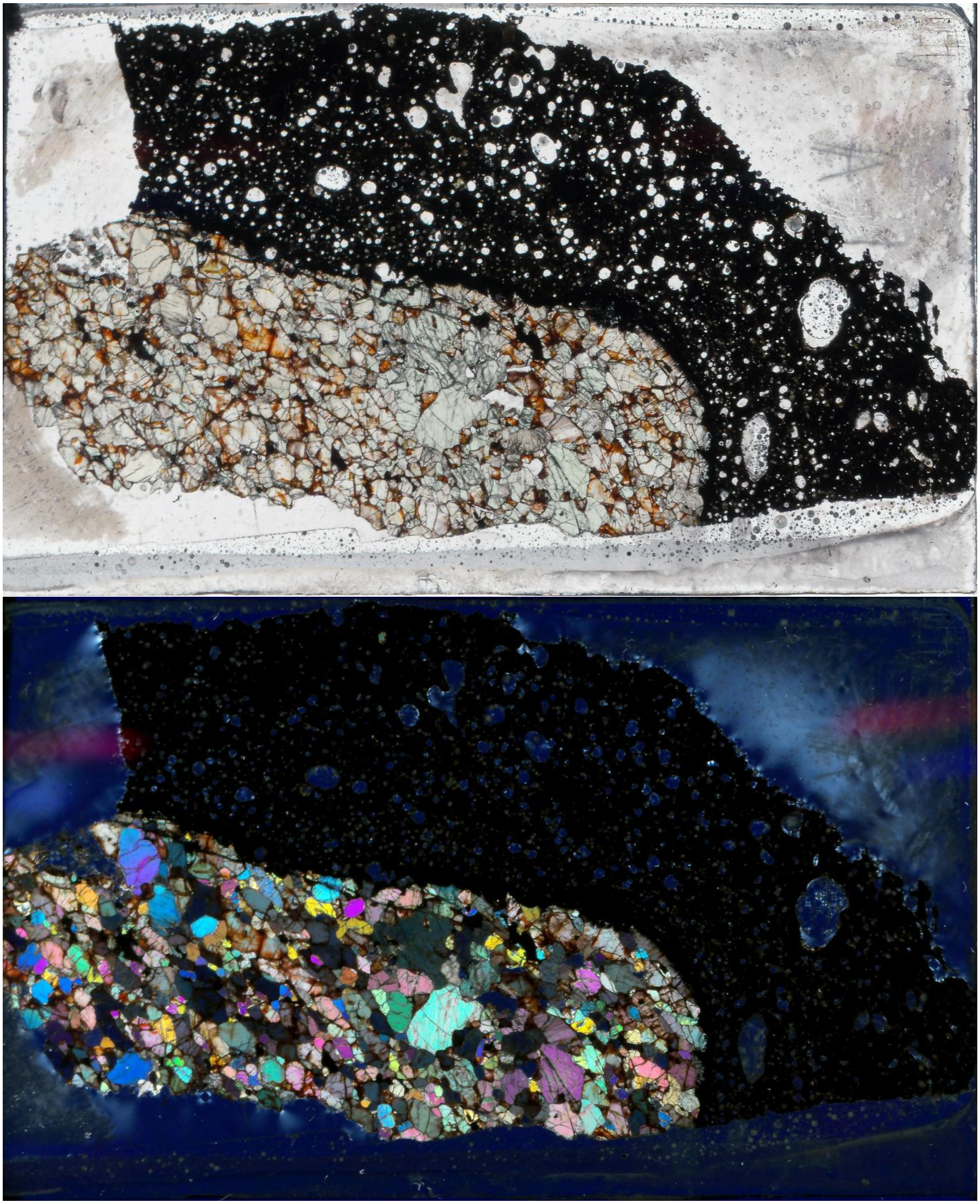

102F-1

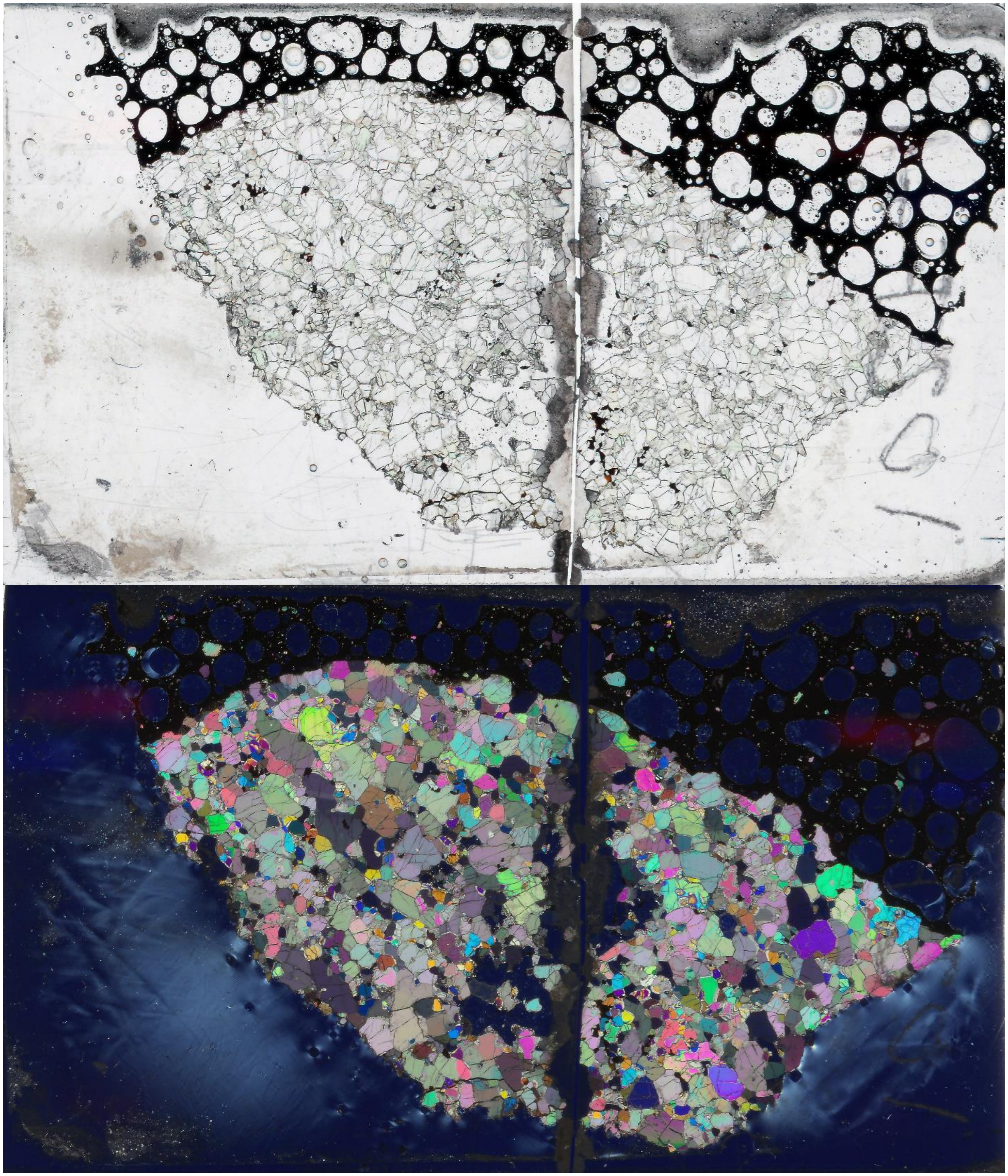

102F-2

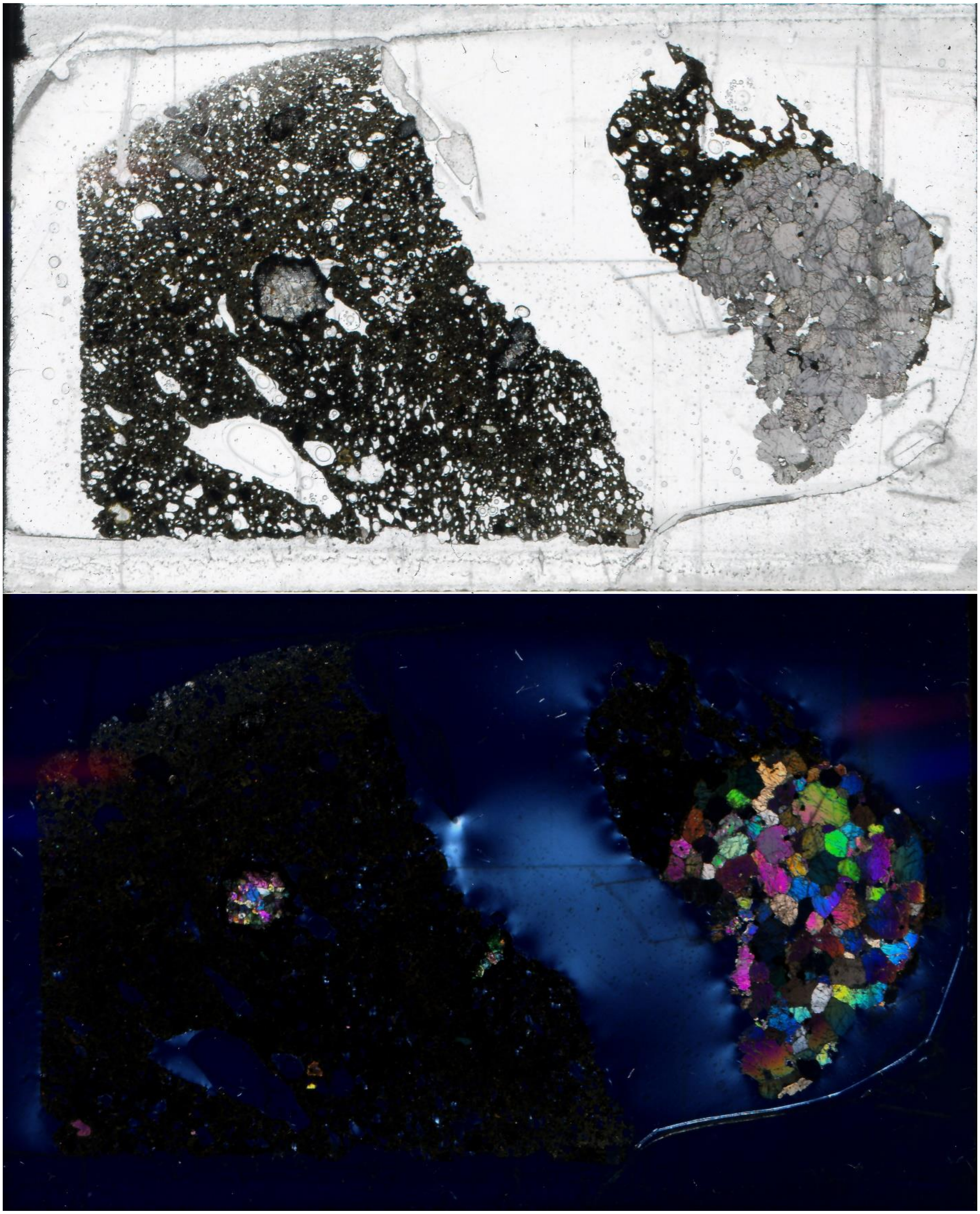

122C-1

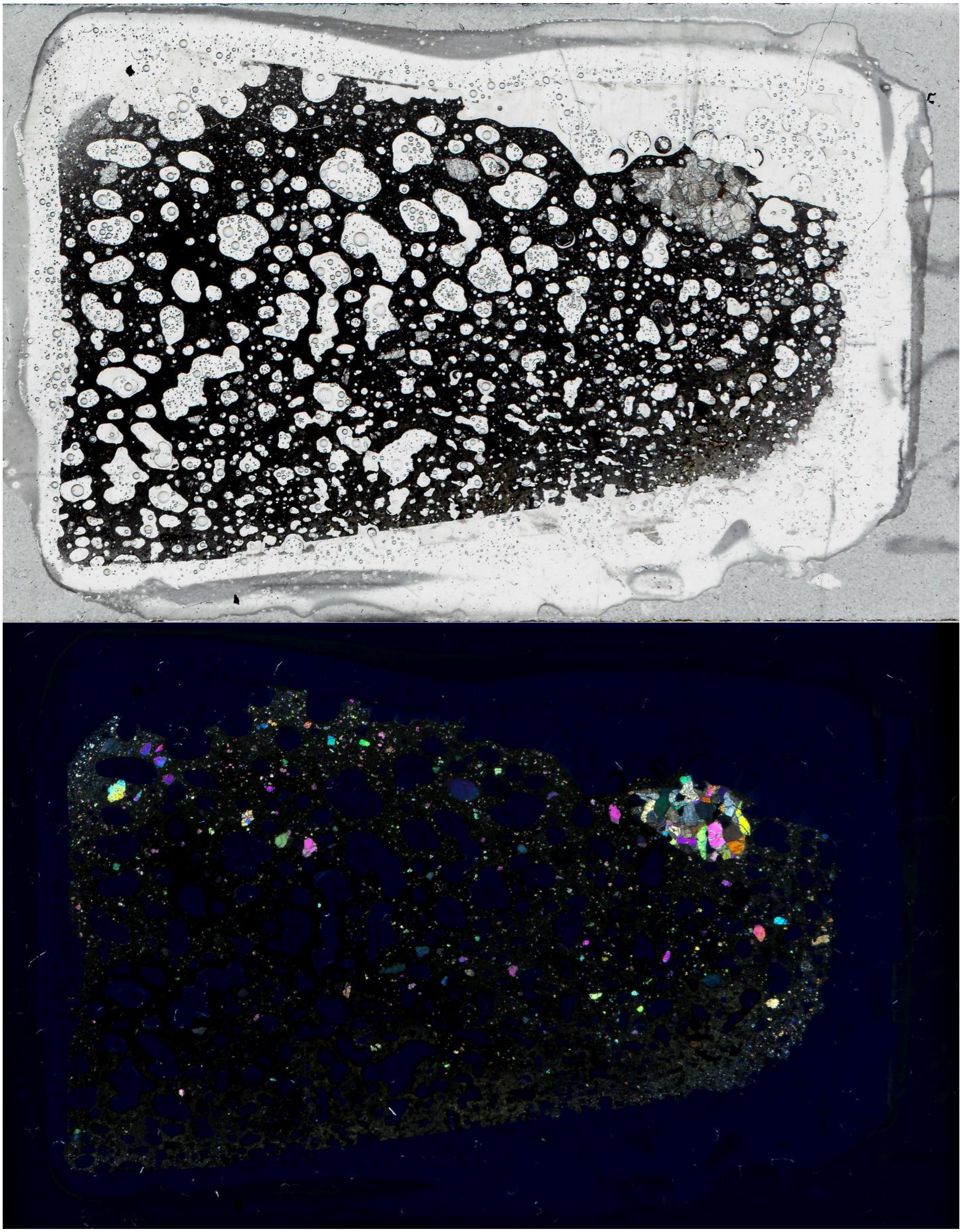

122C-2

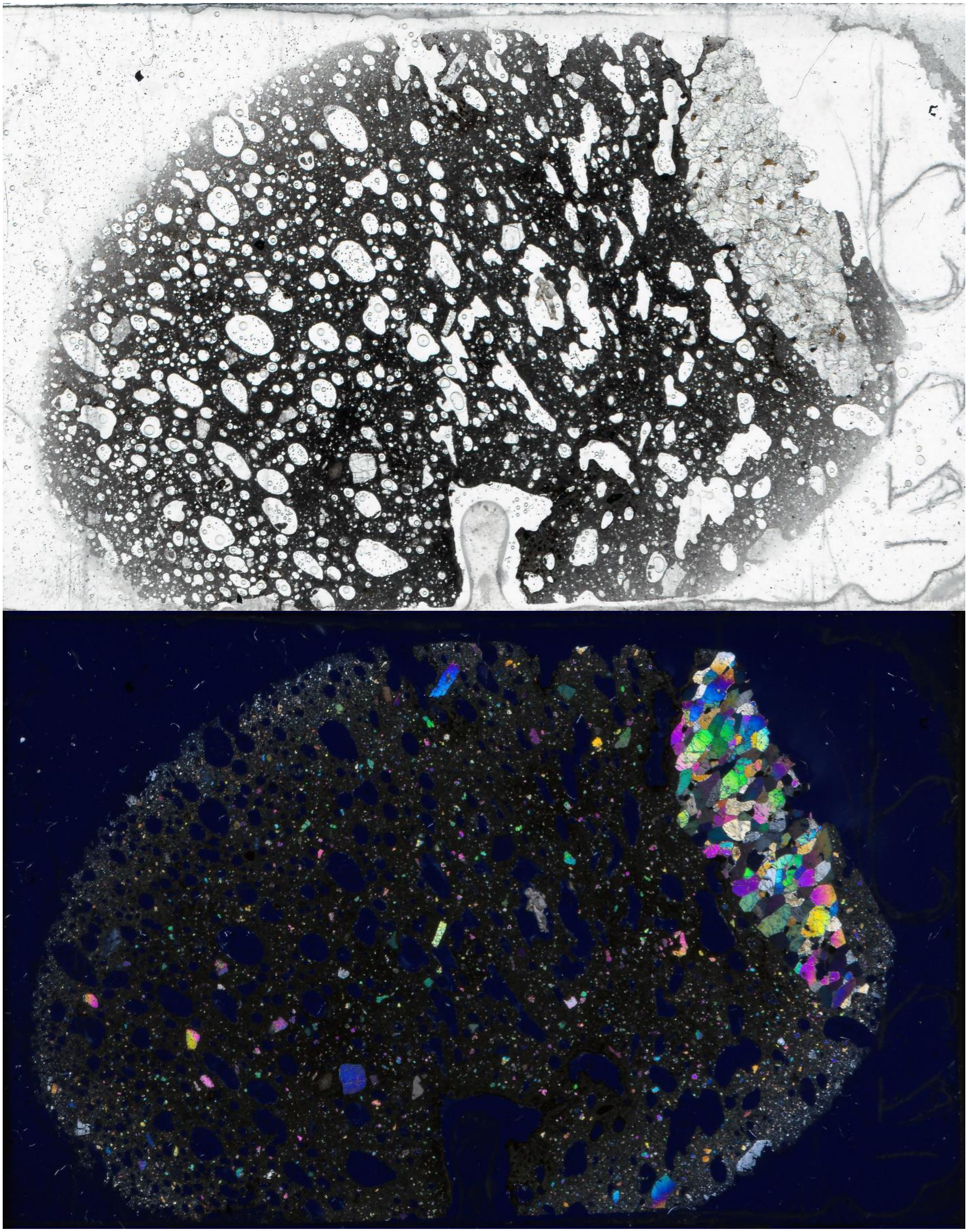

122C3-A

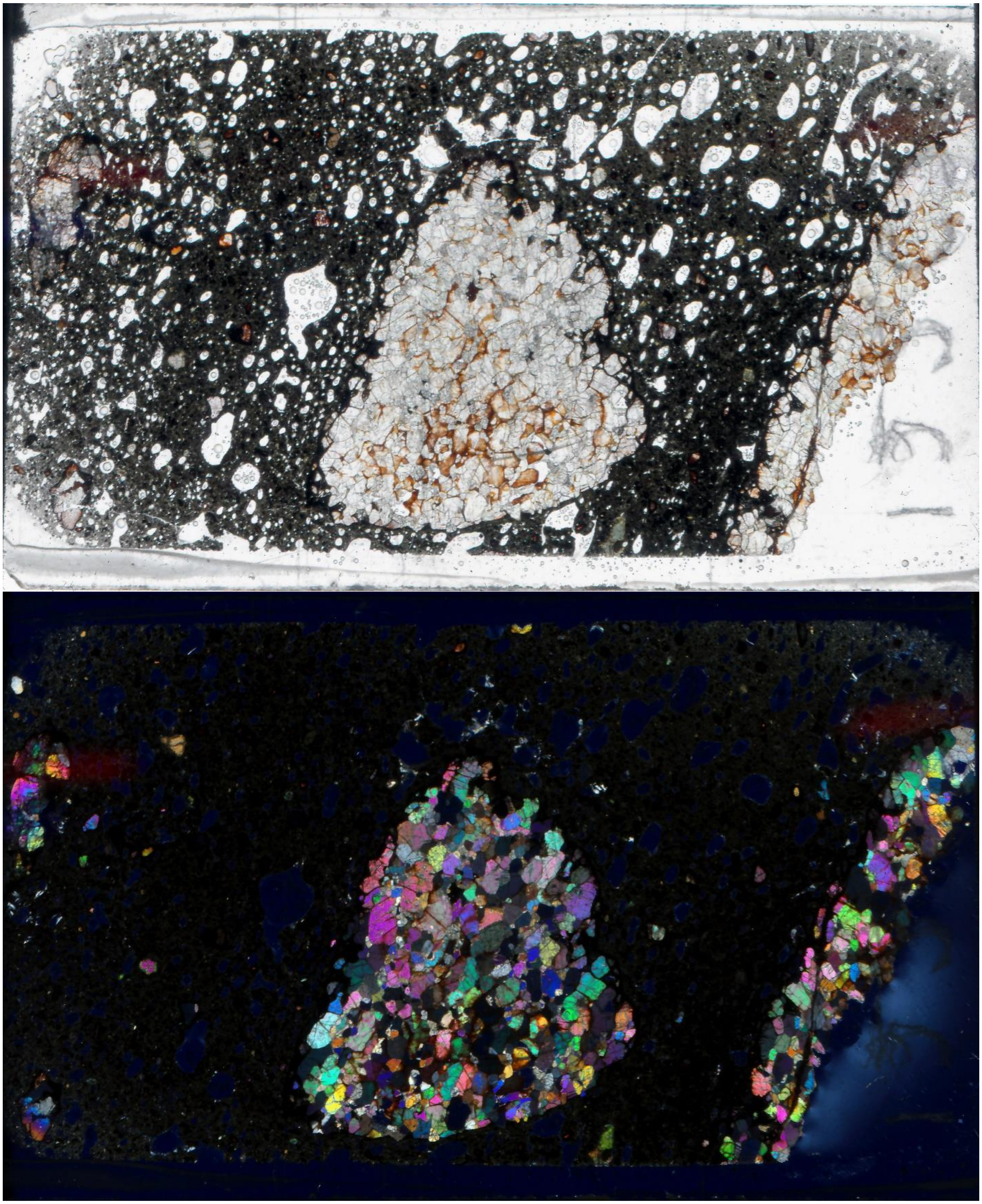

122C3-B

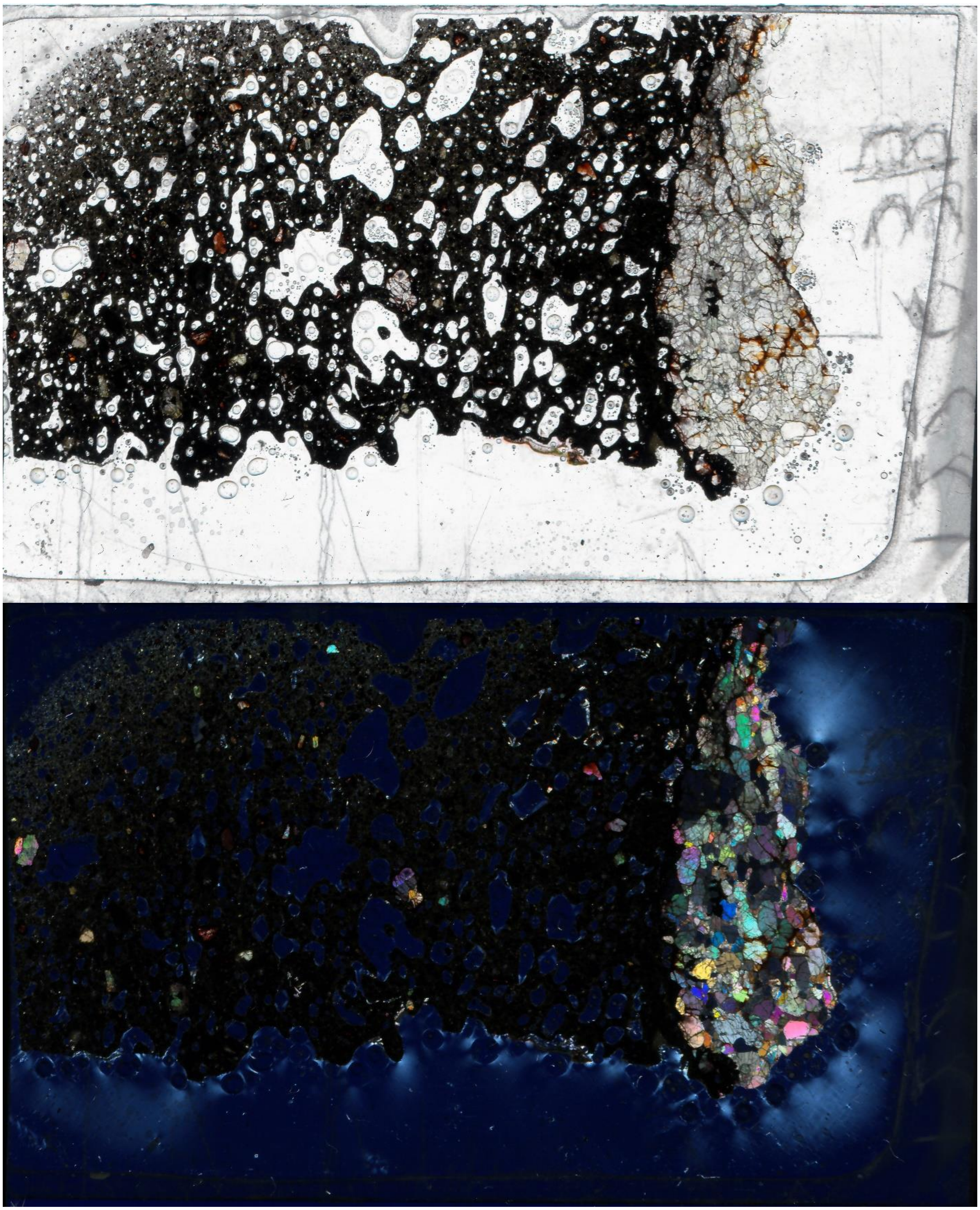

122D-1

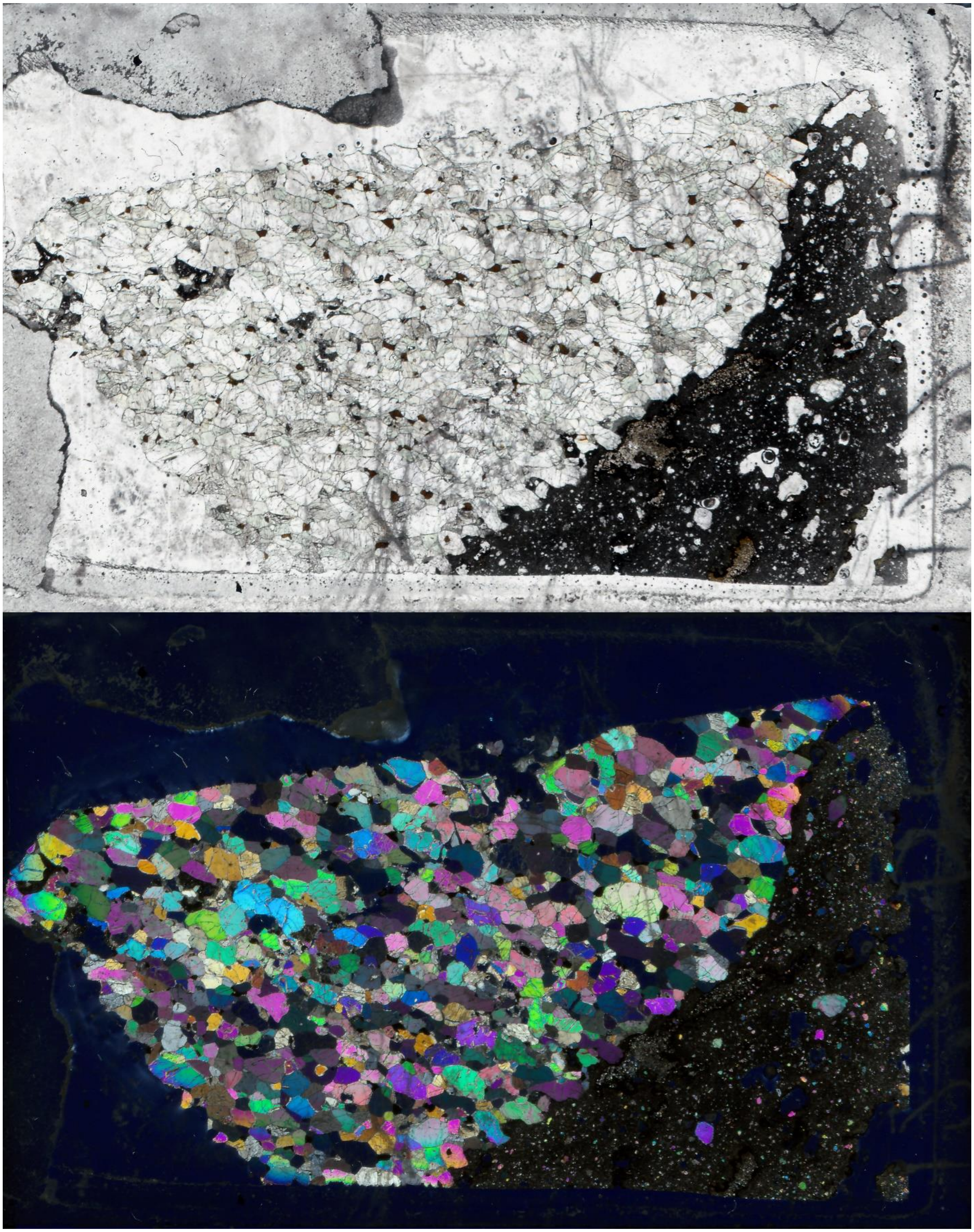

122F1

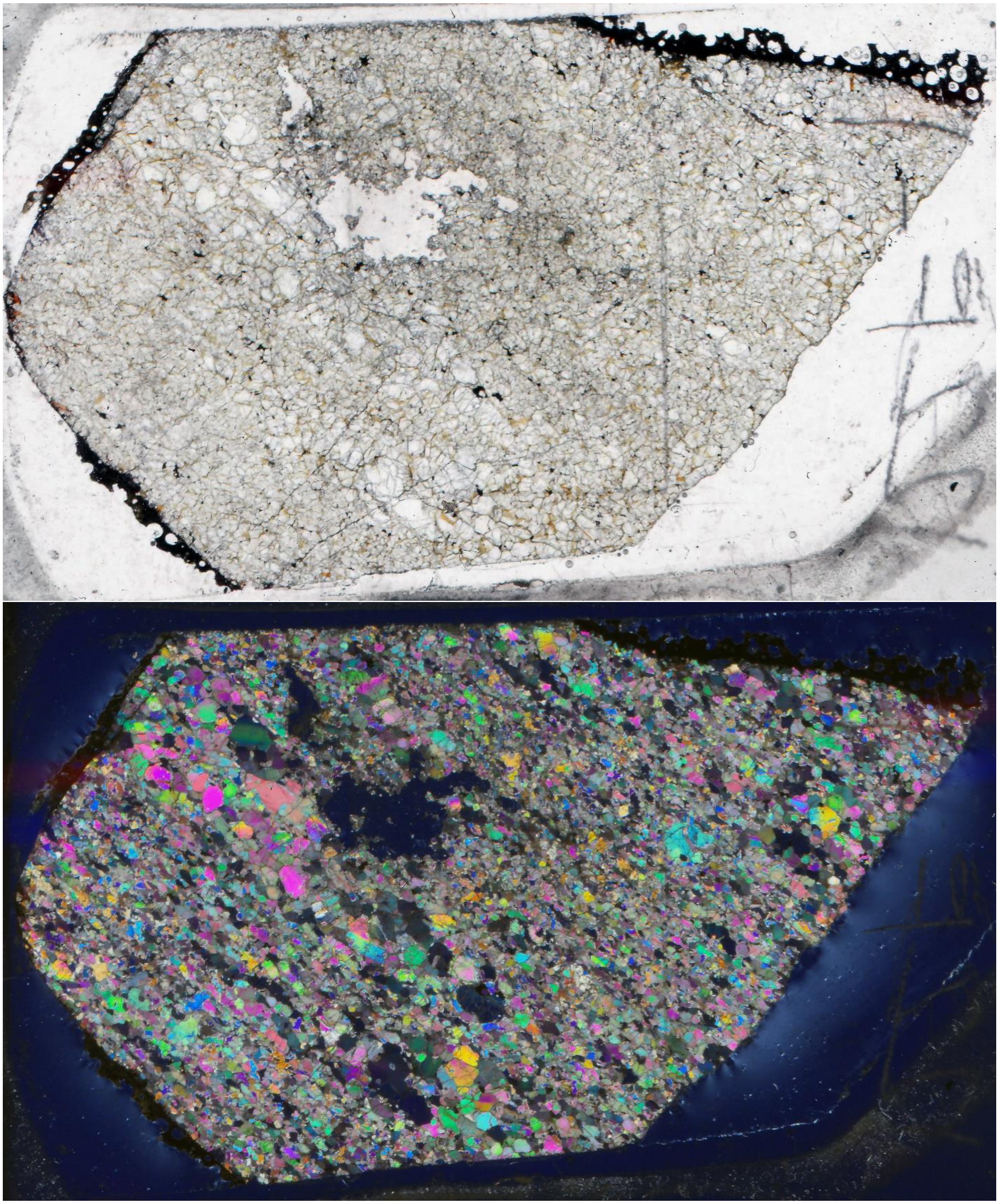

122F2(A)

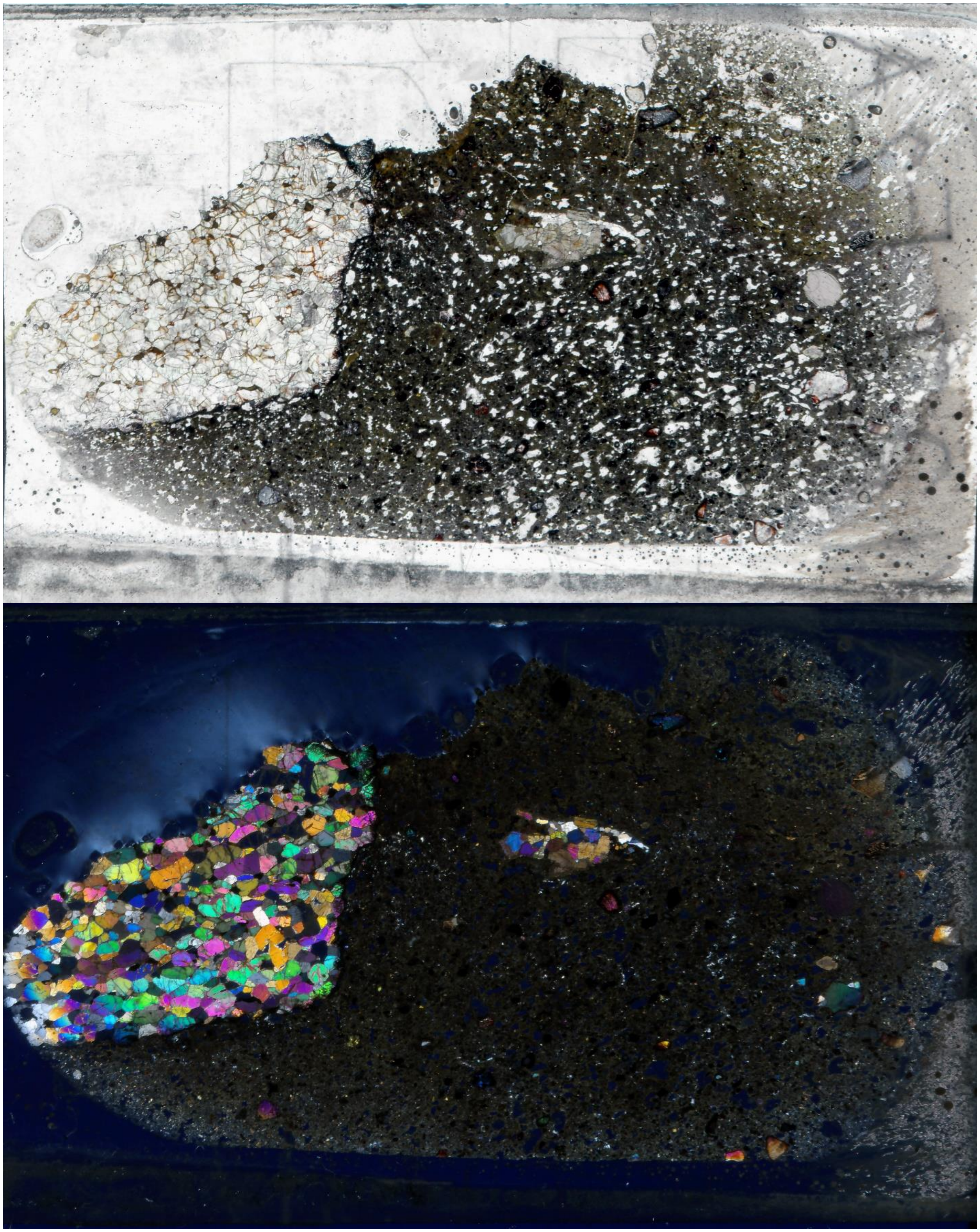

122F2(B)

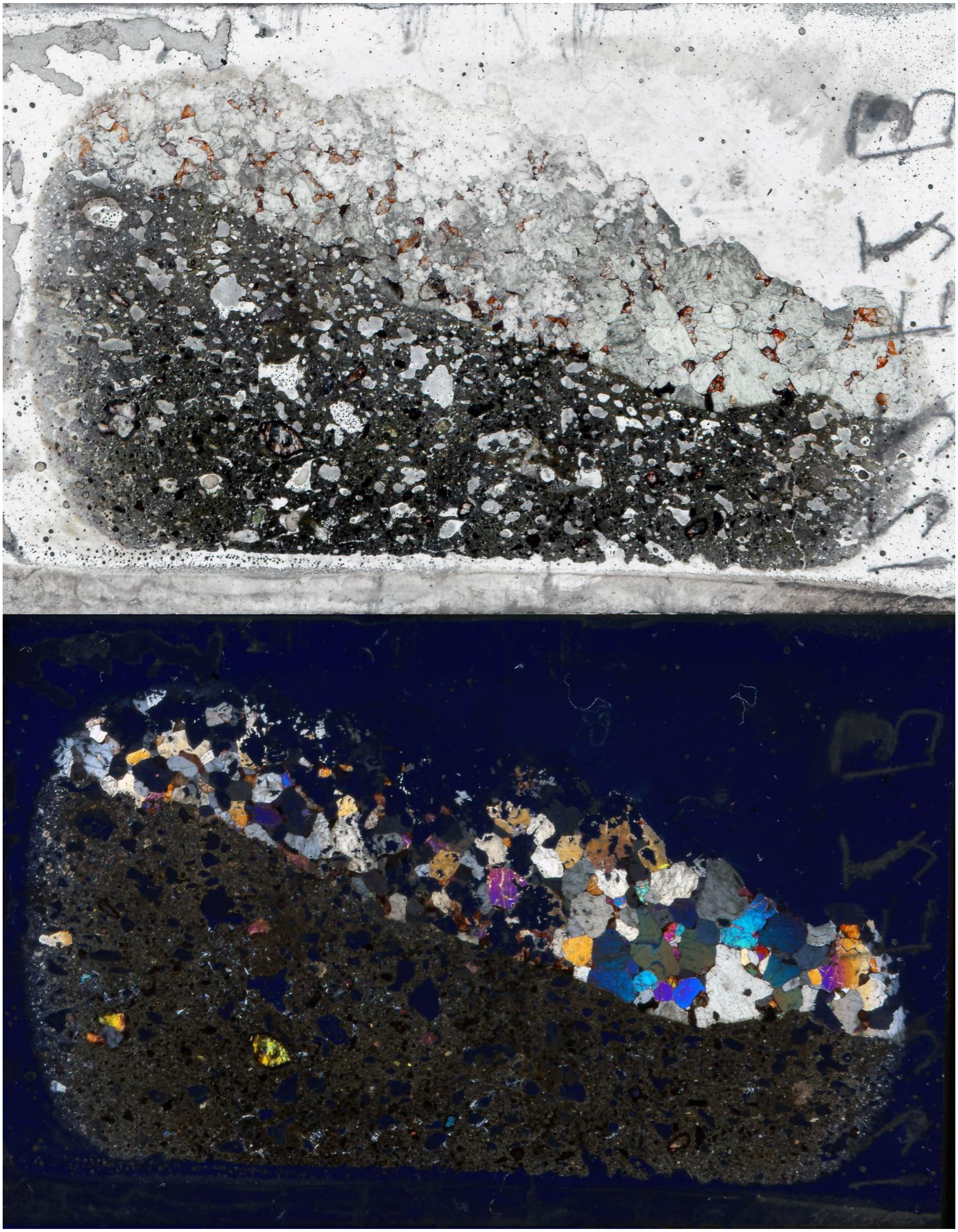

122F2

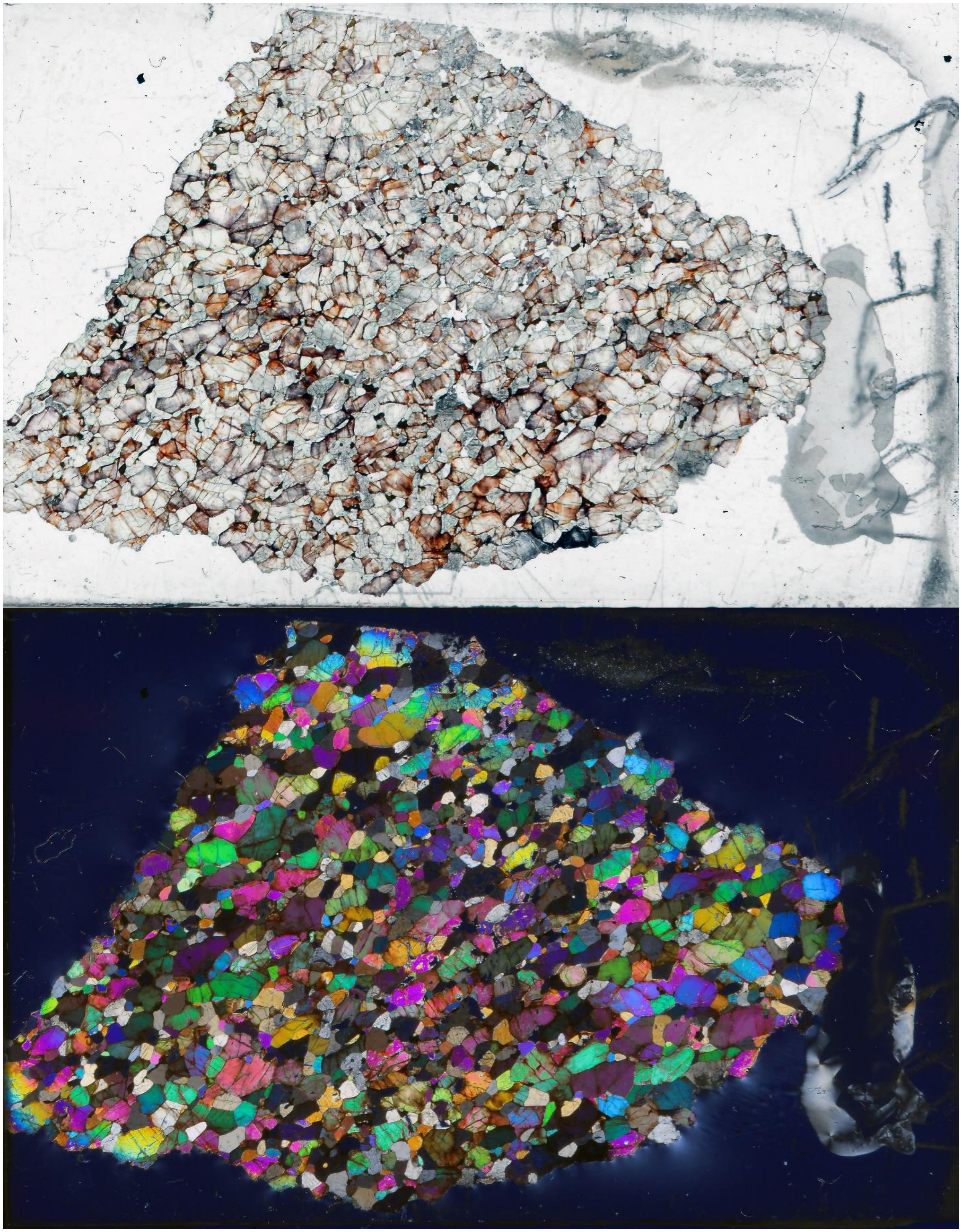

122F3-A

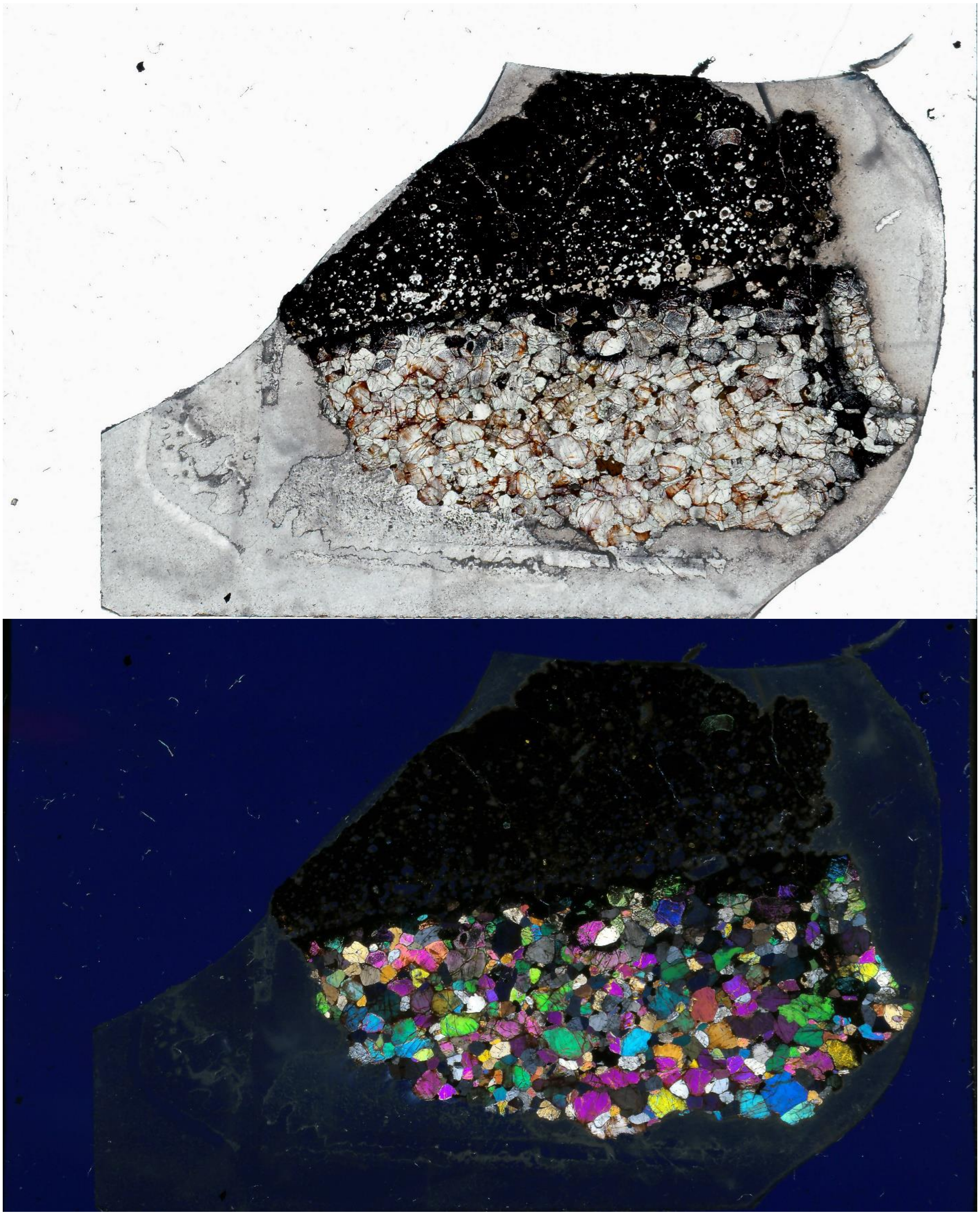

122F3-B

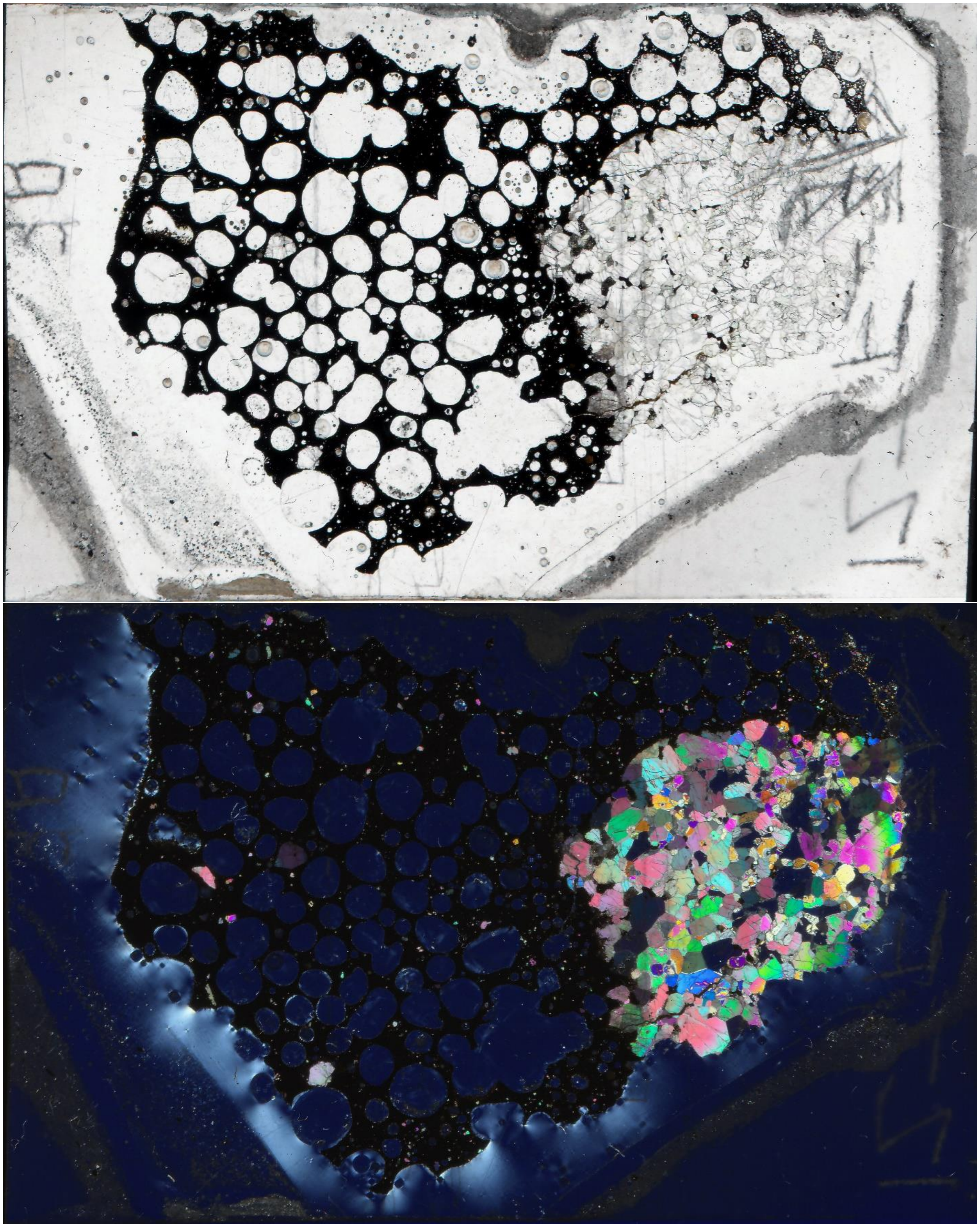

122F4-1

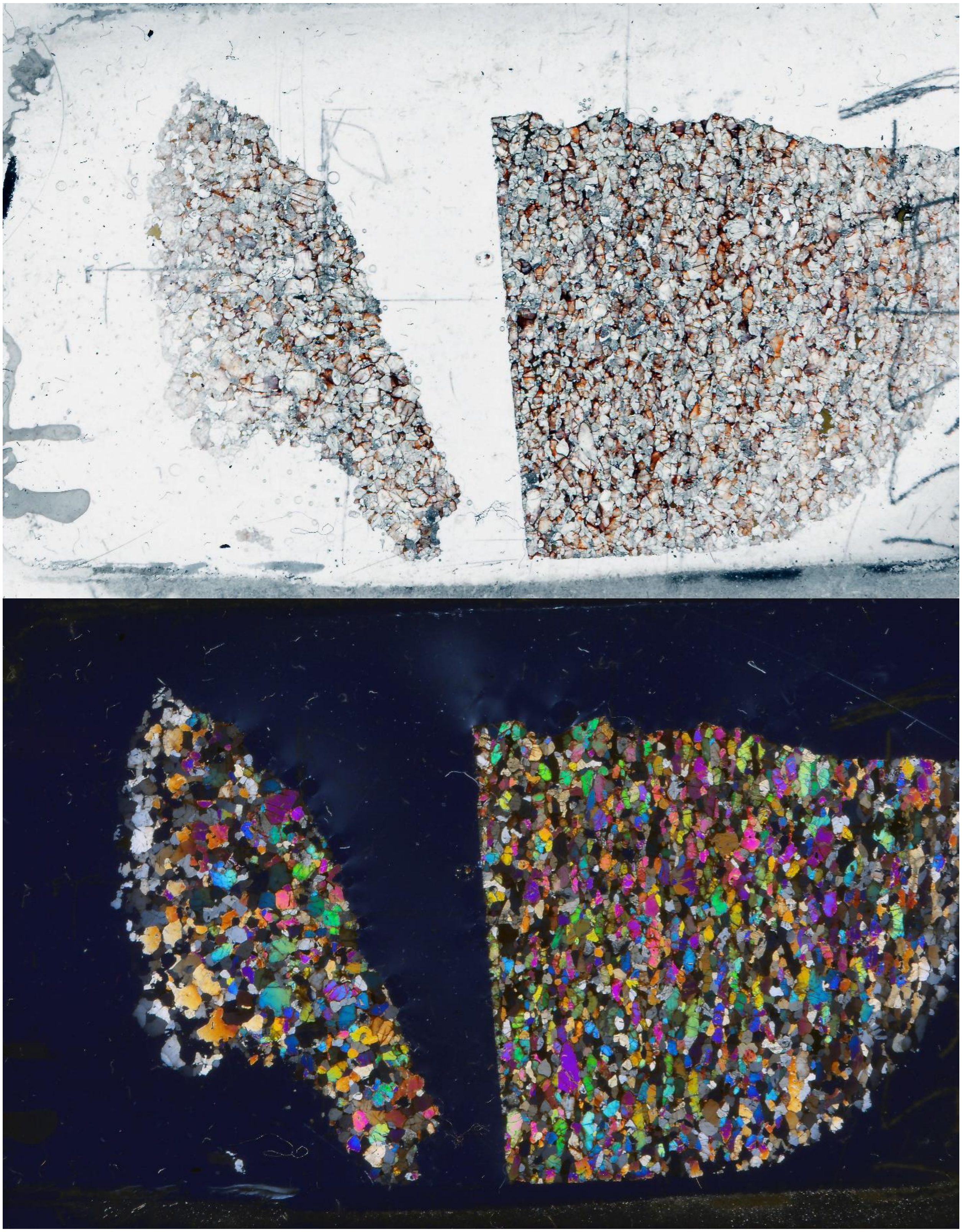

122F4-2

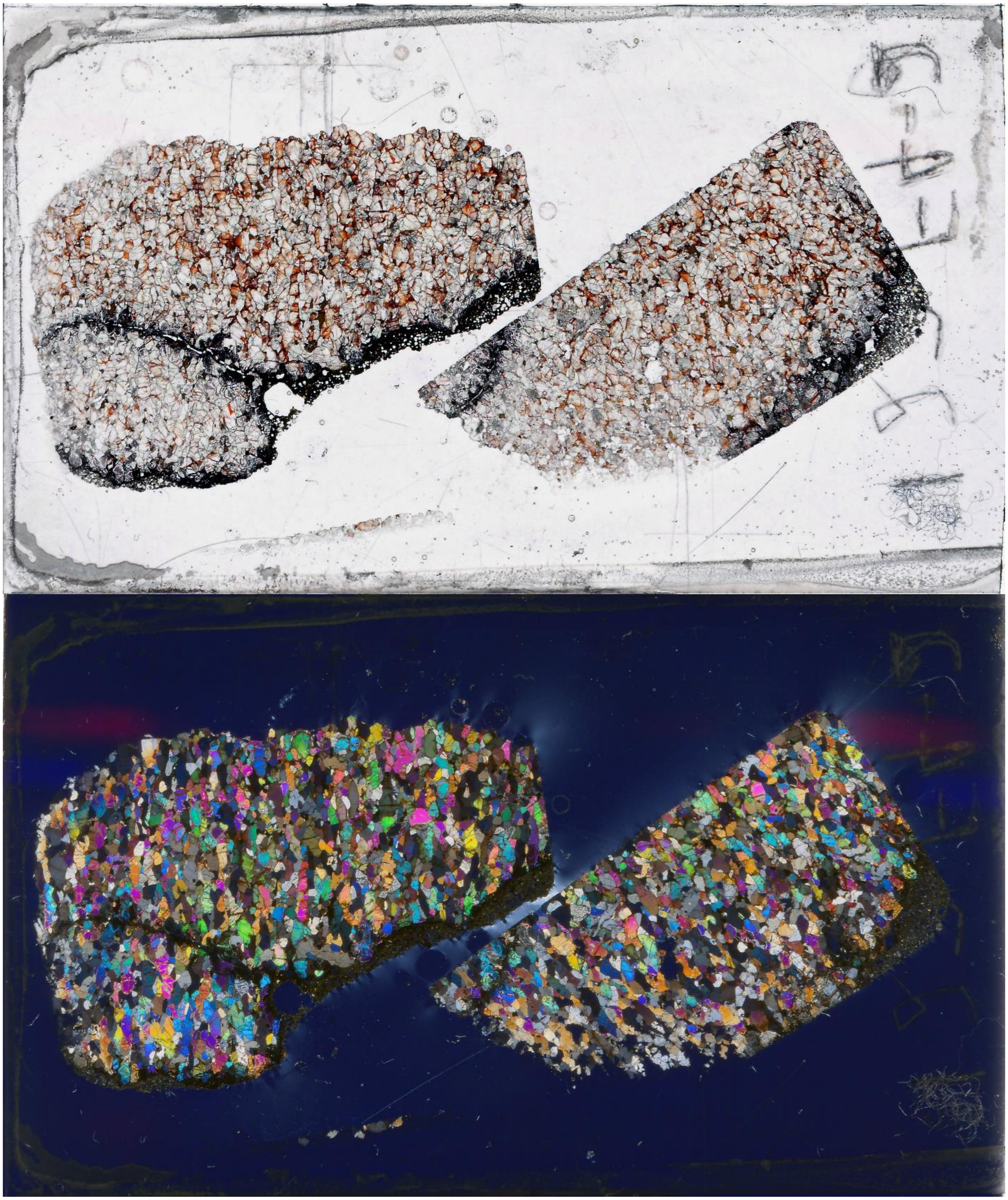

122F5-1

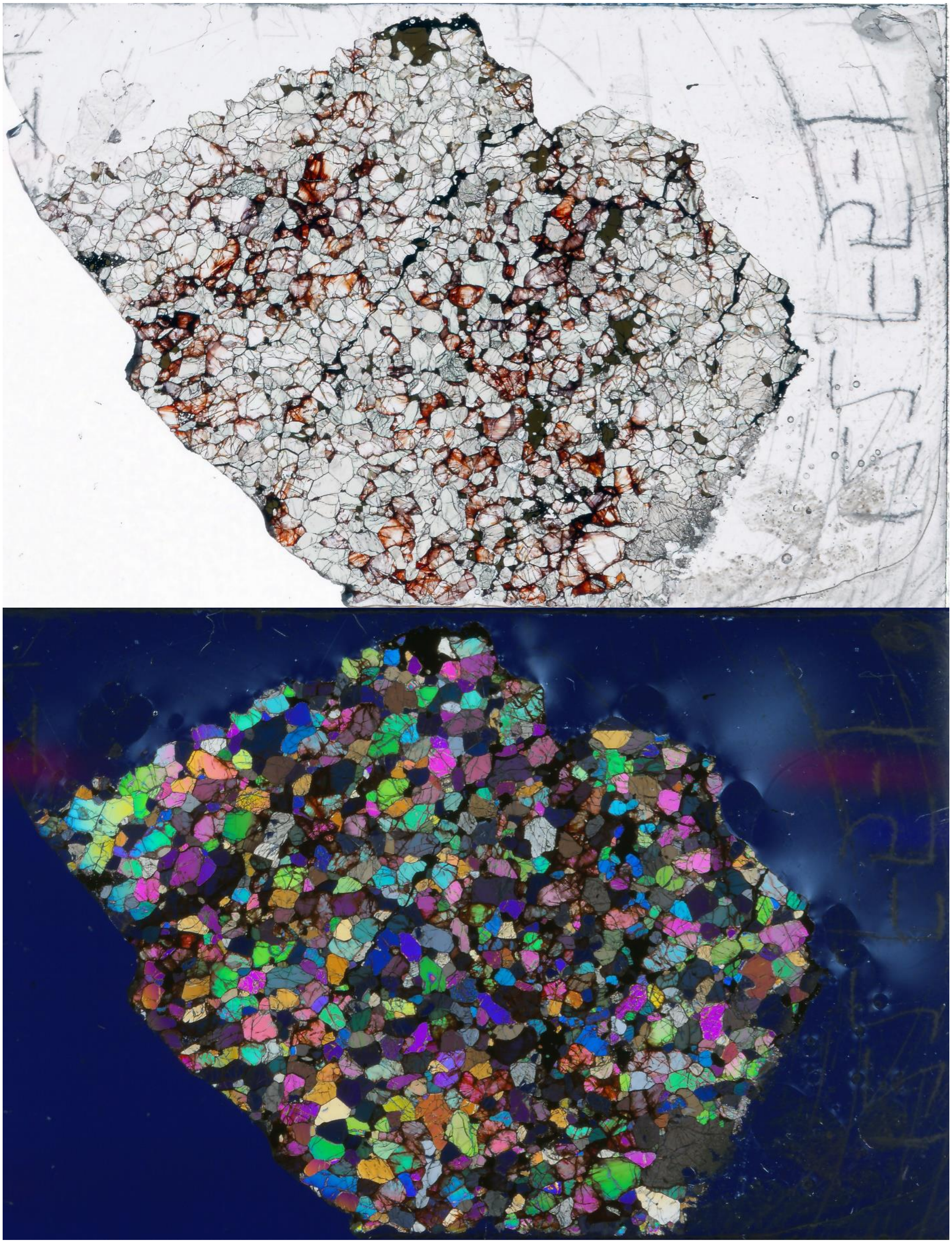

122F5-2

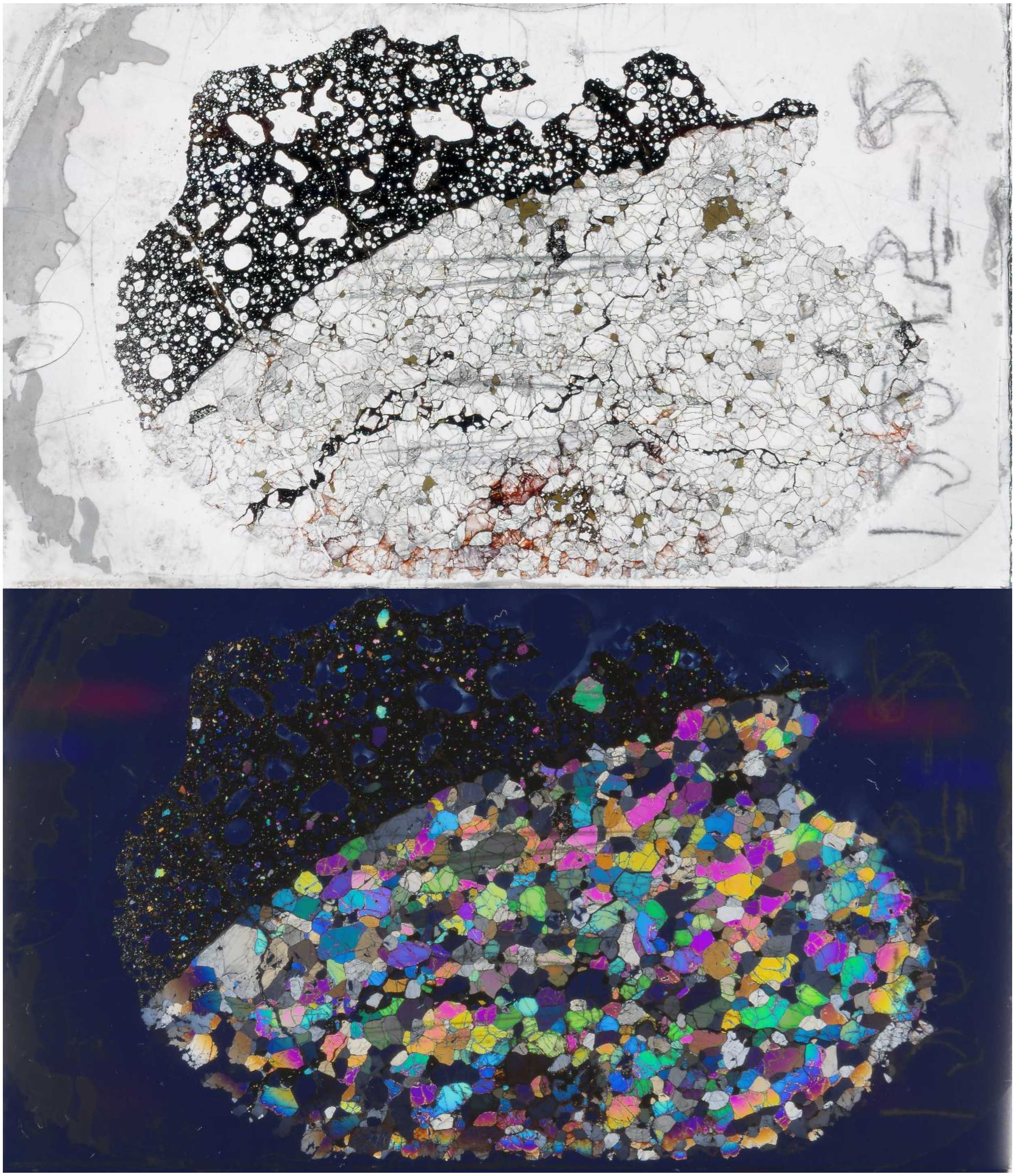

122F6

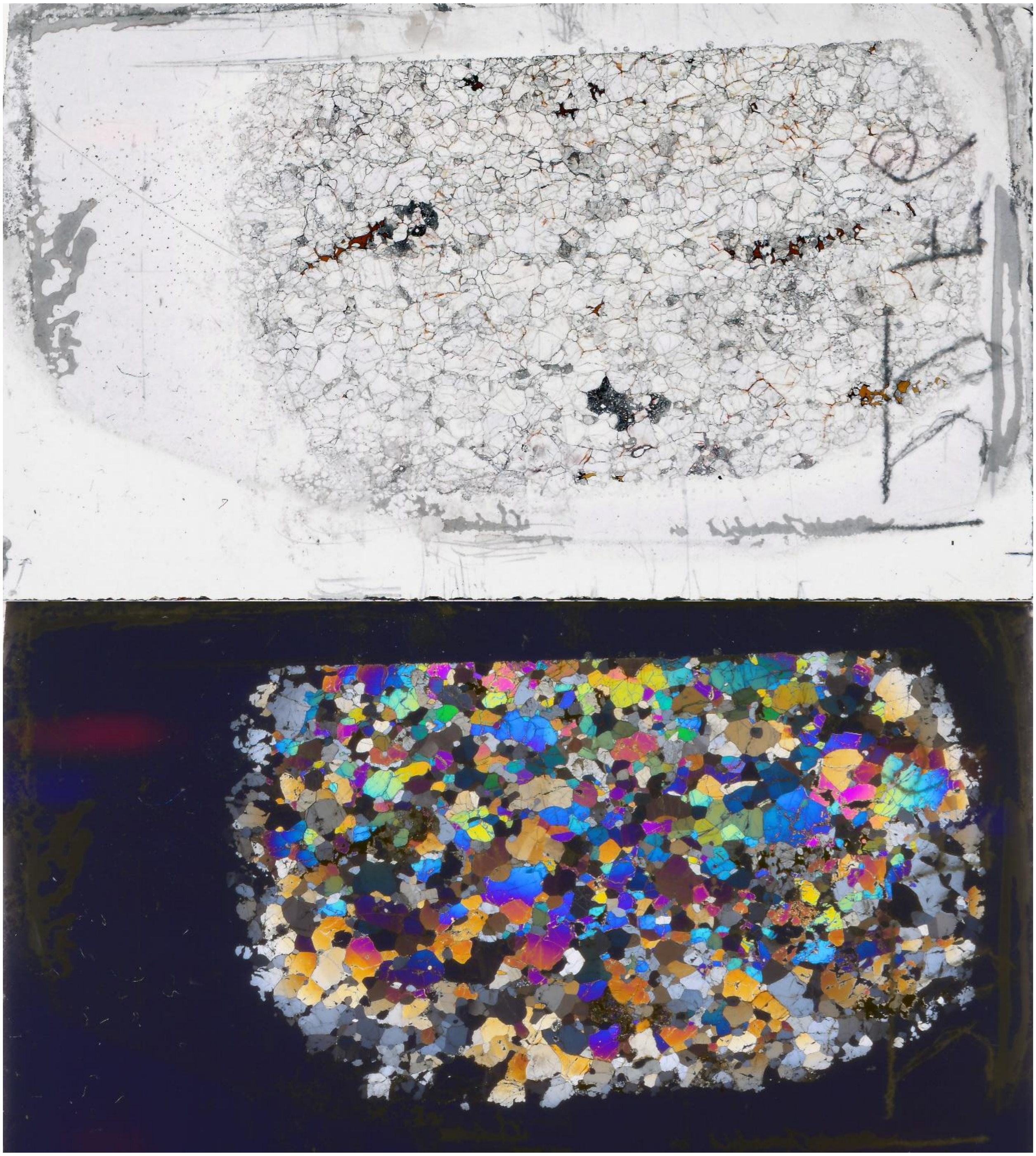

122F7-A

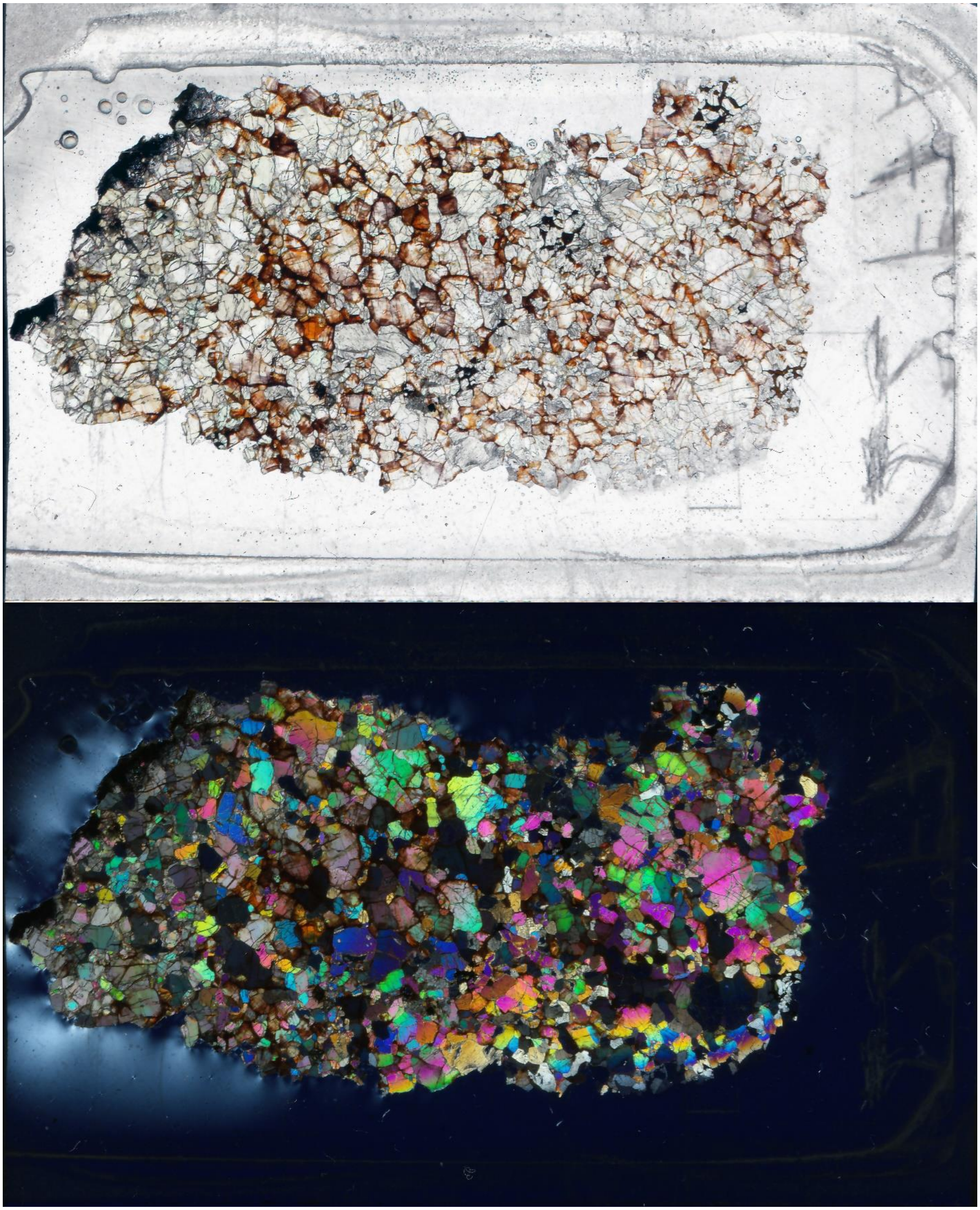

122F7A1

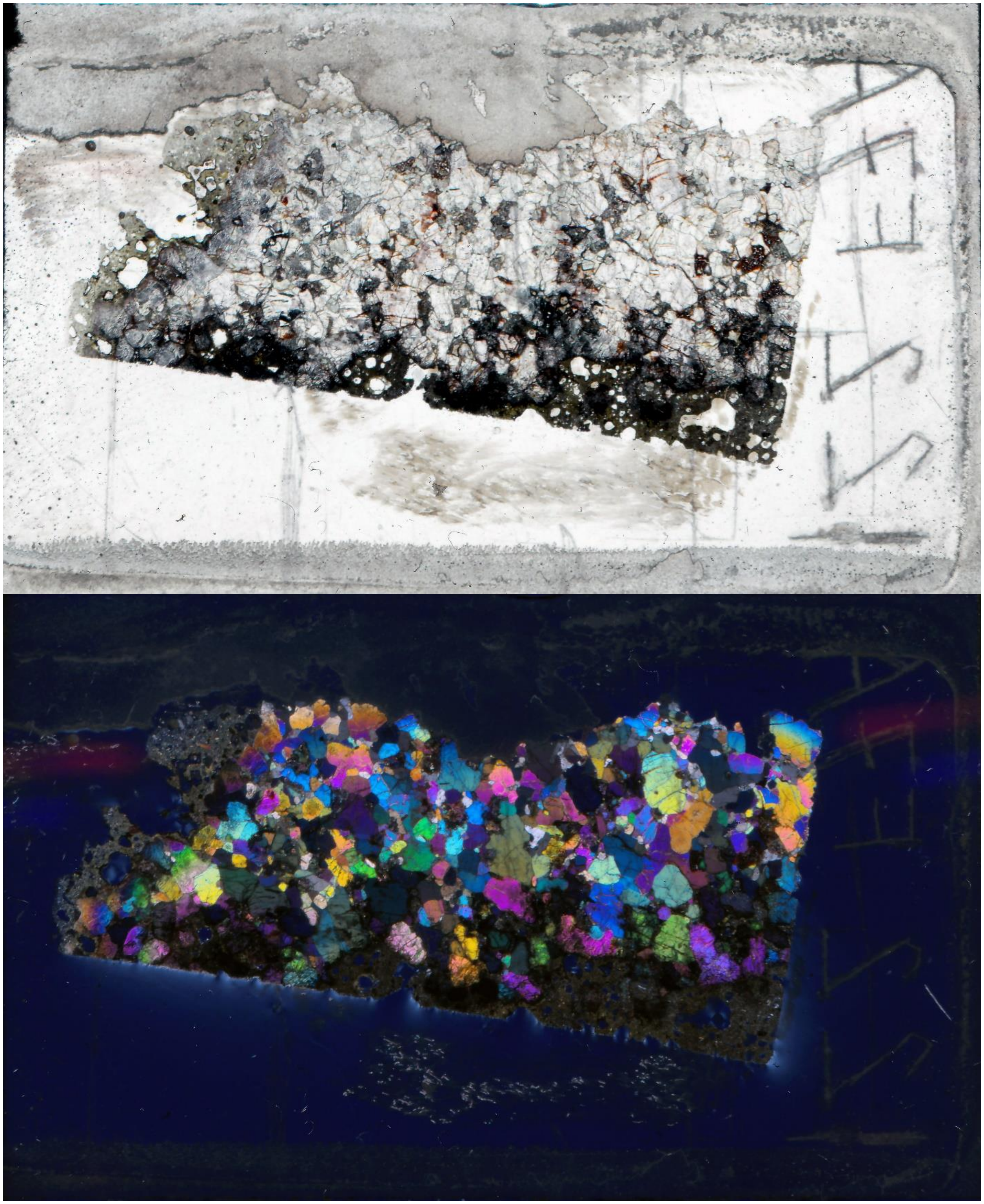

122F7-B

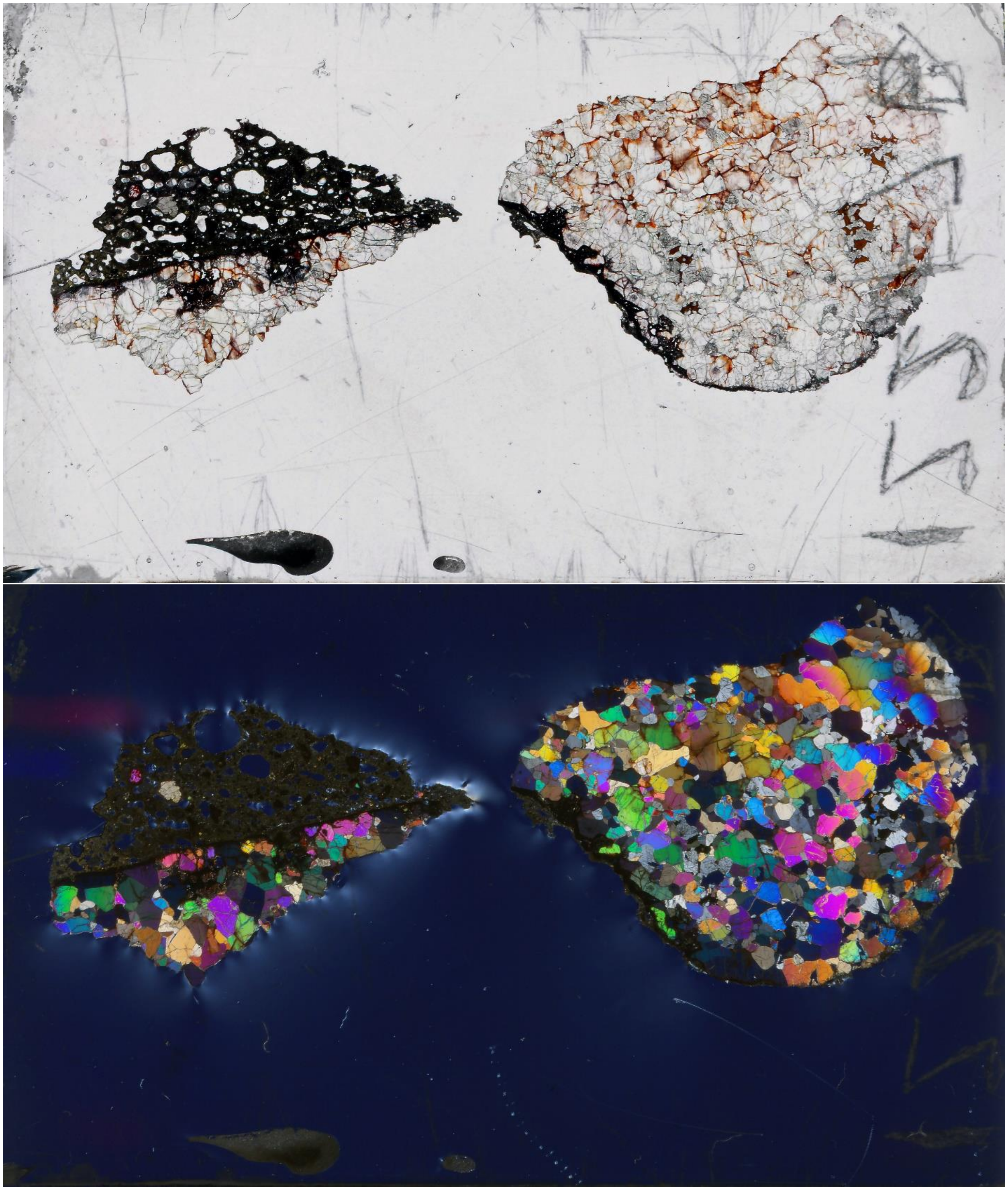

APPENDIX IV:

ANALYTICAL METHODS AND PROCEDURES

Electron Microprobe Methods

All samples which had sufficient grains for analysis were analyzed for olivine, spinel, orthopyroxene, and clinopyroxene major and minor elements. All analyses were performed on the Shimadzu EPMA-1720HT in the Shimadzu Center for Environmental, Forensics, and Material Science at the University of Texas at Arlington during the Summer and Fall of 2018. The compositions of all synthetic and natural standards used for analysis can be found in Table A4.1. The collected data was corrected for absorption, atomic number, and fluorescence (ZAF) effects by the software provided by Shimadzu. Analytical conditions for each phase can be found in Tables A4.2 – A4.4.

The Shimadzu software package applied a ZAF correction to the data after collection. The elemental weight percent data were converted to weight percent oxides assuming four oxygens for olivine and spinel, and six oxygens for the pyroxenes. Fe was speciated into FeO and Fe_2O_3 for spinels based on stoichiometry and the method of Droop (1987).

Table A4.1: Standards used in for EPMA analyses.

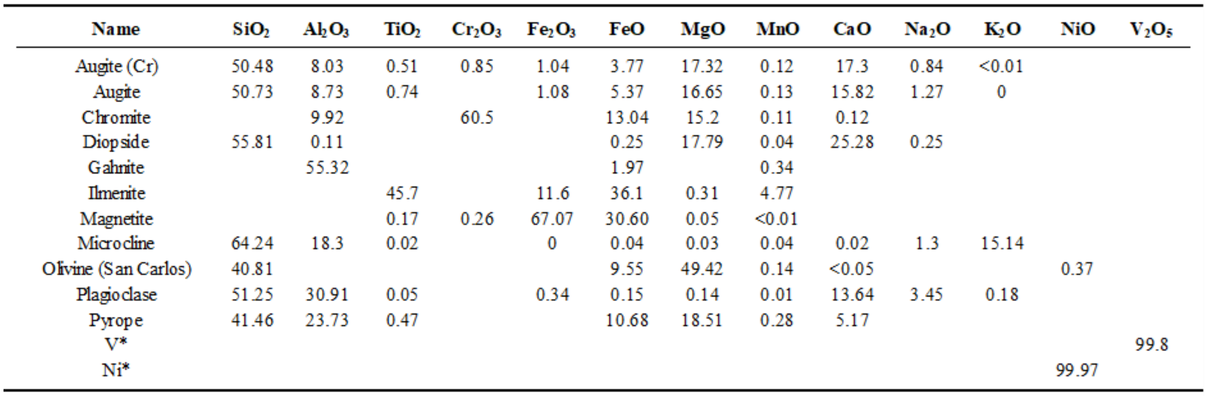

Name	SiO_2	Al_2O_3	TiO_2	Cr_2O_3	Fe_2O_3	FeO	MgO	MnO	CaO	Na_2O	K_2O	NiO	V_2O_5
Augite (Cr)	50.48	8.03	0.51	0.85	1.04	3.77	17.32	0.12	17.3	0.84	<0.01		
Augite	50.73	8.73	0.74		1.08	5.37	16.65	0.13	15.82	1.27	0		
Chromite		9.92		60.5		13.04	15.2	0.11	0.12				
Diopside	55.81	0.11				0.25	17.79	0.04	25.28	0.25			
Gahnite		55.32				1.97		0.34					
Ilmenite			45.7		11.6	36.1	0.31	4.77					
Magnetite			0.17	0.26	67.07	30.60	0.05	<0.01					
Microcline	64.24	18.3	0.02		0	0.04	0.03	0.04	0.02	1.3	15.14		
Olivine (San Carlos)	40.81					9.55	49.42	0.14	<0.05			0.37	
Plagioclase	51.25	30.91	0.05		0.34	0.15	0.14	0.01	13.64	3.45	0.18		
Pyrope	41.46	23.73	0.47			10.68	18.51	0.28	5.17				
V*													99.8
Ni*												99.97	

*Denotes a synthetic standard.

Table A4.2: Olivine analytical conditions used on the University of Arlington Shimadzu EPMA-1720HT EPMA. The analyses used a accelerating potential of 15 kV and a beam current of 20 nA with a beam size of 5 µm. Abbreviations for the crystals are as follows: RAP = Rubidium Acid Pthalate, PET = Pentaerythritol, LIF = Lithium Fluoride.

Element	Standard	Channel (Crystal)	Peak		Backgrounds		
			λ (nm)	Time (s)	λ_1 (nm)	λ_2 (nm)	Time (s)
Mg	SC-Olivine	CH1/RAP	0.9900	30	1.0398	0.9408	15
Si	SC-Olivine	CH3/PET	0.7125	30	0.7245	0.0703	15
Fe	SC-Olivine	CH4/LIF	0.1936	30	0.2055	0.1855	15
Ni	SC-Olivine	CH4/LIF	0.1656	60	0.1738	0.1578	30
Al	Chromite	CH1/RAP	0.8342	30	0.8823	0.7853	15
Ca	Diopside	CH3/PET	0.3361	30	0.3461	0.3241	15
Ti	Ilmenite	CH3/PET	0.2751	30	0.2851	0.2651	15
Mn	Gahnite	CH4/LIF	0.2102	30	0.2242	0.2042	15

Table A4.3: Spinel analytical conditions used on the University of Arlington Shimadzu EPMA-1720HT EPMA. The analyses used a accelerating potential of 15 kV and a beam current of 20 nA with a beam size of 1 µm. Abbreviations for the crystals are as follows: RAP = Rubidium Acid Pthalate, PET = Pentaerythritol, LIF = Lithium Fluoride.

Element	Standard	Channel (Crystal)	Peak		Backgrounds		
			λ (nm)	Time (s)	λ_1 (nm)	λ_2 (nm)	Time (s)
Mg	Chromite	CH1/RAP	0.9899	30	1.038	0.9398	15
Al	Chromite	CH1/RAP	0.8342	30	0.8823	0.7853	15
Cr	Chromite	CH4/LIF	0.2289	30	0.239	0.217	15
Si	Diopside	CH3/PET	0.7123	30	0.7285	0.7004	15
Ca	Diopside	CH3/PET	0.3357	30	0.3521	0.3261	15
Mn	Gahnite	CH3/LIF	0.2102	30	0.2184	0.2024	15
Ti	Ilmenite	CH4/LIF	0.2748	30	0.2829	0.2649	15
Fe	Magnetite	CH4/LIF	0.1935	30	0.2036	0.1836	15
V	V-metal	CH4/LIF	0.2503	30	0.2603	0.2423	15
Ni	Ni-metal	CH3/LIF	0.1657	30	0.1756	0.1556	15

Table A4.4: Pyroxene analytical conditions used on the University of Arlington Shimadzu EPMA-1720HT EPMA. The analyses used a accelerating potential of 15 kV and a beam current of 20 nA with a beam size of 1 µm. Abbreviations for the crystals are as follows: RAP = Rubidium Acid Pthalate, PET = Pentaerythritol, LIF = Lithium Fluoride, ADP = ammonium dihydrogen phosphate.

Element	Standard	Channel (Crystal)	Peak		Backgrounds		
			λ (nm)	Time (s)	λ_1 (nm)	λ_2 (nm)	Time (s)
Mg	Augite (Cr)	CH1/RAP	0.9896	30	1.0371	0.9418	15
Al	Augite (Cr)	CH1/RAP	0.8335	30	0.8824	0.7835	15
Fe	Augite	CH3/LIF	0.1936	30	0.2055	0.1815	15
Si	Diopside	CH4/ADP	0.7123	40	0.7244	0.7004	20
Ca	Diopside	CH4/ADP	0.3361	30	0.3457	0.3237	15
Ti	Ilmenite	CH3/LIF	0.2749	30	0.2888	0.2648	15
Na	Plagioclase	CH1/RAP	1.1920	20	1.2424	1.1444	10
K	Microcline	CH4/ADP	0.3743	30	0.3858	0.3638	15
Cr	Chromite	CH3/LIF	0.2290	30	0.2390	0.2210	15
Mn	Pyrope	CH3/LIF	0.2101	30	0.2200	0.2000	15

Laser Ablation-Inductively Coupled Plasma Mass Spectrometry (LA-ICP-MS)

Time-resolved, *in situ* analyses, were performed on two to three grains per thin section for this study. Each analytical session was begun with 10 spots on the NIST 612 glass standard, which was used as a reference standard, followed by 10 spots on the NIST610 glass standard and then analyses of the Prindle clinopyroxenes. An analysis of each of the NIST glass standards was performed after every eight clinopyroxene analyses throughout the analytical session. Finally, the analytical session was ended with two repeat analyses of each of the NIST glass standards to correct and check for instrumental drift. Each spot analysis consists of three parts.

(1) A ~20-second interval with the laser off is collected to measure the blank or the He+Ar carrier gas.

(2) The laser is turned on, and the clinopyroxene is ablated. The ablated material is carried into the source by the carrier gas and measured for ~30-35 seconds.

(3) The laser is turned off, and the elemental measurements are allowed to ‘wash out’ over an interval of 15-20 seconds.

Laser ablation of the samples used an NWR193 excimer laser system with a 193 nm laser source. The laser was set to a frequency of 5 Hz which allowed for 150-170 bursts over a period of 30-35 seconds to hit the clinopyroxene.

Data reduction was performed using the Iolite software package (Paton et al., 2011) which identifies which part of the time-resolved elemental spectrum corresponds to actual clinopyroxene analysis and which part corresponds to background data. The elemental intensities are corrected for the background by subtracting the average counts per second of the (Cps) background, or blank, measurement from the Cps of sample analyses.

Silicon (^{29}Si) is used as an internal standard element (known from EMPA) to convert the background-corrected elemental intensities to concentrations by weight percent element (in ppm) using the following formula:

$$C_i^{Sa} = C_S^{Sa} \times \frac{I_i^{Sa}}{I_S^{Sa}} \times \frac{C_i^R}{C_S^R} \times \frac{I_i^R}{I_S^R}$$

where C_S^{Sa} is the concentration of the internal standard in the sample (calcium) determined by EMPA, I_i^{Sa}/I_s^{Sa} is the ratio of background-corrected intensity (Cps) of the element i to the internal standard element (calcium) in the sample. C_i^R/C_s^R is the ratio of the concentrations of the element i to the concentration of the internal standard in the reference standard, and I_s^R/I_i^R is the ratio of the background-corrected intensities of the internal standard element to the element i in the reference standard. Each spot is subjected to this conversion. Data rejection occurs automatically within the in-house program as well as by personal inspection of the programs output data.

The average of the NIST glass standards for the analytical run is provided in Table A4.5 along with percentage errors of the measured values compared to certified reference values. The percentage error for each element was calculated using the following equation:

$$\%error = \frac{Difference\ between\ measured\ and\ certified\ concentration}{Certified\ concentration\ of\ the\ element} \times 100$$

The precision of the data can be determined by examining the multiple analyses of the external and internal standards. The precision of a standard sample with respect to each element is represented by the relative standard deviation (RSD). The RSD is a percentage value and is calculated for each element using the following equations:

$$x_\alpha = \frac{\sum x}{n}$$

Where x_α is the average element concentration, x is the element concentration, and n is the number of measurements.

$$s = \frac{\sqrt{\sum(x - x_a)^2}}{n - 1}$$

Where s is the standard deviation.

$$RSD(\%) = \frac{100s}{x_a}$$

Table A4.5: LA-ICP-MS element concentrations for the external standards used in the two analytical runs for the Prindle samples and measures of their precision and accuracy.

	Certified Preferred Values		**Analytical Run 1**								**Analytical Run 2**							
			Average (N = 18)		**Standard Deviation**		**% error**		**RSD (%)**		**Average (N = 16)**		**Standard Deviation**		**% error**		**RSD (%)**	
	NIST 612	**NIST 610**	**NIST 612**	**NIST 610**	**NIST 612**	**NIST 610**	**NIST 612**	**NIST 610**	**NIST 612**	**NIST 610**	**NIST 612**	**NIST 610**	**NIST 612**	**NIST 610**	**NIST 612**	**NIST 610**	**NIST 612**	**NIST 610**
Sc (ppm)	39.90	455.0	39.91	458.33	0.62	17.11	0.03	0.73	1.55	3.73	39.90	462.05	0.37	13.26	0.00	1.55	0.92	2.87
Ti	44.00	452.0	43.76	451.16	0.95	3.56	0.54	0.19	2.18	0.79	44.00	449.06	0.32	3.91	0.00	0.65	0.73	0.87
V	38.80	450.0	39.07	593.00	0.97	10.95	0.71	31.78	2.49	1.85	38.93	451.19	0.75	13.74	0.34	0.26	1.92	3.04
Co	35.50	410.0	35.52	529.61	0.28	9.30	0.06	29.17	0.79	1.76	35.44	412.38	1.48	9.80	0.16	0.58	4.18	2.38
Ni	38.80	458.7	38.81	451.62	0.54	6.53	0.03	1.54	1.39	1.45	38.91	435.94	1.43	20.77	0.29	4.96	3.68	4.76
Cu	37.80	441.0	38.00	427.99	0.65	12.44	0.52	2.95	1.70	2.91	37.84	429.50	1.56	13.57	0.12	2.61	4.12	3.16
Zn	39.10	460.0	39.14	462.03	0.33	14.68	0.10	0.44	0.83	3.18	39.31	468.69	3.01	20.34	0.53	1.89	7.65	4.34
Ga	36.90	433.0	36.92	440.06	0.52	17.14	0.05	1.63	1.41	3.89	37.02	433.81	1.25	5.88	0.32	0.19	3.38	1.36
Ge	36.10	447.0	36.09	414.53	0.43	15.34	0.04	7.26	1.18	3.70	36.36	399.44	3.42	25.01	0.73	10.64	9.39	6.26
Rb	31.40	425.7	31.50	417.56	0.67	12.22	0.31	1.91	2.13	2.93	31.44	428.06	0.64	7.92	0.12	0.55	2.05	1.85
Sr	78.40	515.5	78.42	512.17	0.70	13.42	0.03	0.65	0.89	2.62	78.48	507.00	0.94	13.42	0.10	1.65	1.19	2.65
Y	38.30	462.0	38.21	426.22	0.55	20.66	0.22	7.75	1.44	4.85	38.31	452.44	0.41	18.63	0.03	2.07	1.08	4.12
Zr	37.90	448.0	37.89	434.40	0.39	16.78	0.03	3.04	1.02	3.86	37.96	428.89	1.54	11.11	0.16	4.27	4.05	2.59
Nb	38.90	465.0	38.80	420.96	0.57	17.40	0.26	9.47	1.47	4.13	38.85	459.58	1.12	11.75	0.13	1.17	2.88	2.56
Cs	42.70	366.0	42.76	367.40	0.25	10.65	0.13	0.38	0.59	2.90	42.83	376.31	0.77	6.86	0.31	2.82	1.81	1.82
Ba	39.30	452.0	39.30	452.92	0.48	6.60	0.01	0.20	1.21	1.46	39.36	451.31	1.21	15.13	0.14	0.15	3.07	3.35
La	36.00	440.0	35.98	441.89	0.36	14.11	0.06	0.43	1.01	3.19	36.10	434.75	1.17	10.67	0.28	1.19	3.25	2.45
Ce	38.40	453.0	38.40	466.68	0.59	10.86	0.01	3.02	1.53	2.33	38.53	459.00	1.10	12.29	0.33	1.32	2.86	2.68
Pr	37.90	448.0	37.85	456.81	0.40	11.85	0.13	1.97	1.05	2.59	37.89	447.29	0.18	8.59	0.02	0.16	0.47	1.92
Nd	35.50	430.0	35.46	431.61	0.48	12.99	0.10	0.37	1.35	3.01	35.42	427.13	0.44	9.46	0.23	0.67	1.24	2.21
Sm	37.70	453.0	37.69	423.67	0.39	9.93	0.03	6.48	1.03	2.34	37.76	438.75	0.64	27.40	0.17	3.15	1.69	6.24
Eu	35.60	447.0	35.63	444.77	0.43	12.55	0.08	0.50	1.20	2.82	35.64	442.31	0.38	14.40	0.12	1.05	1.07	3.26
Gd	37.30	449.0	37.27	458.44	0.73	14.21	0.07	2.10	1.97	3.10	37.61	439.31	1.24	16.87	0.82	2.16	3.30	3.84
Tb	37.60	437.0	37.55	436.42	0.42	14.25	0.14	0.13	1.11	3.27	37.60	442.00	0.69	8.70	0.00	1.14	1.83	1.97
Dy	35.50	437.0	35.55	422.44	0.40	14.50	0.13	3.33	1.13	3.43	35.54	433.06	1.10	9.69	0.12	0.90	3.08	2.24
Ho	38.30	449.0	38.28	447.07	0.71	13.33	0.05	0.43	1.85	2.98	38.35	450.55	0.73	11.02	0.12	0.35	1.90	2.45
Er	38.00	455.0	37.91	442.89	0.56	14.77	0.24	2.66	1.49	3.34	38.24	451.56	1.17	13.93	0.62	0.76	3.07	3.09
Tm	36.80	436.0	36.74	424.63	0.36	10.87	0.17	2.61	0.97	2.56	36.83	430.20	0.69	11.47	0.09	1.33	1.88	2.67
Yb	39.20	450.0	39.09	448.94	0.62	13.63	0.28	0.23	1.59	3.04	39.21	457.31	0.34	21.63	0.03	1.63	0.87	4.73
Lu	37.00	439.0	36.91	425.26	0.60	14.52	0.24	3.13	1.63	3.41	37.00	441.63	0.21	11.84	0.00	0.60	0.57	2.68
Hf	36.70	435.0	36.69	424.49	0.48	14.16	0.03	2.42	1.30	3.34	36.82	421.63	1.24	11.13	0.32	3.07	3.37	2.64
Ta	37.60	446.0	37.52	454.44	0.46	15.80	0.22	1.89	1.21	3.48	37.64	443.56	0.97	11.66	0.12	0.55	2.57	2.63
Pb	38.57	426.0	38.55	428.99	0.49	11.31	0.04	0.70	1.28	2.64	38.83	434.81	1.66	7.77	0.68	2.07	4.27	1.79
Th	37.79	457.2	37.71	434.68	0.48	15.52	0.21	4.92	1.26	3.57	37.80	447.31	0.84	11.31	0.03	2.16	2.22	2.53
U	37.38	461.5	37.42	456.19	0.42	16.02	0.12	1.15	1.11	3.51	37.37	464.19	0.40	10.76	0.03	0.58	1.08	2.32

APPENDIX V:

TABLE OF PETROGRAPHIC OBSERVATIONS

This section provides a summary table of the petrographic observations for the extant thin sections of the Prindle xenolith suite. The following is a breakdown and explanation of some of the specific terminology used in reference to the petrographic descriptions.

Textures

Granular: minerals are approximately equidimensional or equant.

Intergranular: angular interstices, such as between feldspars, are occupied by granules (ol, px) of random orientation.

Ophitic: laths of plagioclase lie in a matrix of coarse subhedral pyroxene (augite) so that in thin section, the feldspar laths, whose average length does not exceed the diameter of the pyroxene grains, appear to be largely or entirely closed in pyroxene

Subophitic: If the average length of the plagioclase laths exceeds that of the pyroxene grains, and the pyroxene grains only partly enclose a number of the plagioclase laths.

Pokilitic: numerous grains of various minerals in random orientation are completely enclosed within large, optically continuous crystals of different composition.

Habit

Equant = aspect ratio <1:2

Subequant = aspect ratio 1:2 to 1:3

Tabular = aspect ratio of 1:3 to 1:5

Elongate = aspect ratio >1:5

Interstitial = occurring in the space between more well-defined grains.

Table A5.1: A summary of the petrographic observations for the extant thin section collection of the Prindle xenolith suite.

Sample ID	Thin Section ID	Lith. Group	Petrographic Lithology	Olivine				Clinpyroxene				Orthopyroxene				Spinel				Acc. Minerals	Alteration	
				%	Avg	Max	Min	%	Avg	Max	Min	%	Avg	Max	Min	%	Avg	Max	Min		%	Notes
16ATe101A1	101A1-2	Pyroxenite	Clinopyroxenite	0				100	1.28	2.50	0.05	0				0				Plagioclase and amphibole laths throughout basalt matrix	0	
16ATe102A	102A(A-1)	Lherzolite	Lherzolite	69.5	1.07	2.00	0.14	14.0	0.66	1.20	0.12	13.3	0.85	1.40	0.30	3.2	0.33	0.54	0.12	Sulfides	90	Highly altered olivine grains. Many pockets of CPX in interstetial pockets.
16ATe102A	102A(A-2)	Lherzolite	Lherzolite	67.6	1.05	1.90	0.20	11.4	1.16	2.20	0.12	19.0	0.85	1.30	0.40	1.9	1.95	3.80	0.10	Iddingsite	10	Alteration present but isolated to scattered various grains and phases
16ATe102C	102C	Lherzolite	Lherzolite	64.6	2.92	2.80	0.12	13.5	2.11	4.12	0.10	17.7	0.95	1.70	0.20	4.2	1.4	2.70	0.10	Iddingsite	95	Highly altered olivine grains. Alteration in areas where fracturing has occurred-weathering
16ATe102D	102D-1	Dunite	Dunite	98.2	1.43	2.74	0.12	0.4	0.2	0.36	0.04	0.8	0.2	0.28	0.12	0.6	0.27	0.48	0.05	Iddingsite	5	Isolated olivine grains altered. One main vein of CPX through fracture.
16ATe102D	102D-2	Pyroxenite	Pl-bearing Clinopyroxenite	0.0				90.0	0.82	1.54	0.10	3.9	2.31	4.50	0.12	0.4	0.73	1.40	0.06	Plagioclase, sulfides, and iddingsite fragments in matrix	2	
16ATe102D	102D-3	Lherzolite	Lherzolite	50.9	2.2	4.20	0.20	29.2	0.98	1.60	0.36	18.3	1.05	1.80	0.30	1.6	0.99	1.92	0.06	Iddingsite	2	Interstetial CPX around rim of xenolith
16ATe102E1	102E1(A)	Lherzolite	Lherzolite	58.1	2.2	4.30	0.14	21.1	1.12	2.04	0.20	18.3	1.82	3.30	0.34	2.5	1.06	2.00	0.12	Iddingsite	75	Highly altered olivine grains. Many pockets of CPX in interstetial pockets.
16ATe102F	102F-1	Harzburgite	Harzburgite	94.7	1.41	2.68	0.14	3.0	0.45	0.80	0.10	1.2	0.78	1.40	0.16	1.2	0.64	1.20	0.08		0	A lot of refraction zoning around grain boudaries
16ATe102F	102F-2	Pyroxenite	Pl-bearing Clinopyroxenite	0.0				90.2	1.54	2.84	0.24	0.0				0.0				(8%) plagioclase, (1.8%) Sulfides, and iddingsite	2	Slight alteration in olivine grains located in the harzburgite fragment. Rimming in clinopyroxnite fragment.
15ATe122C	122C-1	Websterite	Ol-websterite	17.6	1.1	2.08	0.14	12.6	0.51	0.82	0.20	65.7	0.83	1.10	0.56	4.1	0.58	0.86	0.30		2	
15ATe122C	122C-2	Lherzolite	Lherzolite	54.4	0.97	1.74	0.20	19.3	1.1	2.00	0.20	24.2	0.84	1.46	0.22	2.1	0.27	0.46	0.08		0	
15ATe122C	122C3-A	Harzburgite	Harzburgite	81.0	1.06	1.92	0.20	3.4	0.98	1.80	0.16	14.3	1.64	1.52	0.12	1.3	0.62	1.12	0.12		30	Alteration in areas where fracturing has occurred-weathering
15ATe122C	122C3-B	Harzburgite	Harzburgite	85.6	1.61	3.14	0.08	6.4	0.77	1.40	0.14	5.9	0.98	1.68	0.28	2.1	0.38	0.65	0.10		20	Alteration around grain boundaries of olivine where fracturing has occurred-weathering
15ATe122D	122D-1	Lherzolite	Lherzolite	68.2	1.85	3.40	0.30	14.4	1.34	2.60	0.08	14.0	1.19	2.30	0.08	3.4	0.39	0.68	0.10		1	
15ATe122F1	122F1	Dunite	Dunite	92.0	1.73	3.40	0.06	0.6	0.25	0.46	0.04	6.4	0.4	0.60	0.20	1.0	0.32	0.60	0.04	Sulfides	10	Strong evidence for flow throughout the thin section or a plastic deformation due to pressure
15ATe122F2	122F2(A)	Lherzolite	Lherzolite	81.5	1.3	2.48	0.12	5.8	1.21	2.30	0.12	9.5	1.18	2.20	0.16	3.2	0.37	0.60	0.14	Piemontite	10	Hydrothermal metasomatism
15ATe122F2	122F2(B)	Pyroxenite	Ol-bearing Clinopyroxenite	9.0	0.79	1.48	0.10	82.0	1.26	2.30	0.16	8.5	1.95	3.60	0.30	0.5	0.45	0.80	0.10	Iddingsite	15	Alteration present but isolated to scattered various grains and phases
15ATe122F2	122F2	Lherzolite	Lherzolite	67.5	1.84	3.48	0.20	12.2	1.14	2.14	0.14	18.3	1.78	3.30	0.26	2.0	0.4	0.74	0.06	Iddingsite	25	Random isolated weathering
15ATe122F3	122F3-A	Lherzolite	Lherzolite	58.0	1.15	2.10	0.20	18.0	1.17	2.18	0.16	21.5	1.01	1.80	0.22	2.5	0.73	1.40	0.06	Sulfides. Piemontite, and Iddingsite	40	Abudent alteration on olivine grains, in addition to piemontite
15ATe122F3	122F3-B	Harzburgite	Harzburgite	60.9	1.47	2.60	0.34	4.9	0.57	0.98	0.16	33.1	0.71	1.02	0.40	1.1	0.38	0.74	0.02		0	Interstetial CPX around rim of xenolith. A lot of refraction zoning around grain boudaries.
15ATe122F4	122F4-1 (small)	Lherzolite	Lherzolite	52.8	0.88	1.60	0.16	21.9	0.91	1.74	0.08	21.3	0.97	1.88	0.05	4.0	0.4	0.74	0.06	Iddingsite, piemontite	30	Alteration present but isolated to scattered various grains and phases
15ATe122F4	122F4-1 (large)	Lherzolite	Lherzolite	60.5	1.22	2.24	0.20	18.4	0.9	1.72	0.08	19.5	0.8	1.50	0.10	1.6	0.77	1.46	0.07	Iddingsite, piemontite	80	Strong evidence for flow throughout the thin section or a plastic deformation due to pressure; Alteration present but isolated to scattered various grains and phases
15ATe122F4	122F4-2	Lherzolite	Lherzolite	61.3	0.98	1.90	0.06	18.9	1.08	2.10	0.06	16.2	0.93	1.78	0.08	3.6	0.82	1.60	0.04	Iddingsite, piemontite	60	Major alteration generated from olivine and branches out into other phases
15ATe122F5	122F5-1	Websterite	Ol-websterite	36.1	1.27	2.36	0.18	27.3	1.28	2.44	0.12	32.7	2.56	4.80	0.32	3.9	1.05	2.02	0.08	Iddingsite, piemontite	40	Alteration located at olivine grain fractures and along grain boundaries where fractures have occured
15ATe122F5	122F5-2	Websterite	Ol-websterite	38.3	1.95	3.70	0.20	26.1	1.72	3.30	0.14	31.4	2.2	4.20	0.20	4.2	1.04	2.00	0.08	Iddiingsite, piemontite(?)	20	Major fractioning in the form of a triple junction. Grain boundaries altered along fractures. Alteration of olivine grains.
15ATe122F6	122F6	Harzburgite	Harzburgite	71.3	1.89	3.70	0.08	5.6	1.89	3.70	0.08	22.0	3.12	4.10	0.14	1.2	0.56	1.06	0.06	Iddiingsite, piemontite	5	Minor fracturing allowing for slight alteration along grain boundaries; predomintly on olivine
15ATe122F7	122F7-A	Harzburgite	Harzburgite	77.9	1.98	3.88	0.08	4.2	1.42	2.80	0.04	17.4	1.52	2.86	0.18	0.5	0.34	0.64	0.04	Iddiingsite, piemontite(?)	15	Olivine grains effected by alteration, many pockets of CPX in interstetial pockets
15ATe122F7	122F7A	Harzburgite	Harzburgite	71.8	1.74	3.30	0.18	3.9	1.1	2.14	0.06	24.1	1.22	2.38	0.06	0.2	0.4	0.72	0.08	Iddiingsite, piemontite	60	Major alteration generated from olivine and branches out into other phases
15ATe122F7	122F7-B	Lherzolite	Lherzolite	54.9	1.95	3.84	0.05	13.9	1.39	2.70	0.08	27.9	1.24	2.40	0.08	3.3	0.73	1.40	0.06	Iddiingsite, piemontite	70	Olivine grains effected by alteration. Piemontite present around grain boundaries. Most boundaries effected by alteration.

REFERENCES

Albarede F (2009). Geochemistry: an introduction. Cam. Univ. Press 2ed., 342p.

Andronikov AV and Mukasa SB (2010). ^{40}Ar/^{39}Ar eruption ages and geochemical characteristics of Late Tertiary to Quaternary intraplate and arc-related lavas in interior Alaska. *Lithos* **115**, 1-14.

Beranek LP and Mortensen JK (2007). Investigating a Triassic overlap assemblage in Yukon: On-going field studies and preliminary detrital-zircon age data. *In*: Yukon Exploration and Geology 2006. Emond, D.S., Lewis, L.L., and Weston, L.H., (eds.), *Yukon Geological Survey*, 83-92.

Blondes MS, Reiners PW, Edwards BR, and Biscontini A (2007). Dating young basalt eruptions by (U-Th)/He on xenolithic zircons. *Geology* **35**, 17-20.

Brandon AD, Creaser RA, Shirey SB, and Carlson RW (1996). Osmium Recycling in Subduction Zones. *Science* **272**, 861-864.

Brearley M and Scarfe CM (1984). Amphibole in a spinel lherzolite xenolith: evidence for volatiles and partial melting in the upper mantle beneath southern British Columbia. *Can. J. Earth Sci.* **21**, 1067–1072.

Brearley M, Scarfe CM, and Fujii T (1984). The petrology of ultramafic xenoliths from Summit Lake, near Prince George, British Columbia. *Contrib. Mineral Petrol.* **88**, 53–63.

Breitsprecher K, Thorkelson DJ, Groome WG, and Dostal J (2003). Geochemical confirmation of the Kula-Farallon slab window beneath the Pacific Northwest in Eocene time. *Geology*. **31**, 351-354.

Brey GP and Kohler T (1990). Geothermobarometry in four-phase lherzolites II. New thermobarometers and practical assessment of existing thermobarometers. *J. Petrol.* **31**, 1353-1378.

Canil D and Scarfe C (1989). Origin of phlogopite in mantle xenoliths from Kostal Lake, Wells Gray Park, British Columbia. *J. Petro.* **30**, 1159–1179.

Canil D, Brearley M, and Scarfe CM (1987). Petrology of ultramafic xenoliths from Rayfield River, south-central British Columbia. *Can. J. Earth Sci.* **24**, 1679–1687.

Canil D, Virgo D, and Scarfe CM (1990). Oxidation state of mantle xenoliths from British Columbia, Canada. *Contrib. Mineral Petrol.* **104**, 453–462.

Carignan J, Ludden J, and Francis D (1994). Isotopic characteristics of mantle sources for Quaternary continental alkaline magmas in the northern Canadian Cordillera. *Earth Planet Sci. Lett.* **128**, 271-286.

Carignan J, Ludden J, and Francis D (1996). On the recent enrichment of a subcontinental lithosphere: A detailed U-Pb study of spinel lherzolite xenoliths, Yukon, Canada. *Geochim. Cosmochim. Acta.* **60**, 4241-4252.

Carlson RW and Irving AJ (1994). Depletion and enrichment history of subcontinental lithospheric mantle: an Os, Sr, Nd and Pb isotopic study of ultramafic xenoliths from the northwestern Wyoming Craton. *Earth Planet. Sci. Lett.* **126**, 457–472.

Chesley JT, Rudnick RL, and Lee CT (1999). Re-Os systematics of mantle xenoliths from the East African Rift: Age, structure, and history of the Tanzanian craton. *Geochim. Cosmochim. Acta* **63**, 1203–1217.

Colpron M, Nelson JL, and Murphy DC (2007). Northern Cordilleran terranes and their interactions through time. *GSA Today* **17**, 4-10.

Colpron M, Nelson JL (2011). A Paleozoic NW passage and the Timanian, Caledonian and Uralian connections of some exotic terranes in the North American Cordillera. *In*: Arctic petroleum geology. *Geological Society, London, Memoirs* **35.1**, 463-484.

Dick HJB (1989). Abyssal peridotites, very low spreading ridges and ocean ridge magmatism. *In*: Magmatism in the Ocean Basins, Saunders, A.D. and Norry, M.J. (eds). *Geological Society, London, Special Publications*, **42**, 71-105.

Dijkstra AH, Barth MG, Drury MR, Mason PRD, and Vissers RML (2003). Diffuse porous melt flow and melt-rock reaction in the mantle lithosphere at the slow-spreading ridge: a structural petrology amd LA-ICP-MS study of the Othris Peridotite Massif (Greece). *Geochem. Geophys. Geosyst. (G^3)* **4**, 1-24.

Downes H, Macdonald RAY, Upton BG, Cox KG, Bodinier JL, Mason PR, and Hearn Jr BC (2004). Ultramafic xenoliths from the Bearpaw Mountains, Montana, USA: Evidence for multiple metasomatic events in the lithospheric mantle beneath the Wyoming craton. *J. Petro*, **45**(8), 1631-1662.

Downes H, De Vries C, and Wittig N (2015). Hf–Zr anomalies in clinopyroxene from mantle xenoliths from France and Poland: implications for Lu–Hf dating of spinel peridotite lithospheric mantle. *Int. J. Earth Sci.*, **104**(1), 89-102.

Ducea M, Sen G, Eiler J, Fimbres J (2002). Melt depletion and subsequent metasomatism in the shallow mantle beneath Koolau volcano, Oahu (Hawaii). *Geochem. Geophys. Geosyst. (G^3)* **3**, 1029.

Dusel-Bacon C, Hansen VL, and Scala JA (1995). High-pressure amphibolite facies dynamic metamorphism and the Mesozoic tectonic evolution of an ancient continental margin, east-central Alaska. *J. of Meta. Geol.* **13**, 9-24.

Edwards BR and Russell JK (1999). Northern Cordilleran volcanic province: a northern Basin and Range? *Geology* **27**, 243-246.

Edwards BR and Russell JK (2000). Distribution, nature and origin of Neogene-Quaternary magmatism in the Northern Cordilleran volcanic province, Canada. *Geol Soc., America Bulletin* **112**, 1208-1295.

Fiesinger DW and Nicholls J (1977). Petrography and petrology of Quaternary volcanic rocks, Quesnel Lake region, east-central British Columbia. *Geological Association of Canada* **16**, 25–40.

Foster HL, Forbes RB, and Ragan DM (1966). Granulite and peridotite inclusions from Prindle Volcano, Yukon-Tanana Upland, Alaska. United States Geological Survey. *Professional Paper* **550-B**, B115-B119.

Francis D (1987). Mantle-melt interaction recorded in spinel lherzolite xenoliths from the Alligator Lake volcanic complex, Yukon, Canada. *J. Petrol.* **28,** 569-597.

Fredricksen AW Bostock MG, VanDecar JC, and Cassidy J (1998). Seismic structure of the upper mantle beneath northern Canadian Cordillera from teleseismic travel-time inversion. *Tectonophysics* **294**, 43-55.

Fujii T and Scarfe CM (1982). Petrology of ultramafic nodules from West Kettle River, near Kelowna, Southern British Columbia. *Contrib. Mineral Petrol.* **80**, 297–306.

Gabrielse H and Yorath CJ (1991). Tectonic synthesis. *In*: Geology of the Cordilleran Orogen in Canada. Gabrielse H. and Yorath C. J. (eds.), *Geol. Survey of Can.* G-2, 677–706.

Gabrielse H, Monger JWH, Wheeler JO, and Yorath CJ (1991). Tectonic framework. *In*: Geology of the Cordilleran Orogen in Canada. Gabrielse, H. & Yorath, C.J. (eds), *Geological Society of America, Geology of North America Series* G-02, 13–28.

Gaetani GA, and Grove TL (1998). The influence of water on melting of mantle peridotite *Contrib. Mineral Petrol*. **131**(4), 323-346.

Ghent ED, Edwards BR, Russell JK, and Mortensen J (2007). Granulite facies xenoliths from Prindle volcano, Alaska: implications for the northern Cordilleran crustal lithosphere. *Lithos* **101**, 344-358.

Green TH, Adam J, Sie SH (1992) Trace element partitioning between silicate minerals and carbonatite at 25 kbar and application to mantle metasomatism. *Mineral Petrol* 46: 179-184.

Halama R, Savov IP, Rudnick RL, and McDonough WF (2009). Insights into Li and Li isotope cycling and sub-arc metasomatism from veined mantle xenoliths, Kamchatka. *Contrib. Mineral Petrol*. **158**(2), 197-222.

Handler MR, Bennet VC, and Esat TM (1997). The Persistence of Off-cratonic Lithospheric Mantle: Os Isotopic Systematics of Variably Metasomatized Southeast Australian Xenoliths. *Earth Planet. Sci. Lett.* **151**, 61-75.

Hansen VL (1990). Yukon-Tanana terrane: A partial acquittal. *Geology* **18**, 365-369.

Harder M, Russell JK (2006). Thermal state of the upper mantle beneath the Northern Cordilleran Volcanic Province (NCVP), British Columbia, Canada. *Lithos* **87**, 1-22.

Hart SR and Dunn T (1993). Experimental clinopyroxene/melt partitioning for 24 trace elements. *Contrib. Mineral Petrol.* **113**: 1-8.

Hart CJR and Villeneuve M (1999). Geochronology of Neogene alkaline volcanic rocks (Miles Canyon basalt), southern Yukon Territory, Canada: The relative effectiveness of laser ^{40}Ar/^{39}Ar and K-Ar geochronology. *Can. J. Earth Sci.* **36**, 1495-1508.

Hauri EH and Hart SR (1994). Constraints on melt migration from mantle plumes: a trace element study of peridotite xenoliths from Savai'i, Western Samoa. *J. of Geophys. Res.* **99**, 24301-24321.

Hellebrand E, Snow JE, Mostefaoui S, and Hoppe P (2005). Trace element distribution between orthopyroxene and clinopyroxene in peridotites from the Gakkel Ridge: a SIMS and NanoSIMS study. *Contrib. Mineral Petrol.* **150**(5), 486-504.

Hyndman RD and Hamilton TS (1993). Queen Charlotte area Cenozoic tectonics and volcanism and their association with relative plate motions along the northeastern Pacific margin. *J. of Geophys. Res.* **98**, 14 257-14 277.

Ickert RB, Thorkelson DJ, Marshall DD, and Ullrich TD (2009). Eocene adakitic volcanism in southern British Columbia: Remelting of arc basalt above a slab window. *Tectonophysics* **464**, 164-185.

Ionov DA, Chazot G, Chauvel C, Merlet C, and Bodinier JL (2006a). Trace element distribution in peridotite xenoliths from Tok, SE Siberian craton: a record of pervasive, multi-stage metasomatism in shallow refractory mantle. *Geochim. Cosmochim. Acta* **70**(5), 1231-1260.

Ionov DA, Shirey SB, Weis D, and Brügmann G (2006b). Os–Hf–Sr–Nd isotope and PGE systematics of spinel peridotite xenoliths from Tok, SE Siberian craton: effects of pervasive metasomatism in shallow refractory mantle *Earth Planet. Sci. Lett*. **241**(1-2), 47-64.

Jacques AL and Green DH (1980). Anhydrous melting of peridotites at 0-15 kbar pressure and the genesis of tholeiitic basalts. *Contrib. Mineral Petrol.* **73**, 287-310.

Johnson KTM, Dick HJB, and Shimizu N (1990). Melting in the oceanic mantle: an ion probe study of diopsides in abyssal peridotites. **95**, 2661-2678.

Kelemen PB (1990). Reaction between ultramafic wall rock and fractionating basaltic magma, I, Phase relations, the origin of calc-alkaline magma series, and the formation of discordant dunite. *J. Petrol.* **31**, 51-98.

Kelemen PB and Dick HJB (1995). Focused melt flow and localized deformation in the upper mantle: juxtaposition of replacive dunites and ductile shear zones in the Josephine peridotite, SW Oregon. *J. of Geophys. Res.* **100**, 423-438.

Kelemen PB, Dick HJB, and Quick JE (1992). Formation of harzburgite by pervasive melt/rock reaction in the upper mantle. *Nature* **358**, 635-641.

Kelemen PB, Shimizu N, and Salters JM (1995). Extraction of midocean ridge basalt from the upwelling mantle by focused flow of melt in dunite channels. *Nature* **375**, 747-753.

Kelemen PB, Hirth G, Shimizu N, Spiegelman M, and Dick HJB (1997). A review of melt migration processes in the adiabatically upwelling mantle beneath oceanic spreading ridges. *Phil. Trans. Roy. Soc. Lon.*, Series A **355**, 283-318.

Kilgore ML, Peslier AH, Brandon AD, and Lamb WM (2018). Water and Oxygen Fugacity in the Lithospheric Mantle Wedge beneath the Northern Canadian Cordillera (Alligator Lake). *Geochem. Geophys. Geosyst. (G^3)*, **19**(10), 3844-3869.

Klemme S (2004). The influence of Cr on the garnet-spinel transition in the Earth's mantle: experiments in the system MgO-Cr_2O_3-SiO_2 and thermodynamic modeling. *Lithos* **77**(1-4), 639-646.

Madsen JK, Thorkelson DJ, Friedman RM, and Marshall DD (2006). Cenozoic to Recent plate configurations in the Pacific Basin: Ridge subduction and slab window magmatism in western North America. *Geosphere* **2**, 11-34.

McBride JS, Lambert DD, Greig A, and Nicholls IA (1996). Multistage evolution of Australian subcontinental mantle: Re-Os isotopic constraints from Victorian mantle xenoliths. *Geology* **24**, 631–634.

McDonough WF and Frey FA (1989). Rare Earth elements in upper mantle rocks. *In*: Geochemistry and mineralogy of rare Earth elements. Lupin B. and McKay G.R. (eds), *Mineral Soc. Am.*, Washington, DC, 99-146.

McDonough WF and Sun SS (1995). The composition of the Earth. *Chem. Geo.*, **120**(3-4), 223-253.

Menzies M (1983). Mantle Ultramafic Xenoliths in Alkaline Magmas: Evidence for Mantle Heterogeneity Modified by Magmatic Activity. *In*: Continental Basalts and Mantle Xenoliths. Hawkesworth C. J. and Norry M. J. (eds.), **272**. Shiva Publishing Limited.

Monger JWH, Price RA, and Tempelman-Kluit DJ (1982). Tectonic accretion and the origin of the two major metamorphic and plutonic welts in the Canadian Cordillera. *Geology* **10**, 70–75.

Morris GA and Creaser RA (2003). Crustal recycling during subduction at the Eocene Cordilleran margin of North America: a petrogenic study from the southwestern Yukon. *Can. J. Earth Sci.* **40**, 1805-1821.

Mortensen JK (1992). Pre-mid-Mesozoic tectonic evolution of the Yukon–Tanana terrane, Yukon and Alaska. *Tectonics* **11**, 836–853.

Mysen BO, Kushiro I (1977) Compositional variations of coexisting phases with degree of melting of peridotite in the upper mantle. *Am. Min.* **62**, 843-865.

Nelson JL, Colpron M, Piercey SJ, Dusel-Bacon C, Murphy DC, and Roots CF (2006). Paleozoic tectonic and metallogenic evolution of the pericratonic terranes in Yukon, northern British Columbia and eastern Alaska. *In*: Paleozoic evolution and Metallogeny of Pericratonic Terranes at the Ancient Pacific Margin of North America. Colpron M., and Nelson J.L (eds.), *Canadian and Alaskan Cordillera: Geological Association of Canada Special Paper* **45**, 323-360.

Nicholls J, Stout MZ, and Fiesinger DW (1982). Petrologic variations in Quaternary volcanic rocks, British Columbia, and the nature of the underlying upper mantle: *Contrib. Mineral Petrol.* **79**, p. 201–218.

Nickel KG (1986). Phase equilibria in the system SiO_2-MgO-Al_2O_3-CaO-Cr_2O_3 (SMACCR) and their bearing on spinel/garnet lherzolite relationships. *N. Jb. Min. Abh.* **155**, 259-287.

Nimis P and Taylor WR (2000). Single-clinopyroxene thermobarometry for garnet peridotites: part I. Calibration and testing of a Cr-in-Cpx barometer and an enstatite-in-Cpx thermometer. *Contrib. Mineral Petrol.* **139**, 541-554.

Olive V, Ellam RM, and Harte B (1997). A Re-Os isotope study of ultramafic xenoliths from the Matsoku kimberlite. *Earth Planet. Sci. Lett.* **150**, 129–140.

Paton C, Hellstrom J, Paul B, Woodhead J, and Hergt J (2011) Iolite: Freeware for the visualisation and processing of mass spectrometric data. *Journal of Analytical Atomic Spectrometry* **26**(12), 2508.

Pearson DG, Carlson RW, Shirey SB, Boyd FR, and Nixon PH (1995a). Stabilization of Archean lithospheric mantle: A Re-Os isotope study of peridotite xenoliths from the Kaapvaal craton. *Earth Planet. Sci. Lett.* **134**, 341–357.

Pearson DG et al. (1995b). Re-Os, Sm-Nd, and Rb–Sr isotope evidence for thick Archean lithospheric mantle beneath the Siberian craton modified by multistage metasomatism. *Geochim. Cosmochim. Acta.* **59**, 959–977.

Perkins D and Anthony EY (2011). The evolution of spinel lherzolite xenoliths and the nature of the mantle at Kilbourne Hole, New Mexico. *Contrib. Mineral Petrol.* **162**, 1139-1157.

Peslier AH, Reisberg L, Ludden J, and Francis D (2000a). Re-Os constraints on harzburgite and lherzolite formation in the lithospheric mantle: A study of Northern Canadian Cordillera xenoliths. *Geochim. Cosmochim. Acta.* **64**, 3061-3071.

Peslier AH, Reisberg L, Ludden J, and Francis D (2000b). Os isotropic systematics in mantle xenoliths; age constraints on the Canadian Cordillera lithosphere. *Chem. Geol.* **166**, 85-101.

Peslier AH, Francis D, and Ludden J (2002). The lithospheric mantle beneath continental margins: melting and melt-rock reaction in Canadian Cordillera xenoliths. *J. Petro.* **43**, 2013-2047.

Piccardo GB and Vissers RLM (2007). The pre-oceanic evolution of the Erro-Tobbio peridotite (Voltri Massif, Ligurian Alps, Italy). *Journal of Geodynamics* **43**, 417-449.

Piccardo GB, Zanetti A, and Muntener O (2007). Melt/peridotite interaction in the Southern Lanzo peridotite: Field, textural and geochemical evidence. *Lithos* **94**, 181-209.

Piercey SJ, Murphy DC, Mortensen JK, and Paradis S (2001). Boninitic magmatism in a continental margin setting, Yukon-Tanana terrane, southeastern Yukon, Canada. *Geology* **29**, 8 731-8 734.

Quick JE (1981). The origin and significance of large, tabular dunites bodies in the Trinity peridotite, Northern California. *Contrib. Mineral Petrol.* **78**, 413-422.

Rampone E and Borghini G (2008). The melt intrusion/interaction history of the Erro-Tobbio peridotites (Ligurian Alps, Italy): Insights on mantle processes at non-volcanic passive margins. *European Journal of Mineralogy* **20**, 573-585.

Rampone E, Piccardo GB, and Hofmann AW (2008). Multi-stage melt-rock interaction in the Mt. Maggiore (Corsica, France) ophiolitic peridotites: microstructural and geochemical records. *Contrib. Mineral Petrol.* **156**, 453-475.

Rampone E, Vissers RLM, Poggio M, Scambelluri M, and Zanetti A (2009). Melt migration and intrusion during exhumation of the Alboran lithosphere: the Tallante mantle xenolith record (Betic Cordillera, SE Spain). *J. Petro.*, **51**(1-2), 295-325.

Ranalli G (1980). Rheological properties of the upper mantle in Canada from olivine microrheology. *Can J Earth Sci.* **17**, 1499-1505.

Ross JV (1983). The nature and rheology of the cordilleran upper mantle of British Columbia: inferences from peridotite xenoliths. *Tectonophysics* **100**, 321–357.

Roughley C, Edwards BR, and Russell JK (2000). Crustal-derived xenoliths from Prindle Volcano. Alaska: implications for the lithospheric stratigraphy of the central Yukon-Tanana terrane. *GAC-MAC 2000 Annual Meeting Program with Abstracts, Calgary, AB, Poster*, **171**.

Sen G and Leeman WP (1991). Iron-rich lherzolite xenoliths from Oahu: origin and implications for Hawaiian magma sources. *Earth Planet Sci. Lett.* **102**, 45-57.

Seyler M, Lorand JP, Dick HJB and Drouin M (2007). Pervasive melt percolation reactions in ultra-depleted refractory harzburgites at the Mid-Atlantic Ridge, 158200N: ODP Hole 1274A. *Contrib. Mineral Petrol.* **153**, 303-319.

Shaw DM (1979). Trace element melting models. *Physics and Chemistry of the Earth* **11**, 577-586.

Shi L, Francis D, Ludden J, Frederikson A, and Bostock M (1998). Xenolith evidence for lithospheric melting above anomalously hot mantle under the northern Canadian Cordillera. *Contrib. Mineral Petrol.* **131**, 39-53.

Shimizu N (1975). Rare earth elements in garnets and clinopyroxenes from garnet lherzolite nodules in kimberlites. *Earth Planet Sci Lett.* **25**, 26-32.

Simon NSC, Neumann ER, Bonadiman C, Coltorti M, Delpech G, Gregoire M, and Widom E (2008). Ultra-refractory domains in the oceanic mantle lithosphere sampled as mantle xenoliths at ocean islands. *J. Petro.* **49**, 1223-1251.

Sinclair PD, Tempelman-Kluit DJ, and Medaris Jr. LG (1978). Lherzolite nodules from a Pleistocene cinder cone in central Yukon. *Can. J. Earth Sci.* **15**, 220-226.

Sun M and Kerrich R (1995). Rare earth element and high field strength element characteristics of whole rocks and mineral separates of ultramafic nodules in Cenozoic volcanic vents of southeastern British Columbia, Canada. *Geochimica et Cosmochimica Acta* **59**, 4863–4879.

Sun M, Armstrong RL and Maxwell RJ (1991). Proterozoic mantle under Quesnellia: variably reset Rb–Sr mineral isochrons in ultramafic nodules carried up in Cenozoic volcanic vents of the southern Omenica Belt. *Can. J. Earth Sci.* **28**, 1239–1253.

Taylor WR (1998). An experimental test of some geothermometer and geobarometer formulations for upper mantle peridotites with application to the thermobarometry of fertile lherzolite and garnet websterite. *N. Jb. Min. Abh.* **172**, 381-408.

Tempelman-Kluit DJ (1977). Transported cataclastic, ophiolite and granodiorite in Yukon: Evidence of arc-continent collision. *Geol. Survey of Can.* **79-14**, 27-28.

Thorkelson DJ and Taylor RP (1989). Cordilleran slab windows. *Geology* **17**, 833-836.

Thorkelson DJ, Madsen JK, and Sluggett CL (2011). Mantle flow through the Northern Cordilleran slab window revealed by volcanic geochemistry. *Geology* **39**, 267-270.

Walker RJ, Carlson RW, Shirey SB, and Boyd FR (1989). Os, Sr, Nd, and Pb isotope systematics of southern African peridotite xenoliths: implications for the chemical evolution of subcontinental mantle. *Geochim. Cosmochim. Acta.* **53**, 1583-1595.

Wells PRA (1977). Pyroxene thermometry in simple and complex systems. *Contrib. Mineral Petrol.* **62**, 129-139.

Williams H, Turner FJ, and Gilbert CM (1954). Petrography: An Introduction to the Study of Rocks in Thin Sections. W.H. Freeman and Co., 197p.

Wilson FH, Smith JG, and Shaw N (1985). Review of radiometric data from the Yukon Crystalline Terrane, Alaska and Yukon Territory. *Can. J. Earth Sci.* **22**, 525-537.

Wittig N, Baker JA, and Downes H (2006). Dating the mantle roots of young continental crust. *Geology*, **34**(4), 237-240.

Wood CA and Kienle J (1990). Volcanoes of North America: United States and Canada. Cam. Univ. Press, 354p.

Workman RK and Hart S R (2005). Major and trace element composition of the depleted MORB mantle (DMM). *Earth Planet Sci Lett.*, **231**(1-2), 53-72.

Wörner G, Zipfel J (1996). A mantle P-T path for the Ross Sea rift margin, Antarctica, derived from mineral zoning in peridotite xenoliths. *Geol. Jb. B.* **89**, 157-167.

Xue X, Baadsgaard H, Irving A, and Scarfe C (1990). Geochemical and isotopic characteristics of lithospheric mantle beneath West Kettle River, British Columbia: evidence from ultramafic xenoliths. *J. of Geophys. Res.* **95**, 15879–15891.